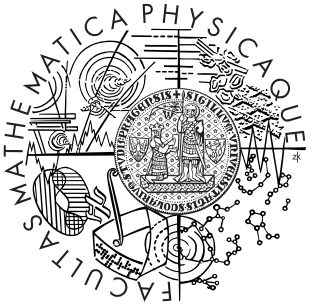
Charles University in Prague

Faculty of Mathematics and Physics

DOCTORAL THESIS



Matthieu Quinquis

A numerical study of subduction zone dynamics using linear viscous to thermo-mechanical model setups including (de)hydration processes

Department of Geophysics

Supervisor: doc. RNDr. Ondřej Čadek, CSc.
Consultant: RNDr. Susanne Buiter, DrSc.

Study programme: Physics
Specialization: Geophysics

Prague 2014

Acknowledgements

I guess it is time for me to try and start to write the "remerciements" for my thesis. This is really not my strong point but I'll try to avoid forgetting and/or upsetting people. I guess that first I have to mention that this thesis was financed by the European Commission through Marie-Curie Research Training Network "c2c" (contract MRTN-CT-2006-035957). Without this financing I would never have had the possibility to try and learn the wildly spoken Norwegain bokmål.

The person who deserves the most credit and that I should have thanked first is my supervisor **Susanne Buiter**. Thank you for your perseverance, your patience and your endless comments and inputs. The amount of stuff you have taught me is unbelievable and I could never thank you enough. Many thanks, also, to my other supervisor **Ondřej Čadek** for all his lessons and his help dealing with the obscure world of Czech administration (not that it is any more obscure than the French or Norwegian ones) and giving me the possibility to see the beautiful city of Praha.

Thanks also to all my, one time, colleagues of the Geodynamics team and NGU. Thanks to all the morning coffee guys for your healthy dose of sarcasm, **Trond Torsvik**, **Bernard Steinberger**, **Per Terje Osmundsen**, **Tim Redfield**, **Bart Hendriks**, **Bernard Bingen**, **Marc Smethurst**, **Robin Watson** and last but far from least **Morgan Garnerød**. Lets not forget the women, **Carmen Gaina**, **Cinthia Labails** and **Katja Svendby**, who for some reason left us "men" alone. I have to also mention my office mate **Reza Khabbaz Ghazian**, the calming presence. A special "merci" goes out to **Joya Tetreault**, who has help me in more ways than I can mention, and **Zurab Chemia**, who was never an early riser.

I must not forget to thank all my co-authors for their participation / help / time / input. The numerical modellers: **Susan Ellis**, **Anne Glerum**, **Petra Maierová**, **Lena Noack**, **Javier Quinteros**, **Cédric Thieulot** and **Nicola Tosi**; and the petrologist **David Dolejš**.

I would also like to thank all the people involved in the c2c project. Many thanks to **Gerd Steinle-Newmann** for putting the network together, and giving us the opportunity to travel around Europe. But also, thanks to all the ER and ESR for the interesting discussions, in domains that I still do not fully understand and for the good times spent together. So thanks **Johannes**, **Etore**, **Michael**, **Richard**,

Julien, **Giacomo**, **Alberto**, **Nico**, **Marco**, **Ute**, **Alexandra** and all those I could, and most likely, have forgotten.

I also have to thank all the people that have helped me along the way and during my different travels, **Hanka Čížková**, **Max Schmidt**, **James Connolly** and **Mark Caddick**. Again I'm sure I have forgotten to mention some people so, sorry.

And now for the friends and family. Tussen takk to all you "Norwegians" out there who helped me live through those cold summers and even colder winters up north. My beer belly especially wanted to thank you all personally, **Nicola**, **Laura**, **Alkesandro**, **Jim**, **Sigrid**, **Mette**, **Luca**, **Stien**, **Aurélien**, **Alenka**, **Jadranka**, **Sofie** ... I'm sure I missed some so sorry about that.

Je vais, malheureusement, devoir changer de langue pour finir. Merci à tous mes amis restés en France. Je ne vous nommerais pas personnellement, ça ferait trop de noms. Merci à ceux qui pensaient toujours à moi à la sixème bouteille des soirées mecs. Il faut aussi ajouter la bande du 93. Votre absence de compréhension total de TOUT ce que je pouvais vous expliquer a été un vrai bonheur. Un jour, je vais vous forcer à la lire cette thèse. J'ai aussi une petite pensée pour mes "copines de Fac" ... j'y suis arrivé à la fin. Et Je ne vais surtout pas oublier mes parents. **Maman** et **Papa**, cette photes elle est pour vous ! **Emily**, tu n'as servi à rien alors je ne te remercie pas, même si je pense à toi.

Marion, je vais finir par toi, et pour la peine tu as le droit à un paragraphe à toi toute seule. Je voulais surtout te remercier, toi qui en as le plus souffert après moi. Tu as toujours eu l'intelligence et surtout la patience de ne jamais pousser. Cette attention, à elle seule, est la raison pour laquelle cette "œuvre" est pour toi.

I'm pretty sure that I've forgotten some people but let's stop here and finish with a literal translation from French to Norwegian and at the same time a very common mistake:

Takk for alt !
(and no, I will not dissapear just yet)

I declare that I carried out this doctoral thesis independently, and only with the cited sources, literature and other professional sources.

I understand that my work relates to the rights and obligations under the Act No. 121/2000 Coll., the Copyright Act, as amended, in particular the fact that the Charles University in Prague has the right to conclude a license agreement on the use of this work as a school work pursuant to Section 60 paragraph 1 of the Copyright Act.

In Prague, date: ..... Signature

Název práce: Numerické studium dynamiky subdukčních zón: Od lineárně viskózních k termo-mechanickým modelům zahrnujícím hydratační a dehydratační procesy.
Autor: Matthieu Quinquis.
Katedra / Ústav: Katedra geofyziky, Matematicko-fyzikální fakulta / Karlova Univerzita v Praze.
Vedoucí doktorské práce: doc. RNDr. Ondřej Čadek, CSc.
Konzultant: RNDr. Susanne J.H. Buiter, DrSc.

Abstrakt:

Subdukční zóny představují složité systémy, které vykazují různé typy materiálového chování, tavení a (de)hydrataci, a to na časových škálách v rozsahu vteřin (zemětřesení) až po desítky miliónů let (plašťové tečení). Zahrnutí takto složitého chování v rámci numerického modelu představuje velmi obtížný úkol jak z hlediska fyzikálních procesů, které musí být v modelu uvažovány, tak i z hlediska numerického a výpočetního. Numerické modely proto často systém zjednodušují, např. tím, že redukují velikost výpočetní oblasti, uměle snižují viskózní kontrasty, používají zjednodušené hraniční podmínky nebo aproximují pohyb vody a taveniny v plašťovém klínu pomocí přibližných rovnic. Cílem této práce je ukázat, jak taková zjednodušení v zadání numerického modelu mohou ovlivnit mechanický vývoj subdukčního systému. První sada experimentů ukazuje, jak numerická implementace hraničních podmínek v modelu zahrnujícím svrchní plašť může ovlivnit, zda se subdukční zóna pohybuje ve směru pohybu desky (trench advance) nebo naopak ustupuje (trench retreat). Hraniční podmínky mohou také určovat tvar litosférické desky zanořené do svrchního pláště. Abychom odlišili vliv zjednodušení modelu od efektů souvisejících s použitím konkrétní numerické metody, vytvořili jsme soubor různě složitých modelových uspořádání a požádali jsme několik pracovníků, používajících různé programy, aby spočetli příslušná řešení. Srovnání těchto výsledků ukazuje, že čím jednodušší je modelové uspořádání, tím větší je shoda mezi jednotlivými výsledky. Modely s newtonovskou viskozitou vykazují pouze pětiprocentní rozptyl základních kvantitativních parametrů, jako je např. sklon subdukce nebo L_2 norma rychlosti. S rostoucí složitostí reologického popisu se rozdíly ve výsledcích zvětšují, ale základní charakter subdukčního procesu zůstává u všech modelů zachován. Poslední sada experimentů pak ukazuje, jak numerická metoda, zvolená pro výpočet migrace volné vody uvnitř plášťového klínu, ovlivňuje prostorové rozložení hydratovaného plašťového materiálu. Tento hydratovaný materiál zde vzniká v důsledku dehydratace zanořující se litosférické desky a zpětně ovlivňuje mechanický vývoj subdukčního systému. Výsledky experimentů ukázané v této práci mohou poskytnout ostatním pracovníkům v oblasti numerického modelování vodítko k testování

jejich vlastních programů a k základnímu pochopení vlivu jednotlivých modelových parametrů na vývoj subdukce.

Klíčová slova: Subdukce, numerické modelování, migrace vody, hraniční podmínky, srovnávací testy, reologie.

Title: - A numerical study of subduction zone dynamics using linear viscous to thermo-mechanical model setups including (de)hydration processes.
Author: Matthieu Quinquis.
Department / Institute: Department of Geophysics, Faculty of Mathematics and Physics, Charles University in Prague.
Supervisor of the doctoral thesis: doc. RNDr. Ondřej Čadek, CSc.
Consultant: RNDr. Susanne J.H. Buiter, DrSc.

Abstract:

Subduction zones are complex systems that include different types of material behaviour, several time-scales from short-term earthquakes to long-term mantle flow, and melting and (de)hydration processes. These complexities can be challenging to include in numerical experiments, both from a physics perspective of representing a process in equations, and from a numerical perspective of keeping calculation times reasonable. Numerical models therefore often simplify the system, by, for example, limiting the size of the model domain, reducing viscosity contrasts, using simple boundary conditions, or approximating water and melt migration through the mantle wedge with simplified equations. The aim of this thesis is to show how simplifications in the set-up of a numerical model could affect the mechanical evolution of the modelled subduction system. A first set of experiments shows how the numerical implementation of surface, side and bottom boundary conditions in an experiment on the scale of the upper mantle can determine whether the model slab will evolve through trench advance or trench retreat. The boundary conditions can also control the large-scale geometry of the subducted slab in the upper mantle. In order to allow a first-order appraisal of the effects of model set-up versus the potential effects of numerical software, a set of model set-ups was created that evolve from linear viscous to thermo-mechanical rheologies. These were run by various modellers with different numerical codes. The more simplified the model set-up, the more similar the results of the different codes are. Linear viscous models provide very similar results, within 5% variability in quantitative parameters such as slab tip depth and root-mean-square velocities. Increasing the rheological complexity increases the differences in results, even though the general model evolution remains similar between codes. A last series of experiments shows how the numerical method for implementing the migration of free water affects the spatial distribution of hydrated mantle material in the mantle wedge that results from slab dehydration, The water distribution in turn affects the mechanical evolution of the subduction system. The experiments in this thesis provide a possible starting point for other numerical modellers for their study of subduction zones by providing them with a series of detailed model setups that can be used to test modelling software, obtain a first-order understanding of the effects

of slab rheology on subduction evolution, and estimate the level of complexity of water migration mechanisms required in a model simulation.

Keywords: Subduction, Numerical Modeling, Water Migration, Boundary Conditions, Benchmark, Rheology.

Contents

1 Introduction **1**
- 1.1 Convergent plate margins . . . 1
- 1.2 Subduction models . . . 4
  - 1.2.1 Models of the first order dynamics of subduction . . . 5
  - 1.2.2 Thermo-mechanical subduction models and the role of rheology . . . 8
  - 1.2.3 Numerical modelling of (de)hydration processes . . . 11
- 1.3 Open questions in subduction modelling . . . 15
- 1.4 Layout of this thesis . . . 17

2 Methods **19**
- 2.1 Description of SULEC . . . 19
- 2.2 Thermodynamic calculations . . . 21
  - 2.2.1 The basics of equilibrium dynamics . . . 21
  - 2.2.2 Chemical equilibrium . . . 23
  - 2.2.3 Perple_X . . . 26
- 2.3 The implementation of dehydration processes into SULEC . . . 29
  - 2.3.1 Determining water content . . . 29
  - 2.3.2 Water migration schemes . . . 30
  - 2.3.3 The influence of water content on viscosity . . . 33

3 The role of boundary conditions in numerical models of subduction **35**
- 3.1 Introduction . . . 36
- 3.2 Modelling method . . . 38
  - 3.2.1 Numerical approach . . . 38
  - 3.2.2 Model setup . . . 40
- 3.3 The influence of the surface boundary in gravitational subduction models . . . 45
- 3.4 Ocean-ocean subduction models . . . 50
  - 3.4.1 The influence of the lateral boundary conditions . . . 50

3.4.2 The influence of the bottom boundary condition 52
3.4.3 The influence of the surface boundary 53
3.5 Discussion 56
3.5.1 The role of the surface boundary 56
3.5.2 The role of the lateral and bottom boundary conditions . . 58
3.6 Conclusions 60

4 A numerical comparison study of thermo-mechanical subduction 62
4.1 Introduction 63
4.2 Numerical Approach 64
4.2.1 Equations for Thermo-Mechanical Slow Flows 64
4.2.2 Description of the Numerical Codes 65
4.3 Constraints on Lithology and Rheology of the Lithosphere and Mantle 68
4.3.1 Petrological Model of the Oceanic Lithosphere 68
4.3.2 Composition and Rheology of the Upper Mantle 69
4.4 Modeling Approach 70
4.4.1 General Model Setup 70
4.4.2 Model Cases from Linear Viscous to Thermo-Mechanical 72
4.4.3 Common Output Values 77
4.5 Results 78
4.5.1 Case 1: Linear Viscous Models 78
4.5.2 Case 2: Linear Viscous Model with Temperature Evolution 82
4.5.3 Case 3: Simplified Thermo-Mechanical Models 85
4.5.4 Case 4: Full Thermo-Mechanical Model 86
4.6 Discussion 91
4.7 Conclusions 93
4.A The Effects of a True Free Surface 93
4.B The Effects of Density Contrast Between Lithosphere and Mantle in Case 1 Models 97

5 Testing the effects of basic numerical implementations of water migration on models of subduction dynamics 105
5.1 Introduction 106
5.2 Modelling approach 109
5.2.1 Thermo-mechanical equations 109
5.2.2 Calculation of water content 111
5.2.3 Water migration schemes 113
5.3 The effects of (de)hydration on a simple model of a sinking wet cylinder 117
5.3.1 Simple model of a sinking cylinder 117

5.3.2 Sinking cylinder results 119
5.3.3 Sinking cylinder discussion 123
5.4 The effects of (de)hydration on subduction 124
5.4.1 Subduction model setup 124
5.4.2 Subduction model results 127
5.4.3 Subduction model discussion 135
5.5 Conclusions 138

6 Discussion **140**

7 Conclusions **143**

References **145**

Chapter 1

Introduction

1.1 Convergent plate margins

The basic hypothesis of plate tectonics as given by Morgan (1968) states that the outer shell of the Earth is divided into a number of thin, rigid plates that are in relative motion with respect to one another. The contact zones between the plates can form three different types of margins: (1) Transform margins, where the plates slide along each other, such as the North Anatolian fault or the San Andreas fault; (2) Divergent margins (constructive margins), where the plates move away from each other, such as the Mid Atlantic Ridge, and (3) Convergent margins (destructive margins), where plates move towards each other, such as, the Western South America (Andean) margin and the boundary between North India and Eurasia, which is marked by the Himalayas (Fig. 1.1). This thesis, focuses on convergent margins where one plate subducts under the other into the mantle below.

Subduction is the only known process which allows recycling of material into the mantle (Fig. 1.2). Subduction involves oceanic plates and often continental plates. At ocean-ocean type subduction zones, an oceanic plate subducts under an other oceanic plate, such as for example, the subduction of the Pacific plate under the Philippine plate at the Izu-Bonin and Mariana trenches. At ocean-continent type subduction zones, an oceanic plate subducts under a continental plate, such as, under the Andes where the Nazca plate subducts under the South American plate. Continental subduction has been put forward in the Alps and the Himalayas (Molnar and Gray, 1979; Pysklywec et al., 2000, 2002; Toussaint et al., 2004c,a; Burov and Toussaint, 2007).

Although these different types of subduction can cause different deformation and volcanic signals, especially in the overriding plate, they share many characteristic structures (Fig. 1.2). Examples are the trench at the plate contact, where

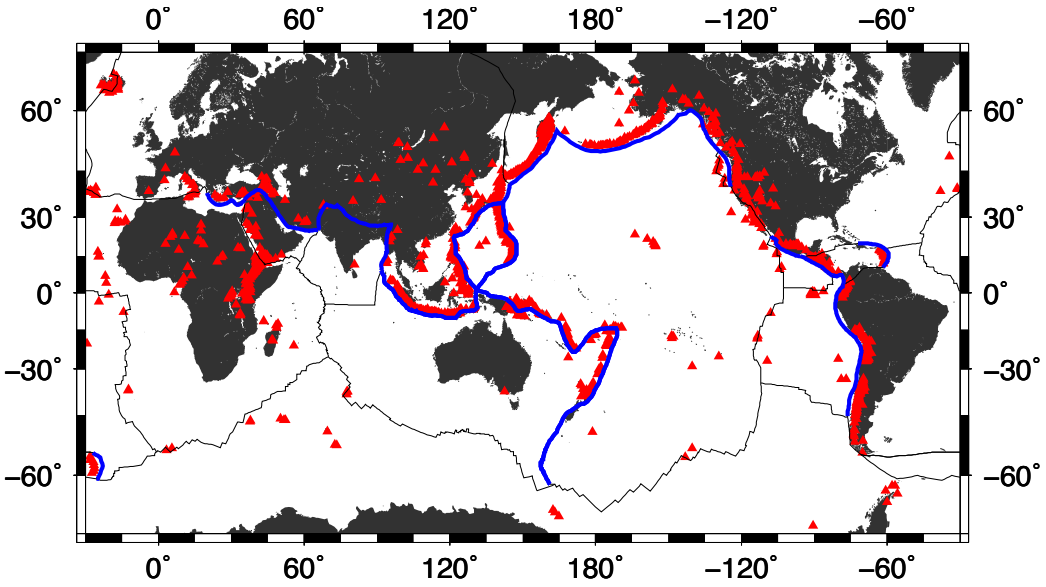


FIGURE 1.1 – Map of the plate boundaries (black lines) and subduction zones (blue lines), as defined in NUVEL-1A (DeMets et al., 1994). The location of volcanoes are in red (Siebert and Simkin, 2002). Most volcanoes are grouped into curved arcs (the volcanic arcs or island arcs) that are parallel to the trenches. This is particularly visible around the Pacific plate, the so-called 'Ring of fire'.

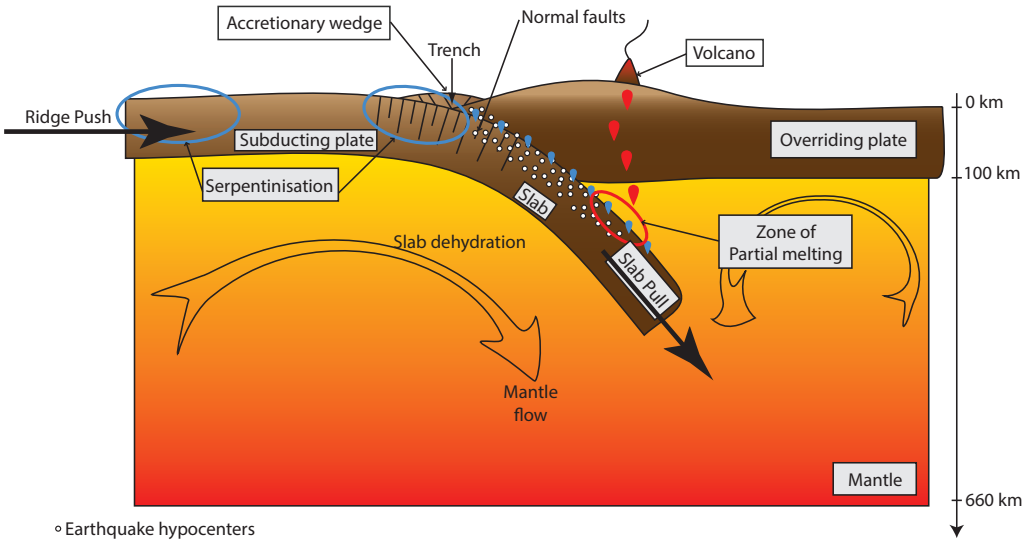


FIGURE 1.2 – Cartoon of the main processes occurring in a subduction system.

an accretionary wedge may form, the flexural bulge of the subducting plate, and seismic and volcanic hazards. The largest magnitude and deepest earthquakes are

found at subduction zones (Fig. 1.3). These earthquakes occur at the interplate interface and within the cold subducting slab. This region of seismic activity within the slab is called the Waditi-Beniof plane. In contrast to detachment zones in continents, where the seismogenic zone extends to a depth of approximately 40 km (Tichelaar and Ruff, 1993), earthquakes in subduction zones earthquakes are observed down to the base of the upper mantle, at a depth of approximately 670 km (Fig. 1.3). The overriding plate is marked by a zone of volcanism (Fig. 1.1). It is hypothesized that the location of these volcanoes is related to slab dehydration processes that result in partial melting of the mantle (Stern, 2002; Syracus and Abers, 2006; Bebout, 2007) (Fig. 1.2).

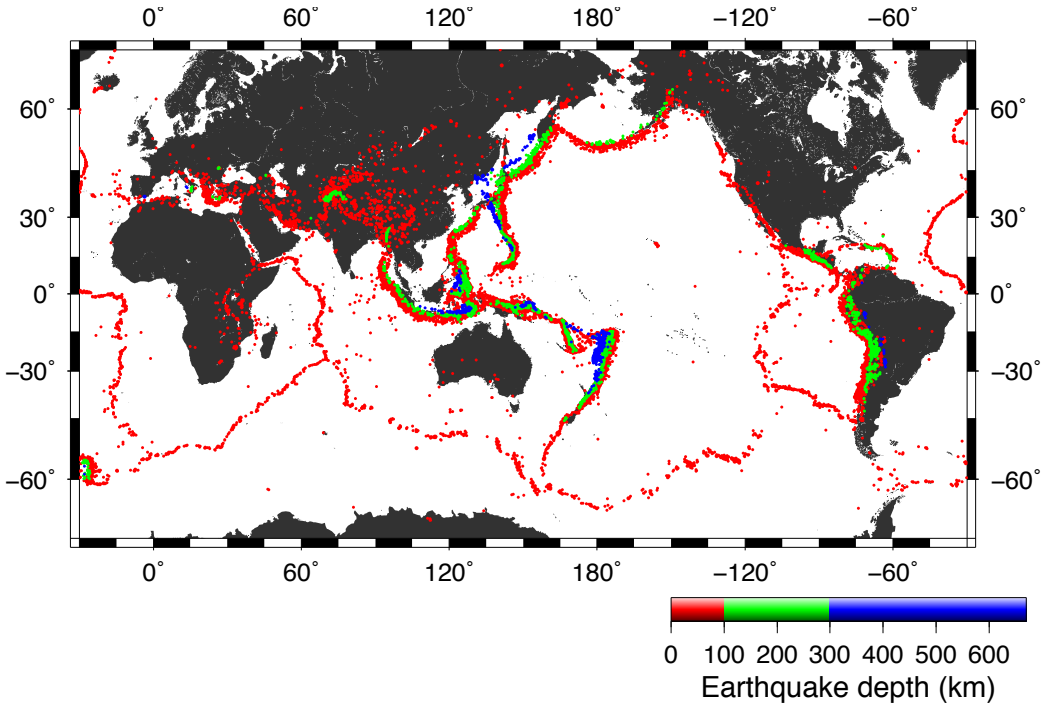


FIGURE 1.3 – Location of upper mantle earthquakes (down to a depth of 670 km) with a magnitude over 4.5 that occurred over the last 5 years. Shallow earthquakes are in red, intermediate earthquakes in green, and deep earthquakes in blue. The earthquake database is from NEIC http://earthquake.usgs.gov/earthquakes/. The polarity of subduction is shown by the distribution of earthquakes, the deep earthquakes are located furthest away from the trench.

It is debated wether subduction is a passive or active signal of mantle convection. In the passive view subduction is the surface manifestation of mantle convection and the lithosphere is the top thermal boundary of the convecting mantle (Schubert et al., 2001). However, a simplified view of the force balance shows that at least regionally subduction is driven by a combination of two forces: ridge push and slab

pull (Fig. 1.2). Ridge push is caused by the lateral density difference in the oceanic plate. As the oceanic plate ages the density and thickness of the plate age increases. Slab pull is caused by the buoyancy contrast between the cold and dense oceanic subducting slab and the hot and less dense upper mantle. The dense lithosphere sinks into the mantle, pulling the attached surface plate. These two forces can be extended to include additional resisting forces, such as, slab bending and friction on the plate interface, and additional driving forces, such as, the density increase associated with the Olivine to wadsleyite phase transition which occurs at a depth of 410 km (Billen, 2008).

The processes that occur during subduction influence the dynamics of the subduction system in different ways and can even interact with each other. Understanding the general evolution of subduction could give further insights into the dynamics of plate tectonics and mantle convection, and hopefully bring us a step further in linking the two together.

1.2 Subduction models

Subduction is a large-scale process that occurs from Earth's surface down to possibly the core-mantle boundary. It also represents a large amount of deformation over geological time scales (*i.e.*, over millions of years). This makes it challenging to observe the system, as we can only use direct information from the surface and need to rely on indirect imaging methods for the subsurface slab and on geological and geophysical interpretations for the past history of subduction zones. Geological and geophysical observations give a snapshot of subduction systems at different stages of evolution and yield information on their geometry, instantaneous surface motions, stress and deformation. To understand the evolution of subduction systems and their sensitivity to, for example, plate strength or subduction velocity, models can be a useful tool. Numerical and analogue models of subduction help to obtain insight into the evolution of the system, with a quantitative basis. However, the simplifications and assumptions that are unavoidable when building a model of subduction imply that we never obtain a complete image of the system. For example, 2 -D models of subduction zones can not give information on the poloïdal flow (*i.e.*, the flow of the mantle in the horizontal plane of the model) (Funiciello et al., 2006; Piromallo et al., 2006) or the influence of lateral plates (Yamato et al., 2009). Linear viscous models of subduction (Schmeling et al., 2008; Yamato et al., 2009; Quinquis et al., 2011) can not explain the seismic distribution observed at convergent plate margins (Isacks and Molnar, 1969; Wadati, 1935; Tichelaar and Ruff, 1993). However, models are convenient tools to perform parametrical studies that focus on the influence of a specific parameter or process on the dynamics of the system (Capitanio et al., 2010; Čížková et al., 2002; Di Giuseppe et al., 2008;

Enns et al., 2005; Quinquis et al., 2011). Numerical and analogue models have greatly improved our understanding of subduction zones.

This thesis focuses on upper-mantle scale (*i.e.*, down to a depth of 670 km) numerical models of subduction, which span several millions of years. These models are used to investigate the dynamic behaviour of slabs in response to numerical, rheological and physical variations in the system. In the next section, examples of previous subduction models are discussed: (1) Simplified models of subduction, that study the first-order behaviour of the system; (2) models that are used to investigate the influence of rheology on subduction dynamics, and (3) models with (de)hydration processes, focussing on the effects of hydration and dehydration processes on the dynamics of the system.

1.2.1 Models of the first order dynamics of subduction

Several studies have successfully explained first-order aspects of subduction zones by simplifying the system considerably. These simplifications mainly concern the rheology and the geometry. Linear viscous rheologies eliminate some of the complex pressure- and temperature-dependent feedback relationships, allowing a more straightforward investigation of the effects of buoyancy and driving forces. These types of models often focus on the geometry of the subducting slab at depth (*i.e.*, the interaction of the slab tip with the bottom of the model domain) and the migration of the trench (*i.e.*, advancing, retreating or stationary). Their results can be compared to geophysical data, such as tomographic images of subduction zones, and GPS data, that give present-day trench migration velocities.

A further simplification is to neglect the influence of the overriding plate on the dynamics of the system. This class of models, with no overriding plate, is called gravitational (or free) subduction models (Heuret et al., 2007; Goes et al., 2008, 2011; Di Giuseppe et al., 2008; Faccenna et al., 2009; Stegman et al., 2010; Goes et al., 2011; Quinquis et al., 2011). These models are used to understand the zero and first order behaviour of the subduction system. This type of setup is used in chapter 3 of this thesis (Quinquis et al., 2011). Gravitational models have shown that the deformation style of subduction zones can change from a retreating to an advancing trench depending on the age of the subducting lithosphere (Di Giuseppe et al., 2008; Faccenna et al., 2009) or the viscosity contrast between the mantle and the slab (Schellart, 2008a). Di Giuseppe et al. (2008) and Faccenna et al. (2009) simulate age variations by lithosphere thickness variations. A young subducting lithosphere (around 60 Myr old) will evolve through trench retreat causing the slab to lie on the bottom of the model domain, while an older subducting lithosphere (around 70-80 Myr) will cause the model to evolve through trench advance, with a slab that folds on the bottom of the model domain. This deformation style can change with time for systems in which the age of the subducting lithosphere varies

with distance from the trench (Faccenna et al., 2009). Gravitational models have also been used to understand how plate age controls whether slabs penetrate into the lower mantle (Goes et al., 2008). In these models, plate age correlates with both density and thickness of the subducting lithosphere and, therefore, with its buoyancy. Hot, young slabs are lighter and thinner than colder and older slabs. The models of Goes et al. (2008) showed that older slabs subduct with a large amount of trench retreat and tend to lie down flat on the 670 km transition zone. The younger slabs, however, subduct with larger subduction velocities and tend to buckle and thicken on the 670 km transition zone. The thickening of the young slabs increases their buoyancy, and therefore, their sinking velocity, helping rapid penetration into the lower mantle.

Schellart (2008a) showed that varying either the thickness of the subducting plate or the viscosity contrast between the slab and the mantle changes the subduction style. Increasing the viscosity contrast between the slab and the mantle while keeping slab thickness constant results at low viscosity contrasts, in the slab lying on the 670 km discontinuity, at higher viscosities the slab folds onto the lower mantle, and finally, at high viscosity contrasts the slab again lies on the 670 km discontinuity.

The numerical models discussed so far are 2 -D studies, but recent advances in computational methods and computer power have opened the realm of 3 -D numerical modelling. 3 -D gravitational models of subduction, without overriding plate, have been used to catalogue styles of subduction, ranging from models with an advancing trench to a retreating trench (Stegman et al., 2010). These models also show that the buoyancy and flexural stiffness of the subducting lithosphere control the deformation style of subduction. These results are in agreement with those of the 2 -D models described above (Goes et al., 2008; Di Giuseppe et al., 2008; Schellart, 2008a; Faccenna et al., 2009). 3 -D models of subduction (analogue and numerical) have also highlighted the influence of the poloïdal flow on subduction dynamics around lateral slab edges (Funiciello et al., 2006; Piromallo et al., 2006).

A next step towards increasing the complexity of a linear viscous subduction model is to add an overriding plate to the system. Numerical, analogue and analytical studies have been used to study the effects of the overriding plate on the subduction system (Heuret et al., 2007; Lallemand et al., 2008; Schellart, 2008b; Capitanio et al., 2010) (Fig. 1.4). Depending on the model setup, this type of model can require an additional driving force to the buoyancy to start subduction. A kinematic driving force, which simulates ridge push, is commonly added to the model setup. These models 'push' the subducting plate into the mantle until enough subduction has occurred for slab pull to become active. Alternatively, a pre-existing piece of subducted slab is included in the initial model. Studies with an overriding plate have highlighted the importance of overriding plate motion on subduction dynamics. A trench-ward motion of the overriding lithosphere

causes the slab to subduct through trench retreat and lie on the bottom of the model domain, while a stationary or ocean-ward motion of the overriding plate can cause the slab to subduct through trench advance, with the slab folding on the bottom of the model domain (Heuret et al., 2007; Lallemand et al., 2008; Schellart, 2008b; Capitanio et al., 2010; Quinquis et al., 2011). Schellart (2008b) pointed out a limitation in subduction models: The overriding plate is generally made stiff in numerical models to allow localisation of deformation at the plate boundary and enable subduction (Heuret et al., 2007; Capitanio et al., 2010; Quinquis et al., 2011). This stiffness of the overriding plate inhibits it's possible deformation which could have allowed a different style of trench motion (Schellart, 2008b).

Yamato et al. (2009) used 3 -D numerical linear viscous models to study the influence of overriding and lateral plates on the dynamics of subduction. They showed that an overriding plate modifies the poloïdal flow and reduces trench retreat velocities. Lateral plates also inhibit the lateral, along-trench, shortening of the subducting plate, which is often visible in 3 -D models of subduction Yamato et al. (2009).

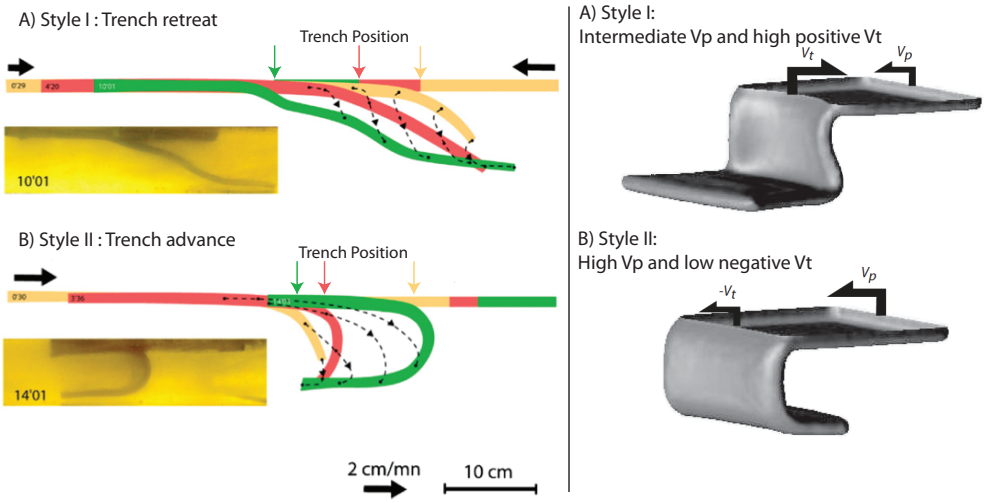


FIGURE 1.4 – Two main styles of deformation of the subducting lithosphere during free subduction obtained using analogue models (left column from Heuret et al. (2007)) and numerical models (right column from Di Giuseppe et al. (2009)). V_t is the trench velocity or the velocity of the overriding plate and V_p is the subducting plate velocity. Trench retreat occurs for a trench-ward motion of the overriding plate, while trench advance occurs for a ocean-ward motion of the overriding plate.

1.2.2 Thermo-mechanical subduction models and the role of rheology

The models discussed in the previous section use simple rheologies in order to focus on the first order dynamics of the system. However, subduction zones are highly complex structures which include viscous, elastic and brittle material behaviour (Bürgmann and Dresen, 2008). Such rheologies require the consideration of history terms (stress for elasticity) and an accurate calculation of pressure (for viscous and brittle rheologies) and temperature (for viscous creep). The rheology, or strength, of the lithosphere has been a subject of debate and different rheological profiles for the crust have been put forward (Burov and Watts, 2006) that can locally be supported by different observations (*e.g.*, the state of stress or depth of earthquakes). In the debate, the upper mantle is either considered strong (the so-called jelly sandwich) or weak (the so-called crème brûlée) (Fig. 1.5). In the jelly sandwich model, the long-term strength of the lithosphere lies in the lithospheric mantle. This type of behaviour would characterize oceanic lithosphere (Jackson, 2002). In the crème brûlée model, the long-term strength of the lithosphere is located in the crust and this model is thought to apply to the continental lithosphere (Jackson, 2002). Burov and Watts (2006) showed that the different rheological profiles result in different evolutions of thermodynamical models: a jelly sandwich type of rheological profile will enable stable subduction, whereas a crème brûlée type of rheological profile will be unstable and not allow subduction.

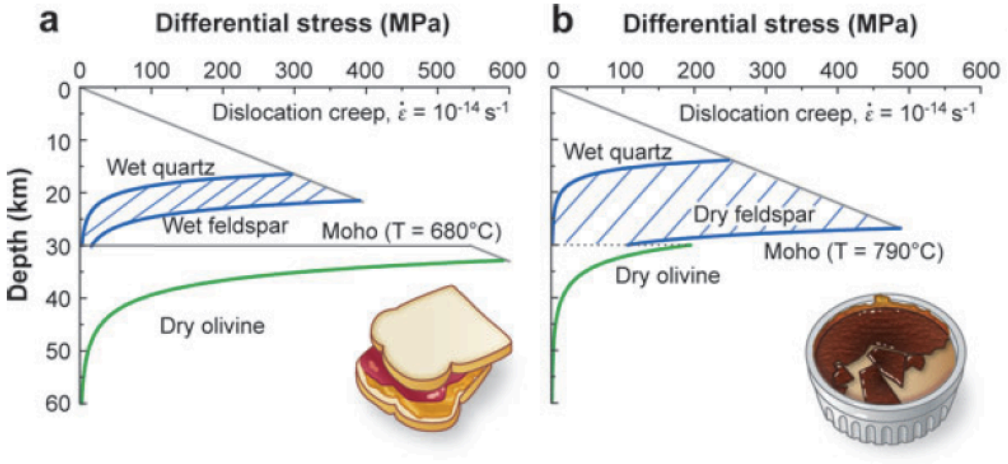


FIGURE 1.5 – The two strength profiles of the lithosphere: **a)** Jelly sandwich characterised by a weak lower crust and a strong uppermost mantle or **b)** Crème brûlée where the uppermost mantle is weak (which could result from a high geotherm, 90 mW m^{-2}, or the addition of water). Figure from Bürgmann and Dresen (2008).

Elastic, viscous and brittle rheologies occur in different parts of the subduction system. At high temperatures, the lithosphere and the mantle deform viscously (Bürgmann and Dresen, 2008; Billen, 2008), an irreversible, time-dependent deformation, where energy is dissipated. Brittle behaviour occurs in the cold lithosphere, mainly in the upper 40 km (Tichelaar and Ruff, 1993), but it can also be observed in the cold slab to the base of the upper mantle (Fig. 1.3). Elastic deformation is instantaneous and fully reversible. No dissipation of energy occurs, but the energy is stored, hence the importance of memory. This type of deformation is particularly important during the bending and the unbending of the subducting slab, and the formation of the flexural bulge. Viscous and elastic rheologies can act simultaneously. In the case of a Maxwell rheology, the instantaneous deformation is accommodated through elastic behaviour, and the stored energy is then dissipated viscously.

Funiciello et al. (2003b) showed that the inclusion of elasticity in a thermo-mechanical model can lead to different stress distributions in the slab at the trench and at the transition zone in the mantle, even if the dynamics of the system are relatively unchanged. Their viscoelastic models could be fit by a linear viscous rheology with slab viscosities ranging from 5×10^{22} to 5×10^{23} Pa s (Funiciello et al., 2003b). Viscoelastic and linear viscous models of subduction zones may result in a similar surface topography. However, Gurnis et al. (1996) found that the addition of elasticity results in the formation of a larger and deeper trench and a foreland bulge which experiences *c.a.*, 200 m more uplift.

Numerical models have been used to understand the stress distribution in the overriding and subducting plate during subduction for linear viscous rheologies (Kaus et al., 2009) and pressure and temperature dependent rheologies (Čížková et al., 2007; Kaus et al., 2009). Kaus et al. (2009) used a quasi-instantaneous modelling approach, restricting the study to the recent state of stress, to investigate the influence of rheology, layering in material properties, and viscosity of the subducting slab. They found that a weak lithosphere does not accumulate stress, whereas a strong lower crust will couple the crustal parts of the overriding and subducting plate, inhibiting subduction (Kaus et al., 2009). Čížková et al. (2007) studied the deformation in thermo-mechanical models over a longer time-scale, focussing on the deformation mechanisms at the upper to lower mantle boundary (at a depth of 670 km). In their models, the state of stress of the slab is strongly influenced by bending and unbending forces and to a lesser extent by the buoyancy forces associated with the phase transitions.

As subduction progresses, the lithologies in the system undergo an increase in pressure and temperature, which results in phase changes and the release of fluids (Turcotte and Schubert, 2002; Stern, 2002). Three major phase changes are observed in the mantle: (1) At a depth of 410 km, Olivine transforms to β-spinel. This phase change is associated with a density increase of approximately 6 %

(Schubert et al., 2001; Turcotte and Schubert, 2002; Stern, 2002) and is exothermic. (2) At 520 km, β-spinel transforms to γ-spinel with a negligible density change. (3) At 670 km, γ-spinel transforms to Perovskite and Magnesiowustite. This phase change is accompanied by an increase in density of 8 % (Schubert et al., 2001; Turcotte and Schubert, 2002; Stern, 2002) and is endothermic. The viscosity jump observed at the 670 km discontinuity, between the upper and the lower mantle, is of *c.a.*, 50 to 200 orders of magnitude (Tosi et al., 2005). Čížková et al. (2002) showed that the phase change at 670 km depth and its associated rheological weakening can deflect the slab, trapping it in the upper mantle. Jarvis and Lowman (2007) and Shahnas and Jarvis (2007) showed that the importance of rheological weakening at 410 km and 670 km depth also depends on the viscosity of the lower mantle. Tosi et al. (2005) and Quinteros et al. (2010) tested viscosity contrasts between the upper and lower mantle ranging from 30 to 100. A low viscosity lower mantle results in a large influence of the phase changes, while a high viscosity lower mantle renders the phase changes negligible (Quinteros et al., 2010).

Numerical models are also used to study more complex systems with the aim to increase our understanding of, for example, collision zones (Toussaint et al., 2004b), slab detachment (Gerya et al., 2004; Burkett and Billen, 2009) or the exhumation of Ultra High Pressure (UHP) domains (Gerya et al., 2002; Gerya and Stöckhert, 2002; Warren et al., 2008b,a). UHP rocks are commonly found in orogenic belts such as the Western Gneiss Region of the Norwegian Caledonides (Chopin, 1984; Guillot et al., 2003; Rosenbaum and Lister, 2005; Hacker et al., 2010) and are thought to have been subducted down to depths approaching 100 km and later exhumed in the final stages of subduction and/or during orogenesis and extensional collapse (Chopin, 1984; Andersen, 1993, 1998). The mechanisms that could lead to exhumation of these UHP rocks are, so far, poorly understood and numerical models have been used to investigate possible mechanisms (Burov et al., 2001; Gerya et al., 2002; Gerya and Stöckhert, 2002; Warren et al., 2008b,a). Low amounts of eclogitization of the lower crust could allow exhumation of UHP rocks through the associated density decrease (and thus positive buoyancy forces) and friction created by the overriding plate that reduces the amount of subducted crustal material (Burov et al., 2001). Exhumation of UHP rocks could also be explained by the rheological weakening of the subduction channel by fluids released during dehydration of the subducting slab (Faccenda et al., 2008b). The weak subduction channel enables light material to rise buoyantly through it. Duretz et al. (2011) showed that exhumation of UHP rocks could also occur through eduction of deeply subducted continental crust after slab break off.

Models with more complex rheologies are the natural step forward in understanding the thermal (Abers et al., 2005; van Keken et al., 2008) and dynamic evolution of the subduction system (Sobolev and Babeyko, 2005; Gerya et al., 2006; Billen and Hirth, 2007; Čížková et al., 2007; Warren et al., 2008b). However, when

building a numerical model of subduction, it is necessary to establish an initial model setup. This requires choosing values for the initial lithosphere thicknesses, mechanical and thermal properties, rheological parameters, initial temperature profiles, as well as model boundary conditions and model domain size. Some of these can be constrained by observations of present-day subduction zones, such as lithosphere age, crust and lithosphere thickness, and surface heat flux, whereas others have a larger uncertainty and require critical evaluation of geophysical and experimental results. The combination of uncertainties in initial model parameters with different numerical solution techniques and varying aims of studies, result generally in different initial model setups. This variability in model setups makes it difficult to compare results of different studies directly. Differences observed in the evolution of a model might be caused by differences in the model setup that are propagated as the model evolves. The initial setup of subduction models is addressed in chapters 3 and 4 of this thesis.

1.2.3 Numerical modelling of (de)hydration processes

Fluids, mainly H_2O, have a weakening effect on viscous and brittle rheologies and can, therefore, influence the dynamics of subduction (Sibson et al., 1975; Peacock, 1987; Hirschmann, 2006; Connolly, 2005). Chapter 5 of this thesis focuses on the role of water during subduction.

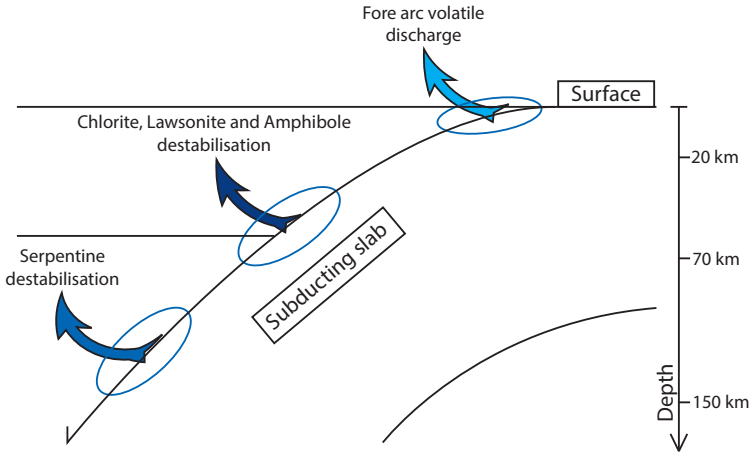


FIGURE 1.6 – Cartoon of the main dehydration processes occurring during subduction.

Water is thought to be present in the subducting slab in two forms. First, free fluids are mainly present in the pores of the oceanic sediments. Water in this form is thought to be expelled rapidly from the subducting slab, within the first 20 km of depth, due to the compaction of sediments (Rüpke et al., 2004). Second, fluids

can be bound to the minerals which are present in the different lithologies in a subducting slab. These fluids are expelled from the system during phase changes (Iwamori, 1998, 2007b; Schmidt and Poli, 1998) (Fig. 1.6). Mineralogically bound water can be found in large quantities in hydrous minerals, such as, Chlorite, Amphibolite, Serpentinite and the Alphabet Phases (*e.g.*, phase A) (Iwamori, 1998; Schmidt and Poli, 1998; Hirschmann, 2006), but can also be found in small quantities in Nominally Anhydrous Minerals (NAM). Because of the abundance of these latter types of minerals, it is thought that, taken together, they can contain large quantities of water (Bolfan-Casanova et al., 2000; Hirshmann et al., 2005, 2009; Hirschmann, 2006; Iwamori, 2007b).

Numerical or analytical models of dehydration of the subducting slab and hydration of the mantle wedge depend strongly on the initial weight percentage (wt.%) of water in the subducting slab (Rüpke et al., 2004; Hirschmann, 2006). Water is mainly incorporated in the crust and the first kilometres of the upper mantle part of the subducting lithosphere in the form of serpentinite (Rüpke et al., 2004; Hensen et al., 2004). The degree of serpentinisation of the oceanic crust therefore determines the amount of water introduced into the subduction system. Serpentinisation, and especially deep serpentinisation, of the crust is possible through hydrothermal processes occurring mainly at the mid oceanic ridge and through faults, such as transform faults and faults associated with the flexure of the lithosphere at the trench, that guide water into the oceanic lithosphere (Rüpke et al., 2004; Faccenda et al., 2008a).

When modelling dehydration processes that occur in the slab during subduction, it is essential to precisely characterise the phase diagrams of the different constituents of the oceanic crust and the mantle (Fig. 1.7). These phase diagrams can either be determined experimentally (Schmidt and Poli, 1998; Ohtani et al., 2004; Komabayashi et al., 2005; Iwamori, 2007b) or obtained from thermodynamical calculations (Connolly, 2005; Lukas et al., 2007; Caddick and Thompson, 2008). Phase diagrams plot the stability fields of the mineral assemblages that form the slab and mantle lithologies as a function of pressure and temperature. Each mineral can contain a maximum amount of water. Knowledge of the components of a mineralogical assemblage and their abundance allows determining the maximum content of water as a function of pressure and temperature. The boundary between two fields of mineral assemblages, also called the Clapeyron slope, represents the location of the phase change or mineralogical reaction and can be associated with a change in the maximum water content of the rock. Phase changes are localised processes that occur at specific pressures and temperatures. It is the location of these phases changes that are used in our numerical models.

Once a fluid has been released from a hydrous mineral through dehydration processes, it will migrate through the system. Different migration mechanisms are thought to exist (Stern, 2002), where the interaction with the surrounding material

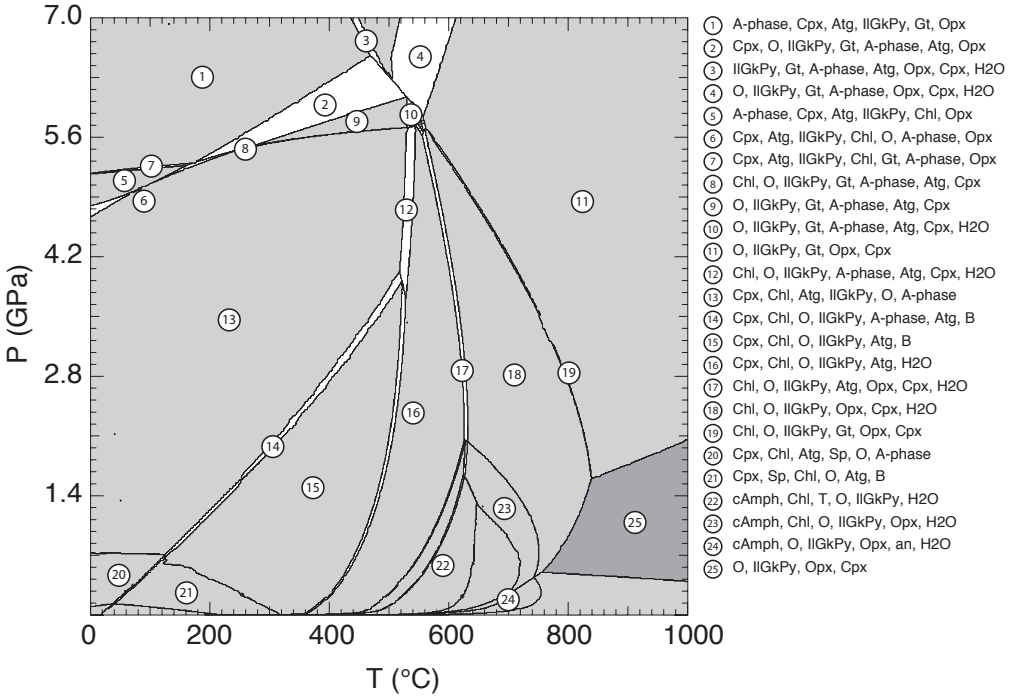


FIGURE 1.7 – Phase diagram for a Serpentinized Hartzburgite calculated using Perple_X (Connolly, 2005) by Zurab Chemia (Chemia et al., 2010). The phases are: A-phase, Cpx = Clinopyroxene, Atg = Antigorite, IlGkPy = Ilmenite, Gt = Garnet, Opx = Orthopyroxene, H2O = Water, O = Olivine, Chl = Chlorite, B = Brucite, cAmph = Clinoamphibole, Sp = Spinel, T= Talk, an = Anorthite.

is a function of the migration velocity: (1) Porous flow, where the migration velocity is on the order of millimeters per year (Zack and John, 2007). However, the porosity of the rocks is not known for mantle pressures (above approximately 3 GPa). (2) Channelised flow, which allows very fast migration of fluids. Because of the high migration velocity, which has been estimated at 1-4 m yr^{-1} (Hawkesworth et al., 1997), interactions with the surrounding rock would be limited (Spiegelman et al., 2001; Spiegelman and Kelemen, 2003; Zack and John, 2007). (3) Diapiric ascent, where the fluid migrates upward along with serpentinite due to the positive buoyancy of serpentinite (Stern, 2002). It is necessary to understand the relative importance of each process during fluid migration in order to find the state of hydration of the materials in the entire subduction system.

Previous studies of the influence of water on the dynamics of subduction have often focussed on specific depth ranges. “Very shallow” studies of dehydration processes are limited to the lithosphere (less than 100 km deep) (Silver et al., 2000; Hensen et al., 2004). These studies have shown that most of the water that is

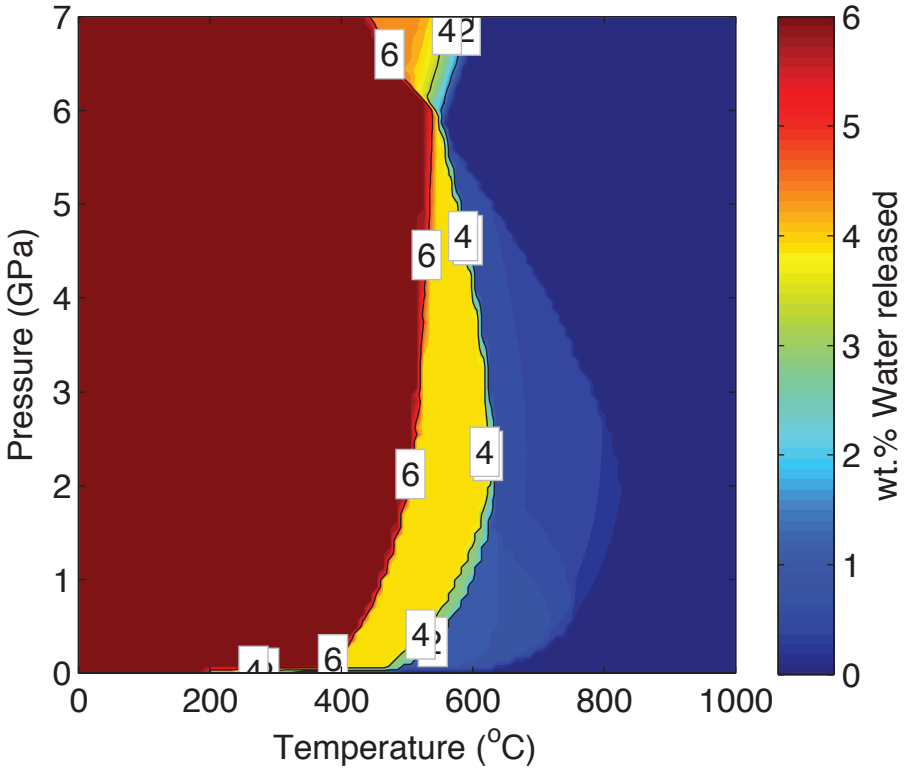


FIGURE 1.8 – Water content in wt.% for a Serpentinized Hartzburgite calculated using Perple_X (Connolly, 2005) by Zurab Chemia Chemia et al. (2010). This figure uses the phase diagram in figure 1.7

present in the pores will be expelled at shallow depths, up to 20 km depth (Rüpke et al., 2004; Hensen et al., 2004). In addition, water that is mineralogically bound to clay minerals is released at shallow depth and expelled through the deep-reaching fault systems which are present at convergent margins (Hensen et al., 2004). These processes occur at temperatures from 85 to 130 ^{o}C. "Shallow" upper mantle studies of dehydration processes to a depth of approximately 250 km focus on the effects of water on the dynamics of the mantle wedge (Rüpke et al., 2004; Arcay et al., 2006; Gerya et al., 2006; Gorczyk et al., 2006, 2007a; Cagnioncle et al., 2007; Iwamori, 2007b). Numerical studies in the mantle at a local scale have found

that rapid channelisation of fluid migration paths can occur, resulting in strong local variations in fluid content (Spiegelman and Kelemen, 2003). "Deep" mantle dehydration processes occur in the transition zone (below 410 km) and in the lower part of the upper mantle (down to the 670 km) (Richard et al., 2006, 2007; Richard and Iwamori, 2010). This deep dehydration of the slab could explain the presence of deep earthquakes (Richard et al., 2007) or the initiation of wet plumes at the transition zone (Richard and Iwamori, 2010). Only few studies of "deep" dehydration processes exist. These are either conceptual models based on experimental data (Ohtani and Zhao, 2009) or simplified 1D numerical models (Richard et al., 2006, 2007; Richard and Iwamori, 2010). These models assume that water can be transported into the transition zone (Komabayashi et al., 2005; Litasov et al., 2003; Ohtani et al., 2004). Shallower models of dehydration processes, however, show that the slab may be entirely dehydrated when it reaches a depth of 250 km (Rüpke et al., 2004; Arcay et al., 2006; Cagnioncle et al., 2007). In this thesis, (de)hydration processes are modelled on the scale of the upper mantle down to 670 km depth. This allows us to investigate the effects of the evolution of water content at different depths on the dynamics of the slab and the mantle wedge.

1.3 Open questions in subduction modelling

The inherent complexity of subduction zones, caused by the lithological stratification of the subducting slab, the presence of viscous, plastic and elastic rheologies, the thermal structure and the spatial time scales of deformation, have motivated the use of numerical, analogue and analytical models to investigate the system. This explains the large number of numerical studies of subduction dynamics, several of which are cited in the previous sections. However, a number of open questions in subduction modelling remain. Modelling subduction requires a large data set of input parameters. These parameters can be constrained through direct observation of subduction zones and by critical evaluation of geophysical and geochemical data. However, this still leaves subduction modellers with a large freedom in the choice of parameter values, and, as a consequence, values will differ between studies. How does the freedom in input parameters affect our interpretation of results?

Boundary conditions: Subduction occurs because of different driving forces: ridge push, slab pull and mantle flow. These processes are understood reasonably well once subduction has started and reached a "stable" regime. However, subduction initiation has so far not been observed on Earth and is still not fully understood (Regenauer-Lieb et al., 2001; Stern, 2002; Nikolaeva et al., 2008). In order to initiate subduction in models, one method is to initially "drive" subduction, often using a "week seed" in addition, to localise the deformation at the plate boundary,

while the other is to use a pre-existing slab. Could the initiation phase in models influence later results (Buiter and Ellis, 2010)? Kinematic boundary conditions that force subduction can influence the large-scale deformation of the subducting slab in models (Čížková et al., 2002; Han and Gurnis, 1999). How is the deformation mode of a subduction model controlled by the kinematic boundary condition which is used? And does the manner in which the free surface of the model is treated (true free surface, sticky air) influence the large scale deformation of the subduction system?

Influence of model setups and solution techniques: Differences in model setups may make it difficult to compare results of different studies directly. Are differences in the model results due to differences in the model setup itself or because of the numerical methods that are used? To estimate the range of variations among numerical codes, "benchmark" studies are often used (Blankenbach et al., 1989; Schmeling et al., 2008; van Keken et al., 2008). Previous numerical benchmarks have investigated linear viscous subduction (Schmeling et al., 2008) and the thermal structure of the mantle wedge (van Keken et al., 2008). No benchmark has so far been proposed for thermo-mechanical models of subduction. Thermo-mechanical models include pressure- and temperature-dependent viscous rheologies, and plastic rheologies, resulting in a strongly non-unique problem. Are the rheology feedback relations resulting in similar subduction dynamics in different codes?

Influence of water: The physical influence of an input parameter can be determined by parametrical studies that systematically vary the value of the parameter under investigation and compare the dynamics of the resulting system. This method has been used to characterise the influence of hydration and dehydration processes on subduction dynamics (Arcay et al., 2006; Gerya and Stöckhert, 2006; Iwamori et al., 2007; Rüpke et al., 2004). However, several aspects of fluids in a subduction system are not fully understood:

- What is the amount of water introduced into the subduction system?
- What is the state (solid, liquid, gas or supercritical) of the mineralogical water released at depth?
- What are the rheological parameters of water as a function of pressure and temperature?
- How does water migrate through the system? Does water migrate using porosity or does water diffuse into the system?

1.4 Layout of this thesis

This thesis gradually builds a fully coupled thermo-mechanical numerical subduction model which includes hydration and dehydration processes, starting from simple linear viscous models of subduction. Chapter two explains the numerical methods used in this thesis: The numerical code, SULEC, and the thermodynamical code, Perple_X, which is used to calculate the water content of minerals as a function of pressure and temperature. Chapters three to five describe the three stages in building the subduction model.

Chapter three consists of the first paper which is published in Tectonophysics as: "The role of boundary conditions in numerical models of subduction zone dynamics" by M.E.T. Quinquis, S.J.H. Buiter, and S. Ellis (*Tectonophysics*, 497: 57–70, 2011). Using linear viscous models of subduction we test the influence of kinematic boundary conditions on subduction zone dynamics. We find that subduction is only possible if the subducting slab can decouple from the surface boundary. This can be achieved through (1) a true free surface, or (2) a weak layer (either a weak crustal layer or a "sticky air" layer) between the free-slip surface boundary and the subducting lithosphere. We show that the choice of the location of the kinematic boundary condition that drives subduction determines the style of subduction, forcing the slab to lie or bend on the bottom of the model domain.

Chapter four contains a paper in preparation: "A numerical comparison study of thermo-mechanical subduction" by M.E.T. Quinquis, S.J.H. Buiter, N. Tosi, C. Thieulot, P. Maierovà, J. Quinteros, A. Glerum, L. Novak, D. Dolejš and S.M. Ellis. We define reference model setups for 4 different subduction models using the same geometries, but different rheologies: linear viscous, and pressure- and temperature-dependent. These model setups are data sets of input parameters that are used to model subduction evolution with the numerical codes ASPECT, CHIC, ELMER, ELEFANT, SULEC, SLIM-3D and YACC. Our results can be used as a benchmark for subduction problems at various levels of complexity. We show that the linear viscous experiments converge to the same result for different numerical methods, highlighting the robustness of the solution for a "Stokes type" problem even when including temperature advection and temperature dependent densities. Increasing the complexity of the rheologies used in the model setup increases differences observed in the results of the various codes.

Chapter five builds upon the thermo-mechanical reference setup used in chapter four to investigate the effects of hydration and dehydration processes on the scale of the upper mantle. The chapter consists of a paper published in Solid Earth as : "Testing the effects of basic numerical implementations of water migration on models of subduction dynamics" by M.E.T. Quinquis and S.J.H. Buiter (Solid Earth, 5, 1–19, 2014). We focus on basic numerical implementation schemes for free water migration and their influence on subduction dynamics and free water and

bound water distribution in the mantle wedge. We show that the implementation of three different numerical schemes for free water migration does not influence the bound water distribution, but does have a significant effect on the free water distribution in the mantle wedge. Depending on the influence of free water on mantle viscosity, this may impact the dynamics of the mantle wedge.

Chapter six discusses what parameters and assumptions are necessary when building a numerical model of subduction, such as the definition of kinematic and thermal boundary conditions, the initial geometry of the model, the rheology of the materials, and the use of phase changes, (de)hydration processes or melts. These parameters will be determined by the focus of the study. The influence of the model setup on the dynamic evolution of the subduction system is discussed. Finally, chapter seven is a general conclusion to the thesis.

Chapter 2

Methods

2.1 Description of SULEC

The numerical models in this thesis are solved using SULEC-2D. SULEC, developed by Susanne Buiter and Susan Ellis, is a standard arbitrary Lagrangian Eulerian (ALE) finite element code that solves the general set of conservation equations:

$$\nabla \cdot \vec{v} = 0 \tag{2.1}$$

$$-\nabla P + \nabla \cdot \bar{\sigma}' + \rho \vec{g} = 0 \tag{2.2}$$

$$\rho C_p \frac{\partial T}{\partial t} = k\nabla^2 T - \rho C_p \vec{v} \cdot \nabla T + H \tag{2.3}$$

where $\vec{v}$ is the velocity vector, P is the pressure (mean stress), $\bar{\sigma}'$ the deviatoric stress tensor, ρ density, $\vec{g}$ gravitational acceleration ($g_x = 0$ and $g_y = -9.81\ m.s^{-2}$), C_p specific heat, T temperature, t time, k thermal conductivity, and H radioactive heat production per unit volume. Equations 2.1 and 2.2 form the incompressible momentum equation for slow creeping flows, while equation 2.3 is the heat equation. The Boussinesq approximation is assumed,*i.e.*, $\frac{\partial \rho}{\partial t} = 0$, but $\rho = \rho_0(1 - \alpha(T - T_0))$, where ρ_0 is the reference density at $T = T_0$ and α the volumetric thermal expansion coefficient. The equations are solved at the nodes of a quadrilateral mesh, while the material properties and deformation histories are stored on particles which are advected through the mesh. In this thesis a $Q4P1$ (4 velocity nodes and constant pressure) type of element is used, but SULEC can also use higher order elements: $Q8P4$ and $Q9P4$. The elements are continuous in velocity, but discontinuous in pressure. The pressure, or mean stress, is calculated using the iterative penalty formulation (Uzawa) (Cuvelier et al., 1986; Pelletier et al., 1989; Zienkiewicz and Taylor, 2000a). The equations for conservation of mass (Eq. 2.1) and conservation of momentum (Eq. 2.2) are perturbed by a small

term (Cuvelier et al., 1986). This introduces an artificial compressibility:

$$\nabla \cdot \bar{\sigma}' - \nabla P^{i-1} + \nabla(k \nabla \cdot u^i) + \rho \vec{g} = 0 \tag{2.4}$$

$$P^i = P^{i-1} - B \nabla \cdot u^i \tag{2.5}$$

i denotes pressure iteration. B is the bulk modulus or otherwise called the penalty or compressibility parameter. B is in $Pa\ s$ and is taken about 7 orders of magnitude above the maximum viscosity of the model (Zienkiewicz and Taylor, 2000a).

Equations 2.3, 2.4 and 2.5 are discretised using the Galerkin method (Zienkiewicz and Taylor, 2000a). Different averaging schemes can be used to average viscosities (majority, arithmetic, geometric and harmonic) and densities (arithmetic and majority) from particles to element.

In this thesis 2 types of rheologies are used: viscous and brittle (or plastic) rheologies. Linear viscous rheologies have constant viscosity η :

$$\bar{\sigma_e}' = 2\eta\, \bar{\dot{\varepsilon}}_e' \tag{2.6}$$

$\bar{\dot{\varepsilon}}_e'$ is the effective deviatoric strain rate ($\dot{\varepsilon}_e' = (\frac{1}{2}\dot{\varepsilon}_{ij}'\dot{\varepsilon}_{ij}')^{\frac{1}{2}}$) and σ_e' is the effective deviatoric stress ($\sigma_e' = (\frac{1}{2}\sigma_{ij}'\sigma_{ij}')^{\frac{1}{2}}$). Temperature- and pressure-dependent viscous rheologies are of a power-law creep type:

$$\eta_{df,ds} = \frac{1}{2}\left(\frac{d^m}{A\, C_{OH}^r}\right)^{\frac{1}{n}} \dot{\varepsilon}_e'^{\frac{1-n}{n}}\, e^{(\frac{Q+PV}{nRT})} \tag{2.7}$$

A is a material constant, n is the power law stress exponent, d the grain size, m the grain size exponent, C_{OH} the water content, r the water content exponent, Q the activation energy, V the activation volume and R the molar gas constant. df and ds refer to diffusion creep or dislocation creep, respectively. Diffusion creep, when $n = 1$, is Newtonian and grain size dependent ($m > 0$). Dislocation creep, when $n > 1$ and $m = 0$, is non-Newtonian and stress dependent. Deformation of the mantle can be accommodated by a simultaneous play of diffusion and dislocation creep (Karato and Li, 1992). In SULEC such a composite viscosity is implemented following van den Berg et al. (1993):

$$\eta_{comp} = \left(\frac{1}{\eta_{ds}} + \frac{1}{\eta_{df}}\right)^{-1} \tag{2.8}$$

In SULEC, a Drucker-Prager yield criterion is used for brittle (or plastic) rheologies. Plastic failure occurs when the deviatoric stress reaches the yield stress:

$$\sigma_e' = P cos\phi + C cos\phi \tag{2.9}$$

ϕ is the angle of internal friction and C is the cohesion. Strain-weakening or hardening is simulated by a linear decrease or increase of ϕ and/or C with effective

strain (measured as the second invariant of the strain tensor). The effective viscosity in the brittle regime is:

$$\eta_e = \frac{Psin\phi + Ccos\phi}{2\dot{\varepsilon}'_e} \tag{2.10}$$

To keep stresses on yield we iterate over η_e.

2.2 Thermodynamic calculations

2.2.1 The basics of equilibrium dynamics

A comprehensive understanding of Earth's interior requires that we study how material properties change with physical conditions. These changes are transformations that require redistribution of matter among and within phases. A phase is a physically separable material in the system. Every unique mineral is a phase, but also melts, liquids, vapors and solid solutions are phases. Examples of phase transformations are mineral transformations and melting in the solid Earth. These induce changes in material properties. The transformations are a function of extensive variables, that depend on the quantity of matter (such as, volume and heat capacity), and of intensive variables, that are independent of the quantity of matter (such as, temperature, pressure, viscosity and concentration). The physical conditions may be determined by, for example, the intensive variables pressure (P) and temperature (T). The study of changes in physical conditions is based on chemical equilibrium. The state of chemical equilibrium in a system at constant pressure and temperature is one in which the Gibbs free energy takes its minimum possible value. This is the Gibbs phase rule (Gibbs, 1878), which can be written as:

$$p + f = c + 2 \tag{2.11}$$

p is the number of phases, c is the minimum number of chemical components necessary to create all phases present in the system, and f is the number of degrees of freedom in the system. When determining phase equilibrium, the degrees of freedom (DOF) generally are pressure, temperature, and bulk composition.

A phase diagram maps phase equilibrium for mineral assemblages as a function of pressure and temperature. As an example, figure 2.1 shows the phase diagram for a one component system of aluminosilicates Al_2SiO_5. In a phase diagram three different types of phase equilibrium occur (Fig. 2.1) (Fraser, 1977; Cemic, 2005): 1) The invariant equilibrium, when $f = 0$, where all DOFs are imposed to reach equilibrium. This is the invariant point in phase diagrams, at the intersection of univariant curves. 2) The univariant equilibrium, when $f = 1$, where a single variable can be changed, but to keep equilibrium, a second variable must be changed by a predetermined amount (*e.g.*, if pressure is changed on the ky = sill

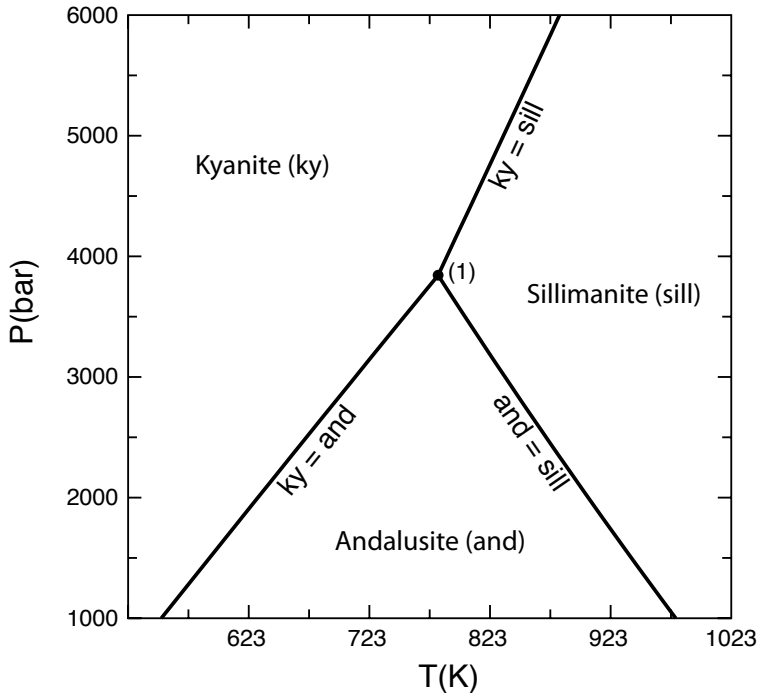


FIGURE 2.1 – A simple example of a one component phase diagram calculated for aluminosilicates (Al_2SiO_5) using Perple_X. Three solid phases are present, that are polymorphs of Al_2SiO_5: andalusite, kyanite and sillimanite. Point (1) is the invariant point where the three univariant curves (*i.e.*, the reaction curves, ky = and, and = sill, ky =sill) intersect.

equilibrium, temperature must change accordingly). This is the univariant curve in phase diagrams along which reactions occur. 3) The divariant equilibrium, when $f = 2$, when 2 variables can be changed independently, within an area bounded by the univariant equilibria, without changing the state of the system. The integer 2 in equation 2.11 is related to the number of parameters independent of mass that are being considered.

All mineralogical phases have a Gibbs free energy of reaction (ΔG = $G_{products}$ - $G_{reactants}$) which represents the amount of energy that is produced or consumed when a phase transition occurs (*i.e.*, when one, or more, phases create one, or more, different phases) (Albarède, 1995). The boundary between stability fields, the univariant curve, represents the condition at which the reaction occurs and where the Gibbs free energy of reaction is zero (ΔG = 0). By convention, the Gibbs free energy for any pure element is assumed to be zero (Fraser, 1977; Cemic, 2005). The Gibbs free energy (G) of any given phase will vary with pressure and

temperature following:

$$G = E + PV - TS \tag{2.12}$$

$$H = E + PV \tag{2.13}$$

P is pressure, T temperature, E internal energy, V volume, H enthalpy, and S entropy. A chemical system will tend to minimize energy. Phases with a greater Gibbs free energy will be unstable compared to phases with a lower Gibbs energy.

For any given pressure, temperature and composition, it is possible to calculate the Gibbs free energy of a reaction, if the starting point $P1$ and $T1$ of the reaction is known and the required thermodynamic data is available (Fraser, 1977; Cemic, 2005). The effective activity (a) of a mineral component describes how reactive a particular end member component is for a given mineral composition and as a function of pressure and temperature. The activity is reduced when the reaction does not include pure end member minerals, such as, quartz, but a solid solution. It is then necessary to include the equilibrium constant, K, in the calculation:

$$\begin{aligned} 0 = \Delta G^o_{P2,T2} = \Delta G^o_{P1,T1} + \int_{P1}^{P2} \Delta V^o_{P,T} dP \\ - \int_{T1}^{T2} \Delta S^o_{P,T} dT + RTlnK \end{aligned} \tag{2.14}$$

$$K = \frac{a_{p1}\ a_{p2}\ a_{p3} \cdots}{a_{r1}\ a_{r2}\ a_{r3} \cdots} \tag{2.15}$$

K is the product of the activities of the reaction products (subscript p), divided by the product of the activities of the reactants (subscript r). $K = 0$ for pure end member minerals.

2.2.2 Chemical equilibrium

Phase equilibrium depends on the second law of thermodynamics and can be calculated by minimizing the Gibbs free energy of the system. Originally, the fundamental principles of phase-equilibrium were used to calculate gas speciation in metallurgy (White et al., 1958; Levine, 1962). These calculations required non-linear minimization methods and were valid for single-phase homogeneous equilibrium. These techniques were later extended to include multiphase systems and applied to geology (Eriksson, 1971; Eriksson and Rosén, 1973; Brown and Skinner, 1974). Non-linear Gibbs free energy minimization techniques are now used in geology to study, among others, magmatic differentiation (Ghiorso, 1994; Ebel et al., 2000), metamorphic phase equilibrium (Biino and de Capitani, 1995; Caddick and Thompson, 2008), high-pressure mantle assemblages (Saxena and

Eriksson, 1985; Fabrichnaya, 1999), and material-science phase diagram computations (Eriksson and Hack, 1990; Andersson et al., 2002; Bale et al., 2002). At present, a number of commercial and freeware packages exist, along with thermodynamic datasets to perform phase equilibrium calculations in solid, melt, gaseous and aqueous-electrolyte systems.

Thermodynamic datasets include enthalpy (H), entropy (S), heat capacity (C_p) and activity coefficients (a). Their application requires equations of state, which are thermodynamic equations which describe the state of matter under a set of physical conditions. They are constitutive equations that determine the relationship between two or more state functions associated with the matter, such as its temperature, pressure, volume, or internal energy. Thermodynamics datasets include :

- Holland and Powell (1998) for metamorphic and magmatic rock-forming silicates, carbonates and oxides. It contains equations of state for H_2O-CO_2 fluids. This database is constantly updated.
- Berman (1988) for rock-forming silicates, carbonates and oxides. This database has not been updated since 1996, but is nonetheless incorporated into various software packages such as TWEEQU, MELTS and QUILF.
- Gottschalk (1997) for rock-forming silicates, oxides and carbonates. The database includes equations of state for multicomponent fluids at high pressures and temperatures (Churakov and Gottschalk, 2003a,b).
- Helgeson et al. (1978) for rock-forming minerals, oxides and sulfides. This dataset is specialised for hydrothermal and ore-forming processes.
- Robie and Hemingway (1995) is an update of the thermodynamic datasets of the U.S Geological Survey calorimetric laboratory. This dataset can be used as a complementary resource for less common phases, such as, sulfides.

Examples of phase-equilibrium software packages include:

- Perple_X (Connolly, 2005; Connolly and Kerrick, 1987; Connolly and Petrini, 2002) minimizes the Gibbs free energy of the system using a linear programming method. It incorporates the thermodynamic datasets of Holland and Powell (1998), Berman (1988) and Gottschalk (1997) and several solution models, which describe interactions between end-members in a multi-component solid solution. This software package is useful for both low-variance and high-variance equilibria, with both simple and complex phases. It is, however, computationally intensive for complex chemical systems.

- THERMOCALC (Holland and Powell, 1998; Powell et al., 1998) uses a non-linear method, the equilibrium-constant method, to calculate phase diagrams. Contrary to Gibbs free energy minimization techniques, the phases of the system are specified. The equilibrium compositions of the coexisting phases are computed, but the stability of the assemblage is not tested. This method is tailored to high variance equilibrium, but requires advanced knowledge of phase stabilities.

- THERIAK-DOMINO (de Capitani and Brown, 1987; Biino and de Capitani, 1995) minimizes the Gibbs free energy of the geological system. This software incorporates the Berman (1988) and Holland and Powell (1998) datasets. The software combines aspects of the approaches of Perple_X and THERMOCALC.

- GEMS-PSI (Kulik et al., 2003) minimizes the Gibbs free energy using the convex method (Karpov et al., 1997, 2001). This software is tailored to low temperature aqueous systems. It incorporates in-house (Nagra and Paul-Scherrer Institute) and the Holland and Powell (1998) databases.

- MELTS (Ghiorso et al., 2002; Ghiorso and Sack, 1995) minimizes the Gibbs free energy for magmatic systems. It incorporates de Berman (1988) dataset and solution models for magmatic systems.

- TWEEQU (Perkins et al., 1986; Berman et al., 1987) calculates metamorphic phase equilibria by averaging geothermobarometric calculations (Gordon, 1992). It incorporates the data from Berman et al. (1987).

- SUPRCT92 (Johnson et al., 1992a,b) calculates the thermodynamic properties (*i.e.*, the Gibbs free energy, enthalpy, entropy, heat capacity, and volume) of specified reactions for geological systems at high temperatures and pressures. It incorporates the datasets of Helgeson et al. (1978) and Oelkers et al. (1995)

- FactSage (Bale et al., 2002) calculates phase equilibrium by minimizing the Gibbs free energy of a system. For geological purposes, it incorporates the datasets of Berman (1988), and the Pelton (1999) and Pelton and Wu (1999) solution models.

In numerical models of subduction, we approximate the lithologies of the crust, lithosphere and mantle, and try to reduce the number of components. In this thesis Perple_X is used to calculate phase equilibrium, because its method is efficient, regardless of the number of phases considered in the calculation. Furthermore, the Perple_X linear method of minimizing the Gibbs free energy provides phase

diagrams as long as physical parameters, such as water content or density, of a bulk composition as a function of pressure and temperature are known. These can be included into the numerical subduction model calculations with SULEC.

2.2.3 Perple_X

Perple_X uses a linear programming algorithm to identify the stable mineral assemblages in a system composed of pure phases (Connolly and Kerrick, 1987; Albarède, 1995). The linear method forces convergence to a minimum, which is not always the case when using non-linear methods. The continuity of the compositional variation of solution phases is approximated by sets of discrete compositions, also called pseudocompounds. The Gibbs free energy of a system can then be expressed by:

$$G^{sys} = \sum_{i=1}^{\Pi} \alpha_i G^i \tag{2.16}$$

G^{sys} is the Gibbs energy of the system, Π the possible number of pseudocompounds present in the system, and α_i the amount of phase i ($\alpha_i \geq 0$). Mass balance requires that the sum of the amounts of the components within the phases be equal to the corresponding amounts in the system:

$$n_j^{sys} = \sum_{i=1}^{\Pi} \alpha_i n_j^i \tag{2.17}$$

where $j = 1 \ldots c$ and c is the amount of independent pseudocompounds in a system. n_j^i is the amount of the jth component in the ith phase. The output of Perple_X is the amount of stable pseudocompounds. Figure 2.2 shows an example of the linear minimisation technique with two phases β and γ that are each represented by the pseudocompounds $\beta_1, \cdots, \beta_7$ and $\gamma_1, \cdots, \gamma_8$ respectively. For the composition X^{sys}, $\beta_4 + \gamma_6$ would be identified as the stable phase assemblage of the system, β_4 and γ_6 representing the approximate composition of β and γ (Fig. 2.2b). The maximum error of the compositions of β and γ depends on the spacing of the initially defined pseudocompounds.

A phase diagram (calculated as a function of pressure and temperature) is a map of the stability fields of various mineralogical assemblages. Due to the approximation, in the minimisation stage, of continuity of the pseudocompounds, the phase fields can be decomposed into smaller fields which are defined by a unique pseudocompound assemblage (Fig. 2.3a). The boundaries represent either a true phase transition (*e.g.*, the reaction $\alpha + \gamma = \beta_4$ in figure 2.3a) or a difference in the composition of the solution (*e.g.*, $\alpha + \beta_4 = \beta_3$ in figure 2.3a). The polygons that define the stability fields are refined using grids of increasing resolution, where the

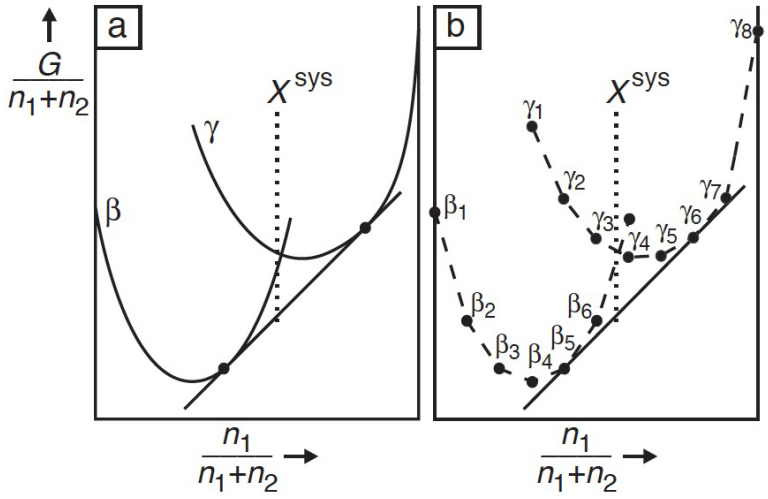


FIGURE 2.2 – Schematic isobaric-isothermal free energy-composition diagrams for a binary system illustrating the distinction between the non-linear solution to the phase equilibrium problem (a) and its linear approximation (b). Figure from Connolly (2005).

equilibrium phase relations are sampled at their nodes. The low resolution grid has n_x and n_y points and is refined by halving the node spacing so that the grid at the i^{th} level of refinement has a horizontal resolution of $N_x = 1 + 2^{i-1}(n_x)$ and a vertical resolution of $N_y = 1 + 2^{i-1}(n_y)$ (Fig. 2.3b). The refining steps give an effective resolution of $N_x \times N_y$ points (Fig. 2.3c), resulting in the phase diagram of figure 2.3d. The properties of the phase assemblages (*e.g.*, composition and density) are then extracted from the data stored at each minimization. The properties of arbitrarily located sample points are estimated using a linear interpolation of the three nearest grid points where the assemblage is stable.

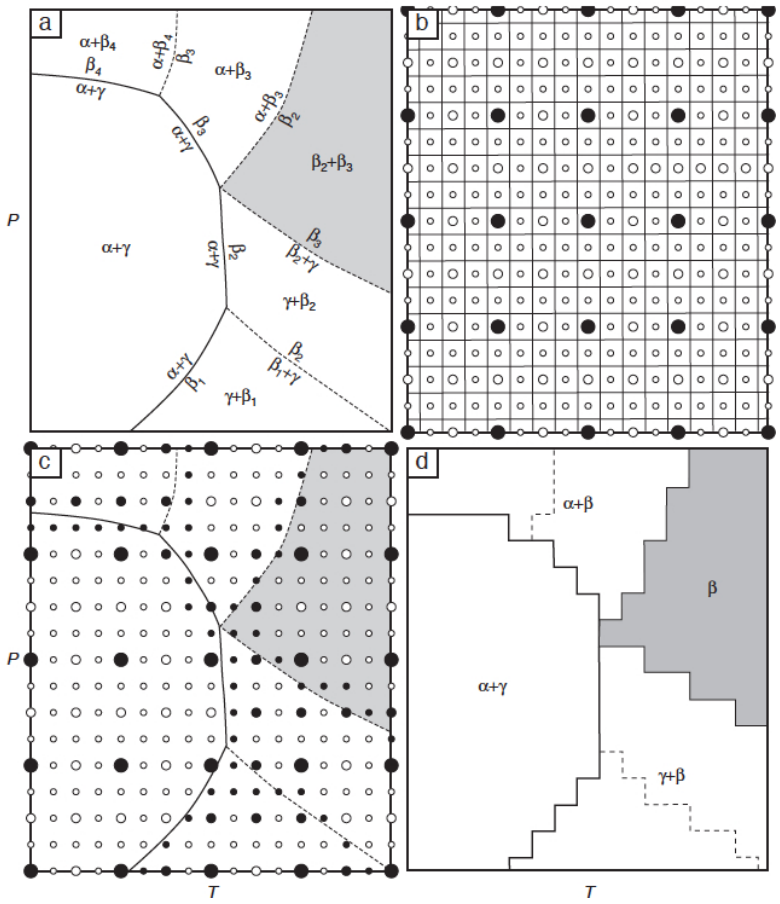


FIGURE 2.3 – Mapping algorithm used in Perple_X illustrated with schematic phase pressure-temperature diagram for a binary system; (a) the solution phase β is represented by pseudocompounds where the boundaries between pseudocompounds (the dotted lines) can approximate true phase boundaries or a difference in composition (the boundaries of the dark gray area) or homogeneous equilibration of a solution as a function of pressure and temperature; (b) Phase relations are mapped by sampling on a four level grid, with grid nodes at progressively higher levels indicated by circles of decreasing size; (c) The nodes at which phase relations would be computed as dictated by the mapping strategy are indicated by filled circles. The algorithm assigns the assemblages associated with the open circles; (d) the final map of the section is constructed by assuming that each node of the grid represents a finite area of the diagram. Figure from Connolly (2005).

2.3 The implementation of dehydration processes into SULEC

2.3.1 Determining water content

In the fifth chapter of this thesis, we use SULEC to investigate the influence of free water migration schemes on the dynamics of a subduction model. The lithospheric plates in the models consist of Bulk Oceanic Crust (BOC), Serpentinized Harzburgite (SHB) and pyrolitic mantle. The mantle is composed only of pyrolitic mantle. We use the thermodynamic code Perple_X to compute grids of bound water content in $wt\%$ as a function of pressure and temperature for BOC, SHB and pyrolitic mantle. These grids are discretized as a matrix of pressure and temperature steps and imported into SULEC. In our models the water content information is attached to the particles as arrays of the amounts of bound water and free water.

The thermodynamic calculations in Perple_X are only valid up to a pressure of 7 GPa and a temperature of 1200°C when using the Holland and Powel (1998) data set. These conditions are outside the mantle wedge domain. To include the hydration capability of the mantle wedge, we use the experimentally determined data set of Schmidt and Poli (1998) which is valid to $1100°C$ and 8 GPa. We extrapolate the Clapeyron slopes linearly to obtain a data set that covers the upper mantle pressures and temperatures of the subduction models.

As the model evolves, the pressure and temperature of particles change requiring that their water content is updated. We use a standard 2-D linear interpolation in pressure and temperature on the discretized water content grids to determine the maximum amount of bound water a particle can possess at its pressure and temperature. If the maximum amount of bound water that the particle can contain is less than the current amount of bound water of the particle, the particle is oversaturated and should dehydrate. The excess water is released as free water and migrates through the matrix of the crystalline rock following one of the numerical schemes described below (Section 2.3.2). If the maximum bound water is more than the amount of bound water of the particle, the particle is under-saturated and can potentially incorporate more water.

The subduction models in this thesis use a variable mesh resolution that allows deformation to be best resolved around the trench and in the mantle wedge. As particles migrate, elements can become empty or overpopulated. We therefore use particle injection and deletion within pre-specified minimum and maximum bounds to the number of particles per element. Particle deletion is used to reduce memory requirements and calculation times. The particle population control requires special care, because the amount of water contained in a model is a physical value and has to remain balanced as the model evolves. In our models, we inject particles with

no initial water (0 wt %). Particle deletion is random in an element. It is therefore necessary to determine the combined amount of free and bound water present in the deleted particle. If a particle flagged to be deleted contains a certain amount of water (either bound or free) this water is evenly distributed among the remaining particles of the element.

This method does introduces some numerical smoothing of the water content at resolution discontinuities in the model, but allows keeping water content balanced in the models while keeping computation and memory requirements reasonable.

2.3.2 Water migration schemes

In the upper mantle, free water that is released during dehydration collects along grain boundary intersections forming a network of interconnected channels and moves with the material flow. We assume that the free water migrates through these channels and with the material flow, whereas bound water moves only with the material flow. We investigate the following three free water migration schemes:

Elemental water migration scheme

This migration scheme (scheme I) is conceptually the simplest (Arcay et al., 2005). Water migrates vertically one element at a time and is unaffected by the material flow. The migration velocity is thus the element size divided by the time step. This is the main limitation of this migration scheme as the water velocity will depend on the model resolution. Furthermore, numerical models often use variable mesh to reduce calculation time while keeping the resolution high in the areas of interest of the models (*e.g.*, the mantle wedge in subduction models). Water migration velocity in variable mesh models would vary as a function of the resolution. This effect can be reduced in subduction models by using a constant grid resolution in the mantle wedge where the main dehydration processes occur.

When a particle undergoes dehydration, the free water is first distributed over the under-saturated particles of the element. If free water is still present after this initial stage the remaining water migrates to the element above, saturating the under-saturated particles from the bottom of the element upwards. If all particles are saturated in water and there is still free water left, the remaining water is evenly distributed among all particles of the element and will migrate onwards in the next timestep.

Vectorial migration scheme

The vectorial migration scheme (scheme II) imposes a constant velocity for water over the model domain ($v_{f,x}$ and $v_{f,y}$) (Fig. 2.4) (Richard et al., 2006; Gorczyk

et al., 2007a; Faccenda et al., 2008a). This method reduces the grid dependence of the migration scheme, though does not necessarily eliminate it totally.

When a particle is over-saturated, it releases water and distributes it along the path defined by the water velocity vector: $v_f \times \Delta t$ (Fig. 2.4). The first step is to hydrate under-saturated particles in the current element. If free water is still present after this step, the remaining free water migrates to the next element along the path (Fig. 2.4), saturating the under-saturated particles of the element from the bottom up, and so on. If all particles along the migration path of this time step are saturated (*e.g.*, all particles in elements 1 to 6 of figure 2.4), the remanding water is distributed evenly over all particles of the last element. We use an element-wise distribution for the water because water migration paths are likely irregular and a linear path for water would be unlikely (Rüpke et al., 2004; Katz et al., 2006). The elementwise distribution of water explains why there is still some grid size dependency to the distribution of water in the method. The solid flow also carries free water and the resultant free water migration path is therefore not necessarily exactly along direction v_f.

Darcy flow migration scheme

This migration scheme (scheme III) follows a simplification of Darcy flow as implemented by Cagnioncle et al. (2007). The fluid follows the pressure gradient caused by the difference in density between the fluid and the solid it is percolating through. We neglect the dynamic component of the pressure gradient which could be caused by the solid flow, because in our subduction models pressures in the mantle wedge region are mainly lithostatic. Migration scheme III is characterised by the Darcy velocity (Turcotte and Schubert, 2002):

$$q = \frac{(\rho_\mathrm{s} - \rho_\mathrm{f}) g \kappa}{\eta_\mathrm{f}} \tag{2.18}$$

where q is the Darcy velocity, ρ_s and ρ_f the density of the solid and fluid respectively, g the gravitational acceleration, η_f the viscosity of the fluid, and k the permeability. The permeability follows the empirical definition of Wark et al. (2003):

$$\kappa = \frac{d^2 \Phi^3}{270} \tag{2.19}$$

where Φ the volume fraction of fluid and d the grain size. The fluid velocity is the sum of the Darcy velocity relative to the volume fraction of fluid and the solid velocity:

$$v_f = \frac{q}{\Phi} + v_s \tag{2.20}$$

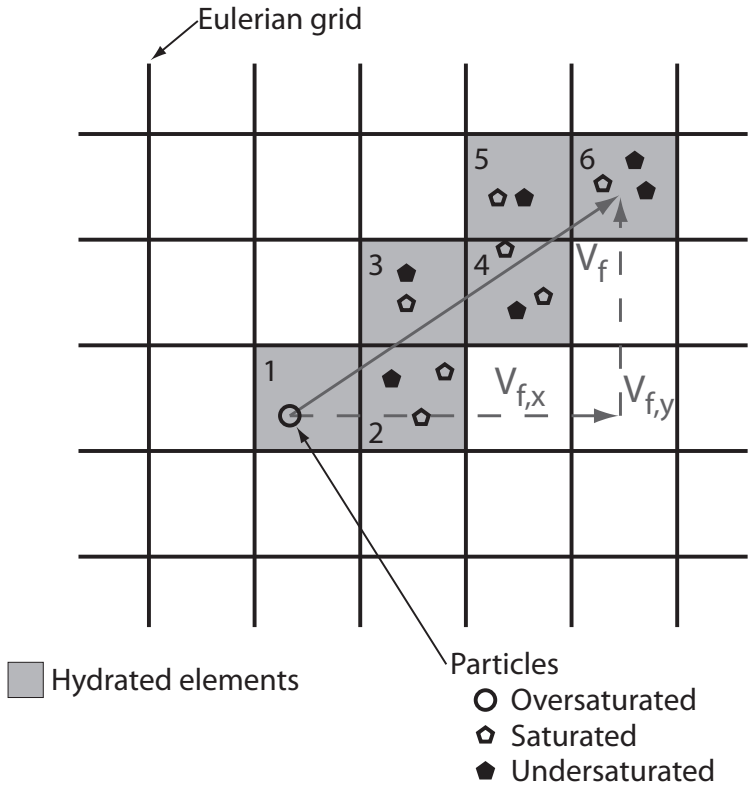


FIGURE 2.4 – Schematic migration of free water and it's distribution along a prescribed path for our velocity controlled water migration schemes 2 and 3 (see text for further explanation). V_f is water velocity.

where v_f is the fluid velocity and v_s the solid phase velocity. /

The water migration and distribution then follow scheme II. Φ, the volume fraction of fluid, is determined from the initial water content and the grids for pressure, temperature and wt.$\%$ H_2O. However, this assumes that all the free water is present in interconnected channels which would result in unnaturally high fluid velocities. We therefore introduce an efficiency factor, ω, that corresponds to the percentage of interconnected channels of the network through which water can migrate. Water can only migrate through the interconnected network thus reducing the effective fluid velocity. The permeability in equation 2.18 then becomes an effective permeability: $\kappa_e = \omega\kappa$.

The Darcy water velocity is calculated for every particle of the model. The water velocity is not constant and areas with higher water content have higher water migration velocities. Also in this scheme, free water is in addition carried by the solid flow.

2.3.3 The influence of water content on viscosity

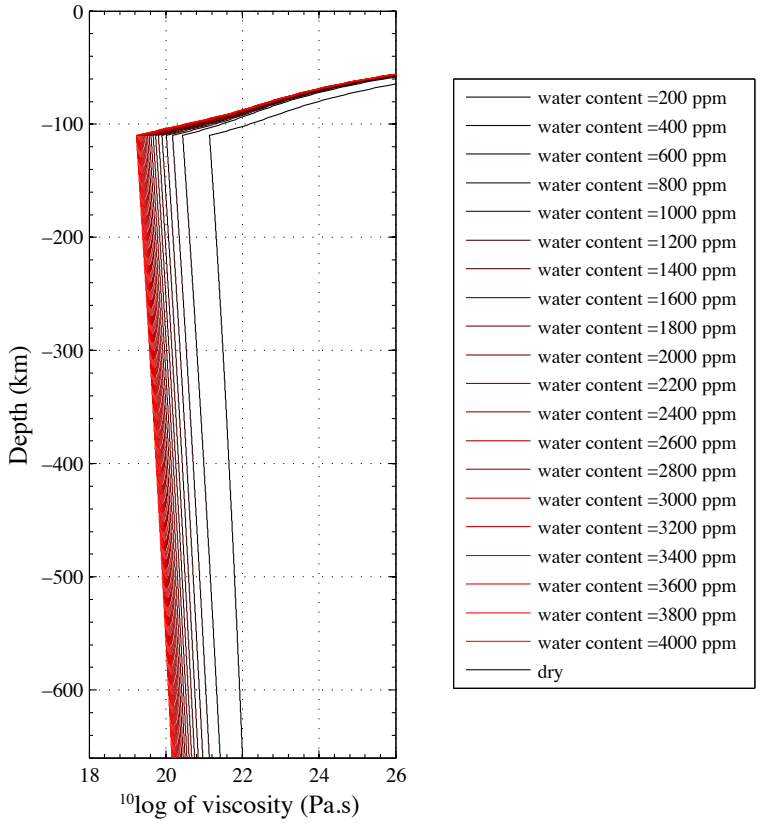


FIGURE 2.5 – Viscosity (Eq. 2.7) as a function of depth calculated using a constant strain rate of 10^{-15} s^{-1}, a water content ranging from 0 to 4000 ppm, and the values in Hirth and Kohlstedt (2003) (Table 2.1).

In chapter 5, linear viscous rheologies are used in some of our experiments. For these rheologies, we use a linear decrease of viscosity with 2 orders of magnitude over a water content ranging from 0 to 4000 ppm. This corresponds to the decrease in viscosity calculated with the flow laws of Hirth and Kohlstedt (2003) (Fig. 2.5). If the water content exceeds 4000 ppm we assume that the material can no longer weaken. In thermo-mechanical models of subduction we use a composite viscosity (Eqs. 2.7 and 2.8) including diffusion and dislocation creep as given by Hirth and Kohlstedt (2003) (Table 2.1). The water content calculated as a function of pressure and temperature using Perple_X is converted to ppm and used in the flow law (Eq. 2.7). Once the water content exceeds 4000 ppm we again assume that the material does not weaken further.

TABLE 2.1 – Flow law parameters from Hirth and Kohlstedt (2003)

Parameter	Unit	Dry Olivine		Wet Olivine	
		Diffusion	Dislocation	Diffusion	Dislocation
A^{a}	$\mathrm{Pa}^{-n}\ \mathrm{m}^{p}\ \mathrm{s}^{-1}\ \mathrm{H}(10^{6}\mathrm{Si})^{-1}$	2.25×10^{-15}	6.514×10^{-16}	1.5×10^{-18}	5.3301×10^{-19}
n	–	1	3.5	1	3.5
Q	$\mathrm{kJ\ mol}^{-1}$	375	530	335	480
V	$10^{-6}\ \mathrm{m}^{3}\ \mathrm{mol}^{-1}$	4	14	4	11
d	mm	5	–	5	–
p	–	3	–	3	–
C_{OH}	$\mathrm{H}(10^{6}\mathrm{Si})^{-1}$	–	–	1000	1000
r	–	–	–	1	1.2

[a] A is given for a general state of stress, and was converted from a uni-axial stress (Ranalli, 1995).

Chapter 3

The role of boundary conditions in numerical models of subduction[1]

Abstract

Numerical studies of subduction zone dynamics on a regional scale usually use a limited spatial extent for their models and therefore need to define boundary conditions on all model edges. These boundary conditions imply a choice for the mechanical and thermal state of the surrounding regions which may influence the evolution of the model system. We investigate the role of the surface and lateral boundary conditions for simple mechanical subduction models using a standard finite element method. We find that subduction is only possible if the slab can decouple from the surface. This decoupling can be achieved by a true free surface, a free-slip surface with a weak crust for the subducting plate, or a free-slip surface with a layer of low viscosity, low density material ('sticky air') between the model surface and the crust. Models of slab dynamics that employ a free-slip surface reproduce trench migration, slab sinking velocities and slab geometry of models with a free surface, as long as they use either a weak crust, which can be viscous, viscoelastic and/or brittle, or a 'sticky air' layer. The vertical topography will however not be reproduced for free-slip models without a 'sticky air' layer. For ocean-ocean convergent models we find that the application of inflow boundary conditions at the edges of the subducting or overriding lithosphere controls trench motion and the geometry of the subducting slab. Inflow on the overriding side causes trench retreat and a slab resting on the lower mantle, whereas inflow restricted to the subducting side can cause trench advance and a slab which folds on the lower mantle.

[1]Published as: Quinquis, M. E. T., Buiter, S. J. H., and Ellis, S. (2011). The role of boundary conditions in numerical models of subduction zone dynamics. Tectonophysics, 497:57–70, doi: 10.1016/j.tecto.2010.11.001

3.1 Introduction

Models can only approximate the complexity of nature and this therefore necessarily implies that they need to simplify rheologies, geometries and the dynamic character of the process under study. Furthermore, models often focus on a limited spatial domain in order to achieve high resolution for a reasonable calculation time (in the case of numerical models), or a feasible physical size (in the case of analogue models). Typical values for numerical and analogue subduction models range from 2400 to 6000 km in length (*e.g.*, Pysklywec et al., 2000; Schellart, 2005) and from 150 to 3000 km in depth (*e.g.*, Han and Gurnis, 1999; Nikolaeva et al., 2008). Such limitations in the size of the model domain imply that the mechanical and thermal evolution of the area located outside the model domain needs to be taken into account through boundary conditions. This implies that a modification of the boundary conditions changes the assumptions that are made concerning the thermal and mechanical state of the region outside the model domain. This could have an influence on the dynamics of the system, and the evolution of subducting slabs in the model in particular. Regional subduction models need to specify boundary conditions at the surface, lateral and bottom edges. Below we discuss these in turn, focusing on numerical studies.

Earth's surface is a so-called free boundary, which is stress free and allows horizontal and vertical displacements. A free surface is straightforward to achieve in Lagrangian-type numerical models (Giunchi and Ricard, 1999; Morra and Regenauer-Lieb, 2006; Hampel and Pfiffner, 2006), but is computationally more expensive in Eulerian methods, as it requires a change in the numerical mesh. Arbitrary Lagrangian Eulerian (ALE) methods (Fullsack, 1995) have a free surface, but still at an efficiency price. Models that do not have a free surface, alternatively use a free-slip condition (*i.e.*, the vertical component of velocity is equal to zero ($v_y = 0$) whereas the horizontal component of velocity (v_x) is calculated) (Piromallo et al., 2006; Arcay et al., 2007; Stegman et al., 2010), a kinematic condition (v_x prescribed and $v_y = 0$) (Han and Gurnis, 1999; Billen and Gurnis, 2001; Čížková et al., 2002) or a so-called 'sticky air' layer (Funiciello et al., 2003b; Gerya et al., 2004; Gorczyk et al., 2007b; Nikolaeva et al., 2008; Schmeling et al., 2008). This 'sticky air' is a low density, low viscosity layer between the surface of the model domain and the surface of the lithosphere. It allows vertical movements of the lithosphere surface. In models with a free-slip or a kinematic condition directly at the top of the lithosphere, vertical topography (*e.g.*, a trench and foreland bulge) cannot develop. A free-slip or kinematic boundary condition by itself is not enough to enable subduction, as the slab may not be able to decouple from the surface of the model domain. We discuss this in more detail in section 3.3: 'The influence of the surface boundary in gravitational subduction models'.

Kinematic surface boundary conditions (v_x prescribed and $v_y = 0$) allow

systematic investigation of the role of trench migration on slab dynamics (*e.g.*, Christensen, 1996; Olbertz et al., 1997; Han and Gurnis, 1999; Billen and Gurnis, 2001; Čížková et al., 2007). Previous studies have shown that the ability of the trench to migrate (either advance or retreat) controls the slab dip angle (Olbertz et al., 1997; Lallemand et al., 2008; Schellart, 2008b). Slow trench rollback allows the slab to penetrate into the lower mantle, while rapid trench rollback leads to a slab lying on the 670 km discontinuity. Han and Gurnis (1999) investigated numerical models of subduction zones in which the top boundary was implemented either as free-slip, or as kinematic. The horizontal velocity imposed at the top boundary in the kinematic models was the average value of the horizontal velocity obtained at the surface in the free-slip models. The authors showed that implementing a free-slip or a kinematic top boundary condition did not affect the dynamics of the subduction system, a result which was later contradicted by Čížková et al. (2007). In our study, we focus on a free surface and free-slip models and do not prescribe surface velocities.

Lateral boundary conditions of regional models can be free-slip (*e.g.*, Arcay et al., 2007; Čížková et al., 2007; Enns et al., 2005; Faccenna et al., 2009; Kaus et al., 2010), periodic (*i.e.*, the material flowing out(in) of the model's left lateral boundary flows in(out) the right lateral boundary) (*e.g.*, Gurnis and Hager, 1988; Han and Gurnis, 1999; Enns et al., 2005) or have a specified velocity (*e.g.*, Pysklywec et al., 2000; Warren et al., 2008b). The inflow condition, in particular, determines the geometry of the subducting slab as we show later (see also Heuret et al. (2007)). A change in the lateral boundary conditions from reflective (or free-slip) to periodic has been shown to change slab geometry for whole mantle subduction models (Gurnis and Hager, 1988; Han and Gurnis, 1999). In these models the periodic boundary condition is applied to the entire lateral boundary including the lithosphere, upper and lower mantle. The choice of lateral boundary conditions is only relevant for regional subduction models, as whole earth models have no lateral edges (*e.g.*, Li and Zhong, 2009; Deschamps et al., 2010). In the case of.3 -D.models, conditions on the front and back of the model domain need to be specified as well. These can be chosen in the same way as.2 -D.lateral boundary conditions, but free-slip (Yamato et al., 2009; Stegman et al., 2010) or no slip boundaries (Piromallo et al., 2006) are most commonly used.

The bottom boundary of subduction models can be open or closed (Christensen, 1996). Closed boundaries may be free-slip (Arcay et al., 2007; Čížková et al., 2007; Billen and Hirth, 2007; Schmeling et al., 2008; Kaus et al., 2010) or no-slip (*i.e.*, the horizontal and vertical component of velocity is zero) (Piromallo et al., 2006; Faccenna et al., 2009). Christensen (1996) showed that a closed bottom boundary condition, at 2500 km depth, causes subducting slabs to bend and undergo large deformation in the mantle, whereas an open bottom boundary condition allows subduction of straight slabs. The 660 km discontinuity is often used to limit the

model domain in numerical (Warren et al., 2008b; Faccenna et al., 2009; Capitanio et al., 2010) and analogue models (Heuret et al., 2007; Lallemand et al., 2008). Most of our models have a free-slip boundary at 660 km depth, but we investigate the case of a limited-slip boundary by including a simple linear viscous lower mantle, similar to the lower mantle used by Kincaid and Olson (1987), Enns et al. (2005) and Stegman et al. (2010).

In this study, we focus on the roles of the surface, lateral and bottom mechanical boundary conditions in.2 -D.numerical models of subduction. We aim to characterise the influence of the surface boundary condition by examining (1) a free surface (*i.e.*, v_x and v_y unconstrained), (2) a free-slip surface (v_y constrained and v_x unconstrained) and (3) an approximation of a free surface, by combining a free-slip surface boundary with a layer of low-viscosity, low density material between the model surface and the top of the lithosphere (so-called 'sticky air'). We perform a parametrical study of the 'sticky air' layer to determine which rheological properties best reproduce a free surface. We quantify our results by considering the evolution of trench position, trench migration velocities, slab tip depth, slab tip subduction velocities, and slab geometry. We use two separate model setups. First, we investigate the case of gravitational subduction of an oceanic plate without an overriding plate (*i.e.*, the only forces acting in the model are the body forces). Second, we extend these models to include an overriding plate and, in one case, a lower mantle.

3.2 Modelling method

3.2.1 Numerical approach

The numerical models are calculated using a standard arbitrary Lagrangian Eulerian (ALE) finite element code developed by Susanne Buiter and Susan Ellis. The code uses a particle-in-cell scheme to solve for large-scale deformations. It solves the equations for conservation of momentum for an incompressible fluid :

$$-\frac{\partial P}{\partial x_i} + \frac{\partial \sigma'_{ij}}{\partial x_j} + \rho g_i = 0 \tag{3.1}$$

$$\frac{\partial v_i}{\partial x_i} = 0 \tag{3.2}$$

P is dynamic pressure (mean stress), σ'_{ij} the deviatoric stress tensor, v the velocity vector, ρ density and g gravitational acceleration ($g_x = 0$, $g_y = 9.81\ m.s^{-2}$). The summation convention over repeated indices is implied.

Because our objective is to study the influence of the boundary conditions on subduction dynamics, we minimise effects of complex rheologies on the dynamics

of the system by keeping our models as simple as possible. The lithosphere and upper and lower mantle in our model are all linear viscous:

$$\sigma'_{ij} = 2\eta\dot{\varepsilon}'_{ij} \tag{3.3}$$

η is the viscosity, $\dot{\varepsilon}'_{ij}$ the deviatoric strain rate tensor. Harmonic viscosity and arithmetic density averaging schemes are used (Schmeling et al., 2008). We do not solve the thermal evolution of the system. We use a Q4P1 element that is linear in velocity (4 velocity nodes with 2 degrees-of-freedom each) and has constant pressure (Zienkiewicz and Taylor, 2000a). The pressure is calculated using the Uzawa iterative penalty formulation (Cuvelier et al., 1986; Pelletier et al., 1989; Zienkiewicz and Taylor, 2000a):

$$P^t = P^{t-1} - k\frac{\partial v_i^t}{\partial x_i} \tag{3.4}$$

k is the bulk modulus or compressibility factor (approximately 10^{31} Pa in our models which is 8 orders of magnitude larger than our lithosphere viscosity (Zienkiewicz and Taylor, 2000b)) and t indicates timestep. These equations are solved on the Eulerian grid, while the material properties (*i.e.*, the rheological values and the densities) and stress history are stored on the particles.

A free surface is obtained following Fullsack (1995). The Eulerian grid is adjusted vertically to accommodate surface displacements, as well as surface processes. Our models have a small amount of diffusive erosion and sedimentation, with a diffusion coefficient on the order of 10^{-5} to 10^{-6} m^2s^{-1} (Culling, 1960). The amount of eroded and sedimented material is so small that the evolution of the model is not affected. In numerical subduction models which include a free surface or other interfaces with large density contrasts, an instability can occur as a result of numerical overshoot when computing restoring forces (Kaus, 2008; Kaus et al., 2010). The effect can be illustrated by considering relaxation of a sinusoidal perturbation of a viscous medium (Johnson and Fletcher, 1994, section 1.4). The relaxation time (t_s) of the perturbation depends on the viscosity of the medium:

$$t_s = \frac{4\pi\eta}{\rho g_y L} \tag{3.5}$$

where *L* is the length of the perturbation, and η is the viscosity. If the numerical timestep, dt, is on the order of or larger than t_s, the body and surface forces computed explicitly will be out of balance with the updated configuration of the free surface. This imbalance is commonly suppressed by using extremely small timesteps and/or a larger value for mantle viscosity, but a more robust solution (as detailed in Kaus et al. (2010)) is to add an extra implicit term to the stiffness matrix

which takes into account the incremental change in normal forces across density interfaces during each timestep:

$$\Delta F_y = \Delta\rho.g_y.dt.v_y \tag{3.6}$$

where ΔF_y is the extra vertical force term across the interface; $\Delta\rho$ is the change in density across the interface; $g_y = -9.81\ m.s^{-2}$, dt is the timestep, and v_y is the vertical velocity of the interface. This extra term is applied to the free surface, and at any other interface with a density contrast. It allows the use of a timestep at least 1 order of magnitude greater than would otherwise be possible.

3.2.2 Model setup

Our first set of models investigates gravitational subduction in which a slab sinks into the mantle under its own weight (*i.e.*, by the density contrast between the subducting lithosphere and the mantle) (Fig. 3.1A). In this case no overriding plate is implemented in the model. This type of model setup shows the zero order behaviour of the subducting slab itself (Goes et al., 2008) and has, for this reason, been widely studied using both analogue (*e.g.*, Guillou-Frottier et al., 1995; Faccenna et al., 2001; Funiciello et al., 2003a; Schellart, 2005) and numerical methods (*e.g.*, Piromallo et al., 2006; Capitanio et al., 2007; Schmeling et al., 2008). The simple boundary conditions and model setup enable a good understanding of the effects of changes in model parameters on the system dynamics.

The model domain (Fig. 3.1A) is 3000 km wide and 660 km deep. We have chosen the model width on the basis of a series of tests that showed that model differences were negligible for widths larger than 3000 km. We investigate the depth of the domain in our second series of models. The subducting slab is composed of a one or two-layer 100 km thick, old viscous slab that subducts in a linear viscous upper mantle. The viscosity contrast between our lithosphere and mantle is three orders of magnitude. It has been shown that the viscosity contrast is a control on the style of subduction, from advancing for strong slabs to retreating for weaker slabs (Di Giuseppe et al., 2008; Faccenna et al., 2009; Schellart, 2009). We keep our rheological parameters constant throughout our study in order to focus on the role of the boundary conditions. Our values for the viscosity and density contrast between the slab and the mantle are within the ranges of published simple, linear viscous, models of subduction (*e.g.*, Pysklywec et al., 2000; Enns et al., 2005; Schmeling et al., 2008; Kaus et al., 2010). The viscosity of the weak crust (10^{20} Pa.s) is an effective viscosity calculated using the von Mises yield criterion (using a cohesion of 2 MPa) and a constant strain rate ($10^{14}\ s^{-1}$). The lateral and bottom boundary conditions are free-slip (*i.e.*, the boundary's perpendicular velocity component is zero and the parallel component is unconstrained). In one

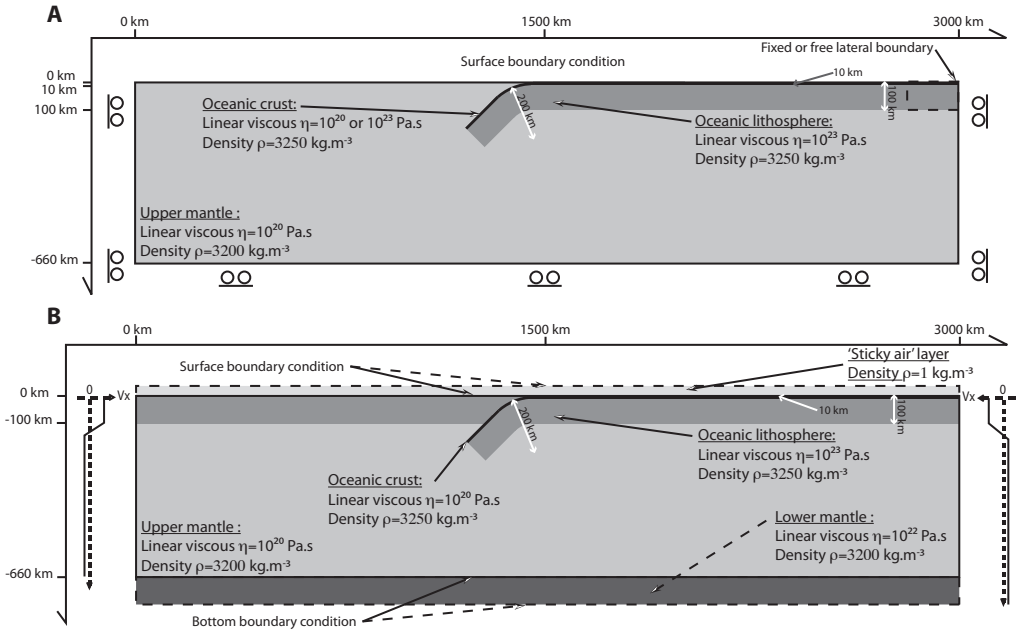


FIGURE 3.1 – A) Gravitational subduction model setup. Lateral and bottom boundary conditions are free-slip. The surface boundary condition is either free surface or free-slip. The subducting lithosphere is either held fixed at its lateral edge or it can be decoupled (dashed box is filled with mantle material in the latter case). B) Ocean-ocean type model setup. The bottom boundary condition is free-slip and can include a linear viscous lower mantle of variable thickness. The lateral boundary conditions include material in- and outflow. The surface boundary condition is either (1) free surface, (2) free-slip or (3) reproducing a free surface using a free-slip model surface and a 'sticky air' layer.

case, the subducting lithosphere is decoupled from its right lateral boundary, the so-called 'free slab' (Kincaid and Olson, 1987). We keep the length of the slab which lies at the surface at 1400 km by using a tracer injection scheme that converts mantle material into 'new' slab at x=2900 km. This can be seen as a simplified ridge. To avoid spontaneous subduction at the right extremity of the subducting slab no oceanic crust is injected, coupling the slab trailing edge to the surface boundary. The surface boundary condition of the gravitational subduction models (Fig. 3.1A) is either free surface or free-slip. To bypass the subduction initiation phase, which is still not fully understood (Branlund et al., 2001; Regenauer-Lieb et al., 2001), we start our models with a pre-existing subducted portion of the lithosphere (following *e.g.*, Heuret et al. (2007); Schellart (2005)). The Eulerian mesh of our models is either uniform or has an increased resolution around the slab. In the variable Eulerian mesh, the minimum element size ranges from $2 \times 2\ km$ (horizontal $\times$ vertical) at the trench to $10 \times 20\ km$ near the model domain boundaries. As a result,

the total number of elements in the model domain ranges from approximately 300 to 450 horizontally and from 76 to 200 vertically (Tabs. 3.1 and 3.2).

Our second set of models is based on the previous gravitational subduction models extended to include an overriding oceanic plate (Fig. 3.1B) which has the same properties as the subducting lithosphere, but without an oceanic crust. The bottom boundary condition is free-slip. For one of our models, we investigate the effect of a lower mantle of variable thickness (ranging from $100\ km$ to $1000\ km$ thick) (similar to, for example, Enns et al. (2005) and Stegman et al. (2010)). The transition between the upper and the lower mantle is defined by a viscosity contrast of 100 (Tosi et al., 2005; Stegman et al., 2010). The surface boundary condition is either (1) free-slip, (2) a free surface or (3) a free-slip model domain surface underlain by a low-density, low-viscosity material ('sticky air') (Gerya et al., 2004; Gerya and Yuen, 2007; Gorczyk et al., 2007a; Schmeling et al., 2008). We aim to determine the rheological and mechanical parameters of the 'sticky air' layer (*i.e.*, viscosity and thickness) that best reproduce a free surface. Subduction is enabled by the imposed convergence rate, the density contrast between the oceanic lithosphere and the mantle, and the low viscosity crustal layer of the subducting slab that serves as a decoupling layer that localises deformation at the plate boundary (Fig. 3.1B). We use a convergence rate of $5\ cm.yr^{-1}$ which is achieved by assigning contractional velocities at the vertical side boundaries of the subducting and overriding lithospheres. The inflow of material into the Eulerian domain is balanced by mantle outflow. The transition from in- to outflow on the lateral boundary, occurs over 10 km (5 elements). This 'velocity gradient region' suppresses mantle deformation and high strain rates, which would otherwise be caused by the velocity contrast. The application of inflow on the overriding or subducting lithosphere edge and the relative magnitudes of the in- and outflow velocities could influence subduction dynamics (Heuret et al., 2007). Using the model setup of figure 3.1B, we therefore test the effects of variations in the lateral boundary conditions on the evolution of the slab in the mantle. To enable comparison among the ocean-ocean subduction models, the convergence rate remains fixed at $5\ cm.yr^{-1}$.

We quantify our results by (1) slab geometry, (2) slab tip depth and trench position and (3) trench migration velocities and the vertical component of the slab tip velocity. We define in this study the trench location as the last particle of mantle, for gravitational subduction models, or of overriding plate material, for ocean-ocean models, observed at the surface of the model when looking from left (mantle surface) to right (slab). Similarly, slab tip is defined as the lowermost particle of lithospheric material of the subducting plate in the model domain. A list of the gravitational subduction and ocean-ocean models with mesh resolutions and surface and lateral boundary conditions is given in tables 3.1 and 3.2.

TABLE 3.1 – List of gravitational subduction models.

Model	Resolution		Surface BC[a]	Oceanic crust	Figure
	Min/Max horiz. (km/el)	Min/Max vert. (km/el)			
1-1	Constant 10	Constant 10	Free-slip	n	Fig. 3.2A
1-2	Constant 10	Constant 10	Free surface	n	Fig. 3.2B
1-3	Constant 10	Constant 10	Free-slip	y	Fig. 3.2C, Fig. 3.3
1-4	5/10	5/10	Free-slip	y	Fig. 3.3
1-5	2/10	2/10	Free-slip	y	Fig. 3.3
1-6	Constant 10	Constant 10	Free surface	y	Fig. 3.2D, Fig. 3.3
1-7	5/10	5/10	Free surface	y	Fig. 3.3, Fig. 3.4A
1-8	2/10	2/10	Free surface	y	Fig. 3.3
1-9[b]-free	5/10	5/10	Free surface	y	Fig. 3.4B

[a] The free surface models have a small amount of diffusive erosion and sedimentation with a diffusion coefficient of $10^{-5}\ m^2.s^{-1}$.

[b] The subducting lithosphere and crust are detached from the right lateral boundary.

	Model	Resolution		Boundary Conditions					Figure
		Min/Max horiz. (km/el)	Min/Max vert. (km/el)	Surface	Lower mantle thickness	Left vel.	Right vel.	Erosion Diff. Coef. ($m^2 s^{-1}$)	
	2-1	3/20	3/10	Free-slip	–	in. / out.	in. / out.	–	Fig. 3.6
	2-2	3/20	3/10	Free-slip	–	in. / out.	–	–	Fig. 3.6
	2-3	3/20	3/10	Free-slip	–	–	in. / out.	–	Fig. 3.6
	2-4	3/20	3/10	Free surface	–	in. / out.	in. / out.	10^{-6}	Fig. 3.5B, 3.6, 3.7B, 3.8, 3.9, 3.10B, 3.11
	2-5	3/20	3/10	Free surface	–	in. / out.	–	10^{-6}	Fig. 3.5A, Fig. 3.6
	2-6	3/20	3/10	Free surface	–	–	in. / out.	10^{-6}	Fig. 3.5C, Fig. 3.6
	2-7	3/20	3/10	Free surface	100 km	in. / out.	in. / out.	10^{-6}	Fig. 3.8
	2-8	3/20	3/10	Free surface	200 km	in. / out.	in. / out.	10^{-6}	Fig. 3.8
	2-9	3/20	3/10	Free surface	400 km	in. / out.	in. / out.	10^{-6}	Fig. 3.8
	2-10	3/20	3/10	Free surface	500km	in. / out.	in. / out.	10^{-6}	Fig. 3.7A, 3.8
	2-11	3/20	3/10	Free surface	1000 km	in. / out.	in. / out.	10^{-6}	Fig. 3.8
'Sticky air'	2-12	3/20	3/10	16 km / 5e17 $Pa.s$	–	in. / out.	in. / out.	10^{-6}	Fig. 3.11A, B, C
	2-13	3/20	3/10	16 km / 1e18 $Pa.s$	–	in. / out.	in. / out.	10^{-6}	Fig. 3.11A, B, C
	2-14	3/20	3/10	16 km / 5e18 $Pa.s$	–	in. / out.	in. / out.	10^{-6}	Fig. 3.11A, B, C
	2-15	3/20	3/10	16 km / 1e19 $Pa.s$	–	in. / out.	in. / out.	10^{-6}	Fig. 3.11A, B, C
	2-16	3/20	3/10	16 km / 5e19 $Pa.s$	–	in. / out.	in. / out.	10^{-6}	Fig. 3.11A, B, C
	2-17	3/20	3/10	40 km / 5e17 $Pa.s$	–	in. / out.	in. / out.	10^{-6}	Fig. 3.11D, E, F
	2-18	3/20	3/10	40 km / 1e18 $Pa.s$	–	in. / out.	in. / out.	10^{-6}	Fig. 3.9, 3.10A, 3.11D, E, F
	2-19	3/20	3/10	40 km / 5e18 $Pa.s$	–	in. / out.	in. / out.	10^{-6}	Fig. 3.11D, E, F
	2-20	3/20	3/10	40 km / 1e19 $Pa.s$	–	in. / out.	in. / out.	10^{-6}	Fig. 3.11D, E, F
	2-21	3/20	3/10	40 km / 5e19 $Pa.s$	–	in. / out.	in. / out.	10^{-6}	Fig. 3.11D, E, F

TABLE 3.2 – List of ocean-ocean convergent models.

3.3 The influence of the surface boundary in gravitational subduction models

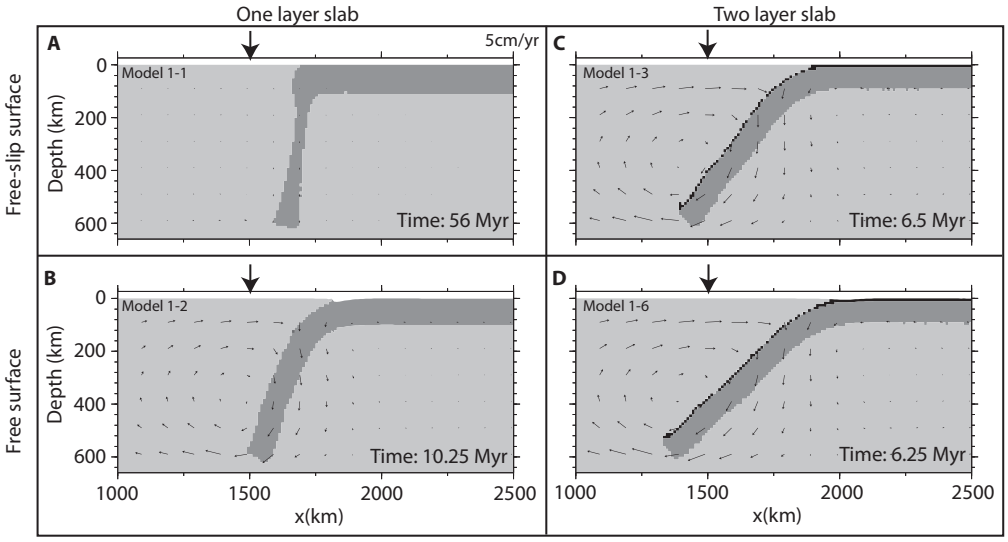


FIGURE 3.2 – A snapshot of four gravitational subduction models, with the slab held fixed at its right hand side, taken when the slab tip reaches a depth of 600 km. The central part of the total model width of 3000 km is shown. The black arrows at the surface of the model domain represent the initial position of the trench. A) A one layer lithosphere with a free-slip surface; B) a one layer lithosphere with a free surface; C) a two layer lithosphere with a free-slip surface and D) a two layer lithosphere with a free surface. The two layer models (C and D) differ from the one layer models (A and B) by inclusion of a weak crust. The time required to reach a depth of 600 km is indicated at the lower right of each frame. The one-layer lithosphere with a free-slip surface (A) subducts substantially slower than the other models. The model setup is shown in figure 3.1A.

Subduction of a slab into the mantle is only possible when the slab can decouple from the surface. This is unproblematic for free surface models, but not entirely straightforward for free-slip models. We show this in figure 3.2. The oceanic lithosphere in these models has a 10^{23} $Pa.s$ viscosity and its crust has either the same properties (Fig. 3.2A, B), resulting in a one-layer slab, or a lower value of 10^{20} $Pa.s$ (Fig. 3.2C, D).

If the surface boundary condition is free-slip, a one-layer slab can not decouple from the surface (Fig. 3.2A). The horizontal segment of the oceanic lithosphere thickens to accommodate a slow retreat of the trench while the pre-existing subducted part of the oceanic lithosphere drips in the manner of a Rayleigh-Taylor instability. 56 Myr are needed for the lowermost point of this lithosphere to reach

a depth of $600\ km$. Only with a free surface boundary condition can the strong, one-layer lithosphere decouple from the surface and subduct (Fig. 3.2B), something which was also recently shown by Kaus et al. (2010). Alternatively, decoupling in free-slip models can be achieved by adding a weak layer at the surface. Figure 3.2C shows that such a weak crust allows the slab to decouple from the surface and subduct. In the models of figure 3.2, the right lateral edge of the slab is held fixed and subduction can only occur by trench retreat. Differences in the dip angle can be observed between figure 3.2B (69^o dip angle), C (52^o dip angle) and D (42^o dip angle). These differences in dip angle can be explained by the capability of the trench to retreat: a slow retreat allows the slab to align with the direction of the gravitational pull (Fig. 3.2B), while faster retreat leads to shallower dip (Fig. 3.2C and D). The ability for the trench to retreat in the gravitational subduction models depends on the effective viscosity at the trench and at the surface of the subducting lithosphere. In figure 3.2C and D, the weak crustal layer allows faster retreat and therefore faster subduction. In our models we use a harmonic averaging of viscosity from particles to elements. The harmonic average results in low viscosities (Schmeling et al., 2008) at the trench. Changing the viscosity averaging scheme lead to slightly higher viscosities of the trench, reducing subduction velocities and increasing slab dip.

The differences observed in slab tip depth (Fig. 3.3A), vertical component of the slab tip velocity (Fig. 3.3B), trench position (Fig. 3.3C), trench retreat velocities (Fig. 3.3D) and dip angle (Fig. 3.2C and D), between two-layer lithosphere models with either a free surface or a free-slip surface are small. The presence of a weak crust therefore seems to reproduce the effects of a free surface in gravitational subduction models to first order. A difference that remains is in the topography of the surface. Free surface models can form a ”trench” at the mantle-slab contact and a foreland bulge ocean-ward (Fig. 3.2B and D). These structures can not form in free-slip models.

When true subduction occurs (Fig. 3.2B, C and D) the models show a 3-step evolution through time (Figs. 3.3 and 3.4A). The first phase is subduction start-up, which is characterised by a rapid increase of trench migration and slab tip subduction velocities and lasts approximately 2 Myr. The second phase is stable subduction, lasting approximately 3 Myr depending on the surface boundary condition and the grid resolution used. It is characterised by a near constant sinking velocity of the slab tip associated with a constant trench retreat. During this phase there is no interaction of the slab with the lower mantle. The third phase occurs when the slab reaches the bottom of the model domain. During this phase the slab tip subduction velocities decrease rapidly while the trench retreat velocities decrease slowly. The slab tip interacts with the lateral flow induced at the bottom boundary and the subducted lithosphere starts to thin once the horizontal velocity of the slab tip exceeds the trench retreat velocity.

The surface boundary condition in these models exerts a second-order influence on the system. The change from a free-slip to a free surface increases the vertical velocity of the slab tip (Fig. 3.3B), and the trench migration velocities (Fig. 3.3D). The slab tip depths are only slightly different (Fig. 3.3A). In addition, we find that the rate of dissipation of energy and the gravitational rate of work are almost equal, implying that the topography of the free surface model is not controlling these quantities (values not shown). Schmeling et al. (2008) showed that the mesh resolution at the trench influences subduction velocities. Our models confirm their findings that the higher the mesh resolution, the higher the slab tip and trench velocities (Fig. 3.3B and D). The time needed for the trench to migrate $500\ km$ horizontally reaching a distance of $2000\ km$ is reduced as the mesh resolution is increased (Fig. 3.3C). Capitanio et al. (2007) showed that in gravitational subduction models, slab sinking velocities tend towards the Stokes sinker velocity. These values are reached in the later stages of subduction, once the slab rests upon the bottom of the model domain. We focus on the stages of subduction before the interaction of the slab tip with the lower boundary. However we do find that the maximum sinking velocities in our gravitational subduction models do not exceed the expected Stokes sinker velocity.

In the above models, the slab right edge was 'held' fixed. This promotes a trench retreat mode because the horizontal displacement of the part of the slab that is still at the surface is inhibited. Decoupling the right edge of the slab (*e.g.*, Kincaid and Olson, 1987; Enns et al., 2005; Faccenna et al., 2009; Stegman et al., 2010) (Fig. 3.4) gives more freedom to the model. A free edge allows less retreat (Fig. 3.4B) accompanied by folding of the slab on the 660 km discontinuity. Such models could even show trench advance, as in the studies of Enns et al. (2005) and Di Giuseppe et al. (2008).

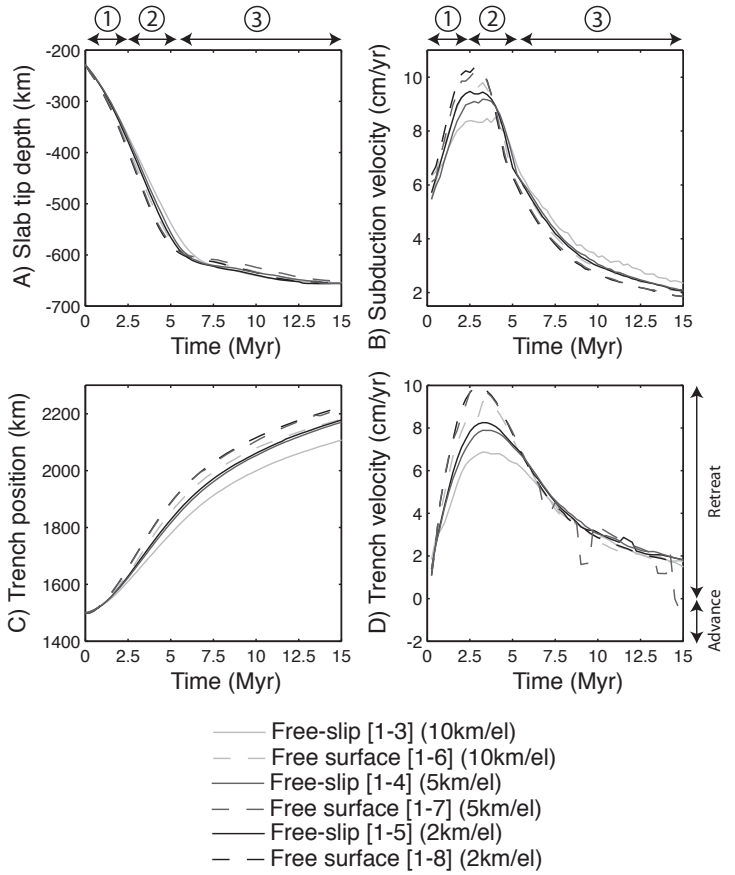


FIGURE 3.3 – Quantification of results for the gravitational subduction models. A) Slab tip depth, B) vertical velocity of the slab tip, C) trench horizontal position and D) trench migration velocity as a function of time using different mesh resolutions at the trench and different surface boundary conditions. The circled numbers at the top of each column denote the subduction phases. A minor spline-type of smoothing is applied to the velocity curves to take out the small wavelength fluctuations caused by particle motions (panels B and D).

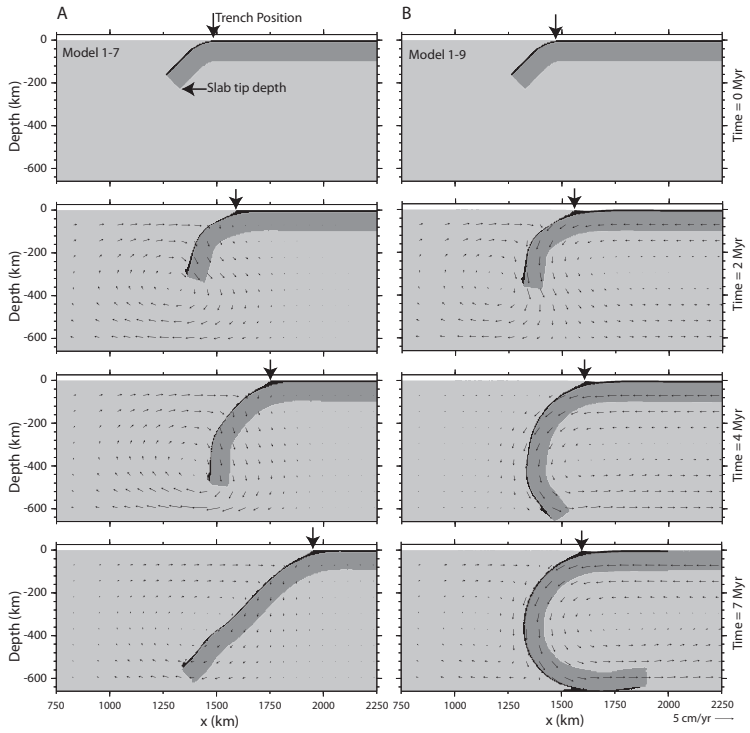


FIGURE 3.4 – Snapshots of the evolution through time of a two-layer gravitational subduction model with a free surface. The models include a subducting lithosphere that is A) 'coupled' or B) 'decoupled' to the right hand side boundary. The elemental material distribution and a sample of the nodal velocities are shown (the velocity scale is at the lower right). See text for further description.

3.4 Ocean-ocean subduction models

3.4.1 The influence of the lateral boundary conditions

In our second series of models, we introduce an oceanic overriding plate. The presence of an overriding plate can influence trench migration and the evolution of the subducting slab in several ways. First, the properties of the interface between the subducting and overriding plate (subduction fault or subduction channel) need to be weak enough so that subduction can occur (Hampel and Pfiffner, 2006). Second, motion of the overriding plate (owing to movements of surrounding plates for example) can force trench migration (Heuret et al., 2007; Schellart, 2008b; Capitanio et al., 2010). And third, trench migration with a stationary overriding plate can only occur if the overriding plate can deform (Heuret et al., 2007; Schellart, 2008b). Using the model setup of figure 3.1B, we first study the influence of the lateral boundary conditions on subduction dynamics by modifying the location and the magnitude of the material in- and outflow velocities. We keep the convergence rate fixed at $5\ cm.yr^{-1}$.

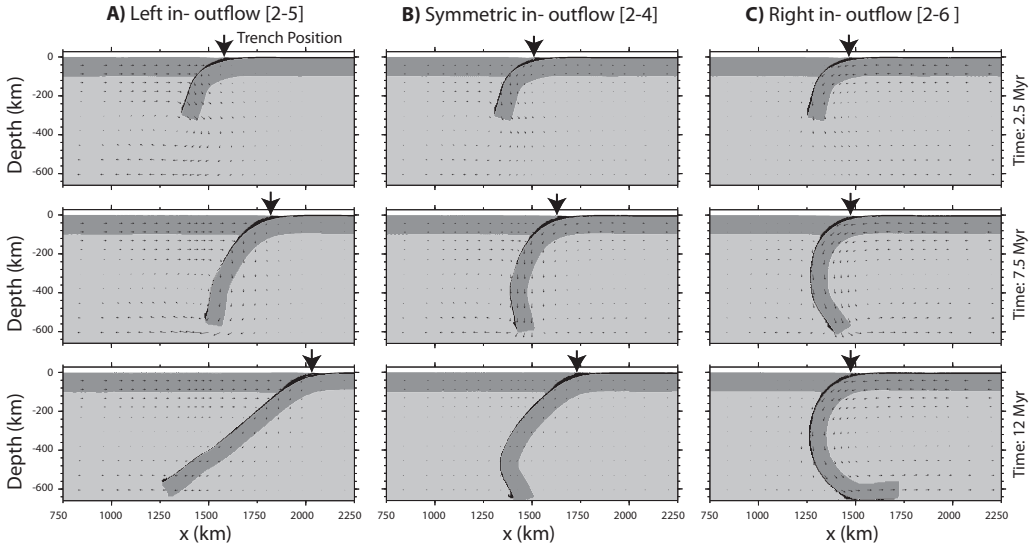


FIGURE 3.5 – Snapshots at 2.5, 7.5 and 12 Myr for ocean-ocean convergence models. The top boundary is a free surface, the bottom boundary is free-slip and the lateral boundaries are varied between A) in- and outflow from the left hand side, B) symmetric in- and outflow and C) in- and outflow from the right hand side. The model numbers are given in brackets.

The in- and outflow velocity fluxes are balanced and the outflow velocities are therefore an order of magnitude lower than the inflow velocities. Because of the low magnitude for the outflow velocity, the influence of implementing outflow symmetrically, only left or only right is small. We find that the slab geometry and

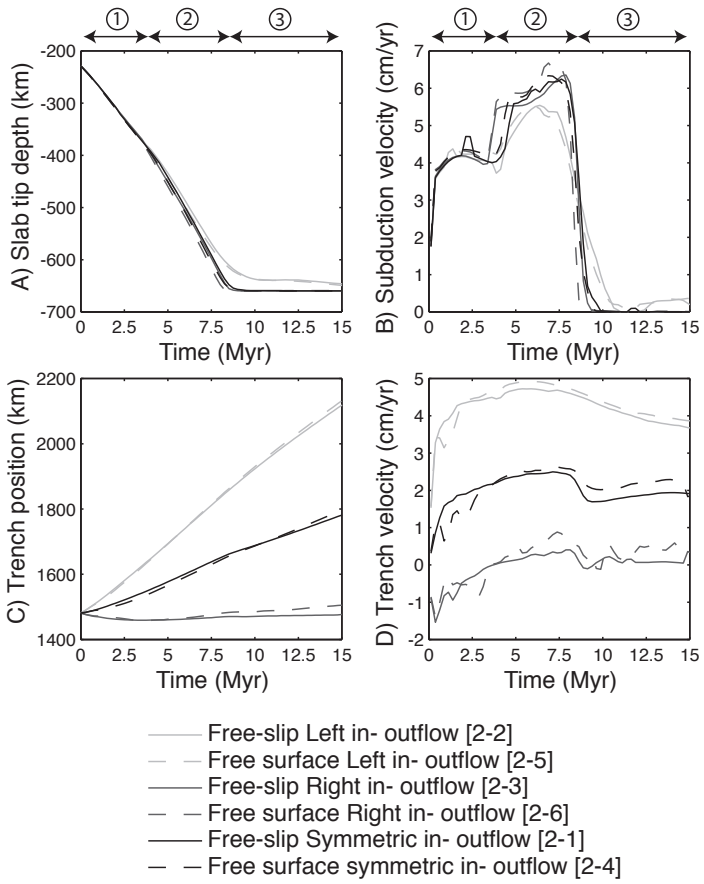


FIGURE 3.6 – Quantification of results for ocean-ocean models. A) Slab tip depth, B) vertical velocity of the slab tip, C) trench horizontal position and D) trench migration velocity as a function of time. The lateral boundary conditions are left material inflow, right material inflow, or left and right material inflow. The surface boundary condition is either free-slip or a free surface and the bottom boundary condition is free-slip. The circled numbers at the top of each column denote the subduction phases. A minor spline-type of smoothing is applied to the velocity curves to take out the small wavelength fluctuations caused by particle motions (panels B and D).

evolution are not modified for variations of outflow location between the left and right model edges. However, the dynamics of the subduction system is sensitive to changes in the velocity inflow from the left edge of the model domain to the right edge (Figs. 3.5 and 3.6). A convergent velocity imposed on the overriding plate (*i.e.*, a portion of the inflow is implemented on the left hand side of the model domain) causes trench retreat and a slab which finally rests on the lower mantle (Fig. 3.5A and B). If the overriding plate is fixed at its side boundary (and inflow is applied at the subducting right edge), the model will evolve through trench advance,

the slab folding on the lower mantle (Fig. 3.5C).

The ocean-ocean models also follow a 3 step evolution. During the initial phase, lasting approximately $3\ Myr$, the slab subducts at a velocity of approximately 4 $cm.yr^{-1}$ (Fig. 3.6B). The second phase is characterised by a vertical velocity of the slab tip between 5 and 6 $cm.yr^{1}$ (Fig. 3.6B). During this phase the slab subducts freely and the maximum trench retreat velocity is observed (Fig. 3.6D). The beginning of the third phase is characterised by a rapid decrease in the slab tip and trench velocities (Fig. 3.6B and D). Once the slab lies on the 660 km discontinuity, the so-called stable subduction phase occurs (Funiciello et al., 2003a; Capitanio et al., 2009; Schellart, 2009; Faccenna et al., 2009). During this phase, the subducting lithosphere can: either rest on the upper mantle (Fig. 3.5A), resulting in a rapid retreat of the trench (Fig. 3.6C and D); or fold on the lower mantle (Fig. 3.5C, resulting in a fixed trench (Fig. 3.6C and D).

3.4.2 The influence of the bottom boundary condition

In the case of symmetric in- and outflow lateral boundary conditions, the angle of the subducting slab when it interacts with the bottom boundary is such that we expect it to penetrate the lower mantle (Fig. 3.5B). However, the free-slip bottom boundary prevents this. In order to investigate the influence of the bottom boundary, we add a lower mantle to the ocean-ocean subduction model setup with symmetric lateral boundary conditions. The lower mantle is kept simple, as the rest of the model, with a linear viscous rheology ($\eta_{(lower\ mantle)} = 100 \times \eta_{(upper\ mantle)}$). When a lower mantle is present, the slab tip penetrates into the lower mantle indenting the upper-lower mantle boundary (Fig. 3.7A). This results in a higher dip angle of the slab. The vertical component of the slab tip velocity decreases gradually once the slab reaches the 660 km discontinuity, the decrease being slower for a thicker lower mantle (Fig. 3.8B). The trench retreat velocity reaches a value between 2 and 2.5 $cm.yr^{-1}$ if the thickness of the lower mantle is less than 500 km (Fig. 3.8D). For a thickness exceeding 500 km the trench retreat velocity decreases gradually.

The 660 km discontinuity in these models is greatly simplified and does not include phase transitions. We have used it as a first order approximation to soften the impact of the impenetrable 660 km discontinuity. Previous models have included a linear viscous lower mantle with thicknesses ranging from 400 km (Stegman et al., 2010) to 1000 km (Enns et al., 2005). We find that with a thickness of the lower mantle of more than 400 km the slab tip depth and trench position curves converge (Fig. 3.8A and C).

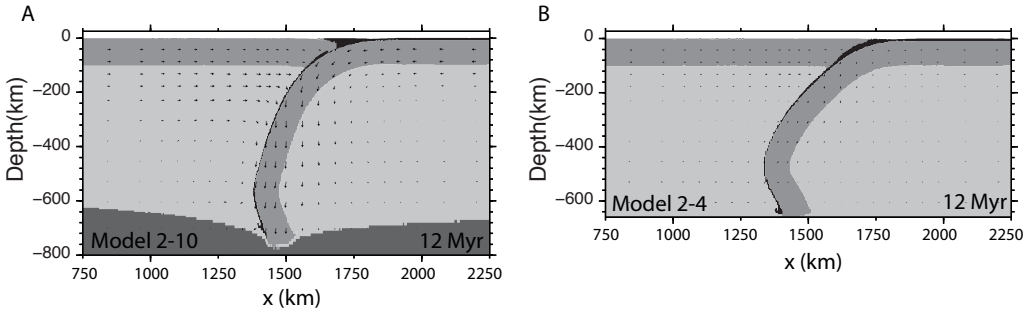


FIGURE 3.7 – The effect of adding a linear viscous lower mantle to ocean-ocean subduction models. The models have symmetric material in- and outflow. A) A 500 km thick lower mantle and B) without lower mantle.

3.4.3 The influence of the surface boundary

We have shown that a free surface enables subduction in gravitational subduction models with a one-layer slab (Figs. 3.2A, B and 3.3) and slightly increases the trench migration and the vertical slab tip subduction velocities of gravitational subduction models with a two-layer slab in comparison with free-slip models (Figs. 3.2C, D and 3.3). We find similar effects for the ocean-ocean models (Fig. 3.6), but the effects are very minor. This is because the the weak crustal layer decouple the subducting lithosphere from the surface boundary condition (this is discussed later on in more detail).

An alternative approach to obtain free surface behaviour in models with a vertically fixed upper boundary is to use a 'sticky air' layer (*e.g.*, Funiciello et al., 2003b; Gerya et al., 2004; Gerya and Stöckhert, 2006; Gorczyk et al., 2006; Nikolaeva et al., 2008). This approach has the advantage over free-slip models that vertical displacements of the surface of the lithosphere are now possible (similar to free surface models). We keep the density of our 'sticky air' layer fixed at $1\ kg.m^{-3}$ and vary its viscosity and thickness (Table 3.2) in an attempt to reproduce the dynamics of the free surface in ocean-ocean convergence models with symmetric in- and outflow. The 'sticky air' models have large contrasts in density and viscosity between the crust and the overlying "air" layer. As a result, velocities in the "air" layer tend to be orders of magnitude higher than in the rest of the model domain. We track the crust-air interface using a connected string of points, which follows the top surface of the lithosphere (and is therefore not disturbed by the "air" velocities). Small instabilities in topography do remain and can be seen as small wave length perturbations (Fig. 3.9).

A small amount of diffusive erosion is applied to the string surface, similar to the free surface models. Adding a 'sticky air' layer between the surface of the

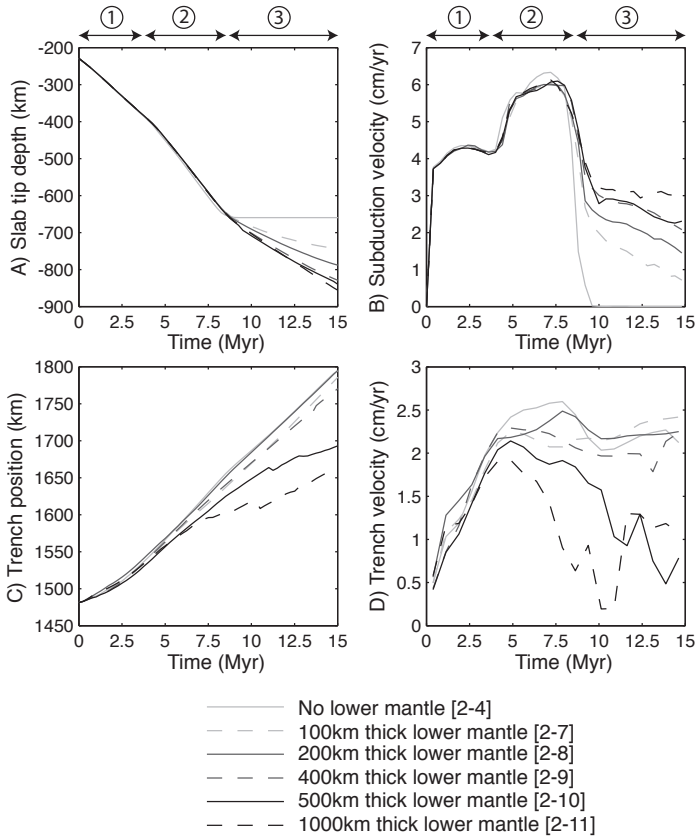


FIGURE 3.8 – Quantification of the effect of adding a lower mantle on A) Slab tip depth, B) vertical velocity of the slab tip, C) trench horizontal position and D) trench migration velocity as a function of time for symmetric ocean-ocean subduction models with a free surface. The bottom boundary condition is free-slip. The thickness of the linear viscous lower mantle is varied between 0 (no lower mantle) and 1000 km. The circled numbers at the top of each column denote the subduction phases. A minor spline-type of smoothing is applied to the velocity curves to take out the small wavelength fluctuations caused by particle motions (panels B and D).

lithosphere and the top free-slip boundary reproduces the topography observed in the free surface models to a large degree (Fig. 3.9). It enables the formation of a foreland bulge and a trench with similar wavelength as in the free surface models. The presence of the 'air' layer also reproduces the slab geometry of a free surface model (Fig. 3.10) and the slab tip depth evolution (Fig. 3.11C, and F). We observe that trench depth (Figs. 3.9 and 3.11A, D) and the foreland bulge height (Figs. 3.9 and 3.11B, E) in the 'sticky air' models are somewhat overestimated in comparison to the free surface models. These models illustrate that a 'sticky air' layer can reproduce the first order features of topography. Variations in the

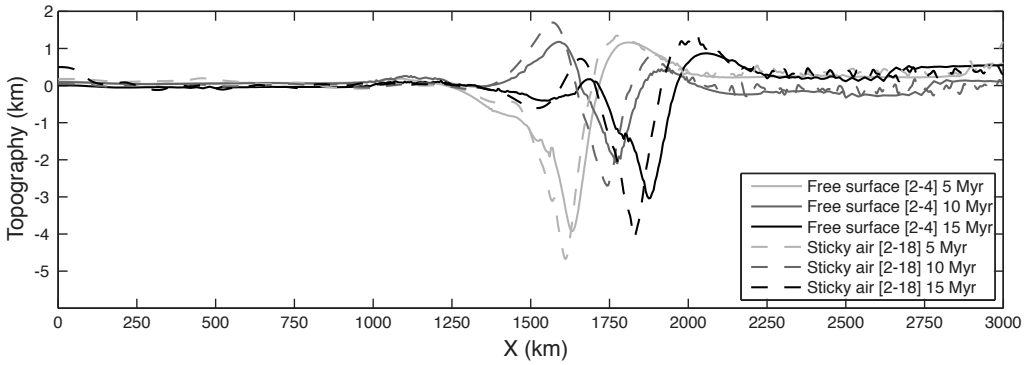


FIGURE 3.9 – A comparison of surface topography at 5, 10 and 15 Myr for a free surface model (model [2-4], solid lines) and a free-slip model with a 'sticky air' layer (model [2-18], dashed lines). The 'air' layer is 40 km thick and has a viscosity of 10^{18} $Pa.s$. The models have symmetric in- and outflow and only differ in the absence/presence of the 'sticky air' layer.

thickness and the viscosity of the 'air' layer do not have a large influence on the large-scale evolution of the model (Fig. 3.11C and F). However, at a local scale (*i.e.*, the trench scale), the evolution of trench depth and foreland bulge height converges once the viscosity difference between the 'sticky air' layer and the crust is of at least 2 orders of magnitude. We find that the thinner the air layer, the larger the viscosity contrast must be at the lithosphere surface in order to reproduce the surface topography of a free surface model. The minimum thickness of the 'sticky air' layer is determined by the maximum topography in the model, as it should allow a foreland bulge to develop which still has 'air' above it.

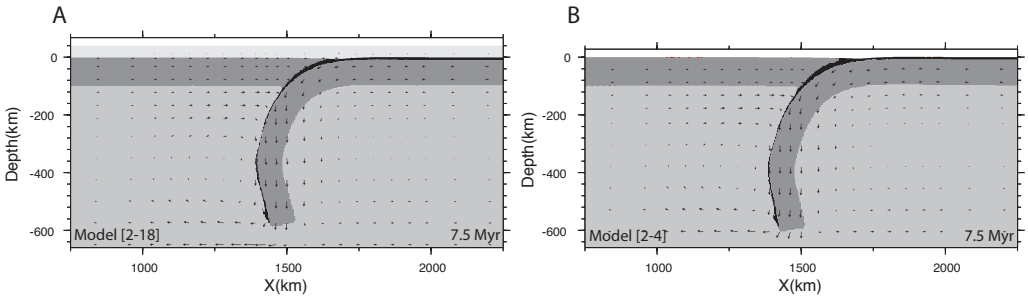


FIGURE 3.10 – Snapshot of ocean-ocean type subduction models at 7.5 Myr with A) a 'sticky air' layer (40 km thick and 10^{18} $Pa.s$ viscosity) or B) a free surface, showing that 'sticky air' models reproduce the overall characteristics of models with a free surface. The model has symmetric in- outflow lateral boundary conditions.

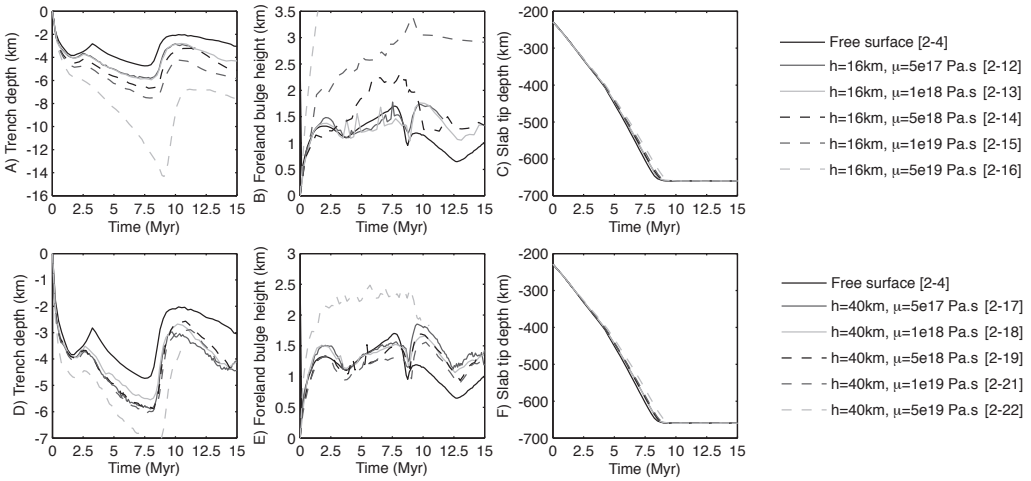


FIGURE 3.11 – Quantification of results from ocean-ocean type models including a 'sticky air' layer. A), D) Maximum trench depth, B), E) maximum foreland bulge height and C), F) slab tip depth as a function of time using symmetrical in- and outflow lateral boundary conditions. The surface boundary is either (1) free or (2) free-slip which includes a 'sticky air' layer with variable viscosities. The top three panels (A, B and C) are for models with a 16 km thick 'sticky air' layer and the bottom three panels (D, E and F) are for a 40 km thick 'sticky air' layer.

3.5 Discussion

3.5.1 The role of the surface boundary

Kaus et al. (2010) recently showed that the nature of the surface boundary has a significant effect on subduction dynamics and that only free surface numerical model results are consistent with laboratory experiments. Our models confirm the importance of the free surface boundary condition. Gravitational subduction of a strong one-layer oceanic lithosphere is only possible if the slab can decouple from the surface boundary (Fig. 3.2). This condition is not automatically fulfilled for a free-slip top surface. A free-slip surface boundary condition only allows surface particles to move along the x-axis (Fig. 3.12). This implies that trench migration is only possible by extending or contracting the part of the plate that is at the surface. The pre-existing subducted part of the slab in this model drips in the manner of a Rayleigh-Taylor instability (Fig. 3.2A) (Kaus et al., 2010).

Decoupling the subducting lithosphere from the surface boundary can be achieved by different methods: (1) Adding an effectively 'weak' crust, with a viscous or plastic rheology, to the subducting lithosphere (Billen and Hirth, 2007; Čížková et al., 2007; Di Giuseppe et al., 2008; Enns et al., 2005; Faccenna et al.,

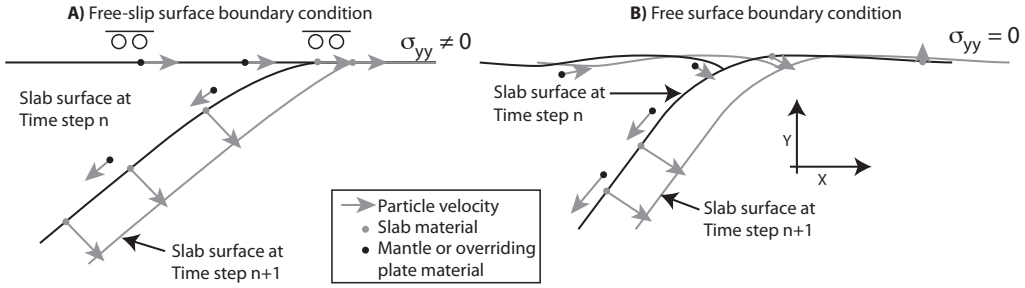


FIGURE 3.12 – Simple schematics of the effects of A) free-slip and B) free surface boundary conditions on the particles located at the trench (see text).

2009; Capitanio et al., 2010; Stegman et al., 2010); (2) adding a 'sticky air' layer above the lithosphere (Gerya et al., 2004; Gorczyk et al., 2007b; Nikolaeva et al., 2008; Schmeling et al., 2008); or (3) implementing a true free surface (Fullsack, 1995; Gurnis et al., 1996; Kaus et al., 2010). A true free surface boundary condition enables vertical displacements and allows the surface particles to migrate along both x- and y-axes. This vertical motion of particles allows the oceanic lithosphere to decouple from the surface boundary (Fig. 3.12). We have shown that a weak crust or a 'sticky air' layer reproduces the effects of a free surface to first order. The particles at the surface of the model domain are still only allowed to migrate along the x-axis, but the particles at the interface of the weak layer and the surface of the strong subducting lithosphere can move horizontally and vertically. However, a weak crust with a free-slip surface boundary condition will not reproduce vertical surface displacements and the associated changes in topography. For this reason, an effective topography is often calculated for free-slip surface models, using the vertical component of the stress tensor ($\sigma_{yy}/\rho g$): the dynamic topography (*e.g.*, Hager and Clayton, 1989; Gurnis et al., 1996). We have not shown dynamic topography results for our models, as the weak oceanic crust and its large viscosity contrast with the overriding plate lead to very low σ_{yy} over the overriding plate and high σ_{yy} over the subducting plate, translating into unrealistic topography differences. Models with a 'sticky air' layer reproduce the topography of free surface models to a large degree (Fig. 3.9).

Numerous models of subduction zone dynamics use a free-slip surface boundary condition (*e.g.*, Billen and Gurnis, 2001; Čížková et al., 2002; Enns et al., 2005; Gerya and Stöckhert, 2006; Gorczyk et al., 2006; Piromallo et al., 2006; Arcay et al., 2007; Clark et al., 2008; Nikolaeva et al., 2008). These models successfully simulate subduction because they use a weak layer at the surface, either in the form of a 'sticky air' layer (Funiciello et al., 2003b; Gerya et al., 2004; Gerya and Stöckhert, 2006; Gorczyk et al., 2006; Nikolaeva et al., 2008), a weak (brittle or viscous) crustal layer (Clark et al., 2008; Yamato et al., 2009; Stegman et al., 2010),

or a brittle-viscous slab (Enns et al., 2005; Billen and Hirth, 2007; Faccenna et al., 2009). Depth-dependent brittle behaviour or a von Mises crust leads to material with a low effective viscosity near the slab surface and at the trench, owing to the high strain rates and stresses at the overriding/subducting plate contact (*e.g.*, Funiciello et al., 2003b; Gorczyk et al., 2006; Stegman et al., 2010). When using a 'sticky air' layer to reproduce the effects of a free surface, it is important to examine the geometrical (*i.e.*, thickness) and rheological (*i.e.*, viscosity) parameters of this layer. We have shown that small differences in these parameters do not have a large influence on the large-scale dynamics of the system (Fig. 3.11C and F), but do influence the dynamics of the system at a regional scale (Fig. 3.11A,B D and E). As a result, a badly defined 'sticky air' layer could have a larger influence than simply using a free-slip surface boundary with a weak upper crust. However, our models have shown that a viscosity contrast of at least 2 orders of magnitude is sufficient between 'air' and crust to reproduce the topography of a free surface model with a minimum thickness of the 'sticky air' layer of 16 km.

3.5.2 The role of the lateral and bottom boundary conditions

Our models are representative of a class of models that are driven by internal density differences in combination with lateral velocity boundary conditions. We use relatively strong subducting and overriding lithospheres (Fig. 3.1). The inflow velocities that are applied along the lateral boundaries of the model domain are then propagated through the strong lithospheres and localise deformation at the contact between the overriding and subducting plates (*i.e.*, the trench). Therefore, we can assume that the material inflow can be associated with subducting and/or overriding plate motions.

Previous numerical, analogue and analytical studies of simplified subduction zones, in which subduction is driven by internal density differences in combination with lateral velocity boundary conditions, have shown three different styles of subduction related to the trench motion: advance, retreat or stationary. These subduction styles have been reproduced for models that include an overriding plate (Heuret et al., 2007; Lallemand et al., 2008; Schellart, 2008b; Capitanio et al., 2010; Stegman et al., 2010) or not (Funiciello et al., 2008; Faccenna et al., 2009; Stegman et al., 2010). An advancing trench may cause the slab to fold on the bottom of the model domain (Heuret et al., 2007; Faccenna et al., 2009) or on the 660 km discontinuity (Stegman et al., 2010), whereas a retreating slab may cause the slab to rest upon the bottom of the model domain (Heuret et al., 2007; Faccenna et al., 2009; Capitanio et al., 2010) or the upper-lower mantle boundary (Stegman et al., 2010). A stationary trench can allow the slab to penetrate the lower mantle, if present (Christensen, 1996; Stegman et al., 2010).

We find similar subduction styles for our models. The gravitational model

setup (*i.e.*, no overriding plate) illustrates the influence of the boundary condition at the trailing edge of the slab. When the trailing edge of the slab is held fixed, the horizontal movement of the flat portion of the slab is inhibited and the model evolves through trench retreat (Fig. 3.4A). A 'free' slab allows the flat portion of the slab to migrate towards the trench and as a result the slab tip folds on the bottom boundary (Fig. 3.4B). Enns et al. (2005) showed similar results. Our ocean-ocean models show that the trench motion (*e.g.*, fixed or retreating) is controlled by the overriding plate motion, or in other words, by applying an inflow on the edges of the subducting or overriding lithosphere (Figs. 3.5 and 3.6C and D). If an inflow velocity is applied along the left lateral edge of the overriding plate (*i.e.*, the overriding plate motion is towards the trench), the trench will retreat, causing the slab to lie on the bottom of the model domain (Fig. 3.5A). If the overriding plate is stationary (*i.e.*, no material inflow implemented on the left lateral boundary), the trench is also stationary, causing the slab to fold onto the bottom of the model domain (Fig. 3.5C). These results are in agreement with those of the analogue study of Heuret et al. (2007) and the numerical study of Capitanio et al. (2010). However, the high viscosity of the overriding plate in our models and those of Heuret et al. (2007) inhibits internal deformation. The deformability of the overriding plate can influence trench dynamics, as a weak stationary overriding plate may deform to enable trench retreat or advance (Schellart, 2008b).

In addition to the control exerted by trench motion, the bottom boundary condition, or the capability of the subducting slab to penetrate the lower mantle, also controls slab geometry. Christensen (1996) demonstrated that a stationary trench facilitates the penetration of the slab into the lower mantle. If the subducting slab is vertical when it interacts with the bottom boundary condition (*i.e.*, when the trench is stationary or, in our models, the material inflow is symmetric), a free-slip bottom boundary represents an impenetrable barrier to the slab, forcing it to bend and later rest upon the bottom boundary (Fig. 3.5B). This behaviour is often visible in studies that have a free-slip or a no-slip bottom boundary at 660 km depth (*e.g.*, Funiciello et al., 2003b, 2008; Faccenna et al., 2009; Capitanio et al., 2010). Adding a lower mantle allows the slab to continue vertically, penetrating the lower mantle (Figs. 3.7 and 3.8). However, if the style of subduction is such that the slab would 'rest' upon or fold on $660\ km$ discontinuity, the presence of the lower mantle does not influence the large scale dynamics of the system, as shown by Stegman et al. (2010).

Our ocean-ocean convergence models show that the dynamics of our subduction system depends on where kinematic inflow is prescribed. The choice of applying an overriding plate motion and/or a subducting plate motion through lateral boundary conditions, in combination with the deformability of the overriding plate, determines the type of subduction setting that is being investigated (Fig. 3.5). The observed variations in the dynamics are such that effects of changes in the surface

boundary are overprinted as long as a weak layer is included at the surface of the subducting plate (Fig. 3.6). A modification in the surface boundary will not change the study setting whereas a change in the lateral boundary conditions will (Lallemand et al., 2008).

3.6 Conclusions

We have investigated the influence of surface, bottom and lateral boundary conditions on the evolution of two widely used model setups: gravitational subduction models and ocean-ocean convergent models. The surface boundary condition in subduction models should allow the subducting slab to vertically decouple from its surface. We show that this can be achieved in the following manners:

1. A true free surface.
2. A free-slip surface in combination with a weak crust for the subducting plate. This crust can be viscous, plastic or viscoelastoplastic, as long as the contrast in strength with the lithosphere is about 2 orders of magnitude.
3. A free-slip model surface underlain by a layer of low viscosity, low density material. We find that a thickness at least 16 km, and a viscosity contrast of at least 2 orders of magnitude with the oceanic crust, best reproduce a free surface.

Our ocean-ocean convergent models show that trench motion and slab geometry are controlled by the motion of the overriding plate. A velocity inflow applied at the edge of the overriding lithosphere leads to trench retreat and a slab that rests on the lower mantle, whereas a stationary overriding plate may lead to a slab that folds on the lower mantle. Prolonged vertical subduction of the slab is only possible if a lower mantle is present beneath the 660 km discontinuity. For these types of models, the dynamics of the subduction system are controlled by the lateral kinematic boundary conditions. As a result, the choice of the lateral boundary conditions determines the type of subduction setting that is being investigated.

Acknowledgements

We acknowledge financial support from the European Commission through Marie-Curie Research Training Network“c2c” (contract MRTN-CT-2006-035957). S. Ellis was supported by Capability Funding from the “Crustal Modelling” project. We greatly appreciated constructive discussions with Joya Tetreault, Reza Khazzab

Ghazian, Boris Kaus, Hana Čižkovà and Ondřej Čadek. We thank Fabio Capitanio and an anonymous reviewer for their helpful reviews.

Chapter 4

A numerical comparison study of thermo-mechanical subduction[1]

Abstract

To test model responses to systematic variations in input parameters, numerical studies often start from a 'reference' model. However, the reference setup, which includes geometries, and values for mechanical and thermal parameters, often differs between studies. This variability in the initial setup may make it difficult to compare results of different studies directly. We here propose a numerical reference model for subduction of a 70 Ma old oceanic plate under a 40 Ma old oceanic plate. We examine four rheological models at increasing complexity, from (1) a linear viscous rheology, through (2) linear viscous with temperature advection, to (3) simplified, and (4) more elaborate thermo-mechanical models, with brittle yielding and viscous creep behavior. We present a quantitative comparison of results for these four setups from seven different numerical codes. The participating codes use finite element (ASPECT, ELEFANT, ELMER, SLIM-3D, SULEC) and finite volume (CHIC, YACC) methods.

The models show a three-stage evolution of subduction: (1) A subduction initiation phase, (2) a free subduction phase during which the slab descends in the mantle, and (3) a phase where the slab tip interacts with the bottom boundary. We compare the evolution of slab tip depth, trench retreat, root-mean-square velocity, viscous dissipation of energy, root-mean- square temperature and maximum depth of the 800 ° C isotherm. The linear viscous models (cases 1 and 2) show a similar mechanical evolution, with less than 10% variation in geometric and kinematic output values. The largest variation is of 20% for the viscous rate of dissipation of energy between the seven

[1]Manuscript in preparation with authors: Matthieu E. T. Quinquis, Susanne J. H. Buiter, Anne Glerum, Petra Maierová, Lena Noack, Javier Quinteros, Cédric Thieulot, Nicola Tosi, David Dolejš and Susan M. Ellis

participating codes. Minimum variability is observed during the free subduction phase, whereas the largest differences occur when the slab tip interacts with the bottom boundary. We show that changing the rheology from linear viscous to pressure- and temperature-dependent non-Newtonian increases the variability in the results. Up to 20% difference in the quantitative output values occurs between the three (case 3) to two (case 4) participating codes. However, the general evolution and geometry of the subducting slab is similar. We hope that our results will be useful for future subduction studies by offering a set of numerical test problems and suggesting a subduction reference model setup.

4.1 Introduction

Building a numerical model of subduction requires choosing values for various geometrical parameters, material properties, initial conditions, and boundary conditions. These include, among others, the initial lithosphere thicknesses, representative lithologies along with their mechanical and thermal properties, initial temperature profiles, as well as model domain size. Some of these values can be constrained by observations of present-day subduction zones, such as lithosphere age and thickness, whereas others have a larger uncertainty and require critical evaluation of geophysical and experimental results. A typical approach to this problem of uncertainty in material properties is to test the response of a model to variations in these parameters.

To evaluate the effects of systematic variations in input parameters, numerical studies often start from a 'reference model'. This reference model can be considered as a data set of initial parameters (*e.g.*, lithological, geometrical, and numerical) that are used to build the initial subduction model. Reference model setups of subduction studies vary and can range between (1) 2-D linear viscous models without an overriding plate (*e.g.*, Schmeling et al., 2008; Faccenna et al., 2009; Kaus et al., 2010; Quinquis et al., 2011), or with an overriding plate (*e.g.*, Capitanio et al., 2010; Quinquis et al., 2011); (2) 2-D thermo-mechanical models (e.g., Abers et al., 2005; Sobolev and Babeyko, 2005; Gerya et al., 2006; Billen and Hirth, 2007; Čížková et al., 2007; Warren et al., 2008b) or (3) 3-D linear viscous (*e.g.*, Yamato et al., 2009) or viscoplastic models (*e.g.*, Piromallo et al., 2006; Stegman et al., 2010). Typically, not only the geometry differs between various studies, but also the values of mechanical, rheological and thermal input parameters. This variability in the initial setup of numerical studies of subduction zones makes it difficult to compare the results of different studies directly. We therefore here propose a numerical reference model for subduction of a 70 Ma old oceanic plate under a 40 Ma old oceanic plate. We progressively increase the rheological

complexity of our subduction model from (1) a linear viscous rheology, through (2) linear viscous with temperature advection, to (3) simplified and (4) more elaborate thermo-mechanical models that include brittle yielding and viscous creep. This will allow future studies to choose an appropriate setup level for comparison of new numerical results. We have kept our setups relatively simple and do not include (de)hydration, melt processes, elasticity, shear heating, or adiabatic heating in any of the proposed setups. We present a quantitative comparison of results for these four setups from seven different numerical codes. The participating codes use finite element (ASPECT, ELEFANT, ELMER, SLIM-3D and SULEC) and finite volume (CHIC, YACC) methods. Our results can therefore also be used to compare the dynamic evolution of linear viscous and thermo-mechanical subduction models which are computed with different softwares and numerical techniques.

4.2 Numerical Approach

4.2.1 Equations for Thermo-Mechanical Slow Flows

Our codes solve the equations for conservation of mass (4.1), momentum (4.2) and energy (4.3):

$$\frac{\partial \rho}{\partial t} + \nabla \cdot (\rho \vec{v}) = 0 \tag{4.1}$$

$$-\nabla P + \nabla \cdot \bar{\sigma}' + \rho \vec{g} = 0 \tag{4.2}$$

$$\rho C_p \frac{\partial T}{\partial t} = k \nabla^2 T - \rho C_p \vec{v} \cdot \nabla T + H \tag{4.3}$$

$\vec{v}$ is the velocity vector, ρ density, t time, P pressure (mean stress), $\bar{\sigma}'$ deviatoric stress tensor, $\vec{g}$ gravitational acceleration ($g_x = 0$ and g_y = -9.81 m s^{-2}), C_p specific heat, T temperature, k thermal conductivity, and H radioactive heat production per unit volume. For incompressible codes (in our study: all except YACC) $\frac{\partial \rho}{\partial t} = 0$ and equation 4.1 simplifies to $\nabla \cdot \vec{v} = 0$. For these codes, the Boussinesq approximation is assumed,*i.e.*, $\rho = \rho_0(1 - \alpha(T - T_0))$ where ρ_0 is the reference density at $T = T_0$ and α is the volumetric thermal expansion coefficient.

Our first model series (cases 1 and 2) uses linear viscous rheologies only:

$$\bar{\sigma}' = 2\eta \bar{\dot{\varepsilon}}' \tag{4.4}$$

η is dynamic viscosity and $\bar{\dot{\varepsilon}}'$ the deviatoric strain rate tensor. For models with pressure- and temperature-dependent rheologies (cases 3 and 4), viscous behavior is defined by power law creep:

$$\eta_{df,ds} = \frac{1}{2} \left(\frac{d^p}{A\, C_{OH}^r} \right)^{\frac{1}{n}} \dot{\varepsilon}_e'^{\frac{1-n}{n}}\, e^{\left(\frac{Q+PV}{nRT}\right)} \tag{4.5}$$

$\dot{\varepsilon}'_e$ is the effective deviatoric strain rate ($\dot{\varepsilon}'_e = (\frac{1}{2}\dot{\varepsilon}'_{ij}\dot{\varepsilon}'_{ij})^{\frac{1}{2}}$), A is a material constant, n power law stress exponent, d grain size, p grain size exponent, C_{OH} water content, r water content exponent, Q activation energy, V activation volume, and R molar gas constant. df and ds refer, respectively, to deformation by diffusion creep ($p > 0$ and $n = 1$) or dislocation creep ($p = 0$ and $n > 1$). A is usually measured experimentally using uni-axial stress conditions and has to be converted to invariants that are independent of the coordinate system by multiplying by $(3^{(n+1)/2})/2$ (Ranalli, 1995). In our full thermo-mechanical model (case 4), diffusion and dislocation creep are assumed to act in parallel. For this case, a composite viscosity (η_{comp}) can be derived from (Karato and Li, 1992; van den Berg et al., 1993):

$$\eta_{comp} = \left(\frac{1}{\eta_{ds}} + \frac{1}{\eta_{df}}\right)^{-1} \tag{4.6}$$

Brittle behavior follows a Drucker-Prager criterion (Handin, 1969; Jaeger and Cook, 1976; Twiss and Moores, 1992):

$$\sigma'_e = Psin\phi + Ccos\phi \tag{4.7}$$

σ'_e is the effective deviatoric stress ($\sigma'_e = (\frac{1}{2}\sigma'_{ij}\sigma'_{ij})^{\frac{1}{2}}$), ϕ angle of internal friction, and C cohesion. In case 3, $\phi = 0$. In case 4, ϕ undergoes a linear decrease with total effective strain (measured as the second invariant of the strain tensor) to simulate strain-weakening. The effective viscosity for plastic flow is (Lemiale et al., 2008):

$$\eta^p_e = \frac{Psin\phi + Ccos\phi}{2\dot{\varepsilon}'_e} \tag{4.8}$$

Harmonic viscosity averaging and arithmetic density averaging schemes from particles to elements are used for particle-in-cell codes (CHIC, ELEFANT, ELMER, SLIM-3D, SULEC and YACC) (Schmeling et al., 2008).

4.2.2 Description of the Numerical Codes

ASPECT ASPECT, the Advanced Solver for Problems in Earth's ConvecTion (Kronbichler et al., 2012), is a 2-D and 3-D finite element code developed under an Open Source licence. The models in our study are run by Anne Glerum and Cedric Thieullot. ASPECT can model both compressible and incompressible fluids (Bangerth and Heister, 2013) and the specific dependence of the density on temperature can be given by the user (Kronbichler et al., 2012). Here the conservation equations (4.1-4.3) are solved for incompressible fluids in the Boussinesq approximation. ASPECT uses the flexible GMRES iterative solver (Saad, 2003)

together with the algebraic multigrid preconditioner (Tuminaro and Tong, 2000; Gee et al., 2006). Quadrilateral elements are used (Kronbichler et al., 2012), which are available through the library deal.II (Bangerth et al., 2007) on which the code builds.

The materials of the lithosphere and mantle are tracked by the advection of phase fields. This requires solving an additional equation for each compositional field c_i (Bangerth and Heister (2013)):

$$\frac{\partial c_i}{\partial t} + \vec{v} \cdot \nabla T = 0 \tag{4.9}$$

ASPECT stabilizes the composition (and temperature) advection equations with the entropy viscosity method of Guermond et al. (2011), which adds artificial dissipation to the equations only in case of a large local Péclet number and a non-smooth solution.

CHIC CHIC developed and run by Lean Noack, employs the finite volume method and finite difference method for solving energy, mass and momentum equations (4.1 - 4.3) in either silicate or icy mantles (Noack et al., 2014). The code uses either Cartesian (2-D and 3-D box) or spherical coordinates (2-D cylinder or annulus). It furthermore contains a 1-D parametrised model to obtain temperature profiles in specific regions, for example in the iron core or in the silicate mantle (solving only the energy equation).

ELMER ELMER is an open-source finite-element software (http://www.csc.fi/english/pages/elmer). ELMER contains several modules designed for the solution of different types of partial differential equations, in particular for thermo-mechanical convection in a domain with a free surface. The setup of a numerical simulation is specified in an input text file, which also serves as an interface for linking of user-written procedures to ELMER. Uses modules were developed to compute the advection of particles using the fourth-order Runge-Kutta method. During the advection of particles, several additional procedures are used for a fast search of particles contained in an element. The continuity equations (4.1 and 4.3) are discretized using bilinear quadrilateral elements. The solution of the discretized system uses direct methods, namely the package UMFPACK (Davis, 2004), which is robust and fast for a relatively small number of unknowns. For the integration of the heat equation, backward differentiation to first order is used. The models are run by Petra Maierovà.

ELEFANT ELEFANT, developed and run by Cédric Thieulot, is a finite element code that solves the Stokes equations (4.1 and 4.2) for an incompressible fluid,

together with the energy equation (4.3). The code is mostly based on the same algorithms as the FANTOM code (Thieulot, 2011). ELEFANT has been purposely designed to address crustal-scale to mantle-scale problems in two and three dimensions. The code is based on an Arbitrary Lagrangian-Eulerian description of the flow field and allows for large deformations of the free surface (Fullsack, 1995). The finite element discretization is based on a regular quadrilateral/tetrahedral division of space and linear velocity/discontinuous constant pressure elements (Q1P0) are used. The pressure P is calculated using the Uzawa iterative penalty formulation (Cuvelier et al., 1986; Zienkiewicz and Taylor, 2000a):

$$P^i = P^{i-1} - B\nabla \cdot \vec{v}^{\,i} \tag{4.10}$$

B is the penalty parameter which has a value of 10^{31} Pa s in our models, which is about 8 orders of magnitude larger than our lithosphere viscosity (Zienkiewicz and Taylor, 2000b). i indicates pressure iteration step. Tracking of the materials is with markers, and a second-order Runge-Kutta algorithm is used to advect them. The large system of algebraic equations that results from the finite element discretization and linearization of the basic partial differential equations is solved using the direct solver MUMPS (Amestoy et al., 2001, 2006) that can efficiently factorize poorly conditioned systems resulting from highly non-linear rheologies. The code can be run both in sequential and parallel modes.

SLIM-3D SLIM-3D, run by Janvier Quinteros, is a 2 -D/3 -D implicit Arbitrary Lagrangian Eulerian Particle-in-Cell Finite Element code (Popov and Sobolev, 2008). SLIM-3D includes a coupled thermo-mechanical treatment of deformation processes and allows for an elasto-visco-plastic rheology with diffusion, dislocation and Peierls creep mechanisms and Mohr-Coulomb plasticity. SLIM-3D is developed and implemented using the C++ object-oriented programming language.

SULEC SULEC, developed by Susanne Buiter and Susan Ellis, is a 2-D/3-D standard arbitrary Lagrangian Eulerian (ALE) finite element code (Fullsack, 1995), which solves the general set of conservation equations (4.1-4.3) for an incompressible fluid. The Boussinesq approximation is assumed. The equations are solved on a slightly deformable Eulerian grid composed of 4, 8 or 9 node quadrilaterals (2-D). In this study, only the Q1P0 element is used, which has 2 degrees-of-freedom for velocity on each corner node and constant pressure, which is discontinuous between elements. The pressure P is calculated using the Uzawa iterative penalty formulation (Cuvelier et al., 1986; Zienkiewicz and Taylor, 2000a) as in equation 4.10. Material properties are stored on tracers that are advected through the Eulerian grid, using a second-order Runge-Kutta algorithm. SULEC has a true free surface with a stabilization term that suppresses numerical overshoot of isostatic

restoring forces (Kaus et al., 2010; Quinquis et al., 2011). The mechanical and thermal equations are solved using the direct sparse solver PARDISO (Schenk et al., 2000), which can be used sequential or parallel. The models are run by Matthieu Quinquis and Susanne Buiter.

YACC YACC, developed and run by Nicola Tosi, solves the conservation equations for a compressible fluid (Eqs. 4.1-4.3) with the finite-volume method. The momentum equation is integrated for the horizontal and vertical velocity components located at staggered nodes, while the continuity equation is integrated explicitly for the pressure located at cell centers (*e.g.*, Gerya and Yuen, 2003). For the energy equation, a semi-Lagrangian operator-splitting method is used (Spiegelman and Katz, 2006). The temperature is first advected through a semi-Lagrangian scheme with bicubic interpolation. Then, a Crank-Nicolson scheme is employed to diffuse the advected temperature. Both linear systems are solved using the parallel direct sparse solver PARDISO (Schenk et al., 2000).

4.3 Constraints on Lithology and Rheology of the Lithosphere and Mantle

4.3.1 Petrological Model of the Oceanic Lithosphere

We use an oceanic plate model based on Chemia et al. (2010), which describes lithologies, thicknesses, and bulk compositions as defined from a petrological point of view. The oceanic lithosphere is composed of 3 layers: (1) A layer of Global Oceanic Subducting Sediments (GLOSS) up to 1 km thick (Plank and Langmuir, 1998); (2) a 7 km thick layer of Bulk Oceanic Crust (BOC) (Chemia et al., 2010), and (3) a 32 km thick layer of Serpentinised Harzburgite (SHB) (McDonough and Sun, 1995). The use of this petrological model of an oceanic lithosphere in large-scale numerical models requires some simplifications. First, the sediment (GLOSS) thickness varies as a function of the age of the oceanic lithosphere and can be averaged to about 500 m thick for a 40 Ma oceanic lithosphere and 1 km thick for a 70 Ma oceanic lithosphere, assuming constant sedimentation rates. This sediment layer requires a high numerical resolution (at least 3 elements or nodal points vertically) in order to be resolved. For numerical codes with a constant spatial discretization, this would lead to a dense mesh and a long calculation time. To avoid this, we neglect the sediment layer for the 40 Ma old overriding lithosphere and combine the GLOSS layer with the crust (BOC) layer to form an 8 km thick crust for the 70 Ma old subducting lithosphere. Second, the petrological model of the oceanic crust results in a total lithosphere thickness of 39-40 km,

which is less than the lithosphere thickness calculated using the plate cooling model (*e.g.*, Turcotte and Schubert, 2002) of 82 and 110 km for a 40 and 70 Ma oceanic plate, respectively. In linear viscous models, we therefore supplement the petrological oceanic plate model with a 'thermal' layer between 43 km (40 Ma) and 70 km (70 Ma) thick. This "thermal" layer is assigned lithospheric properties. In thermo-mechanical models, this layer is not used as these models start with temperature fields for 40 and 70 Ma old lithospheres and therefore implicitly have the correct thermal lithospheric thickness.

In summary, our numerical oceanic plates consist of (1) a 7 (BOC) or 8 km (GLOSS and BOC) crustal layer for the overriding and subduction lithospheres, (2) a 32 km thick serpentinised harzburgite (SHB) layer, and (3) for linear viscous models only, a 'thermal' lithosphere layer between 43 (overriding plate) and 70 km (subducting plate) thick.

4.3.2 Composition and Rheology of the Upper Mantle

The upper mantle is mainly composed of olivine, orthopyroxene, clinopyroxene and garnet (Putnis, 1992; Ringwood, 1975). Olivine is the major constituent and composes more than 50% of the upper mantle (Putnis, 1992). Olivine is also likely to have the weakest rheology at upper mantle pressures and temperatures (Kohlstedt and Goetze, 1974; Ross and Nielsen, 1978; Mackwell, 1991). We therefore assume, as in most other numerical studies of subduction, that the rheology of the upper mantle is controlled by the deformation of olivine.

A historical average viscosity value for the sublithospheric mantle has been 10^{21} Pa s (Haskell, 1935), however, this value overestimates the asthenosphere viscosity (Mitrovica, 1996). More recent studies of post-glacial rebound and relative sea level data constrain the upper mantle viscosity (to a depth of 670 km) to values between 5×10^{19} Pa s to 3×10^{21} Pa s (Paulson et al., 2007a,b; Peltier and Drummond, 2008), while geoid studies give a viscosity of 6×10^{19} to 10^{21} Pa s for the sublithospheric mantle down to 400 km and 10^{21} to 2×10^{22} Pa s from 400 to 670 km depth (Mitrovica and Forte, 2004; Steinberger and Calderwood, 2006). These values are generally accepted in dynamic model studies of subduction along with a viscosity contrast of approximately three orders of magnitude between the lithosphere and the sublithospheric mantle (Enns et al., 2005; Billen, 2008; Capitanio et al., 2010; Kaus et al., 2010; Quinquis et al., 2011).

A large number of experimental studies constrain the power law values for dislocation and diffusion creep of dry and/or wet olivine (*e.g.*, Karato and Wu, 1993; Mei and Kohlstedt, 2000a,b; Hirth and Kohlstedt, 2003; Karato and Jung, 2003; Faul and Jackson, 2007; Korenaga and Karato, 2008). The resulting viscosity profiles span a large range of viscosities (Fig. 4.1). We do here not wish to speculate on the cause of this variation, but instead, in a practical approach, use the composite

flow laws of Hirth and Kohlstedt (2003), because these are within the range of the other flow laws and allow future extensions of our model set-up to include effects of (de)hydration through the C_{OH} term (Eq. 4.5).

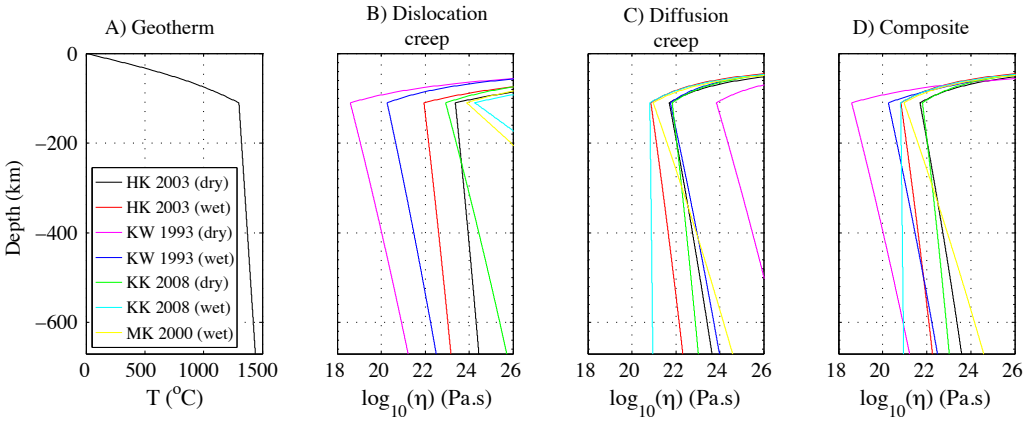


FIGURE 4.1 – A) Oceanic geotherm for a 70 Ma lithosphere. B) Dislocation creep viscosities; C) Diffusion creep viscosities; D) Parallel (composite) diffusion and dislocation creep viscosities (Eq. 4.6). The viscosity profiles in B-D are computed for the 70 Ma geotherm in A). A constant strain rate of 10^{-15} s^{-1} and flow law parameters for olivine are used. HK 2003 = Hirth and Kohlstedt (2003), KW 1993 = Karato and Wu (1993), MK 2000 = Mei and Kohlstedt (2000a,b), and KK 2008 = Korenaga and Karato (2008).

4.4 Modeling Approach

4.4.1 General Model Setup

Figure 4.2 shows the initial geometry for our subduction models. The model domain is 3000 km wide and 670 km deep. The lithosphere consists of two oceanic plates, a 40 Ma overriding lithosphere and a 70 Ma subducting lithosphere, which each have two-three layers. We use a 7 km thick BOC layer and a 32 km thick SHB layer for the overriding plate, and a 8 km thick BOC layer (which includes sediments) and a 32 km thick SHB layer for the subducting plate. For linear viscous models, these are supplemented with a 43 km or 70 km thick "thermal" lithospheric mantle for the overriding and subducting plates, respectively. To initiate subduction and localize deformation at the interplate boundary, we use a "weak seed" (Fig. 4.2). The "weak seed" simulates a pre-existing shear zone in the oceanic lithosphere separating the overriding and subducting plates. It is 14 km thick (defined perpendicular to the dip angle), extends to a depth of 82 km, and has a 35° dip angle (Fig. 4.2B). The top, bottom and left boundaries of the

model are free-slip (the parallel component of velocity is free and the perpendicular component is zero). Balanced material in- and outflow is defined on the right boundary of the model domain (the boundary parallel component is again free). To avoid strong shearing at the transition between in- and outflow, a linear velocity gradient from in- to outflow is defined over a 20 km depth interval (Fig. 4.2C). The inflow velocity is 5 cm yr $^{-1}$ from the surface of the model domain (*i.e.*, z_0) to a depth z_{in} (in our set of models, this is the base of the 70 Ma old lithosphere at -110 km). The outflow velocity (v_{out}) is imposed from a depth of z_{out} (-130 km) to the bottom of the model domain ($z_b = -670$ km). The velocity gradient region is between z_{in} and z_{out} (Fig. 4.2C). To allow subduction, the subducting slab must be able to decouple from the surface boundary (Kaus et al., 2010). Quinquis et al. (2011) have shown that linear viscous subduction models with a free-slip surface boundary condition can reproduce to first order the effects of a true free surface if the subducting lithosphere has a weak crust that allows this decoupling (for more information and examples with a true free surface see appendix 4.A). We therefore use a weak crust (BOC layer) for the subducting plate.

The Eulerian mesh of all models, for all numerical models, has a variable resolution with an increased resolution around the slab. The minimum resolution for the variable meshes is equal to the uniform mesh resolution of ELEFANT and is 1 km per element. This small resolution is necessary in order for the 7-8 km thick BOC layer to be resolved in the numerical calculations. Variable mesh resolutions can influence the kinematic evolution of a subduction model because of how well the interplate contact and the thin decoupling layer in those areas are resolved (Schmeling et al., 2008). However, we reduce this effect by imposing a constant mesh resolution of 2 km by 2 km in the mantle wedge, to 150 km depth.

In temperature-dependent models (cases 2-4), the initial thermal conditions are determined from the plate cooling model (*e.g.*, Turcotte and Schubert, 2002):

$$T = T_S + (T_M - T_S)\left[\frac{y}{y_l} + \frac{2}{\pi}\sum_{n=1}^{2}\frac{1}{n}exp\Big(-\frac{\kappa n^2\pi^2 t_a}{y_l^2}\Big)sin\Big(\frac{n\pi y}{y_l}\Big)\right] \qquad (4.11)$$

T_S is the temperature at the surface, T_M temperature at the base of the plate, y depth, y_l depth of the bottom of the plate, κ thermal diffusivity, and t_a age of the plate. Initial geotherms are defined for the 40 Ma old overriding plate (between 0 to 1500 km in the x direction) and the 70 Ma old subducting plate (between 1500 to 3000 km in the x direction), with $T_S = 0$ °C, $T_m = 1300$ ° C, $\kappa = 10^{-6}$ m^2 s^{-1}, and $z_l = -110$ or -82 km for the 70 Ma or 40 Ma plates, respectively. During model evolution, the surface temperature is held at 0 °C and the bottom temperature (at $y = -670$ km) at 1440 °C, while the heat flux is 0 W m^{-2} on the lateral sides. The mantle adiabat is 0.25 °C km^{-1}. A high conductivity ($k = 183.33$ W m^{-1} K^{-1}) is defined for the upper mantle to enforce the mantle adiabat in our

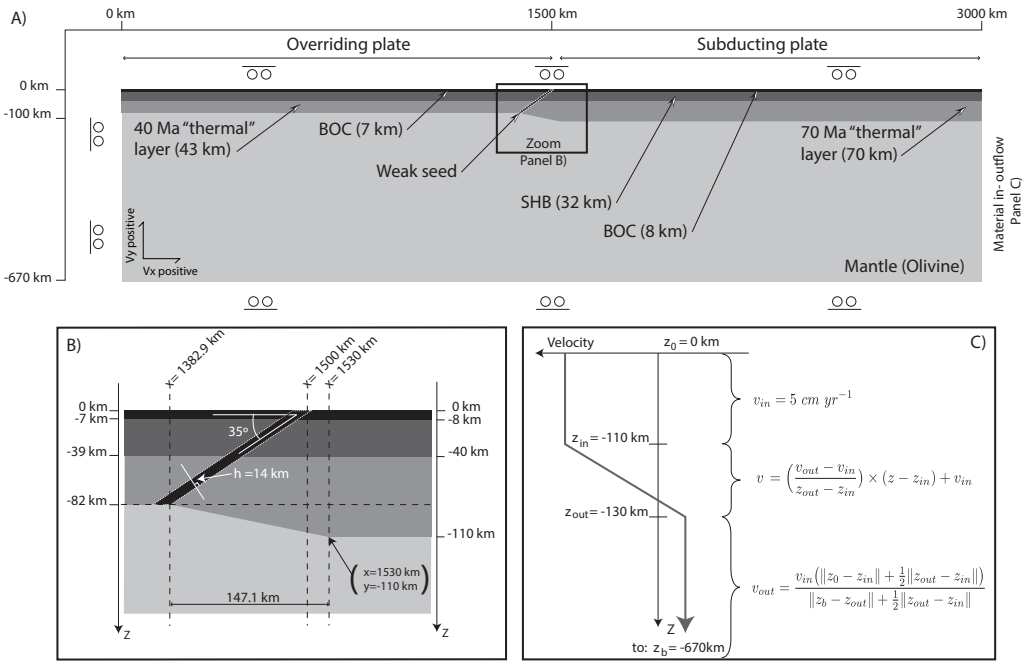


FIGURE 4.2 – Model setup for subduction of a 70 Ma old oceanic plate under a 40 Ma old oceanic plate. A) Setup of the whole model. The top, bottom, and left boundaries are free-slip, while the right boundary condition includes material in- and outflow. SHB: Serpentinised Harzburgite, and BOC: Bulk Oceanic Composition. The 'thermal' layers are only required in the linear viscous models. B) Zoom of the setup at the trench, h is the thickness of the weak zone. C) Definition of the in- and outflow velocities on the right boundary.

slow convection system (Pysklywec and Beaumont, 2004).

4.4.2 Model Cases from Linear Viscous to Thermo-Mechanical

Case 1: Linear Viscous Model

The linear viscous model is kept simple and aimed at comparing results of the participating codes for mechanical flows only. This case does not include thermal effects and the heat equation (Eq. 4.3) is not solved. We use therefore constant densities. All rheological parameters for the linear viscous models are in table 4.1.

Case 2: Advection of Temperature

In this series of models, we solve for the advection and conduction of temperature in addition to the mechanical flow, but do not couple the thermal and the mechanical

TABLE 4.1 – Linear viscous model input parameters

Lithology	Parameter	Unit	Value
Mantle	Density	kg m^{-3}	3200
	Viscosity	Pa s	10^{20}
Weak seed	Density	kg m^{-3}	3250
	Viscosity	Pa s	10^{20}
	Thickness	km	14
Overriding plate			
BOC	Density	kg m^{-3}	3250
	Viscosity	Pa s	10^{23}
	Thickness	km	7
SHB	Density	kg m^{-3}	3250
	Viscosity	Pa s	10^{23}
	Thickness	km	32
"Thermal layer"	Density	kg m^{-3}	3250
	Viscosity	Pa s	10^{23}
	Thickness	km	43
	Age	Ma	40
Subducting plate			
BOC	Density	kg m^{-3}	3250
	Viscosity	Pa s	10^{20}
	Thickness	km	8
SHB	Density	kg m^{-3}	3250
	Viscosity	Pa s	10^{23}
	Thickness	km	32
"Thermal layer"	Density	kg m^{-3}	3250
	Viscosity	Pa s	10^{23}
	Thickness	km	70
	Age	Ma	70

aspects of the models. The mechanical evolution of the model is therefore the same as for case 1 and we compare only the thermal results for this case. The initial thermal state is determined from the plate cooling model (Eq. 4.11).

A variation on linear viscous case 2 (case 2b) includes a temperature dependent density following: $\rho = \rho_0(1 - \alpha(T - T_0))$. ρ_0 and T_0 are the same as for the thermo-mechanical models (case 3 and 4) and are in Table 4.2. In this case, the mechanical evolution will differ from case 1 due to the density variations.

Case 3: Simple Thermo-Mechanical Model

Case 3 is a simplified version of a full thermo-mechanical model which is included to allow a large range of future codes to run our setups. The model builds on case 2, but the thermal and mechanical equations are now coupled. We use a simplified flow law, which does not include the activation volume (Table 4.3). As a result, the sublithospheric mantle viscosity decreases with depth and a large part of the mantle will deform at the viscosity cut-off value of 10^{20} Pa s (this is the mantle

viscosity of the linear viscous cases 1 and 2). The viscosity is initialised using a constant strain rate of 10^{-15} s^{-1}. Density is temperature-dependent following the standard Boussinessq approximation: $\rho = \rho_0(1 - \alpha(T - T_0))$ (Table 4.2). Brittle behavior follows a von Mises criterion with $\phi = 0$. The cohesion value is higher than what is commonly used in thermo-mechanical models in order to reach a similar brittle strength over the entire lithospheric thickness as for depth-dependent brittle behavior (as in case 4). We use the weakened values of the Drucker-Prager yield criterion to derive the approximated cohesion for the subducting crust and the initial values for the other lithologies (see discussion for more details). No strain softening is used. The mechanical and thermal properties are in Table 4.2.

Case 4: Thermo-Mechanical Model

Case 4 is a thermo-mechanical model which includes dislocation and diffusion creep and pressure-dependent brittle behavior (Eqs. 4.5 and 4.7). As in case 3, density is temperature-dependent. We assume that the mantle is composed of dry olivine, while the BOC and SHB layers are hydrated and therefore composed of wet olivine. The viscosities are composite (Eq. 4.6) and calculated using the parameters in Table 4.3. This setup will allow future models to investigate, among others, effects of slab dehydration and mantle hydration (the next chapter of this thesis). A Drucker-Prager pressure-dependent yield criterion is used with strain softening of the angle of internal friction. The rheological parameters are in Table 4.2.

The activation volume term in the dry olivine flow laws used for the mantle results in an increase of viscosity with depth (Fig. 4.1 and Table 4.3). The mantle reaches viscosity values of 10^{20} Pa s and lower, only just below the lithosphere and around the subducting slab. In order to stay within the viscosity estimates for the upper part of the sublithospheric mantle (see section 4.3.2), we use a lower viscosity cut-off value of 5×10^{19} for this setup.

TABLE 4.2 – Thermo-mechanical model parameters (cases 2-4)

Parameter	Symbol	Unit	mantle	Lithospheric mantle	Overriding plate		Subducting plate		Weak seed
					BOC	SHB	BOC	SHB	
Olivine Rheology[a]			Dry	Dry	Wet	Wet	Wet	Wet	Wet
Angle of friction[b]	ϕ		20°/10°	20°/10°	20°/10°	20°/10°	5°/2°	10°/5°	2°
Cohesion	C	MPa	20	20	15	15	5	15	5
Approximated Cohesion[c]	C	MPa	333	333	333	333	39	174	39
Reference density	ρ_0	kg m^{-3}	3200	3200	3000	3250	3000	3250	3200
Reference Temperature	T_o	°C	1300	1300	200	200	200	200	200
Conductivity	k	W m^{-1} K^{-1}	183.33	2.5	2.5	2.5	2.5	2.5	2.5
Heat capacity	C_p	J kg^{-1} K^{-1}	1250	1250	750	750	750	750	750
Thermal expansivity	α	10^{-5} K^{-1}	2.5	2.5	2.5	2.5	2.5	2.5	2.5

[a] The flow law parameters are in table 4.3.
[b] Angle of internal friction (ϕ) softens from first to second value in case 4. For case 3, $\phi = 0$.
[c] Approximated cohesion for thermo-mechanical model case 3 where $\phi = 0$.

TABLE 4.3 – Flow law parameters for cases 3 and 4.

Parameter	Unit	Simplified	Dry Olivine		Wet Olivine	
			df^a	ds^b	df^a	ds^b
A^c	Pa $^{-n}$ m^p s^{-1} H(10^{6}Si)$^{-1}$	6.0543×10^{-12}	2.25×10^{-15}	6.514×10^{-16}	1.5×10^{-18}	5.3301×10^{-19}
n	–	3	1	3.5	1	3.5
Q	kJ mol^{-1}	640	375	530	335	480
V	10^{-6} m^3 mol^{-1}	–	4	14	4	11
d	mm	–	5	–	5	–
p	–	–	3	–	3	–
C_{OH}	H(10^{6}Si)$^{-1}$	–	–	–	1000	1000
r	–	–	–	–	1	1.2
Reference			Hirth and Kohlstedt (2003)			

[a] df: Diffusion creep.
[b] ds: Dislocation creep.
[c] A is given for a general state of stress, and was converted from a uni-axial stress (Ranalli, 1995).

4.4.3 Common Output Values

In order to compare the results from the different numerical codes, both qualitatively and quantitatively, we use the following information:

1. The slab tip depth. The slab tip is defined as the deepest particle of lithospheric material (*i.e.*, of the 70 Ma thermal layer) observed in the model at each time step.

2. The horizontal position of the trench. The trench is defined as the last particle of overriding crustal material (*i.e.*, BOC) observed at the surface of the model domain (when looking from left to right) at each time step.

3. The root-mean-square velocity V_{rms} computed (a) over the entire model domain and (b) for the subducting lithosphere only:

$$V_{\mathrm{rms}} = \frac{1}{A}\sqrt{\int_y \int_x (v_x^2 + v_y^2)\, dx\, dy} \tag{4.12}$$

$$\tag{4.13}$$

   where A is the area of computation.

4. The viscous rate of dissipation of energy D calculated (a) over the entire model domain and (b) for the subducting lithosphere only:

$$D = \frac{1}{2}\int_y \int_x \bar{\sigma}' \cdot \dot{\bar{\varepsilon}}'\, dx\, dy \tag{4.14}$$

5. The maximum depth of the $800°C$ isotherm.

6. The root-mean-square temperature T_{rms} is computed in degree Celsius (a) over the entire model domain and (b) for the subducting lithosphere only:

$$T_{\mathrm{rms}} = \frac{1}{A}\sqrt{\int_y \int_x T^2\, dx\, dy} \tag{4.15}$$

These values are computed from the start of the model until the slab tip reaches the bottom of the model domain at -670 km depth. The thermal output values (5 and 6) are only computed for the cases (2-4) that solve the heat equation.

4.5 Results

4.5.1 Case 1: Linear Viscous Models

The subduction evolution of case 1 models can be separated into three stages (Figs. 4.3 and 4.4). The first stage, which lasts approximately 6 Myr, is the "subduction initiation" phase and is characterized by some tens of kilometres trench advance (Fig. 4.3B). Subduction is caused by a combination of the applied velocity push at the right lateral boundary (a strong simplification of ridge push) and the weak seed which localizes deformation at the interplate boundary. The subducting lithosphere is thus in the first phase "pushed" into the mantle. Slab pull, caused by the difference in density between the subducting lithosphere and the mantle, is negligible during the initiation phase, as the slab is short. The second stage of subduction, the "free subduction" phase that also lasts approximately 6 Myr, starts once a sufficient amount of dense subducting lithosphere is present in the mantle for slab pull to overcome slab push. This phase is characterized by an increase in root-mean-square velocity (Fig. 4.3C and D), an increase in the internal rate of viscous dissipation of energy (Fig. 4.3E and F), and a transition from trench advance to trench retreat (Fig. 4.3B). The final stage begins once the slab tip starts to interact with the bottom boundary (after approximately 12 Myr). The subduction velocity reduces and appears to stabilize (Fig. 4.3C-D).

The linear viscous models of case 1 were run by all seven participating codes. All models show the three-stage evolution of subduction and overall, the results of the seven codes for this setup are very similar (Tables 4.3 and 4.5). The variations in the results, when compared to SULEC, are approximately 5% for the trench position and the root-mean-square velocities of the whole model and the slab, 10% for the slab tip position, and up to 20% for the viscous rate of dissipation of energy. The largest variations are observed in the initiation phase (up to 2 Myr) and once the slab tip interacts with the bottom of the model domain, whereas in the stable subduction phase of the experiments the variations never exceed 5%. These are of the same order as variations within the results from a single code (ELEFANT), for variations in grid and particle resolution and the penalty parameter (Fig. 4.5).

We used the linear viscous model setup to investigate the effects of 1) the viscosity averaging scheme at compositional boundaries (Schmeling et al., 2008), and 2) the density contrast between the lithosphere and the mantle (see appendix 4.B for more information).

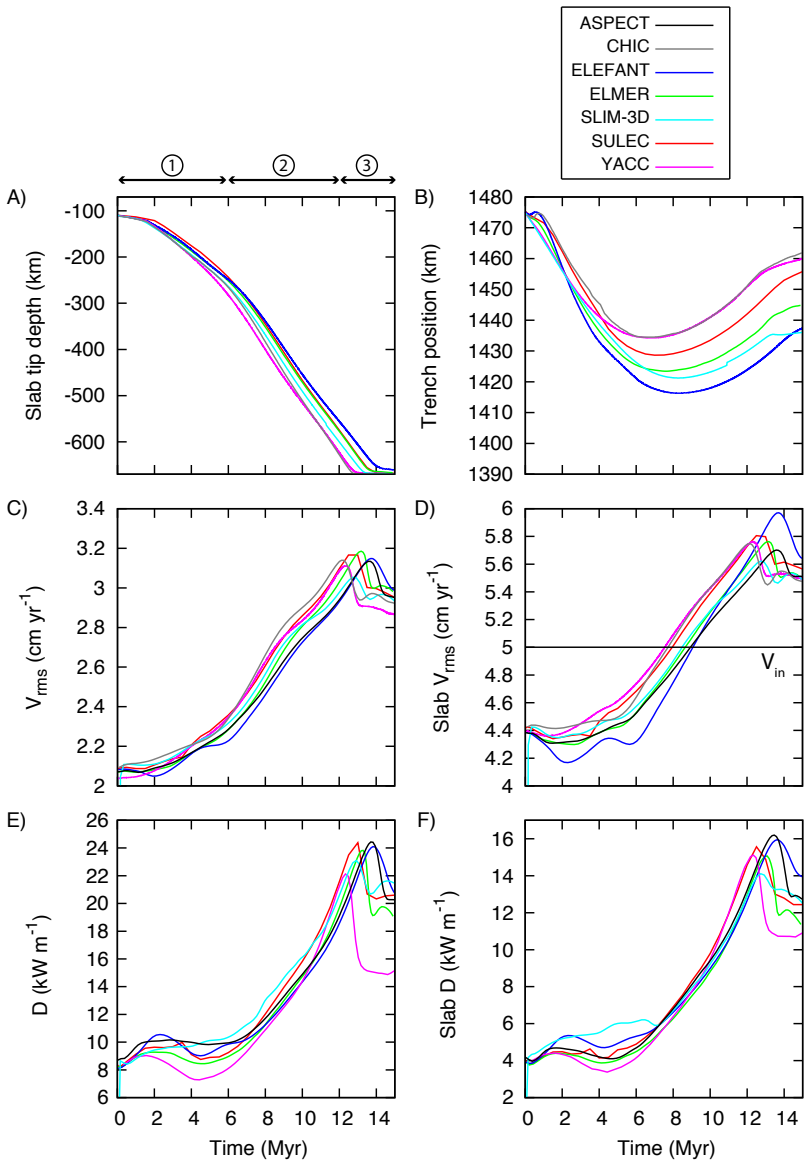


FIGURE 4.3 – Results of 7 codes for case 1 linear viscous models. A) Slab tip depth. B) trench position. Root-mean-square velocity (Eq. 4.12) for C) the whole model and D) the subducting slab only. Viscous rate of dissipation of energy (Eq. 4.14) for E) the whole mantle and F) the subducting slab only. In panels E) and F) the data is smoothed with a Bezier curve of degree n (the number of data points) that connects the endpoints. The smoothing is used to aid the visualization of the plot.

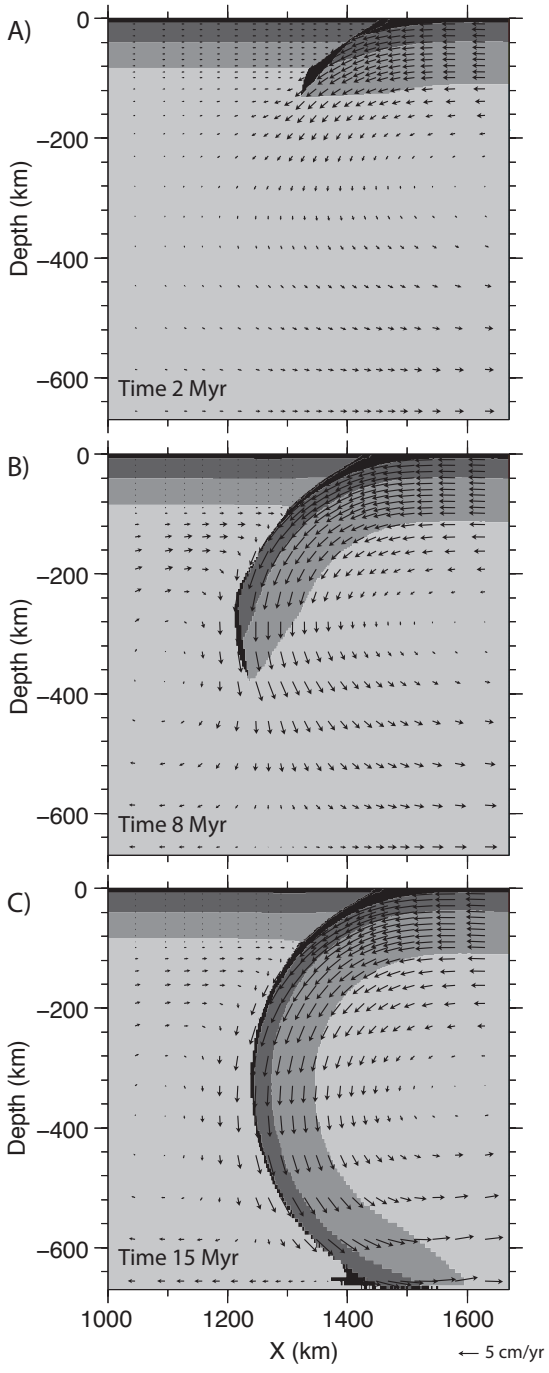


FIGURE 4.4 – Subduction evolution for linear viscous case 1, calculated using SULEC. The materials are shown for a 670 km wide region (from the total 3000 km model width), focused on the trench.

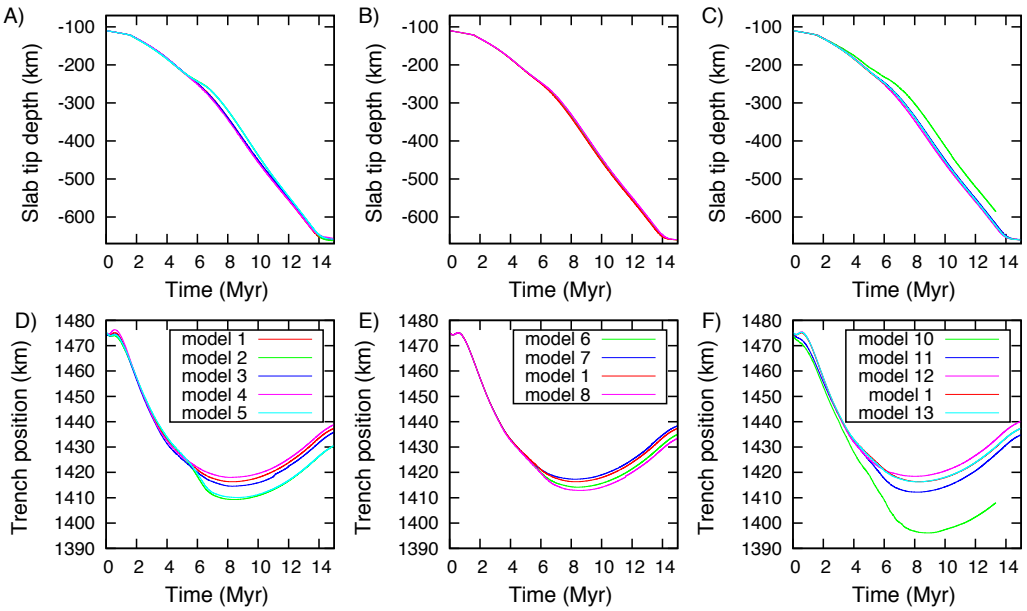


FIGURE 4.5 – Slab tip depth and trench position for a series of case 1 linear viscous models that investigate the effects of grid resolution (the number of elements), particle density and penalty parameter (B in Eq. 4.10) computed with ELEFANT. The models are described in table 4.4

TABLE 4.4 – Model parameters tested when using the code ELEFANT.

Model	Element grid size	Largest Element (km)	Smallest Element (km)	Markers per element Min/Avrg/Max	Total number of markers	Penalty parameter (Pa s)
1	750×167	43×31	2.4×2.4	81/100/121	12.5×10^6	10^{31}
2	1000×223	36×26	1.8×1.8	81/100/121	22.3×10^6	10^{31}
3	600×134	65×45	2.75×2.75	81/100/121	8×10^6	10^{31}
4	600×134	49×35	3.0×3.0	81/100/121	8×10^6	10^{31}
5	900×201	52×36	1.83×1.83	81/100/121	18.1×10^6	10^{31}
6	750×167	43×31	2.4×2.4	81/100/121	12.5×10^6	10^{29}
7	750×167	43×31	2.4×2.4	81/100/121	12.5×10^6	10^{30}
8	750×167	43×31	2.4×2.4	81/100/121	12.5×10^6	10^{32}
9	750×167	43×31	2.4 ×2.4	4/9/16	0.25×10^6	10^{31}
10	750×167	43×31	2.4×2.4	16/25/36	3.1×10^6	10^{31}
11	750×167	43×31	2.4×2.4	36/49/64	6.1×10^6	10^{31}
12	750×167	43×31	2.4×2.4	100/144/196	6.1×10^6	10^{31}

4.5.2 Case 2: Linear Viscous Model with Temperature Evolution

The mechanical evolution of case 2 is identical to case 1. We now additionally solve the heat equation (Eq. 4.3), but temperatures are not coupled to the mechanical flow. This case is run by six codes: ASPECT, CHIC, ELEFANT, SLIM-3D, SULEC, and YACC. The temperature field shows a cold slab which descends into the mantle and warms up with time (Fig. 4.6). When using SULEC, a slight uprising of the isotherms at the base of the lithosphere can be seen on the right hand side of the model (Fig. 4.6), which is caused by an upwelling of hot material from deeper depths.

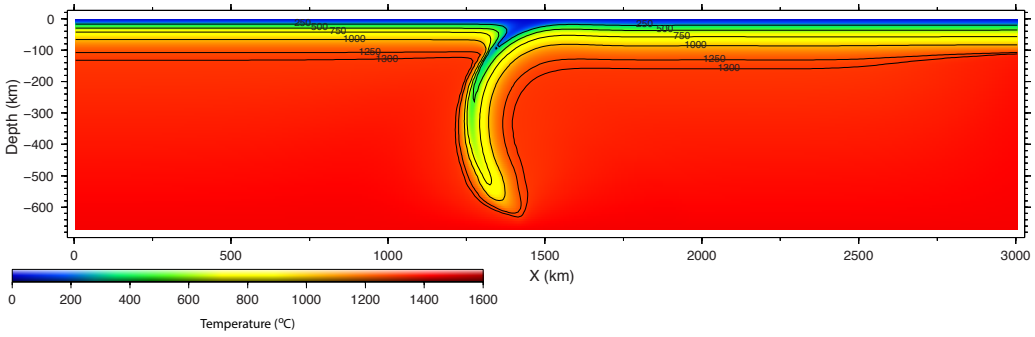


FIGURE 4.6 – Temperature distribution at t=12.5 Myr for linear viscous case 2 model, computed with SULEC.

The thermal evolution of the model is characterized by a constant decrease in the total root-mean-square temperature caused by the input of cold lithosphere into the model domain (Fig. 4.7A). The slab temperature varies according to the

stage of subduction (Fig. 4.7B). When subduction velocities are low (*i.e.*, in the initiation phase when slab push dominates) the slab cools as it is still at the surface and subject to cooling from above. When subduction velocities increase in the subduction phase, the slab temperature stabilizes, before warming up when the slab tip interacts with the bottom boundary. The root-mean-square temperature of the slab shows a series of oscillations in the first 4 Myr of the model evolution for all codes, except ASPECT and ELEFANT. The reason for these oscillations is unclear, but they might be caused by numerical variations in the determination of the size of the thermal slab domain. In the free subduction phase T_{rms} converges.

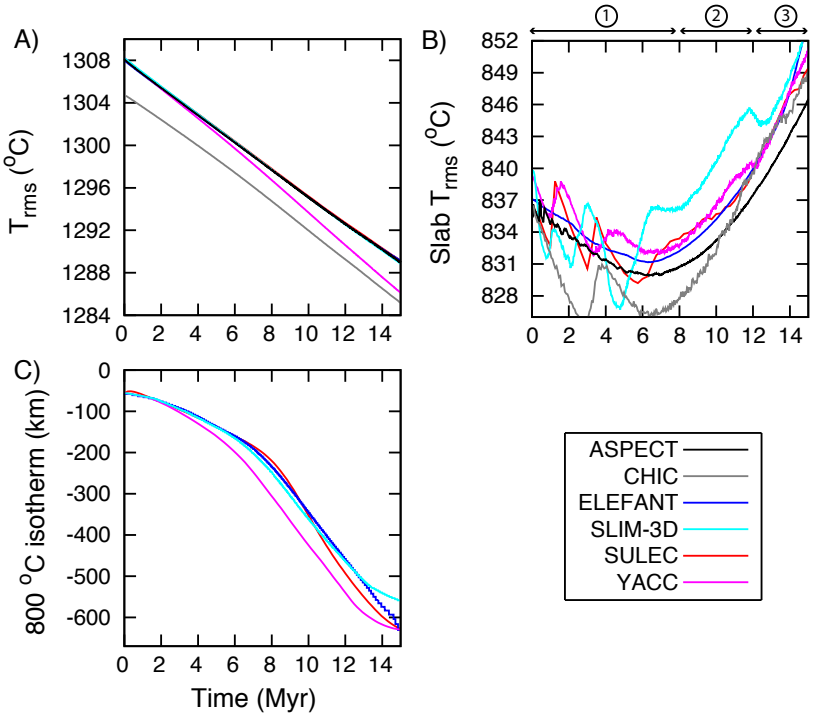


FIGURE 4.7 – Results for case 2, linear viscous models with temperature advection but with constant densities. A) root-mean-square temperature (Eq. 4.15). B) Slab root-mean-square temperature. C) Depth of the 800 °C isotherm.

Case 2b is identical to case 2, except that a temperature-dependent density is used. This case is computed by six codes: CHIC, ELMER, ELEFANT, SLIM-3D, SULEC, and YACC. The results show a similar three-stage evolution as case 1. However, subduction is slower (Fig. 4.8A, C and G) because the density contrast between the slab and the mantle decreases as the slab warms up (Fig. 4.8I). The root-mean-square velocity over the whole domain increases (Fig. 4.8D) due to higher velocities in the mantle in the left part of the model where a second convection cell forms (Fig. 4.9).

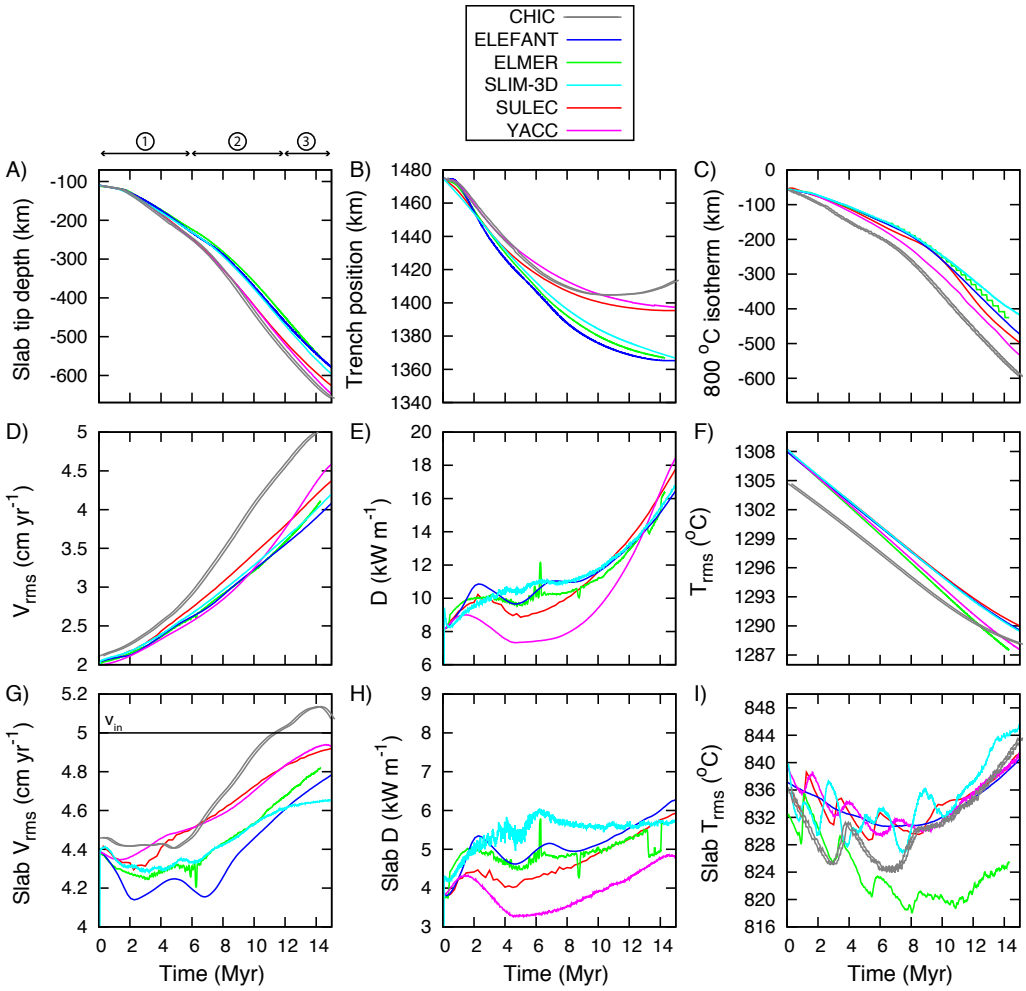


FIGURE 4.8 – Results for case 2b, linear viscous models with temperature-dependent densities. A) Slab tip depth. B) Trench position, C) Depth of the 800 °C isotherm. Whole model D) root-mean-square velocity (Eq. 4.12), E) Viscous rate of dissipation of energy (Eq. 4.14), and F) root-mean-square temperature (Eq. 4.15). Slab G) Root-mean-square velocity, H) Viscous rate of dissipation of energy, and I) Root-mean-square temperature.

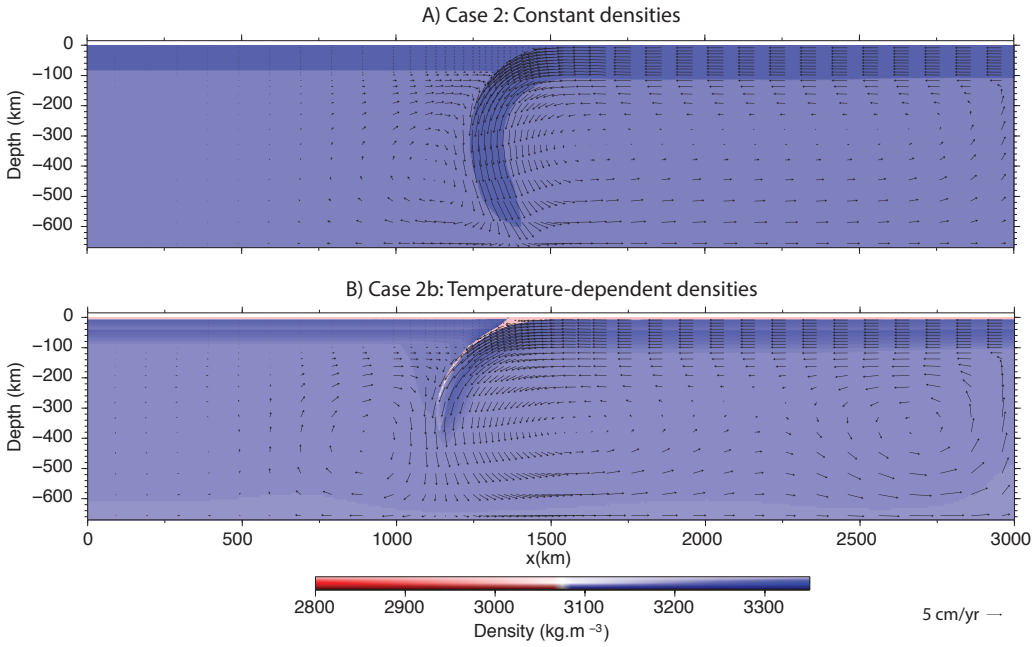


FIGURE 4.9 – Linear viscous model densities and nodal velocities at 12 Myr for A) case 2 linear viscous model with constant densities, and B) case 2b, linear viscous model with temperature-dependent densities. The models were calculated using SULEC.

Similarly to case 1, the differences observed between the results of the six codes are small (Fig. 4.7) and do not exceed 5% variation, when normalised to SULEC, in trench position, root-mean-square velocities, and root-mean-square temperatures and 10% variation in slab tip depth and depth of the 800 °C isotherm. The maximum variability between the codes occurs in the viscous rate of dissipation of energy, reaching a maximum of 20%. The largest variations are again observed during subduction initiation and once the slab tip interacts with the bottom of the model domain. Variations during the free subduction phase do not exceed 5%.

4.5.3 Case 3: Simplified Thermo-Mechanical Models

Case 3 is an intermediate step towards a full thermo-mechanical model. The absence of the activation volume term in the flow law results in low viscosity values in the sublithospheric mantle, which deforms to a large extent on the minimum viscosity value of 10^{20} Pa s (Fig. 4.10). In comparison with cases 1 and 2, only little trench advance occurs in case 3. Trench advance is less than 5 km (Fig. 4.12B), whereas case 1 and 2 show up to 60 km of trench advance (Fig. 4.3B). Trench advance is limited because brittle failure causes fast localization of shortening in the weak seed at the interplate contact. Within these small amounts of trench

motion, ELEFANT shows stages of trench advance when slab push dominates during the subduction initiation phase (from 0 to 6 Myr) and once the slab tip interacts with the bottom of the model domain (from 10 Myr onwards) and retreat when slab pull dominates. SULEC and CHIC show more continuous trench advance and seem less sensitive to the subduction stages for this case.

The three codes that run this case (CHIC, ELEFANT and SULEC), show again a three-stage evolution of subduction. These three subduction stages of subduction are visible in the root-mean-square velocity of the slab and the whole model (Fig. 4.11D and G) and the viscous dissipation of energy (Fig. 4.11E, H). The thermal evolution is similar to case 2 and 2b (Figs. 4.7 and 4.8). The root-mean-square temperature of the whole model decreases as cold lithospheric material is "pushed" into the model domain (Fig. 4.11F). The root-mean-square temperature of the slab decreases when the slab is only about to descend into the mantle (subduction initiation phase) and increases when the slab warms up as it subducts. (Fig. 4.11I).

The three codes share a similar dynamic evolution of subduction as the model evolves (Fig. 4.11A and C). The geometry of the slab in case 3 is the same as in cases 1 to 2b, with the slab folding on the bottom of the model domain towards the end of the experiment. Larger variations in results are visible in the dissipation and root-mean-square velocity of the whole mantle and the slab (Fig. 4.11D, E, G, H). This is especially the case for ELEFANT in the slab root-mean-square velocity.

Case 3 models result in the highest viscosity contrast between the subducting lithosphere and the mantle at middle to lower upper mantle depths. This high viscosity contrast enables a strong response to slab pull, resulting in extension and thinning of the lower part of the subducted lithosphere (Fig. 4.10).

4.5.4 Case 4: Full Thermo-Mechanical Model

Case 4 was only run with CHIC and SULEC. The SULEC results show a similar evolution to the previous cases, with the same three stages of subduction (Fig. 4.12D). This evolution is visible to a lesser degree in the results of CHIC. In both cases, the slab folds on to the bottom of the model domain during the last subduction stage. The subduction velocity of SULEC is larger than for CHIC. Strain softening of the pressure-dependent brittle behavior helps to localize deformation at the interplate boundary, which explains the small amount of trench advance, less than 10 km (Fig. 4.12B). SULEC shows slightly more trench advance than CHIC (*ca.* 7 km after 14 Myr).

The increase in mantle viscosity with depth reduces flow in the mantle and results in reduced whole model root-mean-square velocities (Fig. 4.13D).

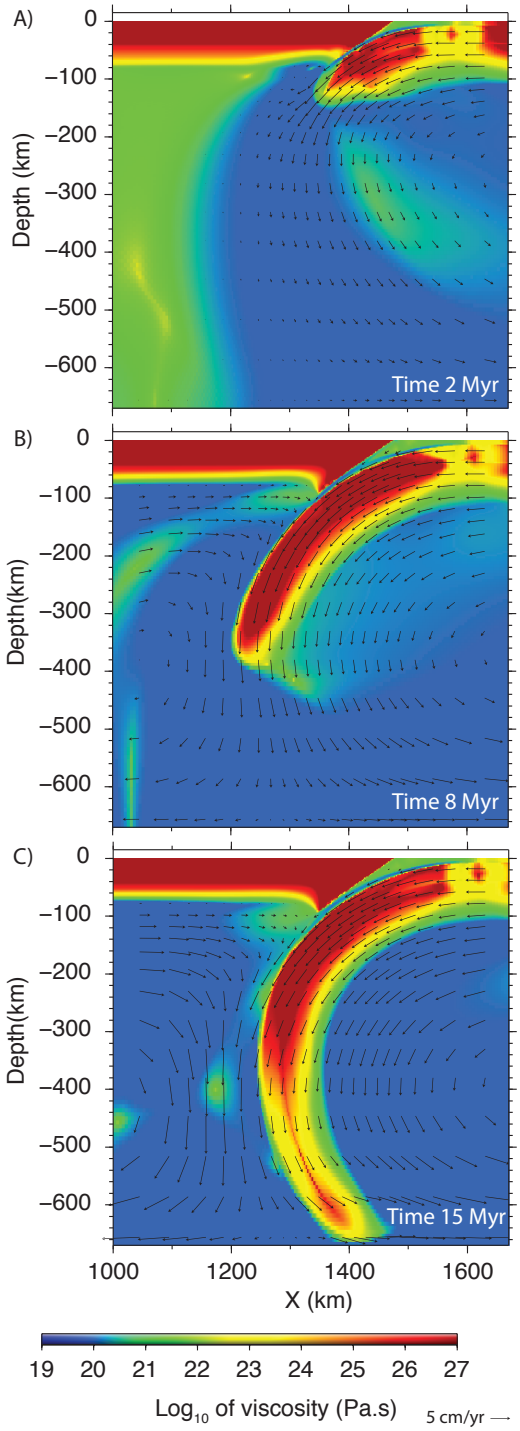


FIGURE 4.10 – Viscosity fields at A) 2, B) 8 and C) 15 Myr for thermo-mechanical case 3. The model was calculated using SULEC.

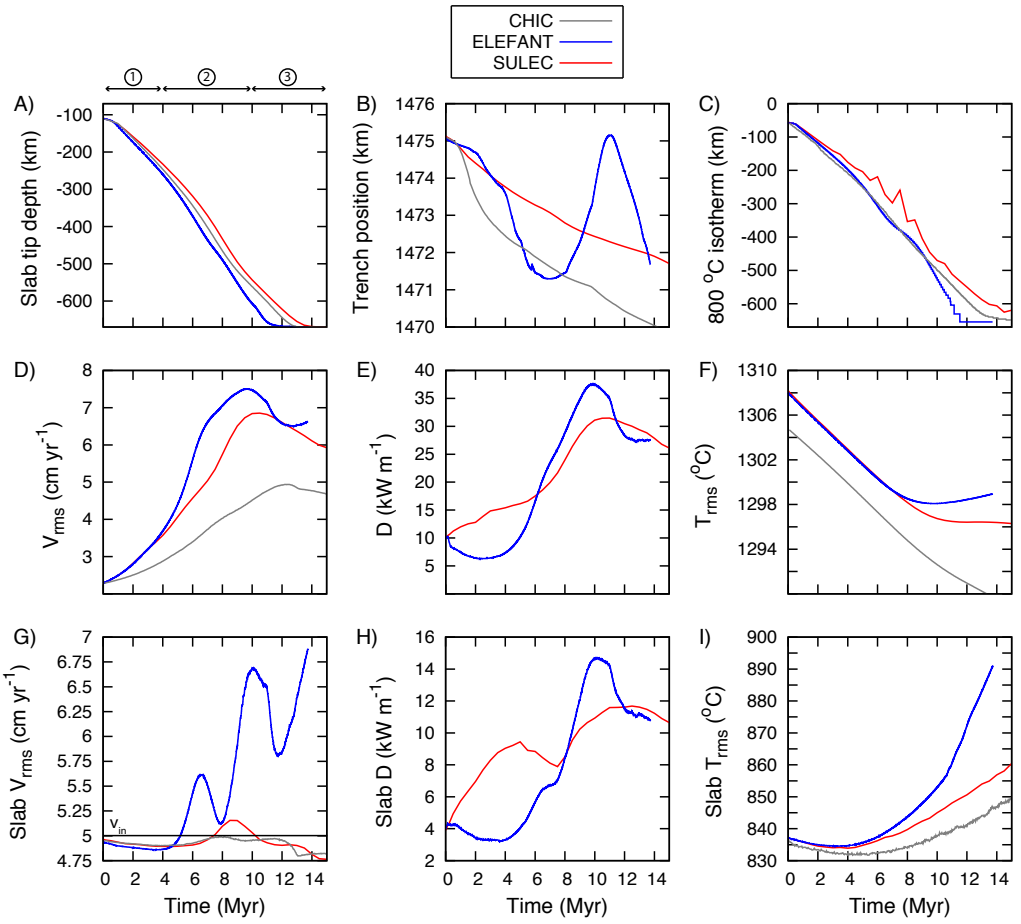


FIGURE 4.11 – Results for simplified case 3 thermo-mechanical models. A) Slab tip depth. B) trench position. C) Depth of the 800 °C isotherm. Whole model D) root-mean-square velocity (Eq. 4.12), E) Viscous rate of dissipation of energy (Eq. 4.14), and F) root-mean-square temperature (Eq. 4.15). Slab G) Root-mean-square velocity, H) Viscous rate of dissipation of energy, and I) Root-mean-square temperature.

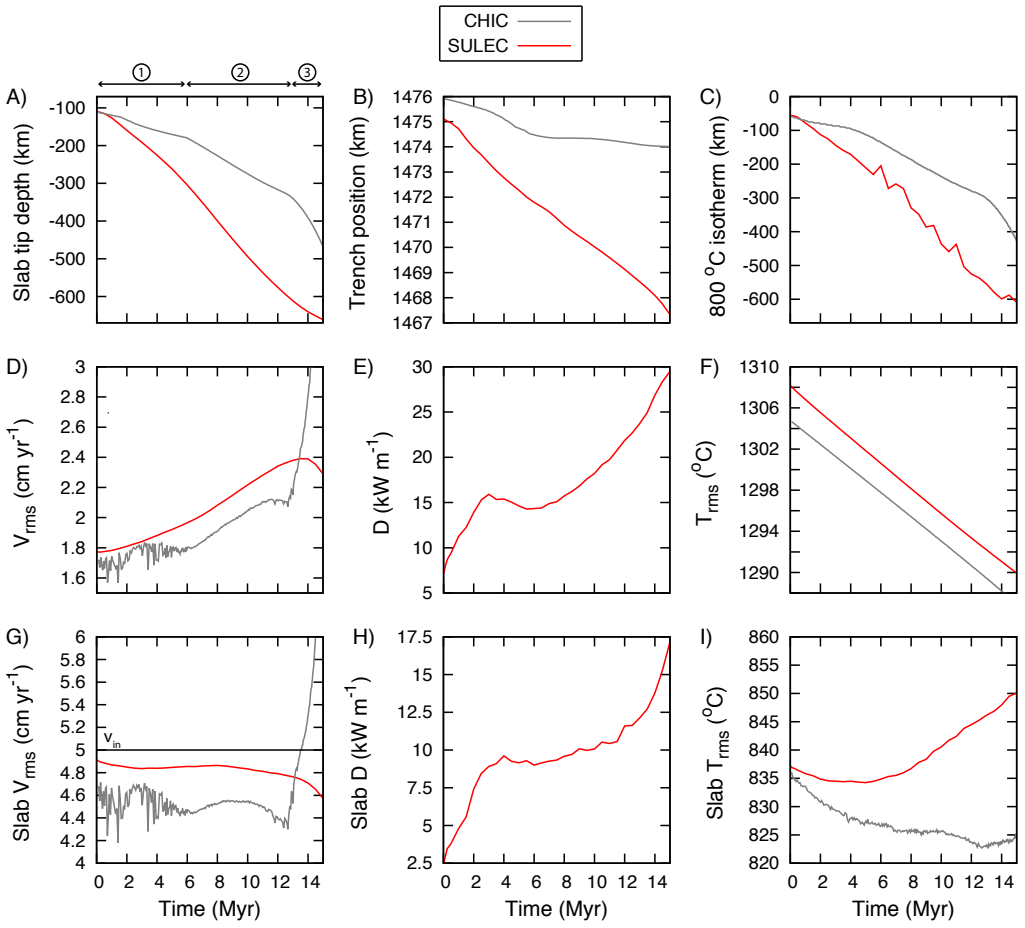


FIGURE 4.12 – Results for case 4 thermo-mechanical models. A) Slab tip depth. B) trench position. C) Depth of the 800 °C isotherm. Whole model D) root-mean-square velocity (Eq. 4.12), E) Viscous rate of dissipation of energy (Eq. 4.14), and F) root-mean-square temperature (Eq. 4.15). Slab G) Root-mean-square velocity, H) Viscous rate of dissipation of energy, and I) Root-mean-square temperature.

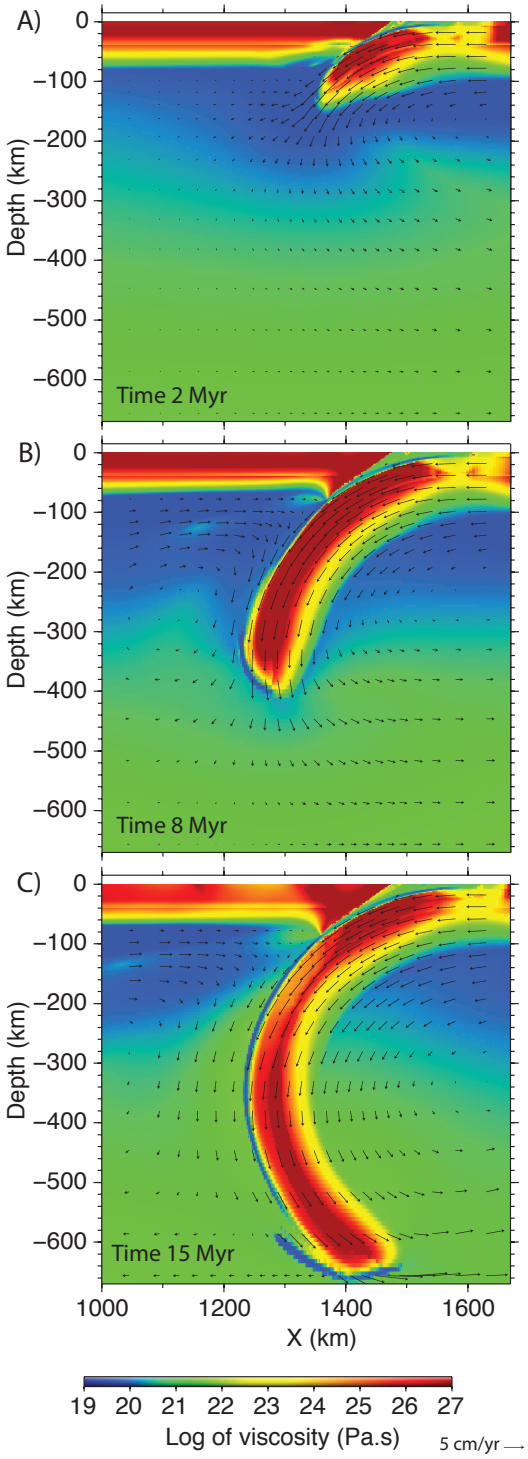


FIGURE 4.13 – Viscosity fields at A) 2 Myr, B), 8 Myr, and C) 15 Myr for thermo-mechanical case 4. The model was calculated with SULEC.

4.6 Discussion

Our models of a 70 Ma oceanic plate subducting under a 40 Ma old oceanic plate share several characteristics, which are independent of the rheological model that was used. The subduction system evolves in three stages: (1) subduction initiation, lasting up to 6 Myr, when the model is dominated by the kinematic boundary condition imposed on the right-hand side of the model, resulting in trench advance; (2) free subduction, from 6 to *ca.* 12 Myr, when the model is controlled by the slab pull caused by the density contrast between the subducting slab and the surrounding mantle, resulting in trench retreat; and (3) the final stage when the slab tip interacts with the bottom of the model domain, starting from *ca.* 12 Myr. These three stages are visible in all cases and for all numerical methods. The final geometry of the slab is the same in all four cases and all numerical methods: the subducting slab folds on the lower mantle, resulting in a sideways U-shape. This is caused by the kinematic boundary conditions, coupled to a strong subducting lithosphere. Even when using a pressure- and temperature-dependent rheology, the subducting lithosphere stays strong. In all cases the root-mean-square velocity of the slab will gradually increase from the initiation phase, when slab push controls the subduction evolution, to a peak when the slab begins to interact with the bottom boundary. When temperature is calculated in cases 2 and onwards, the root-mean-square temperature of the entire mantle gradually cools. The root-mean-square temperature of the slab first decreases during the initiation phase when a large part of the slab is still at the surface and cools. The slab root-mean-square temperature increases as subduction continues and the slab warms up in the mantle. The linear viscous model setups provide a relatively straightforward starting point for a comparison of results of different codes. We find that the results of six codes remained within a maximum of 10% difference when normalized to SULEC during the initiation phase and the phase where the slab tip interacts with the bottom of the model domain. The models show the largest variations in results during these two phases, independent of the numerical method and model setup. During the stable subduction phase the variability in results decreases.

Increasing the complexity of the rheologies, increases the non-linearity of the models and leads to larger variations in the quantifiable output values of the different codes. The viscous rate of dissipation of energy provides the largest difference in model results, reaching up to 20% difference in case 1 and 2, when normalized to SULEC. This is to be expected as in the calculation a large quantity ($\bar{\sigma}'$) is multiplied by a small quantity ($\dot{\bar{\varepsilon}}'$). This implies that small differences in either value can result in large variations in the viscous rate of dissipation of energy.

Adding a temperature-dependent density to linear viscous models leads to slower subduction as the density contrast between slab and mantle decreases as the

subducting slab warms up. But the final geometry at the end of the experiments is similar to linear viscous models with constant density. This may indicate that the slab shape is not only controlled by the interplay of kinematic driving velocity and slab pull, but also by slab strength. This agrees with the results of Schellart (2008a) and Stegman et al. (2010) who have shown that strong slabs tend to a side-ways U-shape, which is similar to our experiments. The largest variations in the results of the different codes occur when introducing non-linear brittle behavior to the model setup. This illustrates that plasticity may not always lead to entirely predictable results as plasticity is not only non-linear but also depends on dynamic pressure in our experiments.

Creating a simplified version of a full thermo-mechanical model is not straight forward. To approximate Drucker-Prager brittle behavior which includes strain-softening, we chose initially to use the average values of the angle of internal friction Φ (between the initial and softened values). However, these values do not allow subduction and cause the subducting lithosphere to buckle. After a series of tests we established that the crust (*i.e.*, the BOC) must be sufficiently weak to localize deformation at the interplate boundary. The strong part of the lithosphere (*i.e.*, the SHB layer and the upper part of the sublithospheric mantle) must be sufficiently strong to transmit deformation to the interplate boundary and sufficiently weak to allow the subducting slab to bend at the trench. We therefore chose to approximate the von Mises cohesion from the softened values of the Drucker-Prager criterion for the BOC layer and to approximate the von Mises cohesion from the unsoftened values of the Drucker-Prager criterion for the rest of the lithologies in the model. This type of brittle behavior would be accomplished automatically when pressure-dependent plastic behavior and strain-softening were used, as in case 4. The definition of the brittle parameters for case 3 models required many tests in order to obtain a model that evolves in a similar manner to the other cases, and resulted in the high values of the approximated von Mises yield criterion (Table 4.2). However, the setup allows codes with less complex viscous and brittle rheologies to run a thermo-mechanical subduction model.

Case 4 was run only with 2 different codes (CHIC and SULEC) and does therefore not provide a full comparison. However, this case does show that codes that behave very similarily when using linear viscous rheologies can show different behaviour when increasing the complexity of the rheologies. Case 4 should therefore be considered as a preliminary step in defining a numerical benchmark for subduction models with non-linear rheologies.

4.7 Conclusions

We present a series of model setups for subduction of a 70 Ma oceanic plate under a 40 Ma oceanic plate. The models progressively increase in rheological complexity from linear viscous with constant density (case 1), to linear viscous with temperature-advection (case 2) and temperature-dependent density (case 2b), through thermo-mechanical models with simplified viscous creep and von-Mises yielding (case 3), to models with Drucker-Prager plasticity, strain softening, and pressure- and temperature-dependent viscous creep (case 4). The descriptions of the model setups include datasets of mechanical, thermal, rheological, and numerical parameters as well as geometries, initial conditions, and boundary conditions. The model cases were each run by 2 to 7 different numerical codes. Subduction evolves from a initiation phase that is dominated by the push exerted by the kinematic boundary condition, through a stable phase when the slab subducts into the mantle by the density contrast between the slab and the mantle, to a final phase where the slab tip interacts with the bottom of the model domain at 670 km depth.

Linear viscous models show less than 5% difference in quantifiable output values, when normalized to SULEC, such as slab tip depth, trench position, and root-mean-square velocity, during stable subduction. This variation is comparable to variations caused by differences in model resolution. Introducing a temperature-dependent density reduces the subduction velocity as the density contrast between slab and mantle is reduced when the slab warms up, but the geometric evolution of the subducted slab is unaltered. Only by introducing brittle behavior and pressure- and temperature-dependent viscosity does the variability between codes increase. This is especially visible in the results of case 3 and 4 (Fig. 4.11 and 4.12).

We hope that our setups may be useful for other numerical modelers by serving as a first step when building a setup for the study of subduction zone dynamics.

4.A The Effects of a True Free Surface

Kaus et al. (2010) and Quinquis et al. (2011) showed that linear viscous models with a free-slip surface boundary condition (*i.e.*, the vertical component of velocity is 0 and the horizontal component is free) can reproduce the effects of a true free surface to first order, provided that the subducting plate has a weak top layer that decouples the plate from the model surface boundary. These results are confirmed in this study (Fig. 4.14).

The free-surface case 1 model subducts faster than the free-slip surface model, as can be seen in the evolution of slab tip depth and root-mean-square velocity (Fig. 4.14A,C and D). Vertical motion at the surface allows "surface particles" to decouple from the surface boundary, increasing subduction velocities (Quinquis et al., 2011). Due to the deformation of the surface, the position of the trench can not be determined with the same accuracy for free surface models. However, within this limitation, we find that the evolution of the trench position is largely the same between free-slip and free surface models (Fig. 4.14B).

We find that the approximation of a true free surface with a weak layer underlying a free-slip surface can be extended to thermo-mechanical models (Fig. 4.15). Also in these models, the free surface has little influence on the mechanical evolution of the model as shown by the small variations in slab tip depth, whole model and slab root-mean-square velocities and temperatures (Fig. 4.15A, D, F, G, and I). However, there are differences in the viscous rate of dissipation of energy of both the whole model and the slab. The values for models with a free surface are on average 2 kW m^{-1} lower (Fig. 4.15E and H). This can be explained by the ability of the surface to deform, reducing stresses at the surface.

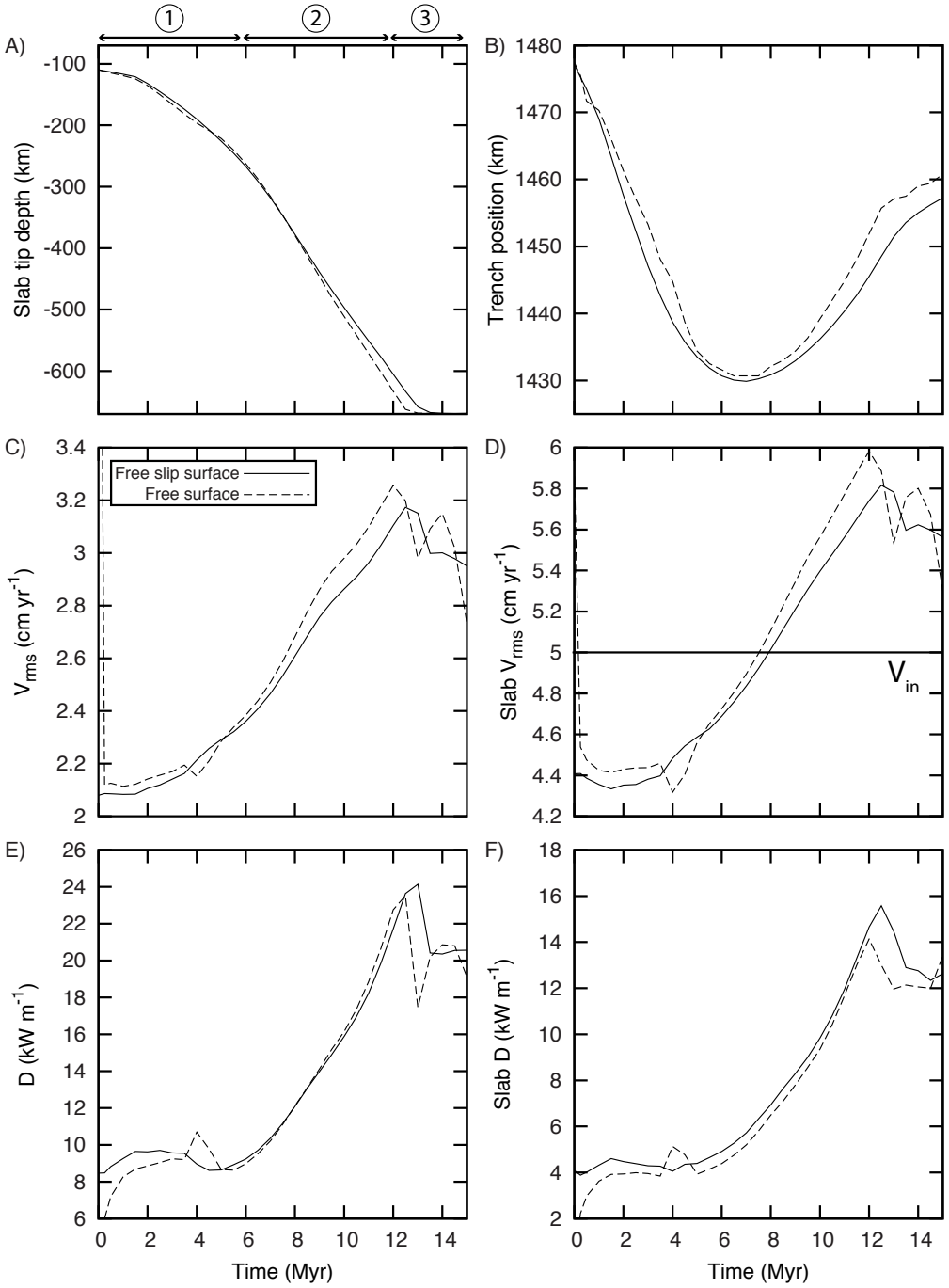


FIGURE 4.14 – Results for linear viscous case 1 models using SULEC with either a free-slip surface or a free surface. A) Slab tip depth. B) trench position. Root-mean-square velocity (Eq. 4.12) for C) the whole model and D) the subducting slab only. Viscous rate of dissipation of energy (Eq. 4.14) for E) the whole mantle and F) the subducting slab only.

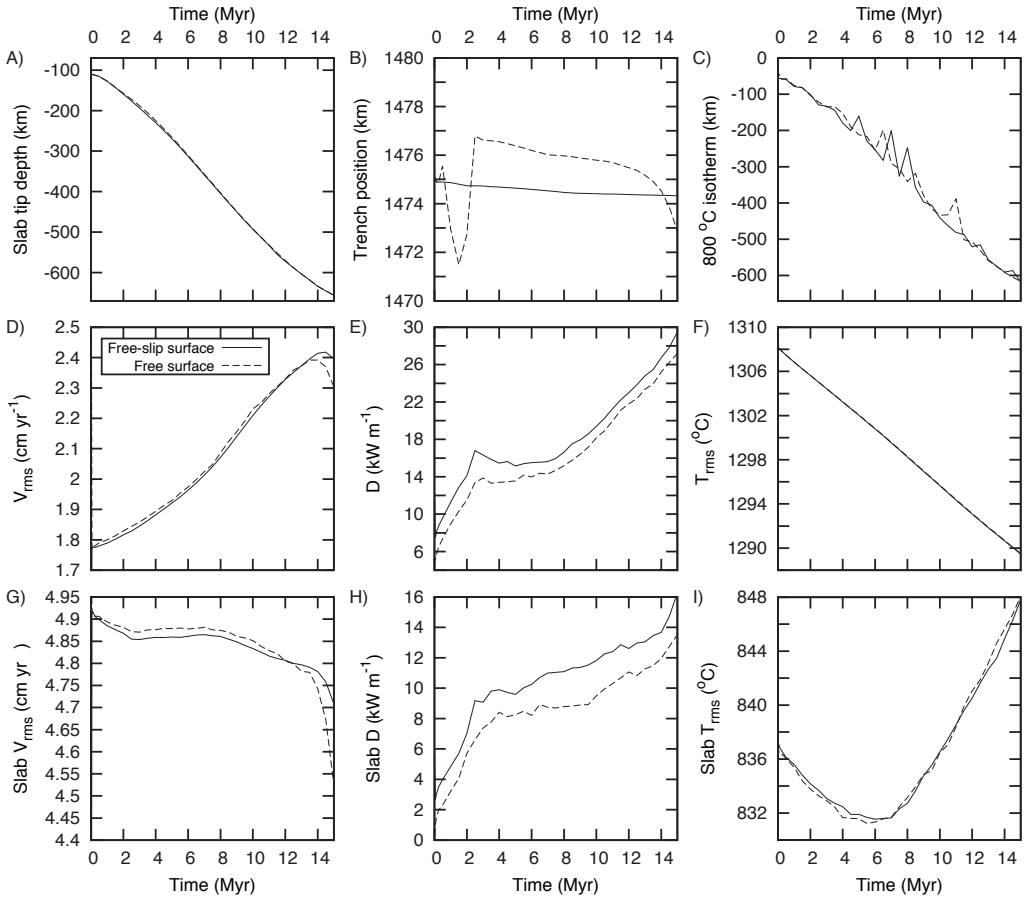


FIGURE 4.15 – Results for thermo-mechanical models (case 4) using SULEC with either a free-slip surface or a free surface. A) Slab tip depth. B) trench position. C) Depth of the 800 °C isotherm. Whole model D) root-mean-square velocity (Eq. 4.12), E) Viscous rate of dissipation of energy (Eq. 4.14), and F) root-mean-square temperature (Eq. 4.15). Slab G) Root-mean-square velocity, H) Viscous rate of dissipation of energy, and I) Root-mean-square temperature.

4.B The Effects of Density Contrast Between Lithosphere and Mantle in Case 1 Models

In models with a temperature-dependent density, the density contrast between the subducting slab and the surrounding mantle changes during model evolution and influences the dynamics of the system (Sec. 4.5.2). The density contrast between the lithosphere and the mantle in the linear viscous case 1 models is not temperature-dependent and fixed at 50 kg m^{-3}. To test the influence of this density contrast on subduction evolution, we vary its value between 40 and 60 kg m^{-3}.

The effects of density contrast become visible once slab pull overcomes slab push (*i.e.*, after approximately 5 Myr) (Fig. 4.16). Increasing the density contrast between the lithosphere and the mantle increases slab pull, and as a result subduction velocities are higher (Fig. 4.16A,C and D) and more trench retreat occurs during the stable subduction phase (Fig. 4.16B).

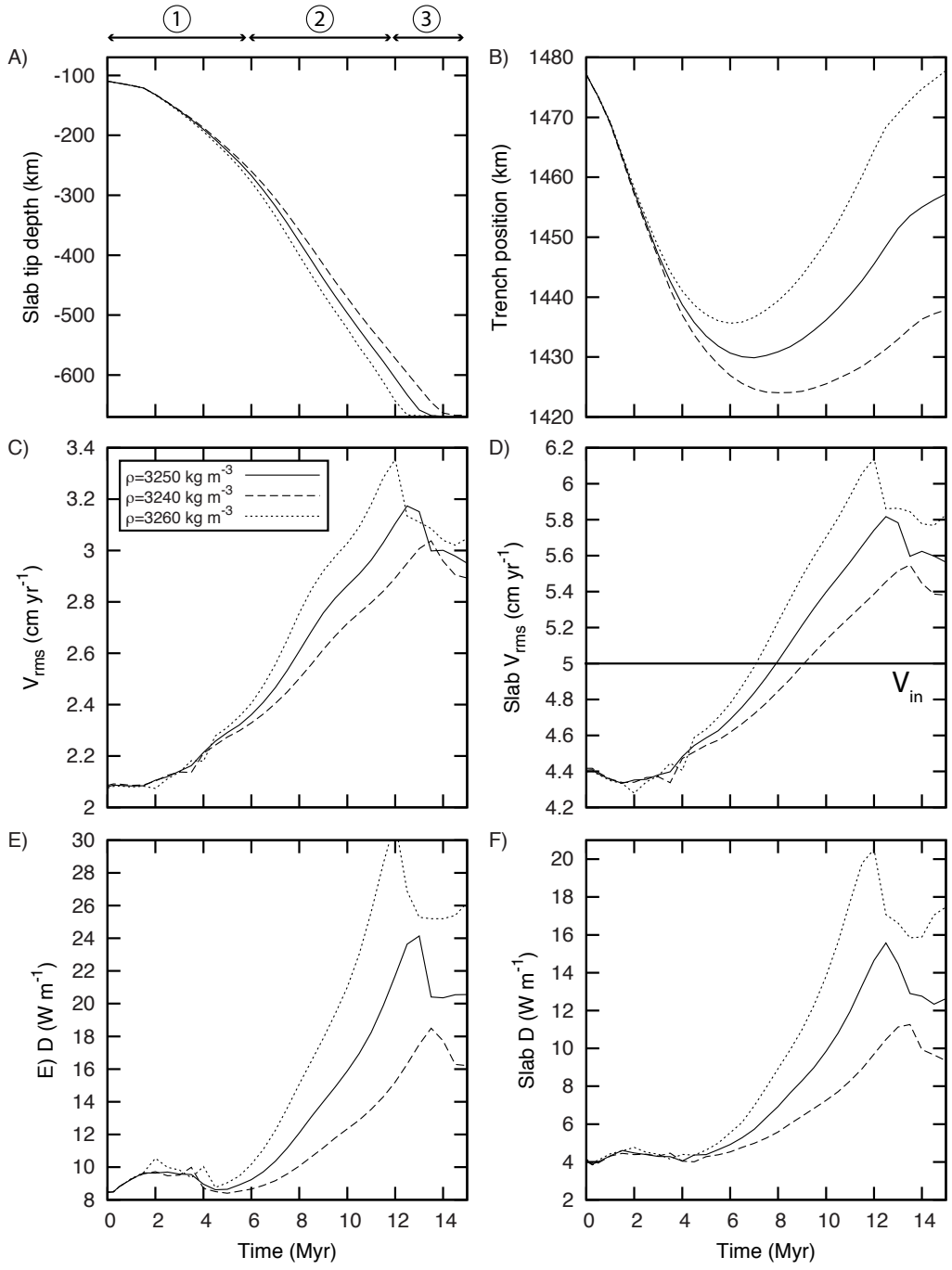


FIGURE 4.16 – Results for linear viscous models with different lithospheric densities. The mantle density is fixed at 3200 kg m-3. Models are calculated using SULEC. A) Slab tip depth. B) Trench position. Root-mean-square velocity (Eq. 4.12) for C) the whole model and D) the subducting slab only. Viscous rate of dissipation of energy (Eq. 4.14) for E) the whole mantle and F) the subducting slab only. The models in this study use ρ=3250 kg m^{-2}.

Acknowledgements

We acknowledge financial support from the European Commission through Marie-Curie Research Training Network "c2c" (contract MRTN-CT-2006-035957). The idea of a subduction model comparison arose at a c2c meeting in Prague in 2008. We greatly appreciated constructive discussions with Bernhard Steinberger, Joya Tetreault, Zurab Chemia, Ondřej Čadek and Hana Čížková.

TABLE 4.5 – Results at 2, 8 and 12.5 Myr for case 1 models.

ASPECT		Unit	2 Myr	8 Myr	12.5 Ma
	Trench position	km	1450.1	1408	1416
	Slab tip depth	km	128.28	342.85	579.96
	Whole model V_{rms}	m s^{-1}	6.6203e-10	7.9133e-10	9.5259e-10
	Whole model D [a]	kW m^{-1}	10.087	11.704	20.716
	Slab V_{rms}	m s^{-1}	1.3667e-09	1.5331e-09	1.7614e-09
	Slab D [a]	kW m^{-1}	4.6748	6.8134	14.541
CHIC					
	Trench position	km	1463.1	1435.6	1454.3
	Slab tip depth	km	-134.88	-383.5	-657.48
	Whole model V_{rms}	m s^{-1}	6.768e-10	8.4374e-10	1.0005e-09
	Whole model D [a]	kW m^{-1}	37.545	34.167	51.155
	Slab V_{rms}	m s^{-1}	1.4005e-09	1.6041e-09	1.8245e-09
	Slab D [a]	kW m^{-1}	255.69	241.56	362.49
ELEFANT					
	Trench position	km	1457.3	1416.4	1425.9
	Slab tip depth	km	-130.66	-338.75	-580.23
	Whole model V_{rms}	m s^{-1}	6.4919e-10	7.7896e-10	9.4995e-10
	Whole model D [a]	kW m^{-1}	10.37	11.199	20.105
	Slab V_{rms}	m s^{-1}	1.3229e-09	1.5032e-09	1.8161e-09
	Slab D [a]	kW m^{-1}	5.1903	6.5625	13.909
ELMER					
	Trench position	km	1457	1423.6	1436
	Slab tip depth	km	-131.66	-351.53	-604.53
	Whole model V_{rms}	m s^{-1}	6.5989e-10	7.996e-10	9.8418e-10
	Whole model D [a]	kW m^{-1}	9.2323	11.283	21.56
	Slab V_{rms}	m s^{-1}	1.3647e-09	1.5446e-09	1.8007e-09
	Slab D [a]	kW m^{-1}	4.3652	6.2536	14.243
SLIM-3D					
	Trench position	km	1455.9	1421.3	1432
	Slab tip depth	km	-136.91	-368.6	-626.24
	Whole model V_{rms}	m s^{-1}	6.6875e-10	8.1309e-10	9.6378e-10
	Whole model D [a]	kW m^{-1}	9347.7	13248	22389
	Slab V_{rms}	m s^{-1}	1.3787e-09	1.5525e-09	1.7777e-09
	Slab D [a]	kW m^{-1}	5092.7	6682.4	13998
SULEC					
	Trench position	km	1462.3	1429.1	1444.7
	Slab tip depth	km	-121.17	-345.34	-601.84
	Whole model V_{rms}	m s^{-1}	6.6153e-10	8.0234e-10	9.8105e-10
	Whole model D [a]	kW m^{-1}	9.5633	11.129	21.569
	Slab V_{rms}	m s^{-1}	1.3755e-09	1.5587e-09	1.815e-09
	Slab D [a]	kW m^{-1}	4.4678	6.2703	14.586
YACC					
	Trench position	km	1456.3	1435.3	1453.6
	Slab tip depth	km	-133.95	-400.26	-650.73
	Whole model V_{rms}	m s^{-1}	6.5803e-10	8.3283e-10	9.8317e-10
	Whole model D [a]	kW m^{-1}	8.9129	10.883	21.9
	Slab V_{rms}	m s^{-1}	1.3878e-09	1.6129e-09	1.821e-09
	Slab D [a]	kW m^{-1}	4.3383	6.379	14.935

[a] D: Viscous rate of dissipation of energy (Eq. 4.14).

TABLE 4.6 – Thermal output values at 2, 8 and 12.5 Myr for case 2 models.

CHIC		Unit	2 Myr	8 Myr	12.5 Myr
	800 °C isotherm depth	km	-96.62	-321.53	-592
	Whole model T_{rms}	°C	1302.4	1294.7	1288.6
	Slab T_{rms}	°C	827.75	827.8	842.07
ELEFANT					
	800 °C isotherm depth	km	-76.523	-234.21	-484.87
	Whole model T_{rms}	°C	1305.4	1297.7	1292
	Slab T_{rms}	°C	834.94	832.2	841.4
SLIM					
	800 °C isotherm depth	km	-75.662	-247.49	-488.12
	Whole model T_{rms}	°C	1305.6	1297.7	1291.9
	Slab T_{rms}	°C	831.47	836.2	844.27
SULEC					
	800 °C isotherm depth	km	-77.893	-237.36	-537.59
	Whole model T_{rms}	°C	1305.5	1297.8	1292.1
	Slab T_{rms}	°C	834.96	833.4	841.5
YACC					
	800 °C isotherm depth	km	-80.113	-304.86	-568.88
	Whole model T_{rms}	°C	1305.3	1296.7	1289.8
	Slab T_{rms}	°C	837.36	832.66	840.97

TABLE 4.7 – Results at 2, 8 and 12.5 Myr for case 2b models.

CHIC		Unit	2 Myr	8 Myr	12.5 Myr
	Trench position	km	1458.9	1409.3	1405.8
	Slab tip depth	km	-133.95	-333.58	-564.83
	800 °C isotherm depth	km	-98.224	-264.63	-485.61
	Whole model V_{rms}	m s^{-1}	7.1722e-10	1.1072e-09	1.4929e-09
	Whole model D[a]	kW m^{-1}	36.14	39.405	46.148
	Whole model T_{rms}	°C	1302.4	1294.9	1289.9
	Slab V_{rms}	m s^{-1}	1.3897e-09	1.4889e-09	1.6029e-09
	Slab D[a]	kW m^{-1}	181.41	308.68	310.8
	Slab T_{rms}	°C	827.22	829.04	836.21
ELEFANT					
	Trench position	km	1454.9	1387.9	1367.6
	Slab tip depth	km	541.1	381.74	186.41
	800 °C isotherm depth	km	-76.154	-190.86	-366.99
	Whole model V_{rms}	m s^{-1}	6.7471e-10	9.1932e-10	1.1504e-09
	Whole model D[a]	kW m^{-1}	10.452	10.792	13.536
	Whole model T_{rms}	°C	1305.4	1297.6	1292.1
	Slab V_{rms}	m s^{-1}	1.3213e-09	1.3544e-09	1.4719e-09
	Slab D[a]	kW m^{-1}	5.0358	4.8984	5.6352
	Slab T_{rms}	°C	1305.4	1297.6	1292.1
ELMER					
	Trench position	km	1455.9	1392.3	1370.8
	Slab tip depth	km	-127.01	-281.22	-473.04
	800 °C isotherm depth	km	-73.844	-189.45	-344.78
	Whole model V_{rms}	m s^{-1}	6.7929e-10	9.2266e-10	1.1669e-09
	Whole model D[a]	kW m^{-1}	10.026	10.34	13.478
	Whole model T_{rms}	°C	1305.2	1296.5	1289.9
	Slab V_{rms}	m s^{-1}	1.3536e-09	1.404e-09	1.4923e-09
	Slab D[a]	kW m^{-1}	5.0017	4.8623	5.3533
	Slab T_{rms}	°C	830.45	818.51	822.74
SLIM					
	Trench position	km	1453.8	1396.2	1374.3
	Slab tip depth	km	-132.66	-292.63	-492.96
	800 °C isotherm depth	km	-72.684	-186.51	-334.27
	Whole model V_{rms}	m s^{-1}	6.8862e-10	9.3839e-10	1.1782e-09
	Whole model D[a]	kW m^{-1}	9.6379	11.081	13.576
	Whole model T_{rms}	°C	1305.5	1297.7	1292
	Slab V_{rms}	m s^{-1}	1.3662e-09	1.4015e-09	1.4662e-09
	Slab D[a]	kW m^{-1}	5.117	5.764	5.5616
	Slab T_{rms}	°C	829.78	830.26	838.77
SULEC					
	Trench position	km	1454.9	1407.1	1396.5
	Slab tip depth	km	-130.95	-326.26	-533.93
	800 °C isotherm depth	km	-76.637	-207.36	-424.92
	Whole model V_{rms}	m s^{-1}	6.9064e-10	9.7204e-10	1.2323e-09
	Whole model D[a]	kW m^{-1}	9.7512	10.016	14.135
	Whole model T_{rms}	°C	1305.5	1297.8	1292.3
	Slab V_{rms}	m s^{-1}	1.3724e-09	1.4595e-09	1.5358e-09
	Slab D[a]	kW m^{-1}	4.4149	4.5294	5.3834
	Slab T_{rms}	°C	834.95	829.65	836.45
YACC					
	Trench position	km	1459.8	1413	1399.7
	Slab tip depth	km	-130.35	-326.21	-542.42
	800 °C isotherm depth	km	-75.998	-230.15	-421.46
	Whole model V_{rms}	m s^{-1}	6.6948e-10	9.0095e-10	1.2351e-09
	Whole model D[a]	kW m^{-1}	8.859	7.8928	13.105
	Whole model T_{rms}	°C	1305.3	1296.9	1290.6
	Slab V_{rms}	m s^{-1}	1.3814e-09	1.4523e-09	1.5398e-09
	Slab D[a]	kW m^{-1}	4.2147	3.5342	4.3832
	Slab T_{rms}	°C	836.9	830.83	836.54

[a] D: Viscous rate of dissipation of energy (Eq. 4.14).

TABLE 4.8 – Results 2, 8 and 12.5 Myr for case 3 models.

CHIC		Unit	2 Myr	8 Myr	12.5 Myr
	Trench position	km	1473.5	1471.4	1470.3
	Slab tip depth	km	-162.94	-465.16	-661
	800 °C isotherm depth	km	-125.74	-405.74	-613.27
	Whole model V_{rms}	m s^{-1}	7.9407e-10	1.2763e-09	1.5641e-09
	Whole model D[a]	kW m^{-1}	28.242	39.489	45.631
	Whole model T_{rms}	°C	1302.4	1294.8	1290.6
	Slab V_{rms}	m s^{-1}	1.5589e-09	1.58e-09	1.558e-09
	Slab D[a]	kW m^{-1}	5.5126	9.3289	13.519
	Slab T_{rms}	°C	833.48	833.99	842.74
ELEFANT					
	Trench position	km	1474.7	1471.5	1473.6
	Slab tip depth	km	496.18	180.26	1.817
	800 °C isotherm depth	km	-119.15	-396.56	-654.46
	Whole model V_{rms}	m s^{-1}	0.063378	0.25351	0.39611
	Whole model D[a]	kW m^{-1}	6.3816	28.85	27.775
	Whole model T_{rms}	°C	1305.4	1298.5	1298.6
	Slab V_{rms}	m s^{-1}	1.5468e-09	1.6282e-09	1.934e-09
	Slab D[a]	kW m^{-1}	3.4375	8.4224	11.358
	Slab T_{rms}	°C	835.01	843.68	877.93
SULEC					
	Trench position	km	1474.8	1474.6	1474.4
	Slab tip depth	km	-160.08	-407.92	-629.76
	800 °C isotherm depth	km	-107.57	-327.75	-558.33
	Whole model V_{rms}	m s^{-1}	7.8858e-10	1.12e-09	1.3699e-09
	Whole model D[a]	kW m^{-1}	14.027	17.558	22.518
	Whole model T_{rms}	°C	1305.5	1298	1293.5
	Slab V_{rms}	m s^{-1}	1.5602e-09	1.5786e-09	1.5385e-09
	Slab D[a]	kW m^{-1}	7.6861	8.4149	10.127
	Slab T_{rms}	°C	834.98	839.89	849.65

[a] D: Viscous rate of dissipation of energy (Eq. 4.14).

TABLE 4.9 – Results at 2, 8 and 12.5 Myr for case 4 models.

CHIC		Unit	2 Myr	8 Myr	12.5 Myr
	Trench position	km	1475.6	1474.3	1474.1
	Slab tip depth	km	-132.05	-226.79	-326.47
	800 °C isotherm depth	km	-81.215	-186.17	-288.37
	Whole model V_{rms}	m s^{-1}	5.5807e-10	6.048e-10	6.6775e-10
	Whole model D[a]	kW m^{-1}	0.069686	0.11122	0.62916
	Whole model T_{rms}	°C	1302.4	1295.4	1290.1
	Slab V_{rms}	m s^{-1}	1.4646e-09	1.4337e-09	1.3927e-09
	Slab D[a]	kW m^{-1}	0.48324	0.71119	4.9745
	Slab T_{rms}	°C	830.78	825.77	823.27
SULEC					
	Trench position	km	1474.7	1474.2	1474.1
	Slab tip depth	km	-160.9	-413.27	-595.83
	800 °C isotherm depth	km	-113.87	-357.93	-549.69
	Whole model V_{rms}	m s^{-1}	5.7607e-10	6.6358e-10	7.5049e-10
	Whole model D[a]	kW m^{-1}	14.068	15.531	22.542
	Whole model T_{rms}	°C	1305.5	1298.1	1292.7
	Slab V_{rms}	m s^{-1}	1.544e-09	1.5451e-09	1.5223e-09
	Slab D[a]	kW m^{-1}	7.7873	9.1795	12.131
	Slab T_{rms}	°C	834.52	834.55	842.08

[a] D: Viscous rate of dissipation of energy (Eq. 4.14).

Chapter 5

Testing the effects of basic numerical implementations of water migration on models of subduction dynamics[1]

Abstract

Subduction of oceanic lithosphere brings water into the Earth's upper mantle. Previous numerical studies have shown how slab dehydration and mantle hydration can impact the dynamics of a subduction system by allowing a more vigorous mantle flow and promoting localisation of deformation in the lithosphere and mantle. The depths at which dehydration reactions occur in the hydrated portions of the slab are well constrained in these models by thermodynamic calculations. However, computational models use different numerical schemes to simulate the migration of free water. We aim to show the influence of the numerical scheme of free water migration on the dynamics of the upper mantle and more specifically the mantle wedge. We investigate the following three simple migration schemes with a finite-element model: (I) element-wise vertical migration of free water, occurring independent of the flow of the solid phase; (II) an imposed vertical free water velocity; and (III) a Darcy velocity, where the free water velocity is a function of the pressure gradient caused by the difference in density between water and the surrounding rocks. In addition, the flow of the solid material field also moves the free water in the imposed vertical velocity and Darcy schemes. We first test the influence of the water migration scheme using a simple model that simulates the sinking of a cold hydrated cylinder into a dry warm mantle. We find that the free water migration scheme has only a limited impact on the water distribution after 1 Myr in these models. We next investigate

[1]Published as: Quinquis, M. E. T., Buiter, S. J. H. (2014), Testing the effects of basic numerical implementations of water migration on models of subduction dynamics, Solid Earth, 5, 537–555, doi: 10.5194/se-5-537-2014

slab dehydration and mantle hydration with a thermomechanical subduction model that includes brittle behaviour and viscous water-dependent creep flow laws. Our models demonstrate that the bound water distribution is not greatly influenced by the water migration scheme whereas the free water distribution is. We find that a bound water-dependent creep flow law results in a broader area of hydration in the mantle wedge, which feeds back to the dynamics of the system by the associated weakening. This finding underlines the importance of using dynamic time evolution models to investigate the effects of (de)hydration. We also show that hydrated material can be transported down to the base of the upper mantle at 670 km. Although (de)hydration processes influence subduction dynamics, we find that the exact numerical implementation of free water migration is not important in the basic schemes we investigated. A simple implementation of water migration could be sufficient for a first order impression of the effects of water for studies that focus on large-scale features of subduction dynamics.

5.1 Introduction

Dehydration of subducting lithosphere and the related hydration of the mantle wedge can influence the dynamics of subduction, as water has a weakening effect on viscous and brittle rheologies (*e.g.*, Sibson et al., 1975; Peacock, 1987; Hirschmann, 2006; Connolly, 2005; Gerya et al., 2008). The amount of fluids carried by subducting oceanic lithosphere is debated, but it is thought that water content can reach up to 3 wt. % at the surface, decreasing with depth (Rüpke et al., 2004). Water is acquired through near-surface hydration, which is aided by flexure-related extensional fractures, and by hydrothermal activity with circulation of hot water and vapour in the upper section of the oceanic crust (Staudigel, 2003; Rüpke et al., 2004; Faccenda et al., 2008a). The subducting crust carries water in two phases: (1) Free fluids that are contained in the porosity of the rock and can percolate along grain-boundaries (Stern, 2002; Bercovici and Karato, 2003; Wark et al., 2003; Rüpke et al., 2004; Cheadle et al., 2004) and (2) mineralogically bound fluids in the form of hydroxyl complexes (OH) (Schmidt and Poli, 1998; Hirschmann, 2006). Once a slab starts to subduct, it undergoes dehydration processes due to the increase in pressure and temperature. Most of the water contained in the porosity of the sediments is expelled near the trench through compaction and is not transported into the mantle. This is known as fore arc volatile discharge (Stern, 2002; Rüpke et al., 2004). Hydrated minerals include, among others, amphiboles, chlorite and serpentine. It has been well documented that mineralogically bound water is released when hydrated minerals udergo certain phase transitions (Schmidt and Poli, 1998; Iwamori, 1998; Kerrick and Connolly, 2001; Hacker et al., 2003; Ohtani et al., 2004; Rüpke et al., 2004; Syracus and Abers, 2006; Hirschmann,

2006). At the same time, experimentally determined phase diagrams suggest that mineralogically bound water can be transported to the base of the upper mantle, or perhaps even greater depths (Iwamori, 1998; Schmidt and Poli, 1998; Stern, 2002; Ohtani et al., 2004).

Dehydration processes can influence subduction in multiple ways. For example, the depth at which major dehydration occurs determines the location of volcanic arcs, which are located extitc.a., 110–120 km above the surface of subducted slabs (England et al., 2004; Syracus and Abers, 2006). It is the melting of mantle wedge materials that is thought to lead to arc volcanism. But water released from the subducting slab decreases the pressure and temperature at which melting occurs, thus enhancing mantle wedge melting and causing volcanism. Mantle material that is hydrated by water released from the slab may also form weak, positively buoyant 'wet plumes' that rise upwards and efficiently hydrate the mantle wedge (Billen and Gurnis, 2001; Billen, 2008; Gorczyk et al., 2007a; Richard and Iwamori, 2010). These fluids can then cause a more vigorous flow in the mantle wedge. Arcay et al. (2005) showed that mantle wedge hydration can result in thermal erosion and softening of the overriding lithosphere. Once subduction has started, (de)hydration processes may further influence the evolution of subduction by enforcing an asymmetrical geometry of subduction zones, causing subduction to be one-sided (Gerya et al., 2008). Dehydration processes can in addition aid the exhumation of high and ultrahigh-pressure metamorphic rocks by creating a wide and weak subduction channel through which rocks are exhumed (Gerya et al., 2002). Dehydration of the subducting slab may in turn increase slab strength, but this effect may be overwhelmed by the strong impact of water on the mantle wedge.

The models mentioned above use similar methods to determine the conditions of pressure and temperature at which dehydration processes occur. These are usually based on thermodynamic calculations (de Capitani and Brown, 1987; Holland and Powell, 1998; Powell et al., 1998; Connolly, 2005) or high pressure experiments (Schmidt and Poli, 1998; Ohtani et al., 2004; Komabayashi et al., 2005; Iwamori, 2007a), and the location of the dehydration fronts during subduction do not greatly vary between models. Water migration can be described by two-phase flow conservation equations (Spiegelman, 1993a,b; Bercovici et al., 2001). However, these are not routinely used in numerical simulations of subduction zone dynamics at the scale of the upper mantle as it adds a fairly complex set of equations to an already highly non-linear model. Usually simplifications are therefore made to migrate water in large-scale subduction models.

Bound water is advected along the solid flow field. Bound water can in addition be affected by diffusion mechanisms which allow water to migrate through the solid phase field as a function of the chemical and temperature gradients (Richard et al., 2006). Because we focus on first order behaviour of free water migration on subduction dynamics, we keep our models relatively simple and neglect the effect

of bound water diffusion. Free water can migrate in the interconnected pore space of the solid phase (Stern, 2002; Wark et al., 2003; Cheadle et al., 2004; Rüpke et al., 2004), create its own hydrated channels (Katz et al., 2006), or be absorbed by non-saturated rocks of the mantle wedge (Iwamori, 1998) to be potentially transported with the mantle flow into the lower mantle (Bercovici and Karato, 2003; Iwamori, 2007a; Richard and Bercovici, 2009; Fujita and Ogawa, 2013). Free water is also advected by the solid flow field through which it migrates and this can result in cases where part of the free water migrates up through the mantle wedge, while the rest is carried with the solid flow and subducted into the mantle (Cagnioncle et al., 2007).

Numerical studies of hydration of the mantle by slab dehydration have used different simplified numerical approximations for the migration of free water in the mantle:

1. Free water migrates vertically in the upper mantle and is not coupled to the solid phase flow in the mantle wedge (Arcay et al., 2005).

2. The migration of free water is vertical, but coupled to the mantle flow. The effective migration path of water is therefore no longer purely vertical, but can include a horizontal component. This method has been implemented as an imposed vertical velocity added to the velocity of the solid phase flow (Gorczyk et al., 2007a) or as a dehydration front with an imposed horizontal and vertical velocity (Gerya et al., 2002).

3. Free water migrates as a Darcy flow, following the density gradient between the solid phase and the fluid phase in the mantle wedge (Cagnioncle et al., 2007). Darcy flow changes the migration paths of fluids which are now no longer necessarily vertical (Cagnioncle et al., 2007). Also here the solid flow phase may advect free water in addition to the Darcy mechanism.

Studies that use the above water migration schemes show differences in the spatial distribution of hydrated material in the mantle wedge as subduction evolves (Arcay et al., 2005; Gerya et al., 2002; Gorczyk et al., 2007a; Cagnioncle et al., 2007). However, as the numerical setup of the subduction models also differs between these studies, it is difficult to evaluate the possible effects of the numerical implementation of water migration. So far, the influence of the basic numerical implementation of water migration on the dynamics of a subduction model has not been investigated. We aim to investigate the effects of the three numerical water migration schemes described above (schemes I, II and III) on the dynamics of a subducting slab and its overlying mantle wedge. These models are kept simple, allowing us to focus on the first order effects of dehydration and water migration. Our models do therefore not include melting, shear heating, or adiabatic heating.

We first illustrate the effects of dehydration and water migration for a simple model of a cold and hydrated cylinder sinking in a warm mantle. Our second series of models examines the effects of (de)hydration and water migration on a thermo-mechanical subduction model at the scale of the upper mantle.

5.2 Modelling approach

5.2.1 Thermo-mechanical equations

We solve the equations for conservation of mass (assuming incompressibility) (Eq. 5.1), momentum (Eq. 5.2) and energy (Eq. 5.3):

$$\nabla \cdot \vec{v} = 0 \tag{5.1}$$

$$-\nabla P + \nabla \cdot \bar{\sigma}' + \rho \vec{g} = 0 \tag{5.2}$$

$$\rho C_p \frac{\partial T}{\partial t} = k \nabla^2 T - \rho C_p \vec{v} \cdot \nabla T + H \tag{5.3}$$

$\vec{v}$ is the velocity vector, ρ density, t time, P pressure (mean stress), $\bar{\sigma}'$ deviatoric stress tensor, $\vec{g}$ gravitational acceleration ($g_x = 0$ and $g_y = -9.81$ m s^{-2}), C_p specific heat, T temperature, k thermal conductivity, and H radioactive heat production per unit volume. In the subduction models, the Boussinesq approximation is assumed *i.e.*, $\frac{\partial \rho}{\partial t} = 0$ but $\rho = \rho_0(1 - \alpha(T - T_0))$ where ρ_0 is the reference density at $T = T_0$ and α is the volumetric thermal expansion coefficient.

Materials deform either viscous or brittle. Our viscous rheologies are linear or pressure- and temperature-dependent:

$$\eta_{\text{df,ds}} = \frac{1}{2} \left(\frac{d^p}{A\, C_{\text{OH}}^r} \right)^{\frac{1}{n}} \dot{\varepsilon}_{\text{e}}'^{\frac{1-n}{n}} \exp\left(\frac{Q + PV}{nRT} \right) \tag{5.4}$$

$\dot{\varepsilon}_{\text{e}}'$ is the effective deviatoric strain rate ($\dot{\varepsilon}_{\text{e}}' = (\frac{1}{2}\dot{\varepsilon}_{ij}'\dot{\varepsilon}_{ij}')^{\frac{1}{2}}$), A is a material constant, n is the power law stress exponent, d grain size, p grain size exponent, C_{OH} water content in ppm, r water content exponent, Q activation energy, V activation volume and R molar gas constant. df and ds refer, respectively, to deformation by diffusion creep ($p > 0$ and $n = 1$) and dislocation creep ($p = 0$ and $n > 1$). Diffusion and dislocation creep are assumed to act in parallel in all materials, resulting in a composite viscosity (η_{comp}) (Karato and Li, 1992; van den Berg et al., 1993):

$$\eta_{\text{comp}} = \left(\frac{1}{\eta_{\text{ds}}} + \frac{1}{\eta_{\text{df}}} \right)^{-1} \tag{5.5}$$

In our models only bound water influences the viscosity and we only consider the impact of water on sub-crustal materials. A water content of 0.4 wt % results in a viscosity decrease by extitc.a., 2 orders of magnitude when using the dislocation or diffusion creep flow law for wet olivine from Hirth and Kohlstedt (2003). This can result in viscosities that are lower than the minimum viscosity of 10^{18} Pa s which is imposed in our models. We therefore assume that viscosity no longer decreases further once water content exceeds 0.4 wt %.

Brittle behaviour in the subduction models follows a Druker–Prager criterion (Handin, 1969; Jaeger and Cook, 1976; Twiss and Moores, 1992):

$$\sigma'_{\mathrm{e}} = P \sin\phi + C \cos\phi \tag{5.6}$$

σ'_{e} is the effective deviatoric shear stress ($\sigma'_{\mathrm{e}} = (\frac{1}{2}\sigma'_{ij}\sigma'_{ij})^{\frac{1}{2}}$), ϕ is the angle of internal friction, and C is the cohesion. ϕ undergoes a linear decrease with total effective plastic strain (measured as the square root of the second invariant of the strain tensor) to simulate strain-weakening. Such strain weakening is thought to result from a reduction in fault rock grain size (Handy et al., 2007), mineral transformations (White and Knipe, 1978; Tingle et al., 1993), or the development of foliation or high fluid pressures (Hubbert and Rubey, 1959; Sibson, 1977). The effective viscosity for plastic flow is (Lemiale et al., 2008):

$$\eta_p = \frac{P \sin\phi + C \cos\phi}{2\dot{\varepsilon}'_{\mathrm{e}}} \tag{5.7}$$

In our thermo-mechanical subduction models, we use a minimum viscosity value of 10^{18} Pa s and a maximum cut-off of 10^{24} Pa s. These values ensure efficient convergence of our mechanical solution, while allowing for viscosity contrasts of 6 orders of magnitude. The minimum viscosity of 10^{18} Pa s is low enough to capture almost all viscosity variations in our model. The cut-off value is only reached very locally in the mantle wedge. We solve the thermal and mechanical equations with a 2-D version of SULEC, which is an Arbitrary Lagrangian Eulerian (ALE) finite element code (Buiter and Ellis, 2012). The mesh consists of quadrilateral elements which have linear continuous velocity and constant discontinuous pressure fields. Particles are used to track the material field (through a material identifier) and properties such as particle strain, stress, and water content. The particles are advected with the solid flow field using a second-order Runge-Kutta scheme. We use harmonic viscosity averaging and arithmetic density averaging schemes from particles to elements (Schmeling et al., 2008). The subduction models have a free surface and we use the surface stabilisation algorithm of Kaus et al. (2010) and Quinquis et al. (2011).

5.2.2 Calculation of water content

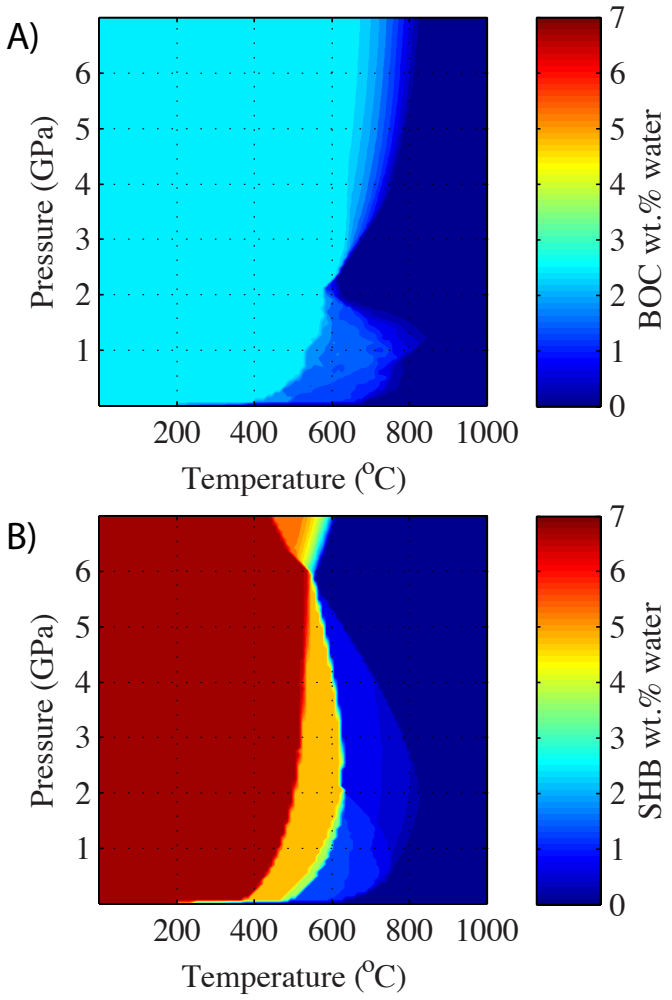


FIGURE 5.1 – Water content as a function of pressure and temperature calculated using Perple_X for **(A)** Bulk Oceanic Crust, and **(B)** Serpentinised Harzburgite lithologies (Chemia et al., 2010). Bulk compositions are in Table 5.1.

Our subduction model includes 3 lithologies: a Bulk Oceanic Crust (BOC), Serpentinised Harzburgite (SHB) for the lithospheric mantle (Chemia et al., 2010), and Pyrolite for the sub-SHB mantle (Schmidt and Poli, 1998). Water content is determined in wt. % as a function of pressure, temperature and bulk composition (*i.e.*, the average chemical composition of each lithology, Table 5.1). The water contents of BOC and SHB are calculated using Perple_X (Connolly, 2005) by Chemia et al. (2010) (Fig. 5.1). Perple_X is a thermodynamic code that minimises the Gibbs free energy of a chemical system to determine the stability fields of the

TABLE 5.1 – Bulk compositions in % for the lithological oceanic lithosphere model (Chemia et al., 2010).

Oxides	BOC	SHB
SiO_2	47.32	41.023
TiO_2	0.63	0.075
Al_2O_3	16.11	1.114
FeO	7.21	7.66
MgO	9.27	42.298
CaO	12.17	1.029
Na_2O	1.65	–
H_2O	2.68	6.8
CO_2	2.95	–
Total	99.99	99.999

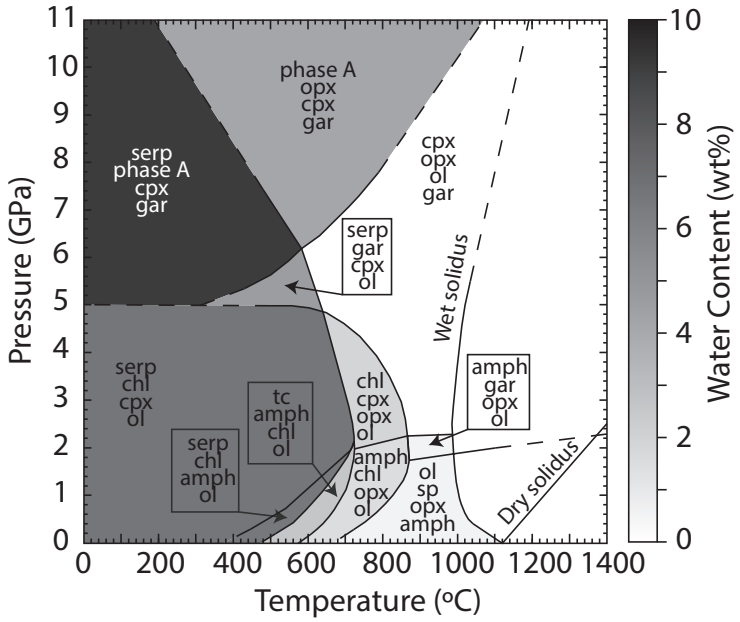


FIGURE 5.2 – Water content as a function of pressure and temperature for mantle material of pyrolitic composition, modified from Schmidt and Poli (1998). The solid lines are experimentally determined Clapeyron slopes (Schmidt and Poli, 1998), while the dashed lines have been extrapolated in a similar manner to Arcay et al. (2005). amph: amphibole; chl: chlorite; cpx: clinopyroxene; gar: garnet; opx: ortopyroxene; ol: olivine; serp: serpentine; sp: spinel; tc: talc.

phases which compose the mineral assemblages. Once these stability fields are calculated, it is possible to determine the maximum allowed water content of each phase as a function of pressure and temperature. The thermodynamic calculations of Perple_X are valid up to pressures of 7 GPa and temperatures of 1300 ^{o} C and do therefore not cover upper mantle conditions. We base our water contents in the upper mantle on Schmidt and Poli (1998) who experimentally determined water storage capacity for pyrolite up to 8 GPa and 1100 ^{o} C. We extrapolate these data to 11GPa and 1400 ^{o} C by linearly continuing the Clapeyron slopes of the stability fields, similar to Arcay et al. (2005) (Fig. 5.2). Serpentinisation of the mantle wedge can locally increase the water storage capacity up to 7 wt. % H_2O (Iwamori, 1998; Rüpke et al., 2004; Connolly, 2005; Férot and Bolfan-Casanova, 2012). We furthermore assume that the water storage capacity in the sublithospheric mantle (*i.e.*, the pyrolitic material) does not converge to zero as shown by the phase diagrams determined by Schmidt and Poli (1998) because this would not allow the transport of bound water into the upper mantle. We impose the minimum storage capacity of the mantle to be 0.2 wt %, following Bercovici and Karato (2003) (Fig. 5.2).

5.2.3 Water migration schemes

Mineralogically bound water is advected along the solid phase flow field. In our models, each particle therefore carries not only a material identifier (that determines its material porperties), but also the amount of bound and free water it contains. Free water migrates following one of these imposed migration schemes: (I) One element vertically up per time step (also referred to as 'elemental'); (II) imposed vertical velocity; or (III) Darcy flow velocity. All water migration schemes follow three stages: (1) determine the maximum water storage capacity of each particle and the amounts of free and bound water, (2) determine the migration path for the free water, if present and (3) distribute the free water along the migration path. For every particle we calculate the maximum bound water that the particle can contain using a standard bilinear interpolation in pressure and temperature of wt % H_2O on gridded versions of Figs. 5.1 and 5.2. If the mineralogically bound water is less than the water storage capacity, the particle is undersaturated and no free water is produced. If the mineralogically bound water of the particle exceeds the water storage capacity, it is oversaturated in water and dehydration occurs. The amount of free water is the difference between the mineralogical bound water of the particle and the maximum allowed water. The free water migrates through the model following one of the schemes we are investigating.

The first migration scheme (scheme I) assumes that free water moves vertically upwards owing to its negative buoyancy, with one element per time step (Δt), and is not affected by the solid phase flow (Arcay et al., 2005). This implies that the

water migration velocity is purely vertical and is imposed as the local vertical grid size divided by the time step. A model using a variable grid size would not have a constant free water velocity and this should therefore be avoided. If free water is present, undersaturated particles in the current element are hydrated first. If free water remains after this first step, it migrates to the element above. There it hydrates the undersaturated particles of that element from the bottom up. If all particles are saturated and free water is still present, it is evenly distributed over all particles of the element, waiting for the next time step for further upward migration.

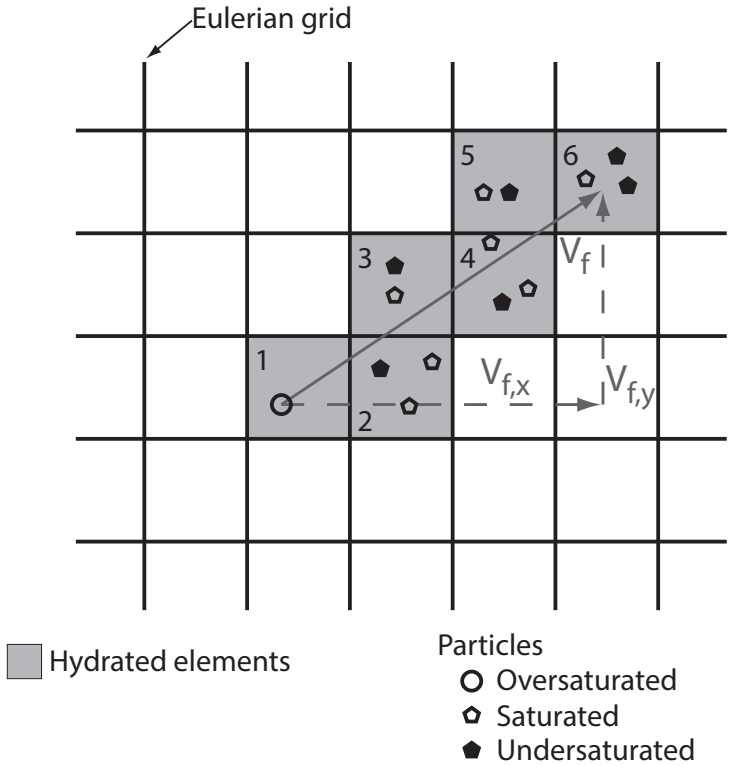


FIGURE 5.3 – Schematic migration of free water and it's distribution along a prescribed path for our velocity controlled water migration schemes II and III (see text for further explanation). V_f is water velocity.

The second migration scheme (scheme II) imposes the velocity for free water ($v_{\mathrm{f},x}$ and $v_{\mathrm{f},y}$) (Gorczyk et al., 2007a). This method reduces the grid dependence of the migration scheme, though does not eliminate it totally as the migration path itself is grid dependent. When a particle is oversaturated, it releases water distributed along the path defined by $v_\mathrm{f} \times \Delta t$ (Fig. 5.3). The horizontal and vertical components of the solid flow phase are added to the respective components of

the free water velocity. Migration of free water is therefore no longer necessarily vertical. As in the case of the migration scheme I, the first step is to hydrate undersaturated particles in the current element. If free water is still present after this step, the remaining free water migrates to the next element, saturating the undersaturated particles from the bottom up, and so on. If all particles along the migration path of this time step are saturated (*i.e.*, all particles in elements 1 to 6 of Fig. 5.3), the remaining water is distributed evenly over all particles of the last element. The motivation for element-wise distribution is that water migration paths are likely irregular and a linear path for free water would be unlikely (Rüpke et al., 2004; Katz et al., 2006). We only show examples with an imposed vertical velocity and $v_{\mathrm{f},x} = 0$.

The third migration scheme (scheme III) follows a simplification of Darcy flow where the fluid follows the pressure gradient caused by the difference in density between the fluid and the solid it is percolating through (Turcotte and Schubert, 2002):

$$q = \frac{(\rho_\mathrm{s} - \rho_\mathrm{f}) g \kappa}{\eta_\mathrm{f}} \tag{5.8}$$

where q is the Darcy velocity, ρ_s and ρ_f the density of the solid and fluid respectively, g the gravitational acceleration, η_f the viscosity of the fluid, and k the permeability. The permeability follows the empirical definition of Wark et al. (2003):

$$\kappa = \frac{d^2 \Phi^3}{270} \tag{5.9}$$

where Φ the volume fraction of fluid and d the grain size (same as in Eq. 5.4). The fluid velocity is the sum of the Darcy velocity relative to the volume fraction of fluid and the solid velocity:

$$v_f = \frac{q}{\Phi} + v_s \tag{5.10}$$

where v_f is the fluid velocity and v_s the solid phase velocity.

The water migration and distribution then follow scheme II. We assume, however, that water migration in scheme III is vertical. This assumption (also previously made by Cagnioncle et al. (2007)) is reasonable as the horizontal pressure gradient in our models in the mantle wedge is much smaller than the vertical pressure gradient (Fig. 5.4). Φ, the volume fraction of fluid, is determined from the initial water content and the grids for pressure, temperature and wt % H_2O. However, this assumes that all the free water that is present in interconnected channels is used to calculate the fluid velocity (Eqs. 5.8-5.10). This would result in unnaturally high fluid velocities. We therefore introduce an efficiency factor,

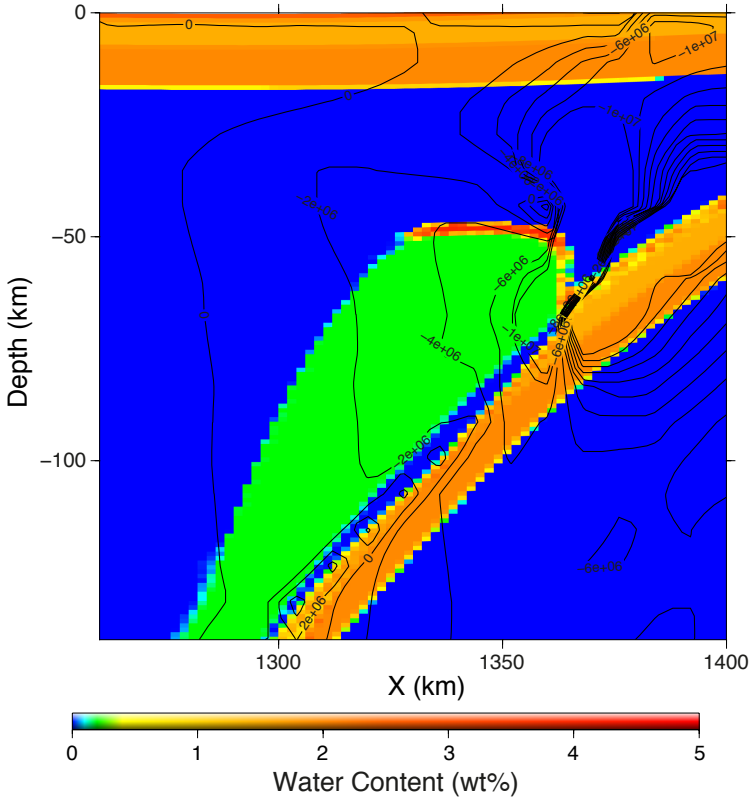


FIGURE 5.4 – A close up of the mantle wedge region at 5 Myr in a subduction model that uses free water migration scheme I in which viscosity decreases with bound water content. Shown is the elemental bound water content with contours at every 2 MPa of the horizontal pressure difference, $\frac{dP}{dx}$. Horizontal pressure variations are low in the region with highest bound water content.

ω, that corresponds to the percentage of interconnected channels of the network through which water can migrate. The effective permeability in Eq. 5.8 then becomes $\kappa_e = \omega\kappa$. This reduces the effective fluid velocity as water can only migrate through the interconnected network. The Darcy water velocity is calculated for every particle of the model. The water velocity is not constant throughout the model and areas with higher water content have higher water migration velocities.

We use the following output values to quantify the influence of the water migration schemes on the water distribution and the dynamic evolution of the models: (1) The water distribution is described by tracking the depths of the top-most, lower-most, and most left and right particles of hydrated material. The top hydrated particle gives insight into the rate of advancement of the hydration front, which is not necessarily the same as the imposed water migration velocity. For example, assuming a high water migration velocity and a low amount of free water,

free water will first saturate undersaturated materials resulting in an effectively lower velocity of the hydration front. (2) The root-mean-square water contents (OH_{rms}) for slab or cylinder and the mantle provide information on the rate of dehydration of the slab or cylinder and rate of hydration of the mantle. It gives the average water content over various domains in the model (*e.g.*, in the mantle or in the slab).

$$OH_{\mathrm{rms}} = \frac{1}{A}\sqrt{\int_y \int_x (OH_{\mathrm{f}}^2 + OH_{\mathrm{b}}^2)\, dx\, dy} \tag{5.11}$$

Where OH_b is the bound water content, OH_f is the free water content, and A is the area of computation. (3) For sinking cylinder models in which viscosity depends on water content, the bottom-most particle of the subducting cylinder is also tracked. This shows the influence of water content on the dynamic evolution of the model.

5.3 The effects of (de)hydration on a simple model of a sinking wet cylinder

5.3.1 Simple model of a sinking cylinder

We first investigate the effects of (de)hydration and water migration with a simple model which simulates the subduction of a detached piece of lithosphere by the sinking of a cold, hydrated cylinder into a warm, dry mantle. These experiments are based on simple Stokes flow and use linear viscous rheologies. We solve for the advection and conduction of temperature in addition to the mechanical flow, but the temperature does not play a role in the mechanical flow as viscosities are linear viscous.

The model domain is $300km \times 300$ km and has a uniform Eulerian resolution of $1km \times 1$ km elements. The initial particle density is 25 particles per element. In this series of experiments no particle injection or deletion scheme is used. The cold cylinder has a radius of 20 km and is centered on the coordinates $x = 150$ km $y = -130$ km (Fig. 5.5). A strong viscosity contrast between the cylinder and the mantle avoids deformation of the cylinder (Table 5.2). The mechanical boundary conditions are free-slip on all sides (*i.e.*, the velocity component parallel to the boundary is free, whereas the velocity component perpendicular to the boundary is zero). A 20 Myr old lithosphere, 58 km thick, overlies the mantle. The initial thermal condition of this oceanic lithosphere is determined from the plate cooling model (*e.g.*, Turcotte and Schubert, 2002) for a surface temperature of 0 $^{\circ}$ C, a temperature of 1300 $^{\circ}$ C at 58 km, and a thermal diffusivity of 10^{-6} m^2 s^{-1}.

TABLE 5.2 – Input parameters for the linear viscous sinking cylinder model. For all materials thermal expansivity $\alpha = 0$ and heat production $H = 0$.

Lithology	Parameter	Symbol	Unit	Value
Dry Lithosphere	Reference density	ρ_0	kg m^{-3}	3200
	Viscosity	η	Pa s	10^{23}
	Thermal conductivity	k	W m^{-1} K^{-1}	4.5
	Specific heat	C_p	J kg^{-1} K^{-1}	750
Dry Mantle	Reference density	ρ_0	kg m^{-3}	3200
	Viscosity	η	Pa s	10^{20}
	Thermal conductivity	k	W m^{-1} K^{-1}	105
	Specific heat	C_p	J kg^{-1} K^{-1}	1250
Hydrated Cylinder	Reference density	ρ_0	kg m^{-3}	3250
	Viscosity	η	Pa s	10^{23}
	Thermal conductivity	k	W m^{-1} K^{-1}	4.5
	Specific heat	C_p	J kg^{-1} K^{-1}	1250

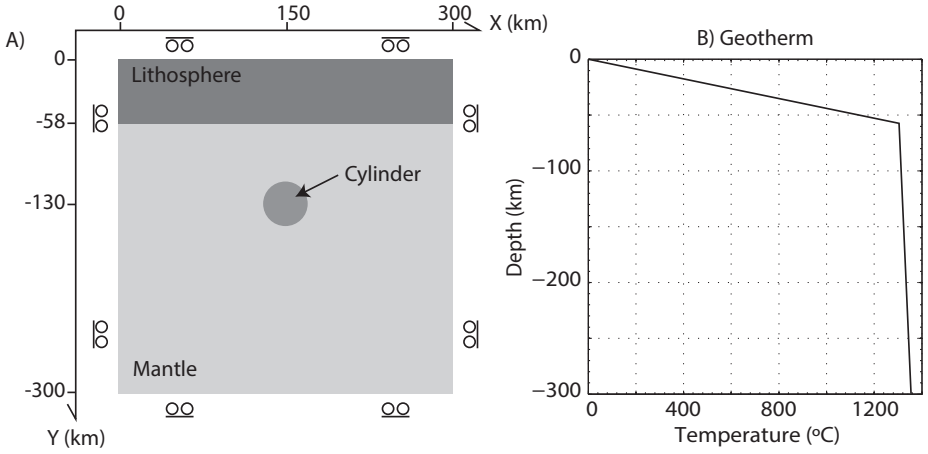


FIGURE 5.5 – **(A)** Model setup for a cold, hydrated cylinder sinking in a warm, dry mantle. All materials are linear viscous and their rheological parameters are given in Table 5.2. **(B)** Initial geotherm for model in **(A)**.

The surface temperature is held at 0 ° C and the bottom temperature (at $y = -300$ km) at 1360.5 ° C throughout model evolution, while the lateral sides are insulated (zero heat flux). A high conductivity ($k = 105$ W m^{-1} K^{-1}) is used in the mantle to enforce a mantle adiabat of 0.25 ° C km^{-1} (Pysklywec and Beaumont, 2004). The initial temperature of the cylinder is 400 ° C which gradually increases as the

cylinder warms up. The mantle is of pyrolitic composition, while the lithosphere and the cylinder are composed of SHB. The material and thermal properties are in Table 5.2. The initial water content of the hydrated cylinder is imposed at 0.2 wt $\%$.

This model setup is run using the three different migration schemes (schemes I, II and III, see Sect. 2.3). First, we use an elemental vertical migration of free water. The water migration velocity is the vertical element size divided by the time step: 20 cm yr^{-1}. Second, we use migration scheme II, imposing a vertical free water velocity of 10, 20 and 60 cm yr^{-1}. These velocities are in line with free water velocities reached in previous models (Gorczyk et al., 2007a; Gerya et al., 2002). As we use a uniform grid resolution, the 20 cm yr^{-1} model should be similar to the elemental scheme. However, the schemes are not identical because the vertical imposed velocity scheme assumes that free water is also displaced by the solid flow phase field. Finally, we use migration scheme III where the vertical water velocity is calculated from the Darcy equation (Eqs. 5.8-5.10).

5.3.2 Sinking cylinder results

We first examine models in which water content does not influence the linear viscosity. The thermal and mechanical evolution of these models are therefore identical. These models are used to test cylinder dehydration and mantle hydration for the three free water migration schemes.

As only the water migration schemes are changed, the evolution of the cylinders dehydration is identical in all cases. Dehydration of the cylinder occurs due to the increase in temperature of the cylinder from the outer rim inwards (Fig. 5.6a). Dehydration processes are assumed to be nearly instantaneous, whereas water migration velocities are more than an order of magnitude larger than the flow velocities of the mantle. Therefore, the influence of pressure on dehydration is negligible as the cylinder does not sink as quickly as it dehydrates. The hydrated cylinder is initially undersaturated as the initial water content is 0.2 wt % (but it could contain up to 6.8 wt % at its initial pressure and temperature). The interior of the cylinder is therefore hydrated by water from the lower rim, which undergoes dehydration. This explains the differences observed in cylinder OH_{rms} during the first 1 Myr of model evolution (Fig. 5.7). Once the centre of the subducting cylinder becomes saturated, dehydration in all models converges (Fig. 5.7c, f, i).

Hydration of the mantle initiates at the lateral sides of the cylinder, as the interior is being hydrated (Fig. 5.6b). This results in a horned-shape area of hydrated mantle, which progresses inwards as the cylinder dehydrates. The spatial distribution of bound water is affected by the flow of the mantle. This is visible in the area of hydrated mantle above the cylinder: a minimum in width of the hydrated domain occurs at a depth of extitc.a., 125 km (Fig. 5.6a, last stage). This

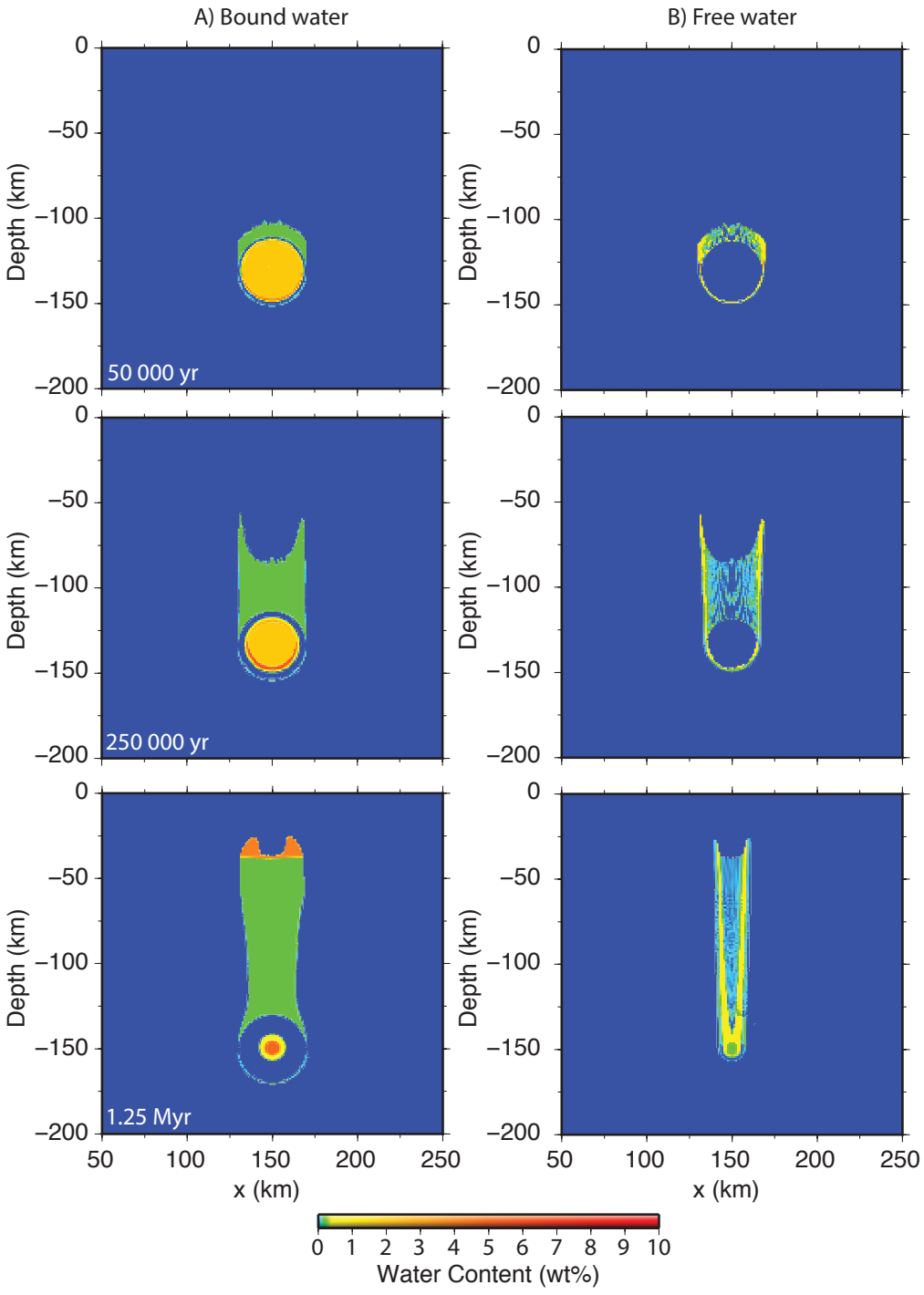


FIGURE 5.6 – Elemental water content for the Stokes flow models using scheme I (20 cm yr^{-1} for a grid resolution of $1km \times 1$ km) showing **(A)** bound water, and **(B)** free water.

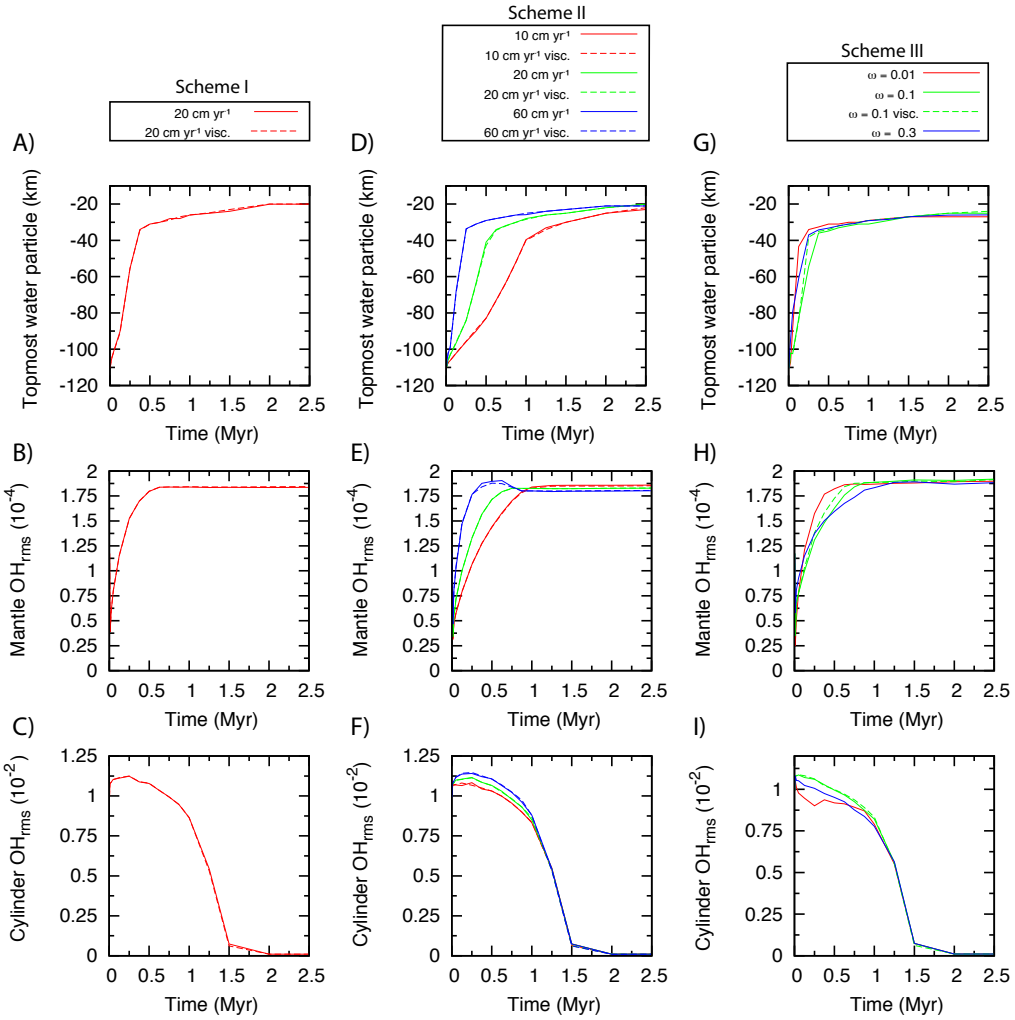


FIGURE 5.7 – Evolution with time of the depth of the top-most particle of hydrated material (top row), mantle OH_{rms} (middle row) and cylinder OH_{rms} (bottom row) for our models of a wet sinking cylinder. The first column show results for scheme I (water migration velocity of 20 cm yr^{-1}), the second for scheme II with different imposed velocities ($v_{f,y}$ = 10, 20 and 60 cm yr^{-1}) and the third for scheme III in which the water migration velocity is calculated using the Darcy law with efficiency factor $\omega = 0.01$, 0.1 or 0.3 (Sect. 2.3). Models labelled "visc" have a decrease in viscosity with increasing water content.

thinning is accentuated as the cylinder sinks towards the bottom of the model domain. The spatial distribution of free water is not affected by the mantle flow as water migration velocities are much higher than the mantle flow velocities.

The final bound water distribution in the model is independent of the water migration scheme, due to the limited amount of initial water, but water migra-

tion schemes do influence the evolution of the water distribution in the mantle (Fig. 5.7d). Due to the limited amount of water that mantle material can absorb, the mantle is rapidly saturated by water released from the dehydrating cylinder. Therefore the faster the vertical migration of water, the faster the mantle hydrates (Fig. 5.7d). Due to the much higher water saturation values in the lithosphere, the rate of advancement of the hydration front in the overlying lithosphere is greatly reduced and differences in migration schemes are negligible there. Increasing the efficiency factor in the Darcy flow models (ω, in Sec. 2.3) by an order of magnitude can locally increase the water velocity by an order of magnitude. However, this has a limited influence on the distribution of water as the average water velocity in the Darcy model stays close to 10 cm yr^{-1} (Fig. 5.7g).

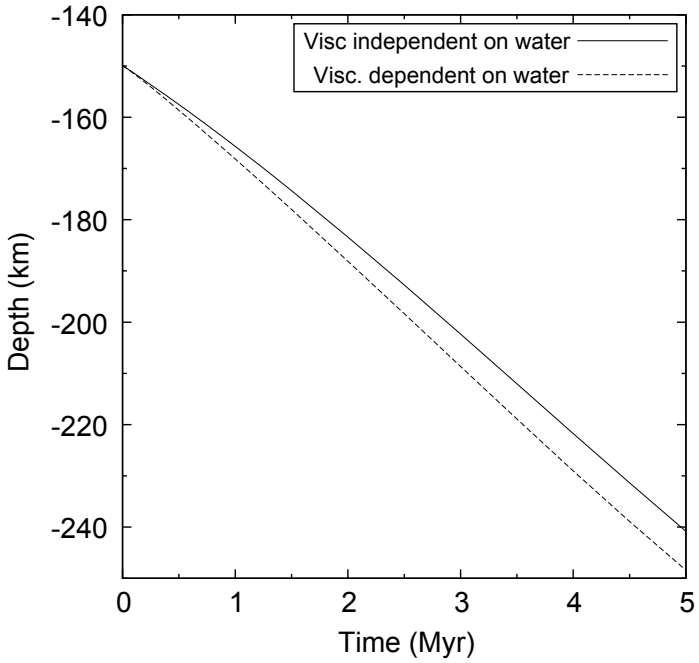


FIGURE 5.8 – Depth of the bottom of the subducting cylinder versus time for linear viscous models with or without including the effects of water on viscosity. This figure is for models that follow free water migration scheme I (Fig. 5.7a-c).

To simulate the effect of water on viscosity in these linear viscous models, a linear decrease in the lithospheric and mantle viscosity of 2 orders of magnitude is used over a water content of 0 to 0.4 wt %. This is of the same order of magnitude as obtained by including 0.4 wt % in the Hirth and Kohlstedt (2003) dislocation or diffusion creep flow law for wet olivine. Including the influence of water on mantle viscosity does not change the overall water distribution of the models (Fig. 5.7).

It does however have a small effect on the mechanical evolution of the model (Fig. 5.8). The lower viscosity values of the hydrated mantle above the cylinder increase the mantle flow velocity in this region, which results in an increase in the sinking velocity of the cylinder. However this effect is limited as it corresponds to a difference in velocity of 0.1 cm yr^{-1}. This is because hydration only occurs directly above the sinking cylinder. The sinking velocity of the cylinder is less sensitive to lowering the viscosity above the cylinder than it would be to changing the mantle viscosity below the cylinder.

5.3.3 Sinking cylinder discussion

Our models of cylinder dehydration and mantle hydration show that different numerical water migration schemes do not result in large differences in the distribution of bound water in the mantle. The sinking cylinder induces a vertical solid flow field in the area of mantle hydration. The free water migration velocities are also vertical. The combined fluid migration velocity is therefore vertical and the difference between the schemes lies mainly in the rate of free water migration. The water migration velocities for our three migration schemes are within the same order of magnitude, resulting in a similar bound and free water distribution. However, changing the magnitude of the water migration velocity does initially increase the hydration rate of the mantle and the hydration front rises at different velocities (Fig. 5.7d). This is a transient phenomenon as the models converge after extitc.a., 2.4 Myr. The low water absorption capability of the mantle material results in rapid effective migration velocities of bound water in the mantle, confirming the results of Arcay et al. (2005). Models that simulate a decrease in mantle viscosity with water content show an increase in mantle velocities and a slightly faster sinking of the cylinder. Our simple models of a sinking wet cylinder in a dry mantle indicate that the three schemes we investigated for numerical implementation of water migration lead to very similar results. Within these schemes, the exact implementation might be secondary to the first-order effect that water could have on the system. We will test this in the next section with thermo-mechanical models that also include horizontal mantle (wedge) flow components. Figure 5.6 shows a one element thick ring of hydrated mantle around the subducting cylinder, on the lateral and bottom sides. This is an artefact of the free water migration scheme. Once a particle dehydrates, undersaturated particles of the element are hydrated first. When the contact between cylinder and mantle lies within that element, mantle particles can absorb the released water resulting in the hydrated ring around the cylinder.

5.4 The effects of (de)hydration on subduction

5.4.1 Subduction model setup

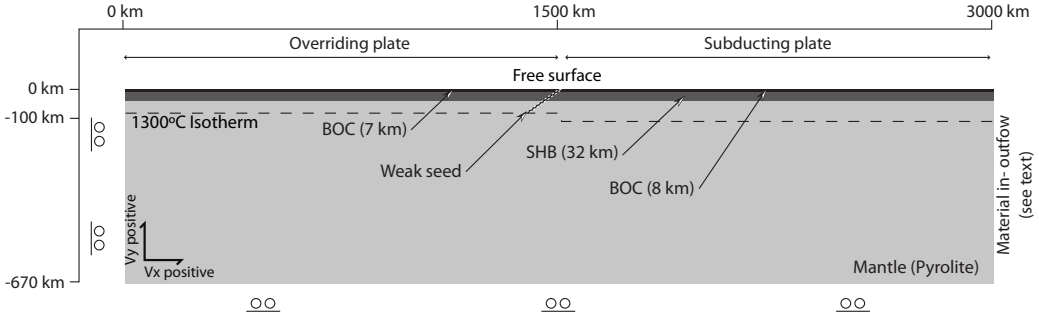


FIGURE 5.9 – Model setup for subduction of a 70 Myr old oceanic plate under a 40 Myr old oceanic plate. The top boundary is free. The bottom and left boundary are free-slip, while the right boundary condition includes material in- and outflow. SHB: Serpentinised Harzburgite, and BOC: Bulk Oceanic Crust.

We investigate the effects of slab dehydration, water migration, and mantle wedge hydration using a model of a 70 Myr old oceanic lithosphere subducting under a 40 Myr oceanic lithosphere. The model without water follows Quinquis et al. (2013) and has been tested with a number of different numerical codes.

The oceanic plates are composed of two layers: (1) a 7 and 8 km crustal layer for the overriding and subducting lithospheres, respectively, composed of Bulk Oceanic Crust (BOC) (Chemia et al., 2010), and (2) a 32 km thick Serpentinised Harzburgite (SHB) layer (Chemia et al., 2010). The rheological and thermal parameters are given in Tables 5.3 and 5.4. We assume that the upper 16 km of the oceanic plates are hydrated to a certain degree through fractures in the oceanic crust. The upper kilometre of BOC is fully hydrated, resulting in an initial water content of 2.68 wt % H_2O. Few faults exceed 1 km depth, resulting in an undersaturation of the remaining BOC. The initial water content of the BOC below 1 km depth is set at 1.5 wt % H_2O. Finally, between 7 (or 8) to 15 (or 16) kilometres depth, the overriding and subducting SHB are also undersaturated at an initial water content of 2 wt % H_2O. These values follow Rüpke et al. (2004) and Faccenda et al. (2012).

TABLE 5.3 – Subduction model parameters. The viscosity ranges from a minimum of 10^{18} to a maximum of 10^{24} Pa s. Heat production $H = 0$.

Parameter	Symbol	Unit	Mantle	Sublithospheric mantle	Overriding plate		Subducting plate		Weak seed
					BOC	SHB	BOC	SHB	
Olivine rheology			Dry	Dry	Wet	Wet	Wet	Wet	Wet
Angle of friction[a]	ϕ		20°/10°	20°/10°	20°/10°	20°/10°	5°/2°	10°/5°	2°
Cohesion	C	MPa	20	20	15	15	5	15	5
Reference density	ρ_0	kg m^{-3}	3200	3200	3000	3250	3000	3250	3200
Reference temperature	T_0	$^{\circ}$ C	1300	1300	200	200	200	200	200
Conductivity	k	W m^{-1} K^{-1}	183.33	2.5	2.5	2.5	2.5	2.5	2.5
Heat capacity	C_p	J kg^{-1} K^{-1}	750	750	750	750	750	750	750
Thermal expansivity	α	10^{-5} K^{-1}	2.5	2.5	2.5	2.5	2.5	2.5	2.5
Initial water content	–	wt % H_2O	0	0	1.5–2.68	2	1.5–2.68	2	2.68

[a] Angle of internal friction (ϕ) softens from first to second value over an effective strain interval of 0.5 to 1.5.

The model domain is 3000 km wide and 670 km deep (Fig. 5.9) and has the highest horizontal and vertical Eulerian resolution at the trench (1 km per element). The total number of elements is 473×269 (horizontal $\times$ vertical) and 16 particles per element are used initially. Due to the variable grid resolution, this series of models requires injection and deletion of particles to maintain elemental particle density between 12 and 36. The particle deletion scheme helps keep the code memory requirements reasonable. To maintain the overall water content of the model, particles are injected dry, whereas the bound or free water content of a deleted particle is distributed evenly over all other particles of the element. Subduction is initialised by a "weak seed" located at the interplate boundary. The "weak seed" simulates a pre-existing shear zone in the oceanic lithosphere separating the overriding and subducting plates. It is 14 km thick (in the direction perpendicular to the dip angle), extends to a depth of 82 km, and has a 35° dip angle. The top mechanical boundary is a true free surface (both v_x and v_y are free), whereas the bottom and left boundaries of the model are free-slip. Balanced material in- and outflow is defined on the right boundary of the model domain (the boundary parallel component is again free). To avoid strong shearing at the transition between in- and outflow, a linear velocity gradient from in- to outflow is defined over a 20 km depth interval. The inflow velocity is 5 cm yr^{-1} over the thermal thickness of the 70 Myr old lithosphere. The outflow velocity is imposed from a depth of -130 km to the bottom of the model domain at -670 km.

The initial thermal conditions of the 40 Myr (from $x = 0$ to $x = -1500$ km) and 70 Myr (from $x = 1500$ to $x = 3000$ km) old oceanic lithospheres are determined from the plate cooling model (Turcotte and Schubert, 2002) for a surface temperature of 0 ° C, a mantle temperature of 1300 ° C at 82 and 110 km depth, respectively, and a thermal diffusivity of 10^{-6} m^2 s^{-1}. The initial step in temperatures at $x = 1500$ km is rapidly diffused. During model evolution, the surface temperature is held at 0 ° C and the bottom temperature (at $y = -670$ km) at 1440 ° C, while the lateral sides are insulated (zero heat flux). A high

TABLE 5.4 – Flow law parameters from Hirth and Kohlstedt (2003).

Parameter	Unit	Dry Olivine		Wet Olivine	
		Diffusion	Dislocation	Diffusion	Dislocation
A[a]	Pa^{-n} m^p s^{-1} H(10^{6}Si)$^{-1}$	2.25×10^{-15}	6.514×10^{-16}	1.5×10^{-18}	5.3301×10^{-19}
n	–	1	3.5	1	3.5
Q	kJ mol^{-1}	375	530	335	480
V	10^{-6} m^3 mol^{-1}	4	14	4	11
d	mm	5	–	5	–
p	–	3	–	3	–
C_{OH}	H(10^{6}Si)$^{-1}$	–	–	1000	1000
r	–	–	–	1	1.2

[a] A is given for a general state of stress, and was converted from a uni-axial stress (Ranalli, 1995).

conductivity ($k = 183.33$ W m^{-1} K^{-1}) is defined for the mantle to enforce the mantle adiabat of 0.25 $^{\circ}$ C km^{-1} (Pysklywec and Beaumont, 2004).

The subduction models are run using the 3 water migration schemes. Because vertical grid size varies (coarsening downwards from 1 to 7 km per element), water migration velocities are no longer constant in the elemental scheme and vary between 10 and 70 cm yr^{-1}. However, the bulk of the dehydration processes occurs in the mantle wedge and there our model has a constant mesh resolution and therefore a constant water migration velocity of 10 cm yr^{-1}. All schemes are used to investigate the evolution of models with or without the effect of bound water content on viscosity (Eq. 5.4). The sinking cylinder models showed that an efficiency factor ω of 0.1 in scheme III (Sec. 2.3) provides realistic water migration velocities. We therefore also use an efficiency factor ω of 0.1 in scheme III in the subduction models. For scheme II, two water velocities are investigated: $v_{\mathrm{f},y} = 5$ cm yr^{-1} and 10 cm yr^{-1}.

5.4.2 Subduction model results

Subduction is initiated at the weak seed by pushing the 70 Myr oceanic plate inwards, resulting in extitc.a., 15 km of advance of the interplate contact until brittle failure helps localise deformation at the trench. The slab subducts at a fairly steep angle and with a more-or-less constant sinking velocity. The hydrated portion of the slab is limited to the top 16 km, and most of the slab is dry and therefore stiff. As we discuss below, the evolution of this stiff subducting slab is affected by (de)hydration processes but not significantly.

Main dehydration occurs at two locations in the slab: at extitc.a., 150 km depth where dehydration occurs at the phase transition of blueschists to eclogite, and 210 km depth where dehydration of chlorite occurs (Figs. 5.10 and 5.11). The mantle wedge is hydrated by these dehydration reactions. Hydrated mantle wedge material is entrained by the downwards flow above the subducting slab. This can bring bound water down to the transition zone. Figure 5.10 shows that the horizontal width of hydrated mantle above the slab decreases with depth. In the wedge, i.e, above 200 km depth, the mantle can be hydrated up to a distance of 100 km away from the surface of the slab. As the slab deepens, the distance of hydrated mantle from the slab surface decreases, from 50 km at extitc.a., 200 km depth to less than 10 km at the slab tip (Fig. 5.10). Including the effects of bound water on viscosity increases the width of the hydrated mantle, BOC and SHB regions (Fig. 5.12E, G, H). The difference is however limited as the width of the hydrated regions increases by *c.a.*, 40 km towards the overriding plate.

Due to inflow of hydrated oceanic lithosphere during model evolution, the $\mathrm{OH}_{\mathrm{rms}}$ of the subducting slab increases as the model evolves (Fig. 5.12J). After 3 Myr, the $\mathrm{OH}_{\mathrm{rms}}$ of the slab decreases slightly. This represents the onset of

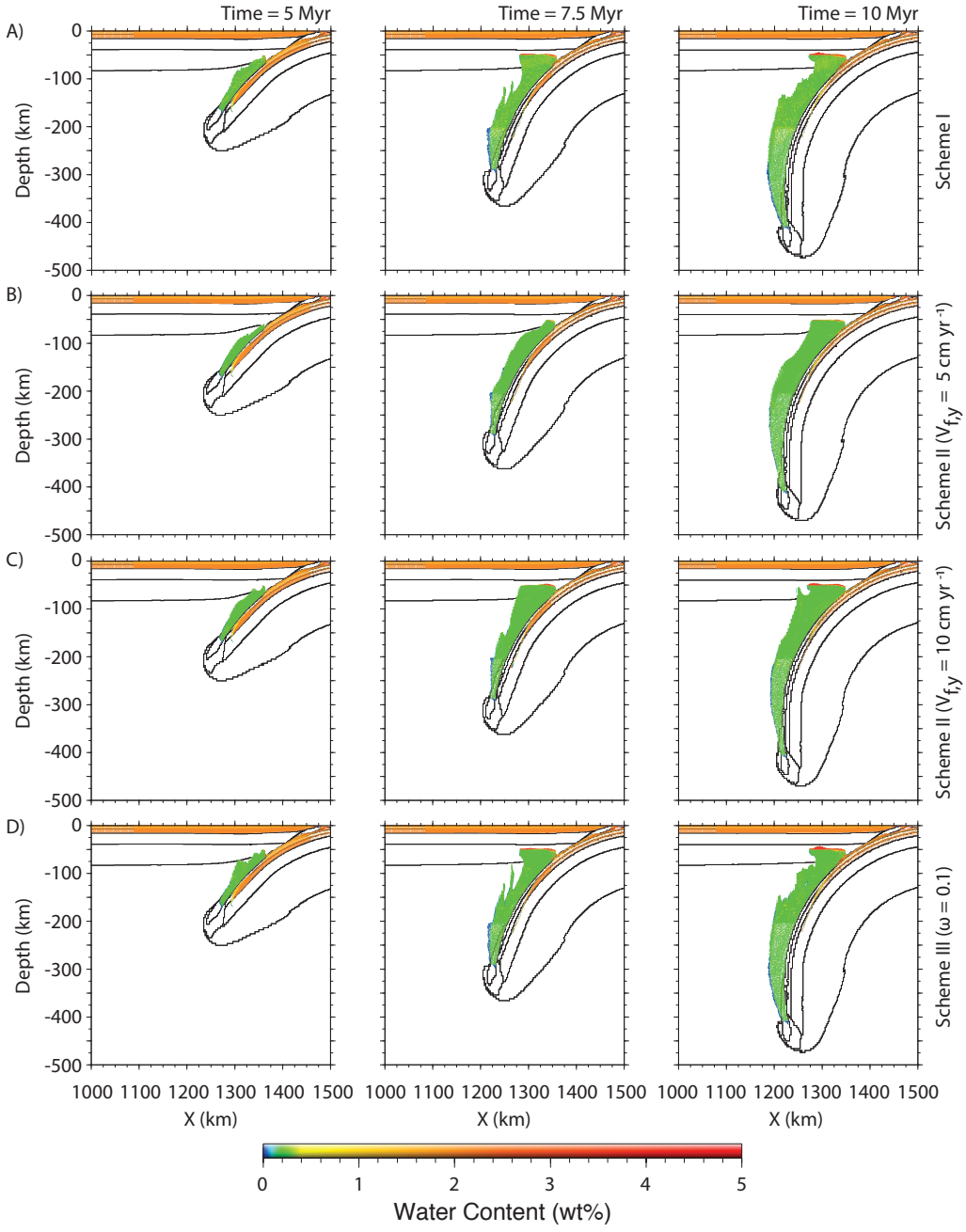


FIGURE 5.10 – Bound water distribution for subduction models after 5, 7.5 and 10 Myr for the following free water migration schemes: **(A)** Elemental water migration scheme I (velocity $v_{\mathrm{f},y}$ increases from 10 cm yr^{-1} just below the lithosphere to 70 cm yr^{-1} at the base of the model where the grid is coarsest); **(B)** imposed vertical velocity $v_{\mathrm{f},y} = 5$ cm yr^{-1} (scheme II); **(C)** imposed vertical velocity $v_{\mathrm{f},y} = 10$ cm yr^{-1} and **(D)** Darcy velocity with efficiency factor $\omega = 0.1$ (scheme III). Bound water moves with the solid phase flow. Viscosity of all materials changes with water content following the flow law of Eq. 5.4.

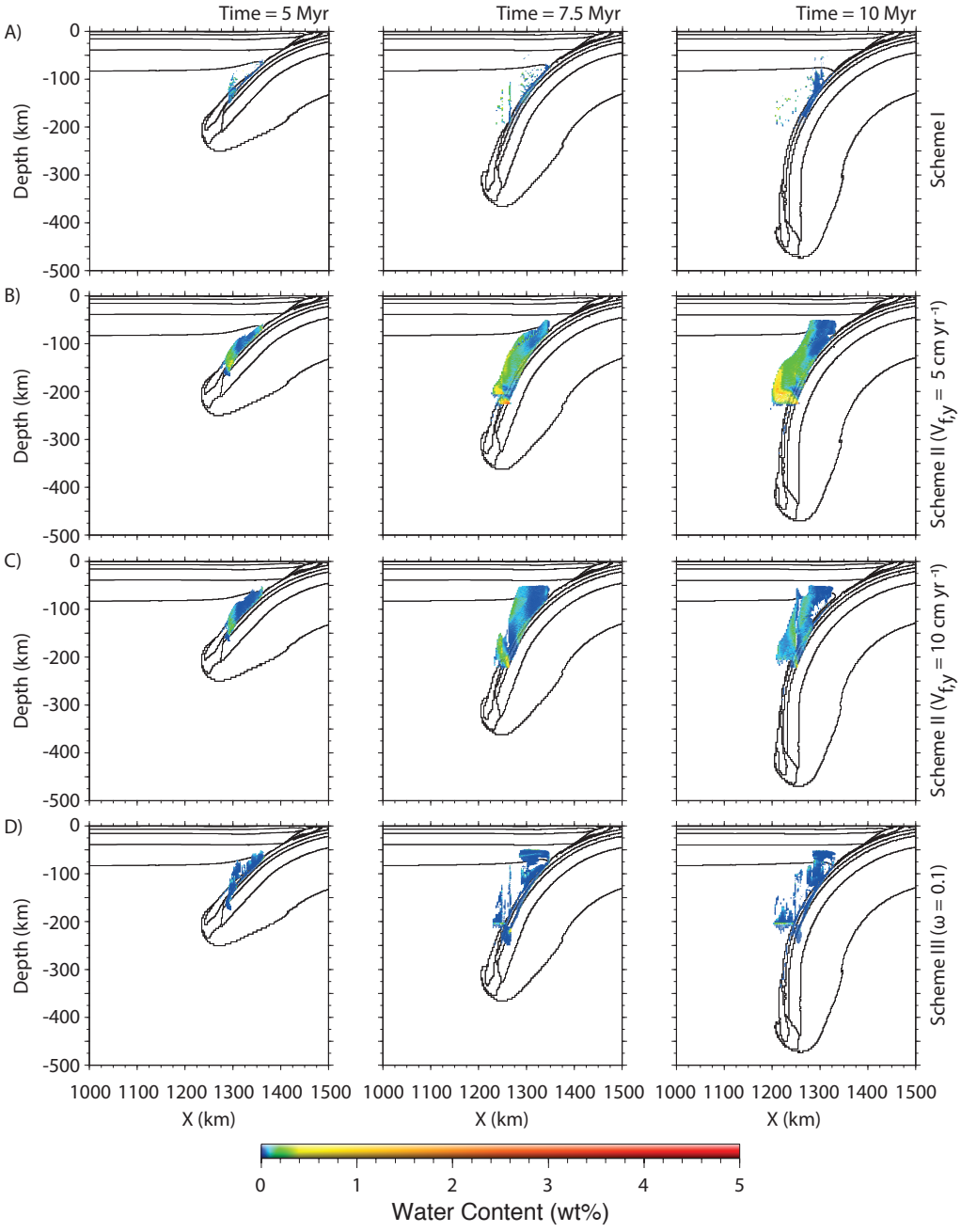


FIGURE 5.11 – Free water distribution for subduction models after 5, 7.5 and 10 Myr for the following water migration schemes: **(A)** Elemental water migration scheme I (velocity $v_{\mathrm{f},y}$ varies between 10 and 70 cm yr^{-1}); **(B)** Imposed vertical water migration scheme II with $v_{\mathrm{f},y} = 5$ cm yr^{-1}; **(C)** Imposed vertical water migration scheme II with$v_{\mathrm{f},y} = 10$ cm yr^{-1}, and **(D)** Darcy water migration scheme III with efficiency factor $\omega = 0.1$. Viscosity of all materials changes with water content following flow law of Eq. 5.4.

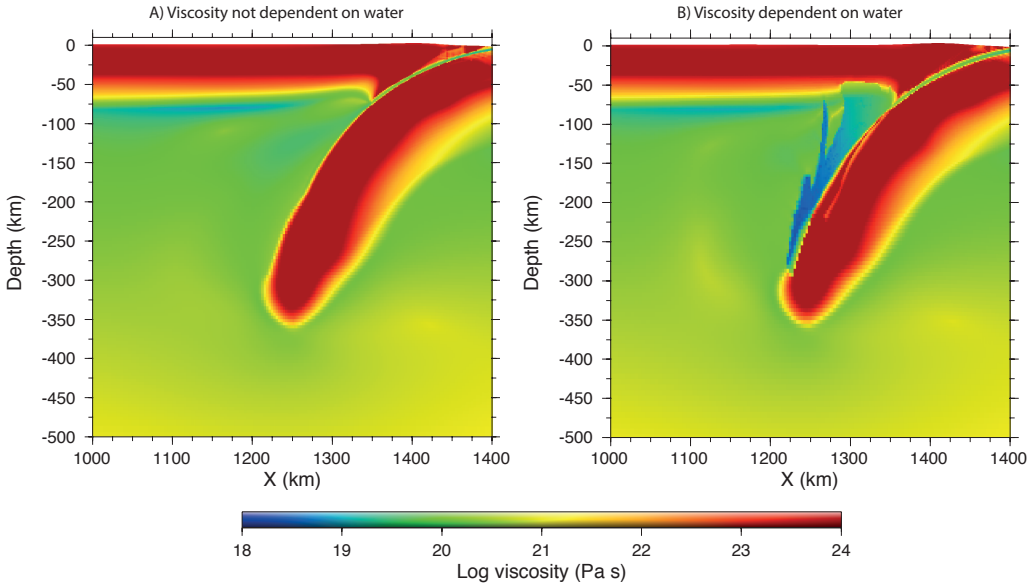


FIGURE 5.12 – Evolution of: **(A)** depth of the topmost particle of hydrated mantle; **(B)** depth of the lowermost particle of hydrated mantle; **(C)** depth of the lowermost particle of hydrated BOC; **(D)** depth of the lowermost particle of hydrated SHB for the subduction models; **(E)** horizontal coordinate of the leftmost particle of hydrated mantle; **(F)** horizontal coordinate of the rightmost particle of hydrated mantle; **(G)** horizontal coordinate of the leftmost particle of hydrated BOC; **(H)** horizontal coordinate of the leftmost particle of hydrated SHB. **(I)** mantle OH_{rms}; and **(J)** slab OH_{rms}; "visc" indicates models that have a decrease in viscosity with increasing water content.

dehydration and is synchronous to the increase in OH_{rms} of the mantle (Fig. 5.12I). The numerical water migration schemes cause small differences in the distribution of bound water in the mantle. The differences in mantle OH_{rms} between the three water migration schemes is small initially, but increases to extitc.a., 1×10^{-5} after 6 Myr and then remains constant (Fig. 5.12I). The difference corresponds to variations in the lateral distribution of hydrated mantle material (Figs. 5.10 and 5.12). Including the effects of water on the viscosity does not change the OH_{rms} of the slab (Fig. 5.12J), but increases the OH_{rms} of hydrated mantle (Fig. 5.12I). The effects on the distribution of free water are more substantial (Fig. 5.11). The distribution of free water for the elemental and Darcy schemes is similar, but the free water domain is somewhat broader, with extitc.a., 40 km (Fig. 5.11) in the Darcy models. This is caused by the horizontal component of the mantle flow that is added to the free water velocity. Larger variations occur in the free water distribution for scheme II and can result in locally large quantities of free water of up to 4 wt % H_2O (Fig. 5.11). However, in our models, free water has no effect on rheology and therefore no influence on the dynamics of the system.

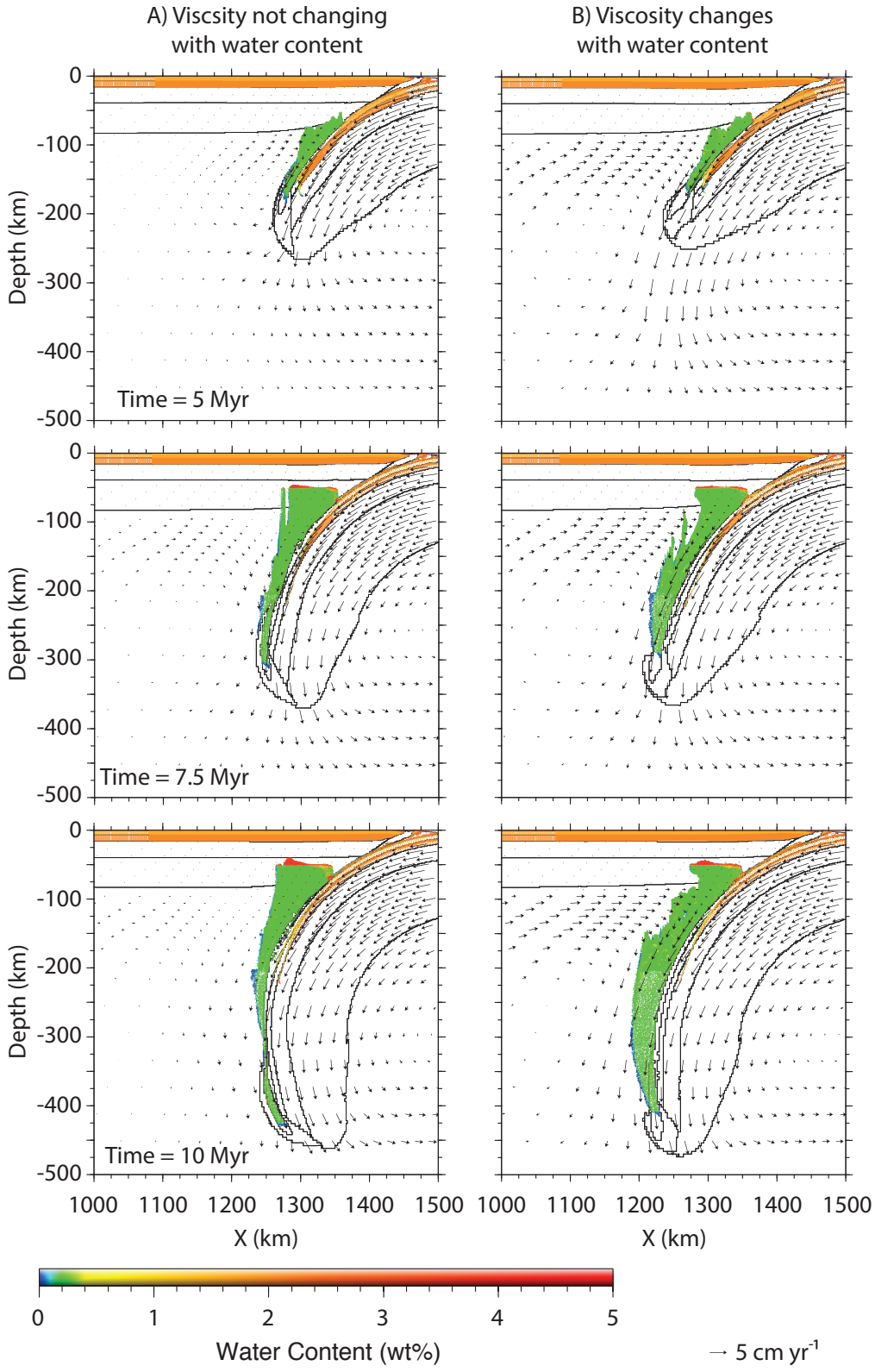


FIGURE 5.13 – Viscosity field for models that follow the Darcy free water migration scheme III with efficiency factor $\omega = 0.1$ after 7.5 Myr for: **(A)** viscosity not dependent on water content, and **(B)** viscosity decrease with water content.

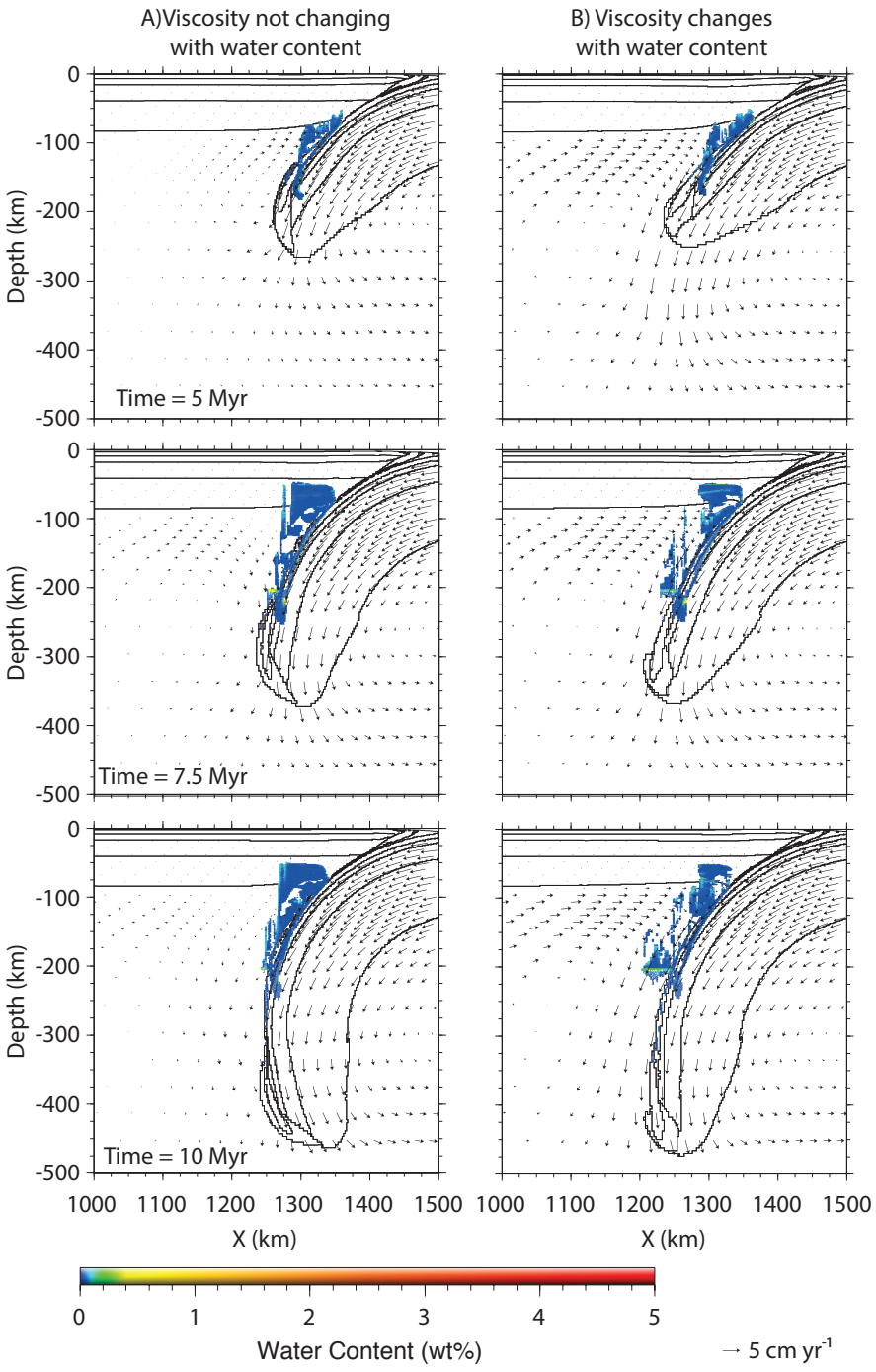


FIGURE 5.14 – Bound water distribution for subduction models using Darcy free water migration scheme III (with efficiency factor $\omega = 0.1$) at 5, 7.5 and 10 Myr. **(A)** Water content does not change viscosity; **(B)** water content decreases the viscosity (following flow law Eq. 5.4).

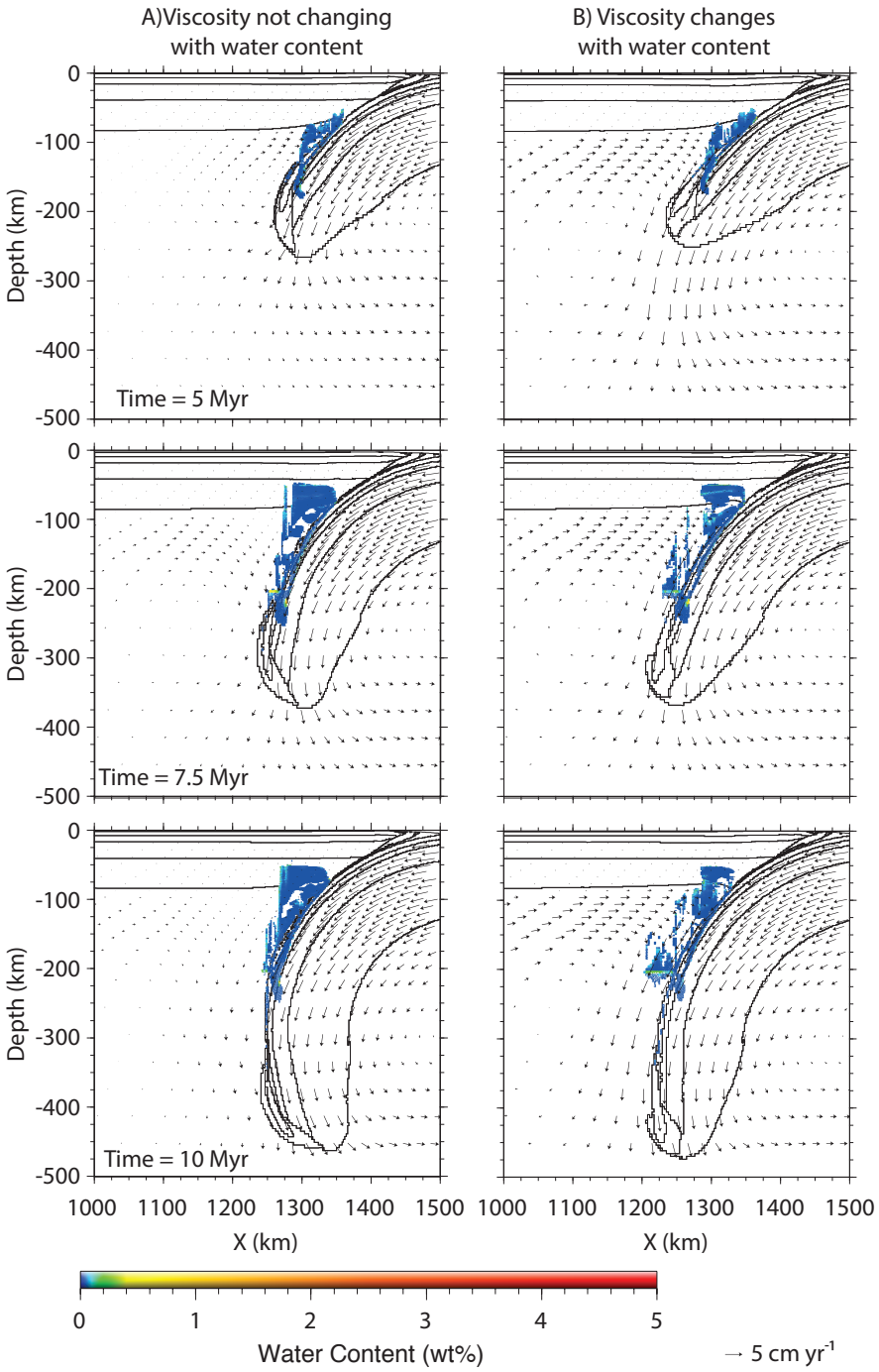


FIGURE 5.15 – Free water distribution for subduction models using the Darcy water migration scheme (with $\omega = 0.1$) at 5, 7.5 and 10 Myr. **(A)** Water content does not change viscosity; **(B)** water content decreases the viscosity (following flow law Eq. 5.4).

Introducing the effect of water content on viscosity does not have a strong impact on the large scale mechanical evolution of the model. This is because the evolution of the subducting slab is controlled by its stiffness. Due to the relatively little amount of water present in the slab (which is initially hydrated up to 16 km depth), dehydration processes will not greatly affect evolution of the already stiff slab. We do find that water weakening of viscosity increases flow in the mantle wedge and slightly reduces the curvature of the slab (Figs. 5.14 and 5.15). Corner flow is more pronounced in the models that have water-dependent viscosity as a large part of the mantle above the slab is hydrated and thus weakened, promoting stronger mantle flow.

5.4.3 Subduction model discussion

Our models show a similar slab dehydration evolution as Rüpke et al. (2004), Arcay et al. (2005) and Cagnioncle et al. (2007). This is because a similar method for determining the locations of dehydration reactions are used in these experiments. The depths at which dehydration reactions occur are slightly different between these studies because of differences in the thermal structure of the slab in the models.

We find that the overall dynamics of our subduction model is not strongly influenced by the viscosity decrease of mantle materials due to increase in water content. We suggest that this may be caused by the subducting slab being fairly stiff. Our slab is largely dry and the flow law of Hirth and Kohlstedt (2003) results in an average viscosity of extitc.a., 5×10^{23} Pa s which is up to 5 orders of magnitude above the viscosity of the mantle. The evolution of this strong slab is not greatly influenced by a further viscosity increase caused by dehydration processes. Our models do show an increase in the corner flow (Fig. 5.14) but not on the same scale as that observed in the models of Arcay et al. (2005). The slab in the models of Arcay et al. (2005) dips at a shallower angle, which could focus corner flow and cause a larger effect of water on the flow field.

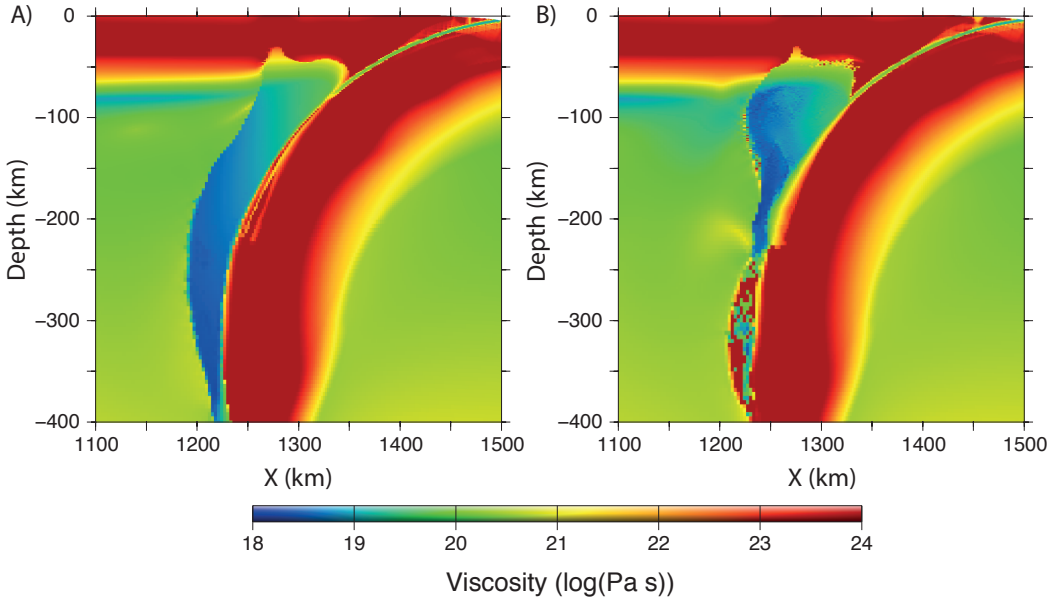


FIGURE 5.16 – Viscosity fields in the mantle wedge for subduction models calculated using the imposed free water migration scheme II with $v_{f,y} = 5$ cm yr^{-1}. **A)** Only the effects of bound water are taken into account in the viscosity calculations (using a maximum cut-off for C_{OH} of 0.4 wt % in Eq. 5.4). This is the same model as Fig. 5.10B. **B)** The effects of both bound and free water are taken into account in the viscosity calculations (using a maximum cut-off for C_{OH} of 1 wt % in Eq. 5.4).

The numerical implementation of water migration has a significant effect on the distribution of free water in the mantle wedge (Fig. 5.11). In our models, this effect is not visible in the overall evolution of the model because free water does not affect the rheology of the mantle materials. However, the distribution of free water in the mantle wedge could influence the dynamics of subduction by changing the pore pressure, thereby changing the stress, and the viscosity. Similarly, the pore pressure effect of free water could reduce the plastic yield stress, thereby reducing effective viscosities in the slab and brittle parts of the mantle wedge. During fluid flow, compaction and dilation of the solid matrix may occur, related to pore pressure effects. This could locally change the pressure field and thus in return effect water migration paths, changing the hydration patterns in the solid matrix. To obtain a first order assessment of the potential impact of free water on the rheology of our models, we calculated a scheme II water migration model with $v_{f,y} = 5$ cm yr^{-1} in which the free water content was added to the bound water content in the calculation of the creep viscosity (Eq. 5.4). As bound water in the model can locally already reach values of 2-3 wt % (Fig. 5.11), we increased the maximum value that is allowed for C_{OH} in the viscosity calculation from 0.4 wt %

to 1 wt %. In the initial stages of subduction, where only small amounts of free water are present, the difference in viscosity between the bound water viscosity model and the bound and free water viscosity model is small. However, as the model evolves and the amount of free water increases, the viscosity field changes (Fig. 5.16). Low viscosity values are localised in the mantle wedge. The amount of hydrated mantle material that reaches the bottom of the model domain is greatly reduced. This is because mantle flow is localized higher up in the mantle wedge. We emphasize that this model is a preliminary result, as the effect of free water (as opposed to bound water) on creep flow laws is not established.

In our simplified models of water migration we did not include melts. Melts are sinks that are thought to absorb most of the excess free water. This would then decrease the potential effects of free water on pore pressures. However, the resulting melt would build up pore pressure instead of a pore pressure increase that would have been caused by the now dissolved free water. Therefore, a potential weakening effect of free water on viscosity could remain. Water also decreases the temperature at which melting can occur, encouraging melting, and because melts have a low viscosity this could impact subduction dynamics. A logical next step would therefore be to include the effects of melts in our models of subduction with (de)hydration processes. Including a decrease of viscosity with water content in the models influences the bound water distribution in the mantle close to the surface of the subducting slab (Fig. 5.14). Due to the limited water absorption capabilities of the mantle and the weak mantle wedge, the flow in the mantle wedge is increased causing a further increase in the area over which the mantle is hydrated and weak. This suggests that subduction and mantle wedge studies that investigate (de)hydration processes should preferably include the dynamic effects of water on viscosity and thus mantle flow during model evolution.

We assumed that the mantle material in our models can contain up to 0.2 wt % water at upper mantle pressures and temperatures (Bercovici and Karato, 2003). We find that hydrated mantle material up to 0.2 wt % is entrained by the flow caused by the subducting slab down to the bottom of the model domain (Figs. 5.10 and 5.13). This therefore supports the initial assumptions used in the studies of slab dehydration at the transition zone (*i.e.*, between 670 and 410 km) of Richard et al. (2006, 2007). It also agrees with experimentally determined phase diagrams that suggest water could be present in the transition zone or deeper (Ohtani et al., 2004; Komabayashi et al., 2005). The amount of water reaching the transition zone could be greatly increased by including other chemical reactions in the mantle wedge, such as serpentinization (Iwamori, 1998).

We show that including the weakening effect of bound water on viscosity increases the amount of water brought down to the bottom of the model domain (Fig. 5.14). This is because the viscosity reduction causes a stronger corner flow that entrains more hydrated mantle material in the downward flow above the

subdcuting slab.

5.5 Conclusions

We have used a linear viscous model of a wet cylinder sinking in a dry mantle and a thermo-mechanical subduction model to investigate the effects of the numerical implementation of basic schemes of free water migration. We find that (de)hydration influences our models, but that the exact manner of water migration is not that important. We suggest that studies of especially large-scale subduction dynamics may use a simple implementation of free water migration to capture the first order effects of (de)hydration, as for example an imposed velocity or simple Darcy flow water migration scheme. Elemental water migration (simply moving free water up one element per time step) can be used as long as grid resolution is constant and it is realised that grid size determines the water migration velocity.

We find that the different water migration schemes influence the distribution of free water in subduction models. Elemental water migration results in a localised distribution of free water, while an imposed water migration velocity and Darcy flow result in a broader distribution of free water in the mantle wedge. This effect is caused by the free water being moved by the mantle flow in the latter migration schemes. Free water could effect pore pressure and thus material strength, but melting could decrease the amount of free water and the effect of free water on a subduction system therefore requires future study.

Including the effects of bound water content on viscosity does not strongly impact the overall evolution of the subducting slab as it is controlled by the slab stiffness. We do find that the decrease in mantle viscosity with increasing water content as slab dehydration continues, causes a more vigorous corner flow. If we assume that the upper mantle contains an average of 0.2 wt % water, this allows saturated hydrated mantle material to be transported down to the base of the upper mantle, supporting previous assumptions of hydrated material residing in the mantle transition zone.

Acknowledgements

We acknowledge financial support from the European Commission through Marie-Curie Research Training Network “c2c” (contract MRTN-CT-2006-035957). SULEC is developed jointly by Susanne Buiter and Susan Ellis. We warmly thank Zurab Chemia, Mark Caddick and James Connolly for help with Perple_X calculations and discussions on water behaviour, and Joya Tetreault for many numerical discussions. This manuscript benefitted from the constructive reviews by Manuele

Faccenda, Tobias Keller and Guillaume Richard.

Chapter 6

Discussion

As illustrated by the models in this thesis, a large number of assumptions are necessary when building a numerical model of subduction. These include numerical, geophysical and geometrical approximations that can potentially affect the dynamics of the model through time. A model setup will therefore need to be tuned to the aim of the study.

Even though subduction has been widely studied, subduction initiation is still poorly understood (Regenauer-Lieb et al., 2001; Nikolaeva et al., 2010). Because of this, the initiation phase of subduction is often bypassed in subduction models. The initial geometry of the subduction model will instead include either a heterogeneity at the interplate contact (*e.g.,* a weak seed) coupled to a kinematic driving force and/or a pre-existing portion of subducted slab. The latter can be coupled to a kinematic driving force or evolve dynamically. In this thesis, subduction was started at a weak seed, with or without a pre-existing short slab. However, the initial geometry of the subduction model may influence the geometry of the slab and control, among others, slab dip (Buiter and Ellis, 2011).

In order to allow high resolution and reasonable calculation times, the spatial size of the study area is often reduced. This then requires the use of boundary conditions. Kinematic and thermal boundary conditions approximate the mechanical and physical properties of the area outside the model domain. In chapter 3, it was shown that boundary conditions can influence model evolution and determine the final geometry of the subducted slab. We found that the location of the material inflow can control the subduction style. If the subducted slab is pushed into the model domain, the model will evolve through trench advance, and the slab will fold on the bottom boundary, forming a sideways U-shape. If instead the overriding lithosphere moves into the model domain, the slab will experience trench retreat and lie on the bottom boundary, forming an S-shape. If material inflow is symmetric, the slab subducts vertically and, assuming that the model includes a lower

mantle, could penetrate into the lower mantle. In chapter 3, the kinematic boundary conditions were defined on the lateral boundaries. It is, however, also possible to drive subduction kinematically by using a surface boundary condition (Manea and Gurnis, 2007) or an internal kinematic boundary condition (van Keken et al., 2008; Ghazian and Buiter, 2013). Alternatively, a pre-existing portion of subducted slab could generate enough slab pull to drive subduction dynamically (Enns et al., 2005; Schmeling et al., 2008; Kaus et al., 2010; Quinquis et al., 2011). Also for these models boundary conditions are important, such as whether the slab is laterally fixed to, or free from the vertical side boundary. A slab that is fixed at the vertical side will experience slab retreat and form an S-shape slab in the mantle, while a free slab will form a sideways U-shape (Enns et al., 2005; Stegman et al., 2010). Not all possible kinematic boundary conditions were tested in this thesis, nor did we investigate thermal boundary conditions. Future models could compare the effects of surface-driven, side-driven or gravitationally-driven subduction, domain size, mantle in- and outflow on upper-mantle size models.

The rheology of the subducting slab and surrounding mantle is one of outstanding challenges in numerical models of a subduction zone. In broad terms, the subduction system is composed of viscous, brittle and elastic rheologies. Different studies use different approximations for the rheological components and for their parameter values.

The rheological variations depend on the time scale of interest for the study, the tectonic setting, and the variations in laboratory measurements of rock strength. The models in this thesis did not include elasticity, as the Maxwell relaxation time of our experiments is on the order of 10 to 100 years and therefore much smaller than our observation time-scale of 20 Myrs.

The implementation of brittle behaviour may also influence the dynamics of a numerical subduction zone. A von Mises yield criterion results in the same brittle strength with depth, whereas a Drucker-Prager yield criterion is depth-dependent and will increase the strength of the slab at depth while keeping the top part of the lithosphere weak. This helps to localise deformation at the interplate boundary and facilitate subduction. Brittle behaviour can also include strain weakening and hardening. Strain weakening will reduce the strength of the material once it has yielded and helps to localise deformation, while strain hardening will increase the strength of the material once it has yielded, dispersing deformation. In this thesis (chapters 4 and 5) strain weakening was used in order to help localise deformation at the interplate boundary. Shear heating was not included in our models. However, it can influence the rheology of a subduction zone by locally increasing temperature, and reducing viscosity. This could also have an effect on the chemical evolution of the model.

In chapter 4 we showed that it is sometimes possible to reproduce the evolution of a model with a non-newtonian visco-plastic rheology by a model with only

linear viscous rheologies, or simplified brittle criterions and creep mechanisms. However, this requires testing in order to find values that reproduce the dynamics of depth-dependent rheologies. The models in this thesis did not include Peierls creep. This creep mechanism is a stress limiting yield viscosity and could reduce the strength of the subducting lithosphere in our models at depth and thereby change the geometry of the slab (Kameyama et al., 1999; Čížková et al., 2002; Gorczyk et al., 2007b).

Subduction zones are heterogeneous structures (Poli and Schmidt, 2002). In this thesis a simplified three-layered petrological model of the subducting plate was used. While this is an improvement over many existing models, we did not test the effects of the chemical composition of the mantle on the temperature profile and the viscosity of the mantle. The exothermic phase transition at 410 km and the endothermic phase transition at 670 km depth were not included into our models. These phase changes can influence the geometry of the slab at depth and facilitate the penetration of the slab into the lower mantle (Čížková et al., 2002). Slab and mantle rheologies are also affected by other parameters than pressure or temperature. These include grain size reduction (Warren and Hirth, 2006), water content (Billen and Hirth, 2007) and melt content. The presence of fluids, both H_2O and CO_2, in a subduction zone influences the dynamics of subduction as they lower the strength of the material (Rüpke et al., 2004; Connolly, 2005; Arcay et al., 2006; Cagnioncle et al., 2007; Iwamori, 2007b; Faccenda et al., 2012). In chapter 5 we focussed on the effects of water, ignoring the influence of melts and carbonates in order to keep the models as simple as possible. In existing models, the method used to numerically approximate the mechanism of free water migration is not unique (Arcay et al., 2006; Cagnioncle et al., 2007; Faccenda et al., 2012; Gorczyk et al., 2007a; Rüpke et al., 2004). We tested different methods of implementing the migration of free water and showed that the migration mechanism will not influence the spatial distribution of bound water to a large degree but can influence the spatial distribution of free water. Free water and melts will influence the rheology of the subduction system (Hirth and Kohlstedt, 1996) and these could be avenues to investigate in future models.

We hope that the series of numerical model setups of subduction zones in this thesis can be used by other numerical modellers to start their investigation of subduction dynamics.

Chapter 7

Conclusions

Numerical modelling of subduction is a process in continuous development. The better the dynamics and physics of the subduction system are understood, the more parameters will be introduced into models. This is made feasible by the continuous increase in computer capabilities that provides the possibility to use complex and detailed rheologies and increase the number of parameters and resolution of the models. The models in the thesis were run in 2-D. This provides reasonable information on the dynamics of a subduction system in two spatial directions. However, in order to study the mechanisms of subduction laterally along-strike of geological structure, 3-D models are necessary. The models in this thesis have shown how modelling assumptions can propagate into model evolution. Specifically, the roles of boundary conditions, rheology, and free water migration were investigated.

In chapter 3 of this thesis, we showed how assumptions made in the initial steps of building a numerical model of subduction can affect the geometry and dynamics of the system in later model stages. Kinematic boundary conditions may determine whether the trench advances or retreats and whether the slab lies forward on the bottom of the model domain or folds on itself. In chapter 3 we also demonstrated that the free surface top boundary condition of a 2-D model can be approximated by a free-slip boundary if this is combined with a weak crustal layer. The weak layer allows the subducting slab to decouple from the free-slip surface boundary and subduct. A free-slip boundary condition is numerically easier to implement as it does not require remeshing for Eulerian methods nor the use of stabilizing algorithms to suppress numerical instabilities at density interfaces. However, free-slip surfaces do not allow the development of topography and the weak crust can over-lubricate the interplate contact.

In chapter 4 the influence of the rheology of the subduction system was investigated. We showed that simple, linear viscous rheologies give results within 10% error of each other regardless of the numerical method or software used.

Increasing the complexity of the model rheologies, increases the variability in the results. We find that it can be difficult to simplify a model setup by averaging rheological parameters over large domains, such as the pressure-dependent parts of viscous or brittle material behaviour. Approximating a depth-dependent brittle behaviour with a constant yield criterion requires unrealistically high values for the von Mises yield criterion in order to reproduce the dynamics of a model using the Drucker-Prager yield criterion.

The effects of free water migration schemes on water distribution and subduction dynamics were studied in chapter 5. We find that for equidistant grids, water migration could in many cases be simplified to a basic vertical element-wise migration and produce similar results as more complex Darcy-type flow. The spatial distribution of bound water is not greatly affected by the water migration scheme, but the free water distribution does differ. However, the effect of free water on rheology is little understood at mantle depths. Future work could focus on the effects of free water on the rheology of the upper mantle and investigate the combined roles of bound and free water on subduction zone dynamics.

In this thesis, we have attempted to provide the numerical modelling community with a series of detailed model setups, that consist of datasets and geometries. These can be used as a starting point for future subduction models, or to test the behaviour of numerical codes. Future models could, for example, explore aspects of subduction, such as, the inclusion of phase changes, shear heating, melts, and the effects of free water on mantle rheology.

References

Abers, G. A., van Keken, P. E., Kneller, E. A., Ferris, A., and Stachnik, J. C. (2005). The thermal structure of subduction zones constrained by seismic imaging: Implications for slab dehydration and wedge flow. *Phys. Earth Planet. Int.*, 241:387–397.

Albarède, F. (1995). *Introduction to geochemical modeling*. Cambridge Univ. Press, Cambridge.

Amestoy, P. R., Duff, I. S., Koster, J., and L'Excellent, J.-Y. (2001). A fully asynchronous multifrontal solver using distributed dynamic scheduling. SIAM *Journal of Matrix Analysis and Applications*, 23(1):15–41.

Amestoy, P. R., Guermouche, A., L'Excellent, J.-Y., and Pralet, S. (2006). Hybrid scheduling for the parallel solution of linear systems. *Parallel Computing*, 32(2):136–156.

Andersen, T. B. (1993). The role of extensional tectonics in the caledonides of south norway: Discussion. *Nova*, 3:303–310.

Andersen, T. B. (1998). Extensional tectonics in the caledonides of southern norway, an overview. *Tectonophysics*, 285(3-4):333–351.

Andersson, J. O., Helander, T., Höglund, L., Shi, P., and Sundman, B. (2002). Thermo-Calc & DICTRA, computational tools for materials science. CALPHAD, 26:273–312.

Arcay, D., Doin, M.-P., and Tric, E. (2007). Slab surface temperature in subduction zones: Influence of the interplate decoupling depth and upper plate thinning processes. *Earth Planet. Sci. Lett.*, 225:324–338.

Arcay, D., Doin, M.-P., Tric, E., Bousquet, R., and De Capitani, C. (2006). Overriding plate thinning in subduction zones: Localized convection induced by slab dehydration. *Geochem. Geophy. Geosys.*, 7:Q02007.

Arcay, D., Tric, E., and Doin, M.-P. (2005). Numerical simulations of subduction zones - effect of slab dehydration on the mantle wedge dynamics. *Phys. Earth Planet. In.*, 149(1-2):133–153.

Bale, C. W., Chartrand, P., Degterov, S. A., Eriksson, G., Hack, K., Ben Mahfoud, R., Melancon, J., Pelton, A. D., and Petersen, S. (2002). FactSage thermomechanical software and databases. CALPHAD, 26:189–228.

Bangerth, W., Hartmann, R., and Kanschat, G. (2007). deal.II - a general purpose object oriented finite element library. *ACM Transactions on Mathematical Software*, 33(4):24/1–24/27.

Bangerth, W. and Heister, T. (2013). ASPECT*: Advanced Solver for Problems in Earth's ConvecTion*. Texas A&M University/Computational Infrastructure in Geodynamics.

Bebout, G. E. (2007). Metamorphic chemical geodynamics of subduction zones. *Earth Planet. Sci. Lett.*, 260:373–393.

Bercovici, D. and Karato, S.-I. (2003). Whole mantle convection and the transition-zone water filter. *Nature*, 425:39–44.

Bercovici, D., Ricard, Y., and Schubert, G. (2001). A two-phase model for compaction and damage 1. general theory. *J. Geophys. Res*, 106:8887–8906.

Berman, R. G. (1988). Internally consistent thermodynamic data for minerals in the system Na_2O-K_2O-CaO-MgO-FeO-Fe_2O_3-Al_2O_3-SiO_2-TiO_2-H_2O-CO_2. *J. Petrol.*, 29:445–522.

Berman, R. G., Brown, T. H., and Perkins, E. H. (1987). Geo-Calc: Software package for calculation and display of pressure-temperature-composition phase diagrams using an IBM or compatible personal computer. *Comput. Geosci.*, 14:279–290.

Biino, G. G. and de Capitani, C. (1995). Equilibrium assemblage calculations: a new approach to metamorphic petrology. *Bollettino Museo Regionale Di Scienze Naturali Supplemento*, 13:11–53.

Billen, M. I. (2008). Modeling the dynamics of subducting slabs. *Annu. Rev. Earth Pl. Sc.*, 36:325–356.

Billen, M. I. and Gurnis, M. (2001). A low viscosity wedge in subduction zones. *Earth Planet. Sci. Lett.*, 193(1–2):227–236.

Billen, M. I. and Hirth, G. (2007). Rheologic controls on slab dynamics. *Geochem. Geophys. Geosyst.*, 8.

Blankenbach, B., Busse, F., Christensen, U., Cserepes, L., Gunkel, D., Hansen, U., Harder, H., Jarvis, G., Koch, M., Marquart, G., Moore, D., Olson, P., Schmeling, H., and Schnaubelt, T. (1989). A benchmark comparison for mantle convection codes. *Geophys. J. Int.*, 98(1):23–38.

Bolfan-Casanova, N., Keppler, H., and Rubie, D. C. (2000). Water partitioning between nominally anhydrous minerals in the mgo–sio2–h2o system up to 24 gpa: implications for the distribution of water in the earth's mantle. *Earth Planet. Sci. Lett.*, 182:209–221.

Branlund, J. M., Regenauer-Lieb, K., and Yuen, D. A. (2001). Weak zone formation for initiating subduction from thermo-mechanical feedback of low-temperature plasticity. *Earth Planet. Sci. Lett.*, 190:237–250.

Brown, T. H. and Skinner, B. J. (1974). Theoretical prediction of equilibrium phase assemblages in multicomponent systems. *Am. J. Sci.*, 274:961–986.

Buiter, S. J. H. and Ellis, S. M. (2010). The initiation of subduction models. Abstract D141B-06 presented at 2010 Fall Meeting, AGU, San Francisco, Calif., 13-17 Dec.

Buiter, S. J. H. and Ellis, S. M. (2011). The role of the initiation phase in numerical subduction models. In *Geophysical Research Abstracts*, volume 13, pages EGU2011–7654–1.

Buiter, S. J. H. and Ellis, S. M. (2012). Benchmarking a new ALE finite-element code. In *Geophysical Research Abstracts*, volume 14, pages EGU2012–7528.

Bürgmann, R. and Dresen, G. (2008). Rheology of the lower crust and upper mantle: Evidence from rock mechanics, geodesy, and field observations. *Annu. Rev. Earth Pl. Sc.*, 36:531–567.

Burkett, E. R. and Billen, M. I. (2009). Dynamics and implications of slab detachment due to ridge-trench collision. *J. Geophys. Res.*, 114(B12):B12402.

Burov, E., Jolivet, L., Le Pourhiet, L., and Poliakov, A. (2001). A thermomechanical model of exhumation of high pressure (HP) and ultra-high pressure (UHP) metamorphic rocks in Alpine-type collision belts. *Tectonophysics*, 342:113–136.

Burov, E. and Toussaint, G. (2007). Surface processes and tectonics of continental subduction and deep processes. *Global Planet. Change*, 58:141–164.

Burov, E. and Watts, A. B. (2006). The long-term strenght og the continental lithosphere; “jelly sandwich” or “crème brûlée”. *GSA Today*, 16(1).

Caddick, M. J. and Thompson, A. B. (2008). Quantifiying the tectono-metamorphic evolution of pelitis rocks from a wide rande of tectonic settings: Mineral compositions in equilibrium. *Contrib. Mineral. Petrol.*, 156:177–195.

Cagnioncle, A.-M., Parmentier, E., and Elkins-Tanton, L. (2007). Effect of solid flow above a subducting slab on water distribution and melting at convergent plate boundaries. *J. Geophys. Res.*, 112:B09402.

Capitanio, F. A., Morra, G., and Goes, S. (2007). Dynamic models of downgoing plate-boundary driven subduction: Subduction motions and energy dissipation. *Earth Planet. Sci. Lett.*, 262:284–297.

Capitanio, F. A., Morra, G., and Goes, S. (2009). Dynamics of plate bending at the trench and slab plate coupling. *Geochem. Geophy. Geosys.*, 10:Q04002.

Capitanio, F. A., Stegman, D. R., Moresi, L. N., and Sharples, W. (2010). Upper plate controls on deep subduction, trench migrations and deformations at convergent margins. *Tectonophysics*, 483:80–92.

Cemic, L. (2005). *Thermodynamics in Mineral Sciences: An Introdution*. Springer.

Cheadle, M. J., Elliott, M. T., and McKenzie, D. (2004). Percolation threshold and permeabiliy of crystallizing igneous rocks: The importance of textural equilibrium. *Geology*, 32(9757–760).

Chemia, Z., Dolejš, D., and Steinle-Neumann, G. (2010). Thermal effects of metamorphic reactions in a three component slab. Geophys. Res. Abstracts 12, EGU2010-5768.

Chopin, C. (1984). Coesite and pure pyrope in high-grade blueschists of the Western Alps, a first record and some consequences. *Contrib. Mineral. Petrol.*, 86:107–118.

Christensen, U. R. (1996). The influence of trench migration on slab penetration into the lower mantle. *Earth Planet. Sci. Lett.*, 140:27–39.

Churakov, S. and Gottschalk, M. (2003a). Perturbation theory based equation of state for polar molecular fluid: I. pure fulds. *Geochim. Cosmochim. Ac.*, 67:2397–2414.

Churakov, S. and Gottschalk, M. (2003b). Perturbation theory based equation of state for polar molecular fluid: II. fluid mixtures. *Geochim. Cosmochim. Ac.*, 67:2415–2425.

Clark, S., Stegman, D. R., and Müller, D. (2008). Episodicity in back-arc tectonic regimes. *Phys. Earth Planet. In.*, 171:265–279.

Connolly, J. A. D. (2005). Computation of phase equilibria by linear programming: A tool for geodynamic modeling and its application to subduction zone decarbonation. *Earth Planet. Sci. Lett.*, 236:524–541.

Connolly, J. A. D. and Kerrick, D. M. (1987). An algorithm and computer program for calculating composition phase diagrams. CALPHAD, 11:1–55.

Connolly, J. A. D. and Petrini, K. (2002). An automated strategy for calculation of phase diagram sedtions an retrieval of rock porperties as a function of physical conditions. *J. Metamorphic Geol.*, 20(697–708).

Culling, W. E. H. (1960). Analytical theory of erosion. *J. Geol.*, 68:336–344.

Cuvelier, C., Segal, A., and van Steenhoven, A. A. (1986). *Finite Element Methods and Navier-Stokes Equations*. D. Reidel Publishing Compagny.

de Capitani, C. and Brown, T. H. (1987). The computation of chemical equilibriumin complex systmes containing non-ideal solutions. *Geochim. Cosmochim. Ac.*, 51:2639–2652.

DeMets, C., Gordon, R. G., Argus, D. F., and Stein, S. (1994). Effect of recent revisions to the geomagnetic reversal time scale on estimates of current plate motions. *Geophys. Res. Lett.*, 21:2191–2194.

Deschamps, F., Tackley, P. J., and Nakagawa, T. (2010). Temperature and heat flux scalings for isoviscous thermal convection in spherical geometry. *Geophys. J. Int.*, pages 137–154.

Di Giuseppe, E., Faccenna, C., Funiciello, F., van Hunen, J., and Giardini, D. (2009). On the relation between trench migration, seafloor age, and the strength of the subducting lithosphere. *Lithos*, 1(2):121.

Di Giuseppe, E., van Hunen, J., Funiciello, F., Faccenna, C., and Giardini, D. (2008). Slab stiffness control of trench motion: Insights from numerical models. *Geochem. Geophy. Geosys.*, 9(2):Q02014.

Duretz, T., Gerya, T. V., and May, D. A. (2011). Numerical modelling of spontaneous slab breakoff and subsequent topographic response. *Tectonophysics*, 502(1-2):244–256.

Ebel, D. S., Ghiorso, M. S., Sack, R., and Grossman, L. (2000). Gibbs energy minimization in gas + liquid + solid systems. *J. Comput. Chem.*, 21:247–256.

England, P., Engdahl, R., and Thatcher, W. (2004). Systematic variation in the depths of slabs beneath arc volcanoes. *Geophys. J. Int.*, 156:337–408.

Enns, A., Becker, T. W., and Schmeling, H. (2005). The dynamics of subduction and trench migration for viscosity stratification. *Geophys. J. Int.*, 160:761–775.

Eriksson, G. (1971). Thermodynamic studies of high temperature equilibria. III. SOLGAS, a computer program for calculating the composition and heat condition of an equilibrium mixture. *Acta Chem. Scand.*, 25:2651–2658.

Eriksson, G. and Hack, K. (1990). ChemSage - a computer program for the calculation of complex chemical equilibria. *Metall. Trans.*, 21B:1013–1023.

Eriksson, G. and Rosén, E. (1973). Thermodynamic studies of high temperature equilibria. VIII. general equations for the calculation of equilibria in mulphase systems. *Chem. Scripta*, 4:193–194.

Fabrichnaya, O. B. (1999). The phase relations in the FeO-MgO-Al_2O_3-SiO_2 system: assessement of thermodynamic properties and phase equilibria at pressure up to 30 GPa. CALPHAD, 23:19–67.

Faccenda, M., Burlini, L., Gerya, T. V., and Mainprice, D. (2008a). Fault-induced seismic anisotropy by hydration in subducting oceanic plates. *Nature*, 455:1097–1100.

Faccenda, M., Gerya, T. V., and Chakraborty, S. (2008b). Styles of post-subduction collisional orogeny: Influence of convergence velocity, crustal rheology and radiogenic heat production. *Lithos*, 103:257–287.

Faccenda, M., Gerya, T. V., Mancktelow, N. S., and Moresi, L. (2012). Fluid flow during slab unbending and dehydration: Implications for intermediate-depth seismicity, slab weakening and deep water recycling. *Geochem. Geophy. Geosys.*, 13(1).

Faccenna, C., Di Giuseppe, E., Funiciello, F., Lallemand, S., and van Hunen, J. (2009). Control of seafloor aging on the migration of the Izu-Bonin-Mariana trench. *Earth Planet. Sci. Lett*, 288:386–398.

Faccenna, C., Funniciello, F., Giardini, D., and Lucente, P. (2001). Episodic back-arc extension during restricted mantle convection in the central mediterranean. *Earth Planet. Sci. Lett.*, 187:105–116.

Faul, U. H. and Jackson, I. (2007). Diffusion creep of dry, melt-free olivine. *J. Geophys. Res.*, 112(B4):B04204.

Férot, A. and Bolfan-Casanova, N. (2012). Water storage capacity in olivine and pyroxene to 14 gpa: Implications for the water content of the earth's upper mantle and nature of seismic discontinuities. *Earth Planet. Sci. Lett.*, 349–350:218–230.

Fraser, D. (1977). *Thermodynamics in Geology*. NATO Science Series: C. Kluwer Academic Publishers.

Fujita, K. and Ogawa, M. (2013). A preliminary numerical study on water-circulation in convecting mantle with magmatism and tectonic plates. *Phys. Earth Planet. Int.*, 216:1–11.

Fullsack, P. (1995). An arbitrary Lagrangian-Eulerian formulation for creeping flows and its application in tectonic models. *Geophys. J. Int.*, 120(1):1–23.

Funiciello, F., Faccenna, C., Giardini, D., and Regenauer-Lieb, K. (2003a). Dynamics of retreating slabs: 2 insights from three dimensional laboratory experiments. *J. Geophys. Res.*, 108(B4).

Funiciello, F., Faccenna, C., Heuret, A., Lallemand, S., Di Giuseppe, E., and Becker, T. W. (2008). Trench migration, net rotation and slab–mantle coupling. *Earth Planet. Sci. Lett.*, 271(1-4):233–240.

Funiciello, F., Moroni, M., Piromallo, C., Faccenna, C., Cenedese, A., and Bui, H. A. (2006). Mapping mantle flow during retreating subduction: Laboratory models analyzed by feature tracking. *J. Geophys. Res.*, 111(B3):B03402.

Funiciello, F., Morra, G., Regenauer-Lieb, K., and Giardini, D. (2003b). Dynamics of retreating slabs: 1. insights from two-dimensional numerical experiments. *J. Geophys. Res.*, 108(B4):2206.

Gee, M. W., Siefert, C. M., Hu, J. J., Tuminaro, R. S., and Sala, M. G. (2006). ML 5.0 smoothed aggregation user's guide. Tech. Rep. 2006-2649, Sandia National Laboratories.

Gerya, T. V., Connolly, J. A. D., and Yuen, D. A. (2008). Why is terrestrial subduction one-sided? *Geology*, 36(1):43–46.

Gerya, T. V., Connolly, J. A. D., Yuen, D. A., Gorczyk, W., and Capel, A. M. (2006). Seismic implications of mantle wedge plumes. *Phys. Earth Planet. Int.*, 156:59–74.

Gerya, T. V. and Stöckhert, B. (2002). Exhumation rates of high pressure metamorphic rocks in subduction channels: the effect of rheology. *Geophys. Res. Lett.*, 29:4.

Gerya, T. V. and Stöckhert, B. (2006). Two-dimensional numerical modelling of tectonic and metamorphic history at active continental margins. *Int. J. Earth Sci.*, 95:250–274.

Gerya, T. V., Stöckhert, B., and Perchuk, A. L. (2002). Exhumation of high pressure metamorphic rocks in a subduction channel: a numerical simulation. *Tectonics*, 21(6):19.

Gerya, T. V. and Yuen, D. A. (2003). Characteristics-based marker-in-cell method with conservative finite-differences schemes for modeling geological flows with strongly variable transport properties. *Phys. Earth Planet. Int.*, 140:293–318.

Gerya, T. V. and Yuen, D. A. (2007). Robust characteristics method for modelling multiphase visco-elasto-plastic thermo-mechanical problems. *Phys. Earth Planet. In.*, 163:83–105.

Gerya, T. V., Yuen, D. A., and Maresch, W. V. (2004). Thermomechanical modelling of slab detachment. *Earth Planet. Sci. Lett.*, 226:101–116.

Ghazian, R. K. and Buiter, S. J. H. (2013). A numerical investigation of continental collision styles. *Geophys. J. Int.*, 193:1133–1152.

Ghiorso, M. S. (1994). Algorithms for the estimation of phase stability in heterogeneous thermodynamic systems. *Geochim. Cosmochim. Ac.*, 58(5489–5501).

Ghiorso, M. S., Hirschmann, M. M., Reiners, P. W., and Kress, V. C. (2002). The pMELTS: A revision of MELTS for improved calculation of phase relations and major element partitioning related to partial melting of the mantle to 3 GPa. *Geochem. Geophy. Geosys.*, 3(5):35pp.

Ghiorso, M. S. and Sack, R. (1995). Chemical mass transfer in magamtic processes. IV. a revised and internally consistent thermodynamic model for the interpolation and extrapolation of liquid-solid equilibria in magmatic systems at elevated temperatures and pressures. *Contrib. Mineral. Petrol.*, 119:197–212.

Gibbs, W. (1878). On the equilibrium of heterogeneous substances. *Transaction of the Connecticut Academy*, III:108–248, 343–524.

Giunchi, C. and Ricard, Y. (1999). High-pressure/low-temperature metamorphism and the dynamics of an accretionary wedge. *Geophys. J. Int.*, 136:620–628.

Goes, S., Capitanio, F. A., and Morra, G. (2008). Evidence of lower-mantle slab penetration phases in plate motions. *Nature*, 451(7181):981–984.

Goes, S., Capitanio, F. A., Morra, G., Seton, M., and Giardini, D. (2011). Signatures of downgoing plate-buoyancy driven subduction in cenozoic plate motions. *Phys. Earth Planet. In.*, 184(1-2):1–13.

Gorczyk, W., Gerya, T. V., Connolly, J. A. D., and Yuen, D. A. (2007a). Growth and mixing dynamics of the mantle wedge plumes. *Geology*, 35:587–590.

Gorczyk, W., Gerya, T. V., Connolly, J. A. D., Yuen, D. A., and Rudolph, M. (2006). Large-scale rigid-body rotation in the mantle wedge and its implication for seismic tomography. *Geochem. Geophy. Geosys.*, 7:Q05018.

Gorczyk, W., Willner, A. P., Gerya, T. V., Connolly, J. A. D., and Burg, J.-P. (2007b). Physical controls of magmatic productivity at pacific-type convergent margins: Numerical modelling. *Phys. Earth Planet. In.*, 163:209–232.

Gordon, T. (1992). Generalized thermobarometry: Solution of the inverse chemical equilibrium problem using data for individual species. *Geochim. Cosmochim. Ac.*, 56:1793–1800.

Gottschalk, M. (1997). Internally consistent thermodynamic data for minerals in the system SiO_2-TiO_2-Al_2O_3-Fe_2O_3-CaO-MgO-FeO-K_2O-Na_2O-H_2O-CO_2. *Eur. J. Mineral.*, 9(175–223).

Guermond, J.-L., Pasquetti, R., and Popov, B. (2011). Entropy viscosity method for nonlinear conservation laws. *J. Comput. Phys.*, 230:4248–4267.

Guillot, S., Garzanto, E., Baratoux, D., Marquer, D., Mahego, G., and de Sigoyer, J. (2003). Reconstructing the total shortening history of the nw himalaya. *Geochem. Geophy. Geosys.*, 4:22.

Guillou-Frottier, L., Buttles, J., and Olson, P. (1995). Laboratory experiments on the structure of subducted lithosphere. *Earth Planet. Sci. Lett.*, 133:19–34.

Gurnis, M., Eloy, C., and Zhong, S. (1996). Free-surface formulation of mantle convection - ii. implication for subduction-zone observables. *Geophys. J. Int.*, 127(3):719–727.

Gurnis, M. and Hager, B. H. (1988). Controls on the structure of subducted slabs. *Nature*, 335:317–322.

Hacker, B. R., Abers, G. A., and Peacock, S. M. (2003). Subduction factory: 1. theoretical mineralogy, density, seismic wave speeds, and h_2o content. *J. Geophys. Res.*, 108(B1):2029.

Hacker, B. R., Andersen, T. B., Johnston, S., Kylander-Clark, A. R. C., Peterman, E. M., Walsh, E. O., and Young, D. (2010). High-temperature deformation during continental-margin subduction & exhumation: The ultrahigh-pressure western gneiss region of norway. *Tectonophysics*, 480(1-4):149–171.

Hager, B. H. and Clayton, R. W. (1989). Constraints on the structure of mantle convection using seismic observations, flow models, and the geoid. In Peltier, W. R., editor, *Mantle Convection, Plate Tectonics and Global Dynamics*, pages 657–763. Gordon and Breach, Newark, N.J.

Hampel, A. and Pfiffner, A. (2006). Relative importance of trenchward upper plate motion and friction along the plate interface for the topographic evolution of mountain belts. In Buiter, S. J. H. and Schreurs, G., editors, *Analogue and Numerical Modelling of Crustal-Scale Processes*, volume 253, pages 105–115. Geological Society of London, Special Publications.

Han, L. and Gurnis, M. (1999). How valid are dynamic models of subduction and convection when plate motions are prescribed. *Phys. Earth Planet. In.*, 110:235–246.

Handin, J. (1969). On the Coulomb-Mohr failure criterion. *J. Geophys. Res.*, 74:5343–5348.

Handy, M., Hirth, G., and Bürgmann, R. (2007). *Continental fault structure and rheology from the frictional-to-viscous transition downward*, chapter 6. MIT press., Cambridge Mass.

Haskell, N. A. (1935). The motion of a viscous fluid under a surface load. *J. Appl. Phys.*, 6:265–270.

Hawkesworth, C. J., Turner, S. P., McDermott, F., Peate, D. W., and van Calstern, P. (1997). U-Th isotopes in arc magas: Implications for element transfer from the subducted crust. *Science*, 276:551–555.

Helgeson, H. C., Delany, J. M., Nesbitt, H. W., and Bird, D. K. (1978). Summary and critique of the termodynamic properties of rock-forming minerals. *Science*, 278A:1–229.

Hensen, C., Wallmann, K., Schmidt, M., Ranero, C., and Suess, E. (2004). Fluid expulsion related to mud extrusion off costa rica: A window to the subducting slab. *Geology*, 32:201–204.

Heuret, A., Funiciello, F., Faccenna, C., and Lallemand, S. (2007). Plate kinematics, slab shape and back-arc stress: A comparison between laboratory models and current subduction zones. *Earth Planet. Sci. Lett.*, 256:473–483.

Hirschmann, M. M. (2006). Water, melting, and the deep earth h_2o cycle. *Annu. Rev. Earth Pl. Sc.*, 34:629–653.

Hirshmann, M. M., Aubaud, C., and Withers, A. C. (2005). Storage capacity of H_2O in nominally anhydrous minearals in the upper mantle. *Earth Planet. Sci. Lett.*, 236:167–181.

Hirshmann, M. M., Tenner, T., Aubaud, C., and Withers, A. C. (2009). Dehydration melting of nominally anhydrous mantle: The primacy of partitioning. *Phys. Earth Planet. In.*, 176:54–68.

Hirth, G. and Kohlstedt, D. L. (1996). Water in the oceanic upper mantle: implications for rheology, melt extraction and the evolution of the lithosphere. *Earth Planet. Sci. Lett.*, 144:93–108.

Hirth, G. and Kohlstedt, D. L. (2003). Rheology of the upper mantle and the mantle wedge: A view from the experimentalists. In Eiler, J., editor, *Inside the Subduction Factory*, volume 138 of *Geophys. Monogr. Ser.*, pages 83–105. AGU, Washington, D.C.

Holland, T. J. B. H. and Powell, R. (1998). An internally consistent thermodynamic data set for phases of petrological interest. *J. Metam. Geol.*, 16:309–343.

Hubbert, M. K. and Rubey, W. W. (1959). Role of fluid pressure in mechanics of overthrust faulting: I. mechanics of fluid-filed porous solids and its application to overthrust faulting. *Geol. Soc. Am. Bull.*, 70:115–166.

Isacks, B. and Molnar, P. (1969). Mantle earthquake mechanisms and the sinking of the lithosphere. *Nature*, 223:1121–1124.

Iwamori, H. (1998). Transportation of H_2O and melting in subduction zone. *Earth Planet. Sci. Lett.*, 160:65–80.

Iwamori, H. (2007a). Seismic evidence for deep-water transportation in the mantle. *Chem. Geol.*, 239:182–198.

Iwamori, H. (2007b). Transport of H_2O beneath the japan arcs and its implications for the global water circulation. *Chem. Geol.*, 239:182–198.

Iwamori, H., Richardson, C., and Maruyama, S. (2007). Numerical modeling of thermal structure, circulation of h2o, and magmatism-metamorphism in subduction zones: Implications for evolution of arcs. *Gondwana Res.*, 11(1-2):109–119.

Jackson, J. (2002). Strength of the continental lithosphere: Time to abandon the jelly sandwich ? *Geology*, 12:4–9.

Jaeger, J. C. and Cook, N. G. W. (1976). *Fundamentals of Rock Mechanics*. Chapman and Hall, New York.

Jarvis, G. and Lowman, J. (2007). Survival times of subducted slab remnants in numerical models of mantle flow. *Earth Planet. Sci. Lett.*, 260:23–36.

Johnson, A. M. and Fletcher, R. C. (1994). *Folding of viscous layers: mechanical analysis and interpretation of structures in deformed rock*. Columbia University Press.

Johnson, J., Oelkers, E., and Helgeson, H. (1992a). SUPCRT92: a software package for calculating the standard molal thermodynamic properties of minerals, gases, aqueous species, and reactions from 1 to 5000 bars and 0 to 1000 °c. Technical report, Earth Sciences Department, Lawrence Livermore Laboratory.

Johnson, J. W., Oelkers, E. H., and Helgeson, H. C. (1992b). Supcrt92: A software package for calculating the standard molal thermodynamic properties of minerals, gases, aqueous species, and reactions from 1 to 5000 bar and 0 to 1000 °c. *Comput. Geosci.*, 18(7):899 – 947.

Kameyama, M., Yuen, D. A., and Karato, S.-I. (1999). Thermal-mechanical effects of low-temperature plasticity (the peierls mechanism) on the deformation of a viscoelastic shear zone. *Earth Planet. Sci. Lett.*, 168:159–172.

Karato, S.-I. and Jung, H. (2003). Effects of pressure on high-temperature dislocation creep in olivine. *Philos. Mag.*, 83:401–414.

Karato, S.-I. and Li, P. (1992). Diffusion creep in perovskite and the linear rheology of the Earth's lower mantle. *Science*, 255:1238–1240.

Karato, S.-I. and Wu, P. (1993). Rheology of the upper mantle: A synthesis. *Science*, 260:771–778.

Karpov, I. K., Chudnenko, K. V., and Kulik, D. A. (1997). Modeling chemical mass transfer in geochemical processes: Thermodynamic relations, conditions of equilibria, and numerical algorithms. *Am. J. Sci.*, 297:767–806.

Karpov, I. K., Chudnenko, K. V., Kulik, D. A., Avchenko, O. V., and Bychinskii, V. A. (2001). Minimization of gibbs free energy in geochemical systems by convex programming. *Geochem. Int.*, 39:1108–1119.

Katz, R. F., Spiegelman, M., and Holtzman, B. (2006). The dynamics of melt and shear localization in partially molten aggregates. *Nature*, 442:676–679.

Kaus, B. J. P. (2008). Lagrangian finite element methods for modelling long-term tectonic processes. 2008 Workshop for Advancing Numerical Modeling of Mantle Convection and Lithospheric Dynamics.

Kaus, B. J. P., Liu, Y., Becker, T. W., Yuen, D. A., and Shi, Y. (2009). Lithospheric stress-states predicted from long-term tectonic models: Influence of rheology and possible application to taiwan. *J. Asian Earth Sci.*, 36:119–134.

Kaus, B. J. P., Mühlhaus, H.-B., and May, D. A. (2010). A stabilization algorithm for geodynamic numerical simulations with a free surface. *Phys. Earth Planet. Int.*, 181:12–20.

Kerrick, D. M. and Connolly, J. A. D. (2001). Metamorphic devolatilization of subducted oceanic metabasalts: Implications for seismicity, arc magamtism and volatile recycling. *Earth Planet. Sci. Lett.*, 189:19–29.

Kincaid, C. and Olson, P. (1987). An experimental study of subduction and slab migration. *J. Geophys. Res.*, 92(B13):13832–13840.

Kohlstedt, D. L. and Goetze, C. (1974). Low-stress high-temperature creep in olivine single crystals. *J. Geophys. Res.*, 79(14):2045–2051.

Komabayashi, T., Hirose, K., Funakoshi, K.-I., and Takafuji, N. (2005). Stability of phase A in antigorite (serpentine) composition determined by in situ X-ray pressure observations. *Phys. Earth Planet. In.*, 151:276–289.

Korenaga, J. and Karato, S.-I. (2008). A new analysis of experimental data on olivine rheology. *J. Geophys. Res*, 113(B2):1–23.

Kronbichler, M., Heister, T., and Bangerth, W. (2012). High accuracy mantle convection simulation through modern numerical methods. *Geophys. J. Int.*, 191:12–29.

Kulik, D. A., Berner, U., and Curti, E. (2003). Modelling chemical equilibrium partitioning with the GEMS-PSI code. *Paul Scherrer Institute Scientific Report*, Vloume IV:109–122.

Lallemand, S., Heuret, A., Faccenna, C., and Funiciello, F. (2008). Subduction dynamics as revealed by trench migration. *Tectonics*, 27:TC3014.

Lemiale, V., Mühlhaus, H.-B., Moresi, L., and Stafford, J. (2008). Shear banding analysis of plastic models formulated for incompressible viscous flows. *Phys. Earth Planet. Int.*, 171:177–186.

Levine, H. B. (1962). Chemical equilibrium in complex mixtures. *J. Chem. Phys.*, 36:3049–3050.

Li, Z.-X. and Zhong, S. (2009). Supercontinent-superplume coupling, true polar wander and plume mobility: Plate dominance in whole-mantle tectonics. *Phys. Earth Planet. In.*, 176:143–156.

Litasov, K., Ohtani, E., Langenhorst, F., Yurimoto, H., Kubo, T., and Kondo, T. (2003). Water solubility in Mg-pervoskites and water storage capacity in the lower mantle. *Earth Planet. Sci. Lett.*, 211:189–203.

Lukas, H., Fries, S. G., and Sundam, B. (2007). *Computational Thermodynamics: The Calphad Method*. Cambridge Univ. Press.

Mackwell, S. J. (1991). High-temperature rheology of enstatite: Implications for creep in the mantle. *Geophys. Res. Lett.*, 18(11):2027–2030.

Manea, V. and Gurnis, M. (2007). Subduction zone evolution and low viscosity wedge channels. *Earth Planet. Sci. Lett.*, 264:22–45.

McDonough, W. F. and Sun, S. (1995). The composition of the Earth. *Chem. Geol.*, 120:223–253.

Mei, S. and Kohlstedt, D. L. (2000a). Influence of water on plastic deformation of olivine aggregates 1. diffusion creep regime. *J. Geophys. Res.*, 105:21457–21496.

Mei, S. and Kohlstedt, D. L. (2000b). Influence of water on plastic deformation of olivine aggregates 2. dislocation creep regime. *J. Geophys. Res.*, 105:21471–21481.

Mitrovica, J. X. and Forte, A. M. (2004). A new inference of mantle viscosity based upon joint inversion of convection and glacial isostatic adjustment data. *Earth Planet. Sci. Lett*, 225(1-2):177–189.

Mitrovica, J. Z. (1996). Haskell [1935] revisited. *J. Geophys. Res.*, 101(B1):555–569.

Molnar, P. and Gray, D. (1979). Subduction of continental lithosphere: Some constraints and incertainities. *Geology*, 7:58–62.

Morgan, W. J. (1968). Rises, trenches, great faults, and crustal blocks. *J. Geophys. Res.*, 73:1959–1982.

Morra, G. and Regenauer-Lieb, K. (2006). A coupled solid-fluid method for modelling subduction. *Philos. Mag.*, 86:3307–3323.

Nikolaeva, K., Gerya, T. V., and Connolly, J. A. D. (2008). Numerical modelling of crustal growth in intraoceanic volcanic arcs. *Phys. Earth Planet. In.*, 171:336–356.

Nikolaeva, K., Gerya, T. V., and Marques, F. O. (2010). Subdustion initiation at passive margins: Numerical modeling. *J. Geophys. Res.*, 115:B03406.

Noack, L., Labbe, F., Boiveau, T., Rivoldini, A., and van Hoolst, T. (2014). CHIC - coupling habitability, interior and crust. In *Geophysical Research Abstracts*, volume 16, pages EGU2014–471.

Oelkers, E., Helgeson, H. C., Shock, E. L., Sverjensky, D. A., Johnson, J. W., and Pokrovskii, V. A. (1995). Summary of the apparent standard partial molal Gibbs free energies of formation of aqueous species, minerals and gases at pressures 1 to 5000 bars and temperatures 25 to 1000°c. *J. Phys. Chem. Ref. Data*, 24:1401–1560.

Ohtani, E., Litasov, K., Hosoya, T., Kubo, T., and Kondo, T. (2004). Water transport into the deep mantle and formation of a hydrous transition zone. *Phys. Earth Planet. In.*, 143-144:255–269.

Ohtani, E. and Zhao, D. (2009). The role of water in the deep upper mantle and transition zone: Dehydration of stagnant slabs and its effects on the big mantle wedge. *Russ. Geol. Geophys.*, 50:1073–1079.

Olbertz, D., Wortel, M. J. R., and Hansen, U. (1997). Trench migration and subduction zone geometry. *Geophys. Res. Lett.*, 24:221–224.

Paulson, A., Zhong, S., and Wahr, J. (2007a). Inference of mantle viscosity from GRACE and relative sea level data. *Geophys J Int*, 171(2):497–508.

Paulson, A., Zhong, S., and Wahr, J. (2007b). Limitations on the inversion for mantle viscosity from postglacial rebound. *Geophys. J. Int.*, 168(3):1195–1209.

Peacock, S. (1987). Thermal effects of metamorphic fluids in subduction zones. *Geology*, 15:1057–1060.

Pelletier, D., Frotin, A., and Camarero, R. (1989). Are FEM solutions of incompressible flows really incompressible? (or how simple flows can cause headaches!). *Int. J. Num. Meth. Fluids*, 9:99–112.

Peltier, W. R. and Drummond, R. (2008). Rheological stratification of the lithosphere: A direct inference based upon the geodetically observed pattern of the glacial isostatic adjustment of the North American continent. *Geophys. Res. Lett.*, 35(16):1–5.

Pelton, A. D. (1999). Thermodynamic calculations of chemical solubilities of gases in oxide melts and glasses. *Glass Sci. Technol.*, 72:214–226.

Pelton, A. D. and Wu, P. (1999). Thermodynamic modeling in glass-forming melts. *J. Non-Cryst. solids*, 253:178–191.

Perkins, E. H., Brown, T. H., and Berman, R. G. (1986). PT-system, TX-system, PX-system: Three programs for calculation of pressure-temperature-composition phase diagrams. *Comput. Geosci.*, 12:749–755.

Piromallo, C., Becker, T. W., Funiciello, F., and Faccenna, C. (2006). Three-dimensional instantaneous mantle flow induced by subduction. *Geophys. Res. lett.*, 33:L08304.

Plank, T. and Langmuir, C. H. (1998). The chemical composition of subducting sediment and its consequences for the crust and mantle. *Chem. Geol.*, 145:325–394.

Poli, S. and Schmidt, M. W. (2002). Petrology of subducted slabs. *Annu. Rev. Earth Pl. Sc.*, 30(207–235).

Popov, A. A. and Sobolev, S. V. (2008). SLIM-3D: A tool for three-dimensional thermomechanical modeling of the lithospheric deformation with elasto-visco-plastic rheology. *Phys. Earth Planet. Int.*, 171:55–75.

Powell, R., Holland, T. J. B. H., and Worley, B. (1998). Calculating phase diagrams involving solid solutions via non-linear equations, with examples using THERMOCALC. *J. Metam. Geol.*, 16:577–588.

Putnis, A. (1992). *Introduction to Mineral Science*. Cambridge Univ. Press, Cambridge, UK.

Pysklywec, R. N. and Beaumont, C. (2004). Intraplate tectonics: Feedback between radioactive thermal weakening and crustal deformation driven by mantle lithosphere instabilities. *Earth Planet. Sci. Lett.*, 221:275–292.

Pysklywec, R. N., Beaumont, C., and Fullsack, P. (2000). Modeling the behavior of the continental mantle lithosphere during plate convergence. *Geology*, 28(7):655.

Pysklywec, R. N., Beaumont, C., and Fullsack, P. (2002). Lithospheric deformation during the early stages of continental collision: numerical experiments and comparison with south island, new zealand. *J. Geophys. Res*, 107(7):1–19.

Quinquis, M. E. T., Buiter, S. J. H., and Ellis, S. (2011). The role of boundary conditions in numerical models of subduction zone dynamics. *Tectonophysics*, 497:57–70.

Quinquis, M. E. T., Buiter, S. J. H., Tosi, N., Thieulot, C., Maierová, P., and Quinteros, J. (2013). A numerical model setup for subduction: From linear viscous to thermo-mechanical rheologies. In 2013, E. G. A., editor, *Geophysical Research Abstracts*, volume 15, pages EGU2013–7255–1.

Quinteros, J., Sobolev, S. V., and Popov, A. A. (2010). Viscosity in transition zone and lower mantle: Implications for slab penetration. *Geophys. Res. Lett.*, 37(9):L09307.

Ranalli, G. (1995). *Rheology of the Earth*. Chapman & Hall, London, UK, 2nd edition.

Regenauer-Lieb, K., Yuen, D. A., and Branlund, J. M. (2001). The initiation of subduction: Criticality by addition of water? *Science*, 294:578–580.

Richard, G. C. and Bercovici, D. (2009). Water-induced convection in the earth's mantle transition zone. *J. Geophys. Res.*, 114.

Richard, G. C., Bercovici, D., and Karato, S.-I. (2006). Slab dehydration in the Earth's mantle transition zone. *Earth Planet. Sci. Lett.*, 251(1-2):156–167.

Richard, G. C. and Iwamori, H. (2010). Stagnant slab, wet plumes and Cenozoic volcanism in East Asia. *Phys. Earth Planet. In.*, 183(1-2):280–287.

Richard, G. C., Monnereau, M., and Rabinowicz, M. (2007). Slab dehydration and fluid migration at the base of the upper mantle: implications for deep earthquake mechanisms. *Geophys. J. Int.*, 168:1291–1304.

Ringwood, A. E. (1975). *Composition and Petrology of the Earth's Mantle*. International series in the Earth and planetary sciences. McGraw-Hill, New York.

Robie, R. A. and Hemingway, B. S. (1995). Thermodynamic properties of minerals and related substances at 298.15 K and 1 bar (105 Pascals) pressure and higher temperatures. *U.S. Geological Survery Bulletin*, 2131:461p.

Rosenbaum, G. and Lister, G. (2005). The western alps from the jurassic to oligocene: spatio-temporal constraints and evolutionary reconstructions. *Earth-Sci. Rev.*, 69(3-4):281–306.

Ross, J. V. and Nielsen, K. C. (1978). High-temperature flow of wet polycrystalline enstatite. *Tectonophysics*, 44(1–4):233–261.

Rüpke, L. H., Phipps Morgan, J., Hort, M., and Connolly, J. A. D. (2004). Serpentine and the subduction zone water cycle. *Earth Planet. Sci. Lett.*, 223:17–34.

Saad, Y. (2003). *Iterative Methods for Sparse Linear Systems*. SIAM, Philadelphia, 2nd edition.

Saxena, S. K. and Eriksson, G. (1985). Anhydrous phase equilibria in earth's upper mantle. *J. Petrol.*, 26:378–390.

Schellart, W. P. (2005). Influence of the subducting plate velocity on the geometry of the slab and migration of the subduction hinge. *Earth Planet. Sci. Lett.*, 231:197–219.

Schellart, W. P. (2008a). Kinematics and flow patterns in deep mantle and upper mantle subduction models: Influence of the mantle depth and slab to mantle viscosity ratio. *Geochem. Geophy. Geosys.*, 9:29pp.

Schellart, W. P. (2008b). Subduction zone trench migration: Slab driven or overriding-plate-driven ? *Phys. Earth Planet. In.*, 170:73–88.

Schellart, W. P. (2009). Evolution of the slab bending radius and the bending dissipation in three-dimensional subduction models with a variable slab to upper mantle viscosity ratio. *Phys. Earth Planet. In.*, 288:309–319.

Schenk, O., Gärtner, K., and Fichtner, W. (2000). Efficient sparse LU factorization with left-right looking strategy on shared memory multiprocessors. *BIT Numerical Mathematics*, 40:158–176.

Schmeling, H., Babeyko, A. Y., Enns, A., Faccenna, C., Funiciello, F., Gerya, T. V., Golabek, G. J., Grigull, S., Schmalholz, S., and van Hunen, J. (2008). A benchmark comparison of spontaneous subduction models - towards a free surface. *Phys. Earth Planet. Int.*, 171:198–223.

Schmidt, M. and Poli, S. (1998). Experimentally based water budgets for dehydrating slabs and consequences for arc magma generation. *Earth Planet. Sci. Lett.*, 163:361–379.

Schubert, G., Turcotte, D. L., and Olson, P. (2001). *Mantle Convection in the Earth and Planets*. Cambridge Univ. Press.

Shahnas, M. H. and Jarvis, G. T. (2007). On the relative importance of mineral phase transitions and viscosity stratification in controlling the sinking rates of detached slab remnants. *Geophys. Res. lett.*, 34:L11302.

Sibson, R. H. (1977). Fault rocks and fault mechanisms. *J. Geol. Soc. London*, 133:191–213.

Sibson, R. H., M., M. J. M., and H., R. A. (1975). Seismic pumping - a hydrothermal fluid transport mechanism. *J. Geol. Soc. London*, 131:653–9.

Siebert, L. and Simkin, T. (2002). Volcaonoes of the world: An illustrated catalogue of holocene volcanoes and their eruptions. *Smithsonian Institution, Global Volcanism Program Digital Information Series*, GVP-3.

Silver, E., Kastner, M., Fisher, A., Morris, J., McIntosh, K., and Saffer, D. (2000). Fluid flow paths in the middle american trench and costa rica margin. *Geology*, 28:679–682.

Sobolev, S. V. and Babeyko, A. Y. (2005). What drives orogeny in the Andes? *Geology*, 33:617–620.

Spiegelman, M. (1993a). Flow in deformable porous media. part 1. simple analysis. *J. Fluid. Mech.*, 247:17–38.

Spiegelman, M. (1993b). low in deformable porous media. part 2. numerical analysis - the relationship between shock waves and solitary waves. *J. Fluid. Mech.*, 247:39–63.

Spiegelman, M. and Katz, R. F. (2006). A semi-Lagrangian Crank-Nicolson algorithm for the numerical solution of advection-diffusion problems. *Geochem. Geophys. Geosyst.*, 7.

Spiegelman, M. and Kelemen, P. B. (2003). Extreme chemical variability as a consequence of channelized melt transport. *Geochem. Geophy. Geosys.*, 4(7):1055.

Spiegelman, M., Kelemen, P. B., and Aharonov, E. (2001). Causes and consequences of flow organization during melt transport: The reaction infiltration instability in compactible media. *J. Geophys. Res.*, 106(B2):2061–2077.

Staudigel, H. (2003). Hydrothermal alteration processes in the oceanic crust. In *Treatise of Geochemistry*, volume 3, chapter 15, pages 511–537. Holland, H. and Turekian, K (eds.).

Stegman, D. R., Farrington, R., Capitanio, F. A., and Schellart, W. P. (2010). A regime diagram for subduction styles from 3-D numerical models of free subduction. *Tectonophysics*, 483:29–45.

Steinberger, B. and Calderwood, A. R. (2006). Models of large-scale viscous flow in the earth's mantle with constraints from mineral physics and surface observations. *Geophys J Int*, 167(3):1461–1481.

Stern, R. (2002). Subduction zone. *Rev. Geophys.*, 40(4):1012.

Syracus, E. M. and Abers, G. A. (2006). Global compilations of bariations in slab depth beneath arc volcanoes and implications. *Geochem. Geophy. Geosys.*, 7:Q05017.

Thieulot, C. (2011). FANTOM: two- and three-dimensional numerical modelling of creeping flows for the solution of geological problems. *Phys. Earth Planet. Int.*

Tichelaar, B. W. and Ruff, L. J. (1993). Depth of seismic coupling along subduction zones. *J. Geophys. Res.*, 98(B2):2017–2037.

Tingle, T., Green, H. W., Scholz, C. H., and Koczynski, T. A. (1993). The rheology of faults triggered by the olivine-spinel transformation in mg_2geo_4 and its implications for the mechanism of deep-focus earthquakes. *J. Struct. Geol.*, 15:1249–1256.

Tosi, N., Sabadini, R., Marotta, A. M., and Vermeersen, L. L. A. (2005). Simultaneous inversion for the earth's mantle viscosity and ice mass imbalance in antarctica and greenland. *J. Geophys. Res.*, 110:B07402.

Toussaint, G., Burov, E., and Avouac, J.-P. (2004a). Tectonic evolution of a continental collision zone: A thermomechanical numerical model. *Tectonics*, 23:TC6003.

Toussaint, G., Burov, E., and Avouac, J. P. (2004b). Tectonic evolution of a continental collision zone: A thermomechanical numerical model. *Tectonics*, 23(6):TC6003.

Toussaint, G., Burov, E., and Jolivet, L. (2004c). Continental plate collision: Unstable vs. stable slab dynamics. *Geology*, 32(1):33–36.

Tuminaro, R. S. and Tong, C. (2000). Parallel smoothed aggregation multigrid: Aggregation strategies on massively parallel machines. In *Super Computing 2000 Poceedings*.

Turcotte, D. L. and Schubert, G. (2002). *Geodynamics*. Cambridge Univ. Press, 2nd edition.

Twiss, R. J. and Moores, E. M. (1992). *Structural Geology*. W. H. Freeman and Company, New York.

van den Berg, A. P., van Keken, P. E., and Yuen, D. A. (1993). The effects of a composite non-newtonian and newtonian rheology on mantle convection. *Geophys. J. Int.*, 115:62–78.

van Keken, P. E., Currie, C., King, S. D., Behn, M. D., Cagnioncle, A.-M., He, J., Katz, R. F., Lin, S. C., Parmentier, E. M., and Spiegelman, M. (2008). A community benchmark for subduction zone modeling. *Phys. Earth Planet. Int.*, 171:187–197.

Čížková, H., van Hunen, J., and van den Berg, A. (2007). Stress distribution within subducting slabs and their deformation in the transition zone. *Phys. Earth Planet. Int.*, 161:202–214.

Čížková, H., van Hunen, J., van den Berg, A., and Vlaar, N. (2002). The influence of rheological weakening and yield stress on the interaction of slabs with the 670 km discontinuity. *Earth Planet. Sci. Lett.*, 199:447–457.

Wadati, K. (1935). On the activity of deep-focus earthquake s in the japan islands and neighbourhoods. *Geophys. Mag.*, 8:305–325.

Wark, D. A., Williams, C. A., Watson, E. B., and Price, J. D. (2003). Reassessment of pore shapes in microstructurally equilibrates rocks, with implications for permeability of the upper mantle. *J. Geophys. Res.*, 108(B1):2050.

Warren, C. J., Beaumont, C., and Jamieson, R. A. (2008a). Deep subduction and rapid exhumation: Role of crustal strength and srtain weakening in continental subduction and ultrahigh-pressure rock exhumation. *Tectonics*, 27:TC6002.

Warren, C. J., Beaumont, C., and Jamieson, R. A. (2008b). Modelling tectonic styles and ultra-high pressure (UHP) rock exhumation during the transition from oceanic subduction to continental collision. *Earth Planet. Sci. Lett.*, 267:129–145.

Warren, J. M. and Hirth, G. (2006). Grain size sensitive deformation mechanics in naturally deformed peridotites. *Earth Planet. Sci. Lett.*, 248:438–450.

White, S. H. and Knipe, R. J. (1978). Transformation-and reaction-enhanced ductility in rocks. *J. Geol. Soc. London*, 135:513–516.

White, W. B., Johnson, S. M., and Dantzig, G. B. (1958). Chemical equilibrium in complex mixtures. *J. Chem. Phys.*, 28:751–755.

Yamato, P., Husson, L., Braun, J., Loiselet, C., and Thieulot, C. (2009). Influence of surrounding plates on 3D subduction dynamics. *Geophys. Res. Lett.*, 36.

Zack, T. and John, T. (2007). An evaluation of reactive fluid flow and trace element mobility in subducting slabs. *Chem. Geol.*, 239(3-4):199–216.

Zienkiewicz, O. C. and Taylor, R. L. (2000a). *The Finite Element Method, Volume 1: The Basis*. Butterworth-Heinemann, fith edition edition.

Zienkiewicz, O. C. and Taylor, R. L. (2000b). *The Finite Element Method, Volume 3: Fluid Dynamics*. Butterworth-Heinemann, fifth edition edition.

List of Figures

1.1 Plate boundaries and subduction zones 2
1.2 Cartoon of the main processes occurring in a subduction system. . 2
1.3 Location of upper mantle earthquakes 3
1.4 The common deformation styles of the subducting lithosphere . . 7
1.5 The two strength profiles of the lithosphere 8
1.6 Cartoon of the main dehydration processes occurring during subduction. 11
1.7 Serpentinized Hartzburgite phase diagrams calculated using Perple_X 13
1.8 Serpentinized Hartzburgite water content calculated using Perple_X 14

2.1 A one component phase diagram calculated for aluminosilicates using Perple_X 22
2.2 Schematic isobaric-isothermal free energy-composition diagrams for a binary system 27
2.3 Mapping algorithm used in Perple_X 28
2.4 Schematic migration of free water 32
2.5 Viscosity as a function of depth 33

3.1 Gravitational and ocean-ocean model setups 41
3.2 The combination of different surface boundary conditions and crustal rheologies 45
3.3 Quantification of results for the gravitational subduction models . 48
3.4 Effects of laterally decoupled slabs 49
3.5 Effects of the lateral boundary conditions 50
3.6 Quantification of results for ocean-ocean models 51
3.7 Effects of adding a linear viscous lower mantle to ocean-ocean subduction models 53
3.8 Quantification of results for ocean-ocean models with a lower mantle 54
3.9 Topography plots when using an ‘air’ layer or a free surface . . . 55
3.10 Effects of a ’sticky air’ layer 55
3.11 Quantification of results from ocean-ocean type models including a ’sticky air’ layer 56

3.12 Simple schematics of free-slip and free surface model evolution . 57

4.1 Compilation of viscosity profiles as a function of depth 70
4.2 Model setup for subduction models 72
4.3 Case 1 common output plots 79
4.4 Case 1 subduction evolution 80
4.5 Effects of grid resolution and particle density on trench position . 81
4.6 Temperature distribution at t=12.5 Myr for linear viscous case 2 model, computed with SULEC. 82
4.7 Case 2 common output plots 83
4.8 Comparison of case 2b results 84
4.9 Density profiles at 12 Myr for cases 2 and 2b calculated using SULEC 85
4.10 Viscosity fields at A) 2, B) 8 and C) 15 Myr for thermo-mechanical case 3. The model was calculated using SULEC. 87
4.11 Case 3 common output plots 88
4.12 Case 4 common output plots 89
4.13 Case 4 thermo-mechanical model viscosity plots at 2, 8 and 15 Myr 90
4.14 Results for linear viscous models using SULEC with either a free-slip surface or a free surface 95
4.15 Results for thermo-mechanical models (case 4) using SULEC with either a free-slip surface or a free surface 96
4.16 Results for linear viscous models with different lithospheric densities 98

5.1 BOC and SHB Water content as a function of pressure and temperature 111
5.2 Water content of mantle material as a function of pressure and temperature 112
5.3 Schematic migration of free water and it's distribution 114
5.4 The effects of bound water coupled to viscosity 116
5.5 Sinking cylinder model setup and geotherm 118
5.6 Elemental water content for the Stokes flow models using scheme I 120
5.7 Sinking cylinder result plots 121
5.8 Depth of the bottom of the subducting cylinder versus time 122
5.9 Subduction model setup 124
5.10 Bound water distribution for subduction models 128
5.11 Free water distribution for subduction models 129
5.12 Subduction model result plots 130
5.13 Viscosity field for models that follow the Darcy free water migration 132
5.14 Bound water distribution for subduction models using Darcy free water migration 133

5.15 Free water distribution for subduction models using Darcy free water migration 134
5.16 Viscosity fields in the mantle wedge for subduction models calculated using the imposed free water migration 136

List of Tables

2.1 Flow law parameters from Hirth and Kohlstedt (2003) 34

3.1 List of gravitational subduction models 43
3.2 List of ocean-ocean convergent models. 44

4.1 Linear viscous model input parameters 73
4.2 Thermo-mechanical model parameters (cases 2-4) 75
4.3 Flow law parameters for cases 3 and 4. 76
4.4 ELEFANT model parameters 82
4.5 Case 1 results at 2, 8 and 12.5 Myr 100
4.6 Case 2 thermal results at 2, 8 and 12.5 Myr 101
4.7 Case 2b results at 2, 8 and 12.5 Myr 102
4.8 Case 3 results at 2, 8 and 12.5 Myr 103
4.9 Case 4 results at 2, 8 and 12.5 Myr 104

5.1 Bulk compositions in % for the oceanic lithosphere model 112
5.2 Input parameters for the linear viscous sinking cylinder model . . 118
5.3 Subduction model parameters 125
5.4 Flow law parameters from Hirth and Kohlstedt (2003) 126